

Multiwavelength Analysis of two Peculiar  
High Mass X-Ray Binary Systems:  
4U 2206+54 and SAX J2103.5+4545  
New insights from *INTEGRAL*



Pere Blay  
PhD Thesis  
February, 2006

UMI Number: U607767

All rights reserved

INFORMATION TO ALL USERS

The quality of this reproduction is dependent upon the quality of the copy submitted.

In the unlikely event that the author did not send a complete manuscript and there are missing pages, these will be noted. Also, if material had to be removed, a note will indicate the deletion.



UMI U607767

Published by ProQuest LLC 2014. Copyright in the Dissertation held by the Author.  
Microform Edition © ProQuest LLC.

All rights reserved. This work is protected against  
unauthorized copying under Title 17, United States Code.



ProQuest LLC  
789 East Eisenhower Parkway  
P.O. Box 1346  
Ann Arbor, MI 48106-1346



UNIVERSITAT DE VALÈNCIA	
BIBLIOTECA CIÈNCIES	
Nº Registre	24977
DATA	22/02/02
SIGNATURA	TD-F /526
Nº LIBIS:	C. 19570508

23 und.

After the plane took off, my brother showed me a piece of scientific apparatus which he had brought along. It was a photoelectric cell connected to a small tape recorder. He aimed the electric eye at clouds. It perceived lightning flashes which were invisible to us in the dazzle of daytime.

The secret flashes were recorded as clicks by the recorder. We could also hear the clicks as they happened – on a tiny earphone.

"There's a hot one," my brother announced. He indicated a distant cumulus cloud, a seeming Pike's Peak of whipped cream.

He let me listen to the clicks. There were two quick ones, then some silence, then three quick ones, then silence again.

"How far away is that cloud?" I asked him.

"Oh – a hundred miles, maybe," he said.

I thought it was beautiful that my big brother could detect secrets so simply from so far away.

*Kurt Vonnegut, in Slapstick*



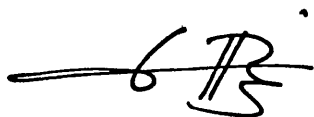


**Dr. Pablo Reig Torres,**  
investigador del *Skinakas Observatory* (University of Crete and Foundation  
for Research & Technology – HELLAS, Grècia),

CERTIFICA:

Que la present memòria, "Multiwavelength Analysis of two peculiar  
High Mass X-Ray Binary systems: 4U 2206+54 and SAX J2103.5+4545.  
New insights from INTEGRAL", ha sigut realitzada sota la seua direcció,  
per Pere Blay Serrano, i que constitueix la seua tesi doctoral per tal d'optar  
al grau de Doctor en Física.

I per tal que quede constància i tinga els efectes que corresponga, signa  
el present certificat en València, a 1 d'Octubre de 2005.

A handwritten signature in black ink, consisting of a stylized 'P' and 'R' with a horizontal line through them, and a small dot above the 'R'.

Signat: Pablo Reig Torres

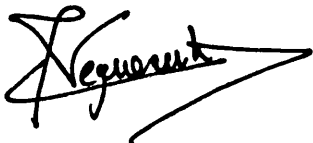


**Dr. Ignacio Negueruela Díez,**  
investigador de la Universitat d'Alacant,

CERTIFICA:

Que la present memòria, "Multiwavelength Analysis of two peculiar High Mass X-Ray Binary systems: 4U 2206+54 and SAX J2103.5+4545. New insights from INTEGRAL", ha sigut realitzada sota la seua direcció, per Pere Blay Serrano, i que constitueix la seua tesi doctoral per tal d'optar al grau de Doctor en Física.

I per tal que quede constància i tinga els efectes que corresponga, signa el present certifica en València, a 1 d'Octubre de 2005.



Signat: Ignacio Negueruela Díez



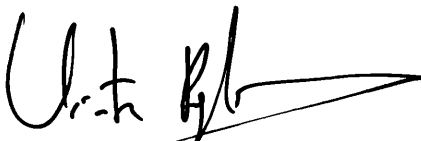


**Dr. Víctor Reglero,**  
catedràtic de la Universitat de València,

CERTIFICA:

Que la present memòria, "Multiwavelength Analysis of two peculiar High Mass X-Ray Binary systems: 4U 2206+54 and SAX J2103.5+4545. New insights from INTEGRAL", ha sigut realitzada sota la seua direcció, per Pere Blay Serrano, i que constitueix la seua tesi doctoral per tal d'optar al grau de Doctor en Física.

I per tal que quede constància i tinga els efectes que corresponga, signa el present certificat en València, a 1 d'Octubre de 2005.

A handwritten signature in black ink, appearing to read 'Victor Reglero Velasco', with a long horizontal stroke extending to the right.

Signat: Víctor Reglero Velasco



**Para Irene y Maribel,  
por el amor en nuestras vidas.**

**To Irene and Maribel,  
for the love in our lives.**





## Acknowledgments / Agraïments

It was seven years ago when I sat down in front of a computer to analyse for the very first time the spectrum of a Be star. I was in charge to confirm the spectral classification of the optical counterpart to LS5039, now known to be a microquasar. Like LS5039, data from many other sources kept me busy all along these years. I was lucky to be able to treat such a large amount of data, thanks to all the people who shared their data and/or knowledge with me and also thanks to all the resources available in the Internet. From that heap of data this thesis work arose.

I want to thank my thesis supervisors, Ignacio, Pablo and Victor, for all the support and all the collaborations from long before they became my thesis supervisors. Without Pablo's and Ignacio's guidance the scientific course I have followed would not have been so straightforward. Victor always supplied funding for everything I needed, and optimism to push me on the adventure of researching new fields.

The results of this work would not have been possible without collaborations with many individuals. The excellent work of Silvia Martínez with JEM-X data, and the thorough, detailed, and accurate work of Choni (Ascensión Camero) and Paul Connell with SPI data, are a very important part of this thesis work. Thanks a lot to them all. Let us hope we can go on sharing data, work, results, comments, etc., for a very long time.

The working atmosphere is also a very important part of everyday routine. Thanks to the very nice people in the GACE, this atmosphere was (also is; and surely will be) always the best. Hand shakes for all GACE people, the ones presently active and the ones who were part of it in the past (still part of it in the minds and hearts of many of us).

Related to science, I also need to thank those who helped me in many issues, which may seem unimportant but which pushed a lot my work. Thanks to people like C. Allard, T. Marsh, M. Bly, L. Georgiev, P. Dufton, N. Produit, P. Kretschmar, A. Herrero, and many others who shared pieces of software and/or knowledge that solved some of the problems I found in my way. Thanks also to M. Ribó for the long conversations on the phone about scientific topics, they helped me a lot to focus in the actual problems and not to loose time with distractions.

During the last two years, the more intense ones in terms of work related to the thesis, Maribel was the one who has most bore with me. She was always so patient as to listen to my boring tales about work, to push me to go further on, and to share with me all her love and care. There are not enough words to give thanks for that. Now we are three, i.e., I am three times more happy and infinite times more thankful.

Thanks also to my two families, the old (my parents, my brothers and my sister) and new ones (Maribel's family). They all make many hard times more bearable and smoother. And the most interesting thing, they all have always believed in me, even in this unstable world of science.

Last, but not least, thanks to Ricard, Pau, Miquel, Ivan, Lluís, Pep, Hector for the very good past and present times, for the laughs and the talks, for the beers and the trips, and for being friends.

Thanks (for forgiving me) to all the ones who I should thank, but i didn't, surely they will know how much forgettable i can be.

A last word of thanks for the three referees of this thesis: J. Casares, P. Kretschmar and M. Ribó, and to Rüdiger Staubert, for all the patience and dedication in reading carefully this work and sending a whole bunch of useful and interesting comments and corrections. They all have helped a lot to improve the scientific quality of this work.

---

Va ser set anys enrera quan, per primera vegada, vaig seure davant d'un ordinador per tal d'analitzar l'espectre d'un estel Be. Aquell estel era LS5039, del qual és sabut ara que es tracta d'un microquasar. La tasca encomanda va ser la confirmació de la classificació espectral de l'objecte. Dades de molts més objectes m'han mantigut ocupat all llarg de tots aquests anys. Vaig tindre sort de poder accedir a una quantitat molt gran de dades, gràcies a totes les persones que han compartit amb mi dades i/o coneixements i gràcies a tots els recursos que es poden trobar a la xarxa. El meu treball de tesi ha emergit de tot aquest muntó de dades.

Vull donar les gràcies als meus supervisors, Ignacio, Pablo i Víctor, per tot el recolzament i totes les col·laboracions dutes a terme, des de molt abans de convertir-se en els meus supervisors. Sense el guiatge d'Ignacio i Pablo, el meu rumb científic no haguera estat tant ben encaminat. Víctor sempre ha aportat fons per a tot allò que he necessitat, i el seu optimisme ha sigut sempre una espenta per a sumergir-me en l'aventura de la recerca.

Els resultats d'aquest treball de tesi no hagueren sigut possibles sense col·laboracions amb moltes persones. El treball excel·lent de Silvia Martínez amb les dades de JEM-X, i la minuciositat, el detallisme i la precisió del treball de Choni (Ascensión Camero) i Paul Connel amb les dades d'SPI, són una part molt important d'aquest treball. Gràcies als tres. Esperem que puguem continuar compartint dades, treball, resultats, comentaris, etc., per molt més temps.

L'ambient de treball és molt important a l'hora d'enfrontar-se a la rutina diària. Gràcies a la bona gent del GACE, aquest ambient ha sigut (i és, i segurament serà) sempre el millor. Apretons de mans per a tots els membres del GACE, els que som ara i els que han passat per ací (encara membres del GACE per a molts de nosaltres).

Relacionats amb el món de la ciència, he d'agraïr a tots aquells que m'han prestat ajut en moltes ocasions, de vegades en detalls que podem semblar sense importància, però que han suposat una gran espenta al meu treball. Gràcies a gent com C. Allard, T. Marsh, M. Bly, L. Georgiev, P. Dufton, N. Produit, P. Kretschmar, A. Herrero, i molts més, per compartir programes i/o coneixements que solucionaren molts dels problemes que vaig trobar en el meu camí. Gràcies també a Marc Ribó per totes les llargues converses telefòniques sobre temes científics, m'han ajudat molt a saber enfocar el meu treball en els problemes científics de debó i no predre temps amb distraccions.

Al llarg dels últims dos anys, els més intensos en quant al meu treball de tesi, Maribel ha sigut la persona que m'ha hagut de suportar. Ella sempre ha tingut una gran paciència a l'hora d'escoltar els meus aborrits comptes relacionats amb temes de treball, m'ha animat a continuar treballant i ha compartit amb mi tot el seu amor i les seues atencions. No existeixen prou paraules per agrair tot açò. Ara som tres, és a dir, sóc tres vegades més feliç i estic infinitament més agraït.

Gràcies a les meues dues famílies, la de sempre (els meus pares, ger-

mans i germana) i la nova (la família de Maribel). Tots han fet més suaus i suportables els moments durs. El més curiós de tot: han cregut sempre en mi, tot i que el món de la ciència és tan inestable.

Per últim, però no menys important, gràcies a Ricard, Pau, Miquel, Ivan, Lluís, Pep i Hèctor per tots els bons moments, passats i presents, per les rialles i les converses, per les cervesses i els viatges, i per ser amics.

Gràcies (per perdonar-me) a totes les persones que hauria d'haver inclòs en els agraïments, però que no hi són, segurament tots ells sabran com de despistat puc arribar a ser.

Unes últimes paraules d'agraïment per als tres evaluadors: J. Casares, P. Kretschmar i M. Ribó, a més de Rüdiger Staubert, per tota la paciència i dedicació a l'hora de llegir-se detenidament aquest treball, i enviar-me un bon grapat de comentaris i correccions. Tots han contribuït, sens dubte, a millorar la qualitat científica d'aquest treball.

## Preface

This work summarises several years of efforts trying to understand the physics behind the behaviour of HMXRBs (which stands for High Mass X-Ray Binaries).

HMXRBs are composed of a compact object (neutron star or black hole) and an early type star (with an important loss of mass). Matter leaving the early type star will accrete onto the compact object. The energy gained by this matter, by its acceleration in the compact object's gravitational potential well, will be released as high energy photons when interacting with the compact object's surface (in the case of neutron stars) and/or will be emitted thermally if an accretion disk is formed (this is valid for both, neutron stars and black holes).

In low energy bands (optical, IR, UV), these systems are characterised by the spectrum of a star with high mass loss rate: with prominent P-Cygni profiles, in the case of supergiant systems; or by one or more Balmer lines in emission and infrared excess typical of Be stars. If the compact companion is a neutron star the high energy emission is modulated by the rotational velocity of the compact object and detected as pulses. There exists a correlation between the pulse period of the compact companion and the orbital period of the system (direct correlation in the case of BeX systems, but anti-correlation in the case of supergiant systems).

Why 4U 2206+54 and SAX J2103.5+4545?

We present a multiwavelength analysis of two of these systems, namely 4U 2206+54 and SAX J2103.5+4545. Both of them show peculiarities which make them difficult to classify in the general scheme. We will discuss their observational properties and review why they are so peculiar. New, previously unpublished, results about their nature will be presented.

- **4U 2206+54:** This source shows X-ray variability typical of those systems in which the matter available for accretion onto the compact object is supplied by the stellar wind of the optical component. In these *wind-fed* systems the optical component is a supergiant. In the case of 4U 2206+54, its optical counterpart (BD+53°2790), shows a spectrum typical of a main sequence star. Furthermore, BD+53°2790 has a circumstellar envelope which reminds that of the

Be stars. Then, we could think of 4U 2206+54 as a BeX system, in which the compact component is a neutron star. A priori, whether there is a neutron star or a black hole in 4U 2206+54, it is not yet clear. In this work we show evidence that point towards the neutron star as the most likely compact component in 4U 2206+54. Yet, the absence of pulsations in the X-ray emission of this systems is difficult to conciliate with the neutron star interpretation. Thus, it is not straightforward to classify 4U 2206+54 as a BeX. We are facing a system that does not fit in the classical classification scheme of the HMXRBs.

- **SAX J2103.5+4545:** There is no doubt about the classification of this system as a BeX. In spite of that, SAX J2103.5+4545 shows a set of peculiarities which make it different from rest of BeXs: it does not follow the correlation between the orbital period and the pulsation period found in BeXs; it is one of the BeXs with the shortest orbital period known; the proximity of the two components of the system, and the interaction of the neutron star with the Be star's circumstellar envelope, lead to a very special phenomenology. This system shows periods of increased brightness, with X-ray emission modulated with the orbital period, and low luminosity periods in which no orbital modulation is detected.

This thesis work is divided in three parts. They are organised as follows:

- **Part I.** High Energy Astrophysics.

In this part we will introduce the general properties of HMXRBs and its constituents (early type stars and compact objects). Emphasis will be given to those properties which will be reviewed observationally along the thesis work. The INTEGRAL satellite and the tools used to analyse its data will be described in a dedicated chapter.

- **Part II.** The HMXRB 4U 2206+54.

This part is dedicated to the source 4U 2206+54. After introducing the source and describing its properties, a review of all the observations and measurements, in all the energy bands analysed, will be presented:

1. Radio bands: with data from VLA.
2. Infrared bands: with spectroscopy and photometry from several astronomical facilities.
3. Optical bands: with a very comprehensive set of spectroscopic data and photometry from several astronomical facilities.
4. UV: with IUE spectra
5. High energies (X and  $\gamma$ -rays): with INTEGRAL and RXTE data.

In the discussion, the observational peculiarities described in all the above bands will be collected and commented, always with the multiwavelength approach in mind. Only when data from very diverse energy bands is combined, this system starts to unveil its secrets. This multiwavelength study allowed us to reveal, for the first time, the true nature of the two components of this peculiar HMXRB.

From Radio observations and *INTEGRAL* data, we can reach conclusions about the nature of the compact object in 4U 2206+54. Evidence points toward the neutron star interpretation.

From a combination of UV, Optical and IR observations a classification of O9.5V is derived for BD+57°2709, the optical counterpart to the system. Furthermore, for the first time, a radial velocity analysis is presented and the orbital parameters are constrained.

All the results presented in this thesis work about this source have been accepted for publication. They are distributed in three papers. In two of them I am the first author:

– P. Blay, M. Ribó, I. Negueruela, J.M. Torrejón, P. Reig, A. Camero, I.F. Mirabel, and V. Reglero 2005, *A&A*, 438, 963

– P. Blay, I. Negueruela, P. Reig, M.J. Coe, R.H.D. Corbet, J. Fabregat, and A.E. Tarasov, 2005, *A&A*, 406, 1095

and in the third one I am a co-author and contributed only partially:



– Ribó, M., Negueruela, I., Blay, P., Torrejón, J. M., & Reig, P. 2005, *A&A*, in press astro-ph/0511408

- **Part III. The BeX SAX J2103.5+4545.**

In this part the BeX system SAX J2103.5+4545 is analysed in detail. Optical data collected mainly from the Skinakas observatory, Crete (Greece) will give us clues about the spectral classification of the optical counterpart and the behaviour of its circumstellar disk. These topics will be reviewed in the second chapter of this part, after a general introduction to the source and its previously known properties are given in the first chapter. The correlation of the vanishing of the shell profile (characteristic of Be stars) with the offset of the bright state of the source will also be discussed. In the following chapter, the high energy data from INTEGRAL will be analysed and important conclusions about the pulse period history and the spectral behaviour of the source will be derived. High energy data will show us for the first time alternate spin-ups and spin-downs in the pulse period of the system. Furthermore, a spectral characterisation of the faint and bright state can be performed in energies above 20 keV for the first time with SPI data. In the discussion all the available data (optical and high energies) will be put together. A discussion about the interaction of the neutron star with the Be star circumstellar disk is possible when the multiwavelength approach is considered.

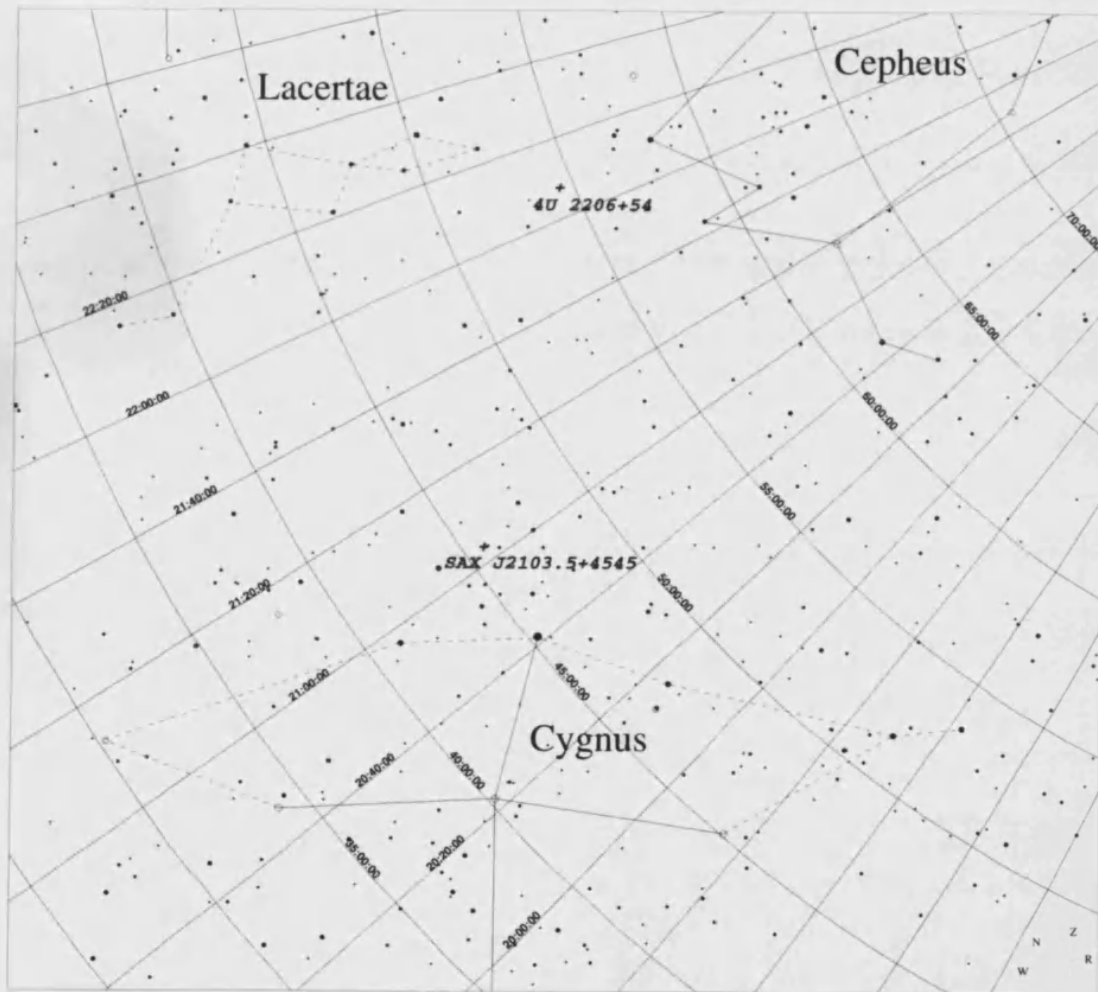
Part of the results on this source have been published in:

– P. Blay, P. Reig, S. Martínez Núñez, A. Camero, P. Connell, and V. Reglero 2004, *A&A*, 427, 293

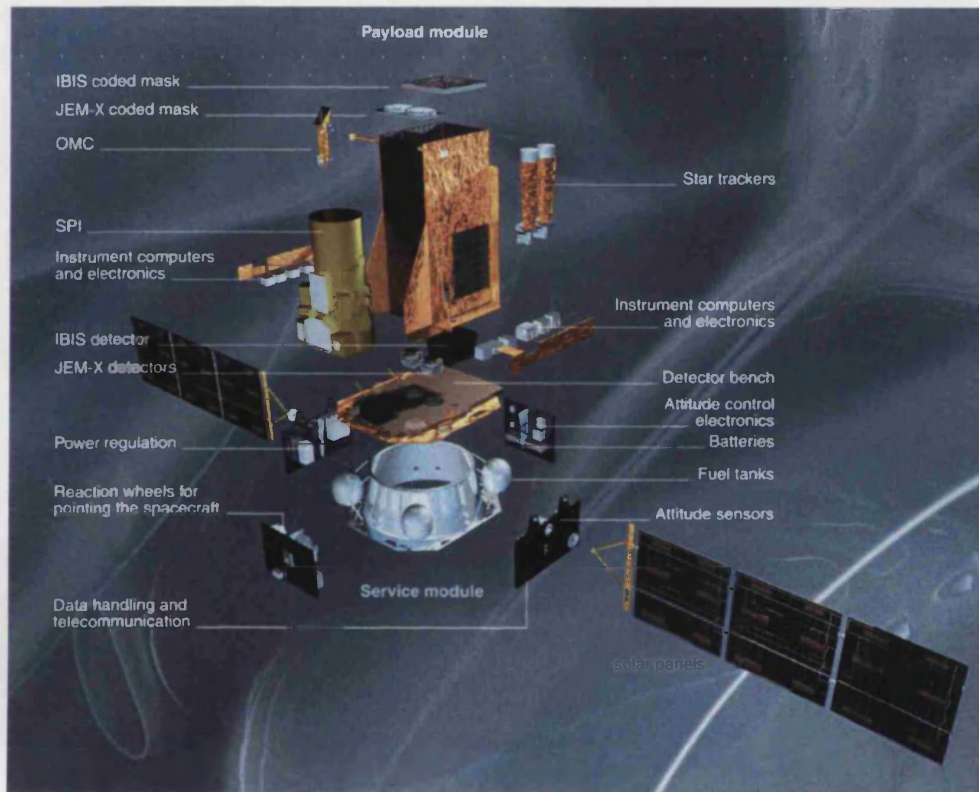
and I have a small contribution in:

– P. Reig, I. Negueruela, J. Fabregat, R. Chato, P. Blay, and F. Mavromatakis, 2004, *A&A*, 421, 673

Finding chart of the two systems analysed in this work,  
SAX J2103.5+4545 and 4U 2206+54.







All pictures courtesy of ESA.



# Contents

<b>I</b>	<b>High Energy Astrophysics</b>	<b>1</b>
<b>1</b>	<b>Observation of the High Energy Universe</b>	<b>3</b>
1.1	General Introduction . . . . .	3
1.2	Astrophysical processes and scenarios related to High Energy photons . . . . .	7
<b>2</b>	<b>High Mass X-Ray Binary Systems</b>	<b>13</b>
2.1	X-ray binary systems . . . . .	13
2.2	Massive (OB) stars . . . . .	16
2.2.1	Stellar winds . . . . .	17
2.2.2	Be phenomenon . . . . .	20
2.3	Compact objects . . . . .	24
2.4	Accretion onto compact objects . . . . .	25
2.4.1	Spherical accretion (and wind-fed accretion) . . . . .	25
2.4.2	Accretion through a disk . . . . .	28
2.4.3	In the presence of magnetic fields . . . . .	29
2.5	BeX systems . . . . .	31
<b>3</b>	<b>INTEGRAL</b>	<b>35</b>
3.1	Coded Mask aperture systems . . . . .	36
3.2	INTEGRAL observing time and observational strategy . . . . .	41
3.3	Instruments . . . . .	42
3.3.1	IBIS . . . . .	42
3.3.2	SPI . . . . .	44
3.3.3	JEM-X . . . . .	46
3.3.4	OMC . . . . .	48

3.4	Software . . . . .	49
3.4.1	INTEGRAL data repository . . . . .	49
3.4.2	INTEGRAL Data Analysis Software . . . . .	52
3.5	Analysis Tools . . . . .	56
3.5.1	High Energy Astrophysics software . . . . .	56
3.5.2	Imaging . . . . .	57
3.5.3	Timing analysis . . . . .	57
3.5.4	Spectral analysis . . . . .	58
3.5.5	Alternative methods . . . . .	60
<b>II</b>	<b>The High Mass X-Ray Binary system 4U 2206+54</b>	<b>67</b>
<b>4</b>	<b>Introduction</b>	<b>69</b>
<b>5</b>	<b>Radio Observations</b>	<b>77</b>
<b>6</b>	<b>The Infra-Red region</b>	<b>81</b>
6.1	Infrared Spectroscopy . . . . .	81
6.2	Infrared Photometry . . . . .	82
<b>7</b>	<b>Optical Band</b>	<b>89</b>
7.1	Optical Spectroscopy . . . . .	89
7.1.1	Observations . . . . .	89
7.1.2	Data Reduction . . . . .	92
7.1.3	Analysis . . . . .	95
7.1.4	Intensive monitoring campaigns . . . . .	106
7.1.5	Radial Velocities and Orbital Parameters . . . . .	117
7.2	Optical Photometry . . . . .	126
<b>8</b>	<b>Ultra-Violet Spectrum</b>	<b>131</b>
<b>9</b>	<b>X-Rays and <math>\gamma</math>-Rays</b>	<b>141</b>
9.1	INTEGRAL data. . . . .	141
9.2	RXTE data . . . . .	142
9.3	Timing . . . . .	142
9.4	Spectral Analysis . . . . .	146

<b>10 Discussion</b>	<b>155</b>
10.1 The optical counterpart to 4U 2206+54 . . . . .	155
10.1.1 Why BD +53°2790 is not a classical Be star . . . . .	155
10.1.2 What is BD +53°2790? . . . . .	157
10.2 The compact object in 4U 2206+54 . . . . .	159
10.2.1 Conflicts in the neutron star scenario . . . . .	159
10.2.2 Excluding the black hole scenario . . . . .	160
10.2.3 The cyclotron feature . . . . .	162
10.3 Conclusions and Future Work . . . . .	163
<b>III The BeX system SAX J2103.5+4545</b>	<b>173</b>
<b>11 Introduction</b>	<b>175</b>
<b>12 Optical band</b>	<b>179</b>
<b>13 X-Rays and <math>\gamma</math>-Rays</b>	<b>189</b>
13.1 PV phase, analysis of an outburst . . . . .	190
13.1.1 Imaging . . . . .	190
13.1.2 Timing . . . . .	192
13.1.3 Pulse Period . . . . .	193
13.1.4 Spectral Analysis . . . . .	193
13.2 GPS Long term analysis: the nature of the system . . . . .	198
13.2.1 Imaging . . . . .	198
13.2.2 Modulation of type-I outbursts . . . . .	204
13.2.3 Orbital variability . . . . .	210
13.2.4 Hardness ratios . . . . .	214
13.2.5 Pulse Period . . . . .	215
13.2.6 Pulse period evolution on short time scales . . . . .	220
13.2.7 Pulse period at higher energies . . . . .	223
13.2.8 Analysis of GPS spectra . . . . .	226
<b>14 Discussion</b>	<b>249</b>
14.1 Conclusion and Future Work . . . . .	254
<b>A Resum del treball de tesi</b>	<b>259</b>





## Part I

# High Energy Astrophysics



# Chapter 1

## Observation of the High Energy Universe

### 1.1 General Introduction

When we look upwards at night from our cities, we can maybe see a couple or three bright stars with some difficulty. Living in big, very illuminated cities we get less familiarized with the idea that a great amount of information is arriving to us from outside the Earth. If we go to the countryside and have a look again upwards at night, then we will be amazed by the beautiful picture extended above us. At naked eye we can already grab some information about what is happening outside there. There seems to be a milky agglomeration of stars spanning the sky, with a large concentration of stars and matter there compared to the rest of the sky. We are watching the Milky Way, our host galaxy. There can also be a couple, maybe three if lucky, bright stars which are not blinking, like the rest. Actually, they are not stars, but planets. If we observe the nightly sky for a sufficiently long time span (a few weeks), we will realize that those non-blinking stars, the planets, will be changing position with respect the rest of the stars. We will also realize that those stars which were, for example, at zenith position the first night we observed the sky, will have past this position in the following nights. They will have moved further away the more time has passed with respect to our first observing night. All this observational evidence is giving us information about the relative

motion of the Earth, the planets, and the stars with regard to each other. Only with the information obtained by our eyes, we can already experience a lot about the distribution of matter in our surroundings (our galaxy). Surely we will be able to watch some shooting stars. Shooting stars are actually small pieces of solid matter falling to the Earth. What we see as a bright tail is just the light emitted by the interaction of these tiny solid pieces of matter with the Earth's atmosphere. We have found the amazing discovery that not only visible light is arriving to us from outside the atmosphere. Also we have learned that sometimes we *see* matter indirectly, that is, we actually *see* (or detect) the result of its interaction with the surrounding environment.

There are enormous amounts of particles arriving at the Earth's atmosphere continuously. Many of them come from the nearby Sun, but some others are visitors from far away which have traveled for thousands of years (or longer) before reaching our atmosphere. Some are stopped in the upper layers of the atmosphere (heavy energetic particles, like protons) or caught by the Earth's magnetic field (if the particle is charged) and some others just cross through the Earth without interacting (like the very light neutrinos, which hardly interact with matter).

Correspondingly, photons (particles of light) from the whole electromagnetic spectrum, not only visible light, are arriving to the Earth continuously. The electromagnetic radiation reaching the Earth's atmosphere is stopped at the outer layers or passes through depending on the energy of the incident photons (which is equivalent to its wavelength or frequency).

The electromagnetic spectrum is divided artificially according to our experience with each energy range, as light from different energy ranges interacts in a very particular way with its surroundings. Fig. 1.1 shows the electromagnetic spectrum with indications of common names given to the different energy ranges. Fig. 1.2 illustrates how far away energy ranges (microwaves and X-rays) interact with matter in a very different way. Microwaves have a size and energy which let them only move molecules and induce rotations and torsions. On the other hand, X-rays, with much shorter wavelengths and higher energies, interact directly with the atoms' electrons and nuclei.

The energy range with which we are more familiar is the optical range, which corresponds to wavelengths from 4000 up to 7500 Å, or energies

from 3.1 down to 1.7 eV. Our perception of the world around us was adapted to this wavelength because of two reasons: **A)** it is the range of maximum emission from the Sun (see Fig. 1.3); and **B)** the atmosphere allows photons within these energies propagate down to the biosphere.

Electromagnetic waves interact in different ways with the atmosphere according to their wavelength. Some wavelengths are scattered and some others are absorbed. Ozone, carbon dioxide, and water vapor are the three main atmospheric constituents which absorb radiation. Fig. 1.1 shows schematically which energies are absorbed by the atmosphere. Although high energy photons were discovered from radioactive decays and cathode ray tube experiments, and used widely for many applications, it was not possible to detect such energies from outside the Earth until the first rockets were launched outside the atmosphere.

The first rockets with dedicated high energy detectors were launched from the early 1960s on. Explorer 11 was the first gamma-ray detection satellite flown. It was launched on 27 April 1961 and the instrument aboard was designed to detect gamma rays above 50 MeV. On 19 June,

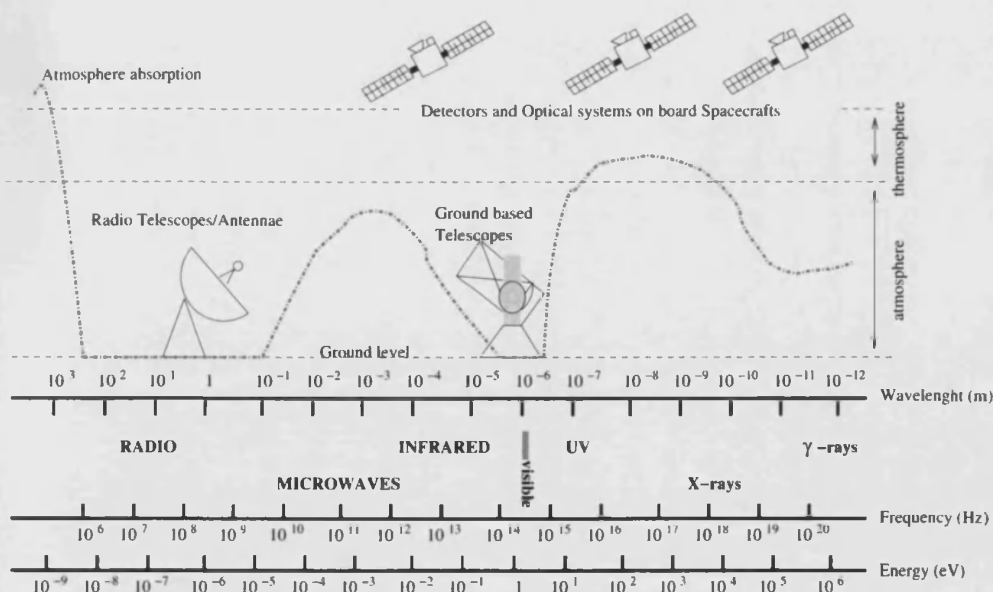


Figure 1.1: Electromagnetic spectrum. The common names used to make reference to the different energy ranges are shown. Only visible light, a bit of infrared, and radio wavelengths reach us from outside the atmosphere. For each range, the detection system commonly used is also shown.

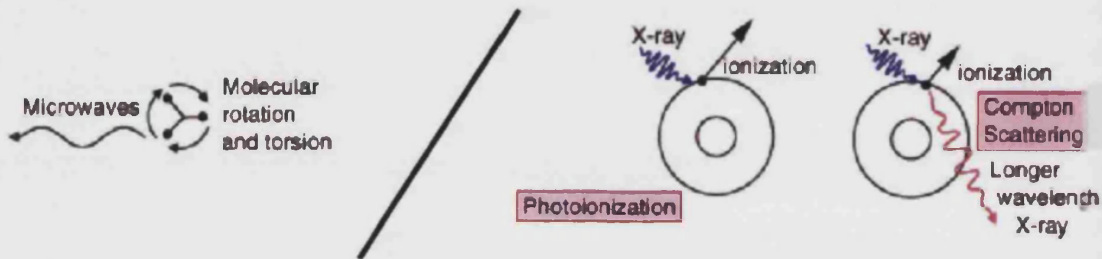


Figure 1.2: Left panel: Interaction of microwaves with matter. Its size and energy induces rotation and torsions in molecules. Right panel: X-ray interactions with the electrons in the atoms.

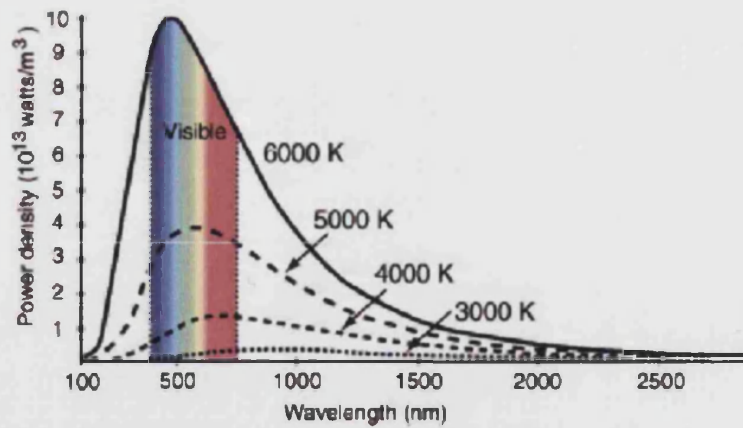


Figure 1.3: Radiation of the Sun as a function of the energy. Some other radiation curves corresponding to black bodies at different temperatures are also shown for comparison.

1962 the third ASE-MIT experiment was launched. This experiment was the first one to detect the diffuse X-ray background and the first point-like X-ray sources: Sco X-1 and a secondary source in the Cygnus direction which likely was Cyg X-2. A few more missions during the 1960s discovered high energy emission from the Crab, the Galactic Center and Cyg X-1. Table 1.1 lists 24 high energy dedicated missions launched from the late 1960s on and which have already finished operations. To them we owe the first advances in the technology of detection, time accuracy and fine imaging, and the first discoveries and catalogs of astrophysical high energy sources.

In the present days, a handful of spacecrafts are dedicated to the observations of high energy phenomena in the Universe. Table 1.2 gives a list of the present high energy missions still in operational phases.

In the next section we will review briefly the main areas of research in high energy astrophysics in the present days. In chapter 2 we will put some emphasis on those topics covered by this thesis work, i.e., those related to high mass X-ray binary systems. Afterwards, in chapter 3, we will introduce in more detail the *INTEGRAL* mission and the analysis tools used to extract information from *INTEGRAL* data. We will finish with an introduction to some other software and tools used and those which will become important in the forthcoming work (see section 3.5.5).

## 1.2 Astrophysical processes and scenarios related to High Energy photons

High energy photons in the X and  $\gamma$ -ray bands come from a great variety of sources. Production of X-rays is quite common in the Universe. Close by, our Sun emits X-rays from the corona, due to heating processes. This happens also to all stars. X-rays have been detected also from Solar System planets. One of the major processes occur when these bodies scatter the solar X-rays produced by the hot, tenuous solar corona.

Massive hot stars, in addition, can also emit X-rays from shocks produced in the stellar wind. Supernovae and Supernova remnants (through the interaction of the expanding shock waves with the interstellar medium) and the compact objects left, black holes and neutron stars (through the accretion of matter) are also well known sources of high energy photons.



Table 1.1: High Energy missions from late 1960s which have already finished operations. Data taken from NASA's HEASARC pages (<http://heasarc.gsfc.nasa.gov>).

Mission Name	Lifetime	Energy Range Observed
<i>VELA 5B</i>	23 May 1969 – 19 Jun 1979	3 – 750 keV
<i>UHURU (SAS-1)</i>	12 Dec 1970 – Mar 1973	2 – 20 keV
<i>OSO-7</i>	29 Sep 1971 – 09 Jul 1974	1 keV – 10 MeV
<i>COPERNICUS</i>	21 Aug 1972 – Feb 1981	0.5 – 10 keV
<i>SAS-2</i>	19 Nov 1972 – 08 Jun 1973	20 MeV – 1 GeV
<i>ANS</i>	30 Aug 1974 – 14 Jun 1977	0.1 – 30 keV (X-ray) 1500-3300 Å (UV)
<i>ARIEL V</i>	15 Oct 1974 – 14 Mar 1980	0.3 – 40 keV
<i>SAS-3</i>	May 1975 – Apr 1979	0.1 – 60 keV
<i>OSO-8</i>	21 Jun 1975 – 01 Oct 1978	0.15 keV – 1 MeV
<i>COS-B</i>	09 Aug 1975 – 25 Apr 1982	2 keV – 5 GeV
<i>HEAO-1</i>	12 Aug 1977 – 09 Jan 1979	0.2 keV – 10 MeV
<i>EINSTEIN</i>	12 Nov 1978 – Apr 1981	0.2 – 20 keV
<i>HAKUCHO</i>	21 Feb 1979 – 16 Apr 1985	0.1 – 100 keV
<i>HEAO-3</i>	20 Sep 1979 – 29 May 1981	50 keV – 10 MeV
<i>TENMA</i>	20 Feb 1983 – 22 Nov 1985	0.1 keV – 60 keV
<i>EXOSAT</i>	26 May 1983 – 09 Apr 1986	0.05 – 50 keV
<i>GINGA</i>	05 Feb 1987 – 01 Nov 1991	1 – 500 keV
<i>GRANAT</i>	01 Dec 1989 – 27 Nov 1998	2 keV – 100 MeV
<i>ROSAT</i>	01 Jun 1990 – 12 Feb 1999	0.1 – 2.5 keV (X-ray) 62-206 eV (UV)
<i>BBXRT</i>	02 Dec 1990 – 11 Dec 1990	0.3 – 12 keV
<i>CGRO</i>	05 Apr 1991 – 04 Jun 2000	30 keV – 30 GeV
<i>ASCA</i>	20 Feb 1993 – 02 Mar 2001	0.4 – 10 keV
<i>DXS</i>	13 Jan 1993 – 19 Jan 1993	0.15 – 0.28 keV
<i>BeppoSAX</i>	30 Apr 1996 – 30 Apr 2002	0.1 – 300 keV

Table 1.2: High energy missions presently in flight. Data taken from NASA's HEASARC pages (<http://heasarc.gsfc.nasa.gov>).

Mission Name	Launch	Energy Range Observed
<i>ROSSI XTE</i>	30 Dec 1995	2 – 250 keV
<i>CHANDRA</i>	23 Jul 1999	0.1 – 10 keV
<i>XMM-NEWTON</i>	Dec 1999	0.1 – 15 keV
<i>HETE-2</i>	09 Oct 2000	0.5 – 400 keV
<i>INTEGRAL</i>	17 Oct 2002	5 keV – 10 MeV
<i>Swift</i>	20 Nov 2004	0.2 – 150 keV(X-rays) 1700–6500 Å (UV/Optical)

At larger scales, galaxies can also be sources of X-rays, specially those with active nuclei (as the very luminous quasars). Hot gas between galaxies can emit X-rays, as well as the interstellar medium.

All these processes involve cooling of a very hot gas or heating in shocks and high energy emission is generated in two different ways: either by electrons changing energy levels within an atom, or by interactions encountered by free electrons (bremsstrahlung, synchrotron radiation, Compton scattering).

On the other hand,  $\gamma$ -ray photons are produced in a well known phenomenon which is produced here on Earth as well, the radioactive decay of heavy nuclei. Collisions of particles and their disintegration into less massive particles and matter-anti-matter collisions are also important sources of  $\gamma$ -rays. Charged particles in the presence of a magnetic field or in presence of nearby photons can emit  $\gamma$ -rays through bremsstrahlung, cyclotron or synchrotron radiation, or scattering processes.

In the 10–100 keV energy range we have overlap of X-ray and  $\gamma$ -ray regimes. In this range we have X-rays processes and true  $\gamma$ -ray emission lines, for example  $\text{Ti}^{44}$  decay lines.

The astrophysical processes resulting in the emission of high energy photons can be summarized as follows:

- Hot gas can produce thermal emission in the form of a **black body radiation** whose maximum can be in the X-ray regime (when the

emitting matter is optically thick). This situation is common in very hot plasma-like shocks in hot star winds, stellar coronae, accretion disks or expanding gas caused by matter expelled by a supernova explosion.

- Charged particles moving in a magnetic field suffer accelerations due to the interaction with it. The electron can find its trajectory modified, losing energy, which is emitted in the form of **synchrotron radiation**. Charged particles can also find their trajectories bound to the magnetic field lines, their movement is then limited to circles around the magnetic field lines. The energy components perpendicular to the magnetic field are quantized. Thus, photons can be emitted or absorbed in frequencies corresponding to the energy difference between such levels. **Cyclotron emission or absorption** can be produced in this way. Emission is produced in thinner media, however absorption will take place when photons encounter a resonant, hugely increased, cross-section. Both phenomena are likely to be produced very commonly, as magnetic fields are usual all around the observed Universe. However only when very strong magnetic fields are present (like those related to compact objects) the resulting emission (or absorption) is linked to the high energy regime.
- Charged particles can also interact with electrostatic fields, as is, for example, the case of an electron passing by an ionized atom. In this case the charged particle is 'braked' and the energy lost is emitted in the form of **bremsstrahlung emission**.
- High energy photons can suffer **Compton scattering**. This is the interaction of photons with stationary electrons, in such a way that the high energy photon loses energy which is gained by the electron. If the interaction happens, instead, with a very energetic particle, an **inverse Compton scattering** is produced, the photon gains energy which is lost by the initially very energetic particle. This results in a very interesting effect, photons from lower energies are brought to higher energies. In those environments where the interaction of light and matter is dominated by the Compton scattering, we say that the high energy spectrum is comptonised or that comptonisation is present in the system. It is likely to be produced when the radiation

crosses matter in which we find electrons with a cross section large enough to cause the interaction. The plasma must be thin enough that other processes, such as bremsstrahlung, do not dominate the spectrum instead. This is the case of the corona surrounding black holes or neutron stars in X-ray binary systems (hot plasma highly ionized, i.e., with a large amount of very energetic free electrons).

- Unstable atomic configurations can lead to **decays** to an energetically more favored configuration. In this process high energy photons can be emitted. This is likely to happen in regions of active nuclei forming, such as supernova explosions
- **Matter-anti matter annihilation** (like electron-positron interactions) leads to the generation of high energy photons.

For a more detailed analysis of these processes see Longair (1981) and Schönfelder (2001).



## Chapter 2

# High Mass X-Ray Binary Systems

In this chapter we will introduce the main topic of this thesis work. First a general introduction to X-ray binaries will be presented. After that, the main properties of the two constituents of a High Mass X-Ray binary system, that is, a massive early type star and a compact object, will be introduced. From an evolutionary point of view, the histories of these objects, both the massive and the compact companions, differ considerably from those of isolated stars. Although the topic on how these systems come to be formed is very interesting, it will not be treated in this introduction, and the reader is referred to the very nice reviews of De Loore (2001), Karttunen et al. (1987), Weigert and Kippenhahn (1967) and van den Heuvel (1993).

### 2.1 X-ray binary systems

The discovery of pulsars represented the observational evidence for the existence of neutron stars, which had just been theoretical objects until that moment. The first pulsars discovered were radio pulsars, whose pulsed emission is produced at radio wavelengths. The radio emission is the resulting rotating magnetic dipole emission. Some of these pulsars, like the Crab, were found to pulse also at other wavelengths, like high energy X-rays and  $\gamma$ -rays, and in the optical bands. The term *rotation-powered*

pulsars was then preferred to indicate the source of power in these objects. As more pulsars were found in the X-ray bands, it became evident that most of them were part of binary systems. In these systems the source of power is the accretion of matter, donated by the normal component of the system, onto the compact component (black hole or neutron star). Thus, they are also called *accretion-powered* pulsars. The discovery of pulsars in binary systems represented a great push to the theories of compact objects, because for the first time the masses of such objects could be estimated by finding the orbital solution of such binary systems. The combined use of optical and X-ray observations allowed the determination of the mass function of the two components. An interesting case is that of the systems where the occurrence of eclipses is found. For those systems even an estimation of the inclination of the orbit with respect to the plane of the sky can be derived, allowing a more accurate mass determination.

In fact, X-ray binaries can be composed of a variety of components: the normal companion can be an early type massive star or a low mass late type star, and the compact companion can be a black hole, a neutron star or a white dwarf. A binary system composed by two early type hot stars with strong winds can also result in detectable X-ray emission produced by the collision of the winds, but the luminosities are much lower and this picture is completely out of the scope of this thesis work. From now on, when talking about X-ray binary systems we will be referring to those systems made up of a normal star and a compact companion as components. In these systems, the high X-ray luminosity can be explained as the result of accretion, that is, matter leaves the surface of the normal companion (by wind, Roche lobe overflow or other means) and is accelerated and deposited onto the compact companion. All the potential energy accumulated by matter is released during the accretion process.

Initially, X-ray binaries were classified according to this scheme (see Corbet 1986 and Nagase 1989):

- High Mass X-Ray Binary systems (HMXRBs):
  1. Supergiant systems: The optical counterpart to the system is a massive early type supergiant. The compact companion is a neutron star or a black hole. According to observational evidence, they were divided in two subgroups:

- a) Systems with high luminosity and short pulse period. Examples are SMC X-1 (see Butler and Byrne, 1973; Schreier et al., 1972) and Cen X-3 (see Peterson, 1972; Shklovsky et al., 1972).
  - b) Systems with moderate luminosity and long pulse periods. Examples are GX 301-2 (Pakull, 1982) and 4U 1907+09 (Marshall and Ricketts, 1980).
2. Systems with Be companions (BeX systems). The optical counterpart to the system is an O or B main sequence star showing the Be phenomenon. The compact companion is a neutron star. Examples are 4U 0115+63 (see Rappaport et al., 1978; Hutchings and Crampton, 1981), A0535+26 (see Rappaport et al., 1976; Rossiger, 1976), and X Per (see van den Bergh, 1972; Braes and Miley, 1972).
- Low Mass X-Ray Binary systems (LMXRBs). In these systems the optical companion is a late (later than type A) low mass star. Examples are Her X-1 (Crampton and Hutchings, 1972) and 4U 1626-67 (Joss et al., 1978).

In some cases pulsations have never been detected, like in the BeX system  $\gamma$  Cas (for which the white dwarf nature of the compact companion has been proposed by Frontera et al. 1987) or 4U 2206+54 (see below in this thesis work), and in some other cases pulsations were detected only once, as is the case of 4U 1700-37 (despite exhaustive searches the pulse period could not be measured again, see Nagase 1989).

We can advance that the responsible for this variety of behaviours is the way mass transfer occurs from the normal companion to the compact object. The strength of the magnetic field of the compact companion is a determining factor in the process. In some systems (called wind-fed systems) matter from the wind of the normal star is caught in the gravitational potential of the compact object. In some other cases (called disk-fed systems) the transfer of matter is produced in such a way that the runaway matter possesses enough angular momentum to form an accretion disk around the compact object (i.e, matter is falling in a spiral-like motion towards the compact object). The magnetic field of the neutron star determines the way the accretion column is formed from the accretion disk inner boundary or from the mater caught from the stellar wind.



In those systems where the pulse period can be measured, a great variety of spin changes (accelerations and decelerations) can be found. Contrary to the radio pulsars (which suffer a secular spin-down process), spin up and spin down changes have been observed in X-ray binary pulsars on many time scales and amplitudes. Some of them seem to show cyclical changes, like EXO 2030+375 (see Wilson et al., 2005). Furthermore, variations of the pulse profile with orbital phase and with energy are quite common among X-ray binary systems. Changes with phase are thought to be related to changes in the geometry of the system relative to the observer (inclination of the magnetic axis with respect to the rotation axis of the compact object, and the relative inclination of both with respect to the observer). In one particular case, these phase variations lead to the determination of the precession movement of the compact object. It was the case of Her X-1 (see Nagase 1989 and Trümper et al. 1986). To explain the variations of pulse profiles with energy, however, models of anisotropic transfer of radiation must be taken into account (this is not strange, for example, it is known that Thomson scattering becomes anisotropic in the presence of a strong magnetic field). Changes of the pulse profile and pulse period correlated with the luminosity are thought to be linked to changes in the structure of the accretion column and/or the inner parts of the accretion disk.

In the next subsections we will review the general properties of those components in HMXRBs, the massive early type star and the compact object. Then we will review the accretion processes which can occur in these systems and at the end we will describe these systems as a whole and how both components of the system can interact.

## 2.2 Massive (OB) stars

Early type massive OB stars, because of their fast and peculiar evolution, are very interesting laboratories to test all the theories of stellar structure and evolution. While in the main sequence, they are perfect probes of the composition of their surroundings, as they are very little evolved and their envelopes present practically the same composition as the local interstellar matter from which they formed. Because of this reason they are used often as metallicity indicators. When they are fast rotators their

evolution becomes even more peculiar, presenting some interesting effects, like possible surface abundance anomalies or the Be phenomenon (which will be discussed later).

### 2.2.1 Stellar winds

Stars of all types are known to lose matter continuously in the form of a stellar wind. However, this process is especially critical in OB stars. Their mass loss rates can be so important as to affect dramatically the evolution of the star and the structure of its photosphere. In hot stars, stellar wind can remove more than half of their mass before they explode as a supernova.

The fleeing matter which forms the stellar wind contributes to the enrichment of the interstellar medium, or is accreted onto a companion compact object (white dwarf, neutron star, or black hole). The picture becomes more complicated with the presence of strong magnetic fields and fast rotation in the mass-losing star. Magnetic field lines can be modified by the radiation pressure of the plasma and at the same time can drive the plasma to the magnetic equator, likely developing a torus-like structure around the mass-losing star (see Townsend and Owocki, 2005).

Resonance scattering has become a powerful tool to explain most of the observed properties of stellar wind from hot stars. Most of the ions present in the outermost layers of the photosphere are in their fundamental state. Photons from the photosphere excite the electrons of the ground state of these ions. The transitions to excited levels from the ground state of the ions participating in this process correspond to ultraviolet wavelengths. The lifetime of these excited levels usually is very short (of the order of  $10^{-9}$  s) and then the photon is re-emitted, with the same energy but in a direction different from the incident one. This interaction of light with matter produces a radiation pressure which will be enough to drive matter away from the photosphere. By the time the radiation dilution is important and there is not enough pressure to support the outgoing flow, the matter has been accelerated to velocities greater than the escape velocity or will be far enough as to not feeling the gravitational attraction. A *radiatively driven wind* has been formed. Radiatively driven winds are thought to be the common physical mechanism producing strong winds in early type stars. This process has two observable effects: the so called P-

Cygn profiles; and the presence of stellar wind absorption lines displaced to shorter wavelengths due to the overall movement towards the observer (Doppler effect). For the initials of the radiation driven wind theories see Lucy and Solomon (1970) and Castor et al. (1975). A more up-to-date review about radiatively driven winds can be found in Lamers and Cassinelli (1999) and Kudritzki and Puls (2000).

The wavelength of ultraviolet lines involved in this process and their respective ions are shown in Table 2.1.

There are two important parameters regarding stellar winds, the mass loss rate ( $\dot{M}$ ) and the wind terminal velocity ( $v_\infty$ ). They are not direct observables, but can be derived from observations. Usually  $v_\infty$  will be determined from the observed profiles of certain lines, and assuming a standard velocity law of the type:

$$v(r) = v_0 + (v_\infty - v_0) \left(1 - \frac{R}{r}\right)^\beta$$

where  $v_0$  is the initial velocity of the matter leaving the photosphere,  $v_\infty$  is the matter velocity at infinity (a distance far enough from the photosphere as to be considered free from interactions with the mass-losing star),  $R$  is the stars' radius and  $r$  the distance from the photosphere measured outwards. Once we know the velocity law parameters, we can find the mass loss rate through the equation of continuity:

$$\dot{M} = 4\pi r^2 \rho(r) v(r)$$

if we have determined also  $\rho(r)$  (the density structure of the wind) through the observation of certain UV lines. This can be done by comparing the observed lines to those predicted by models, where the relative abundances of the ions are included. The model giving the best match against observations will be very likely describing the distribution of ions along the wind. This distribution of ions can be related to  $\rho(r)$ .

On the one hand, P-Cygn profiles producing saturated lines (reaching the zero level) will be best suited to derive the terminal velocity of the wind. On the other hand, unsaturated lines will be more suitable to derive the mass loss rate.

Table 2.1: Ions which participate in the radiatively driven winds models. Typical abundances are given in units of  $\times 10^{-4}$  and relative to hydrogen. Values extracted from Lamers & Cassinelli (1999).

Ion	Typical Abundance	Ionisation Potential (eV)	Wavelength (Å)
C II	3.7	11.26	1334.532
			1335.708
C III	3.7	24.38	1175.67
C IV	3.7	47.89	1548.195
			1550.770
N IV	1.1	47.45	1718.551
N V	1.1	77.47	1238.821
			1242.804
O VI	6.8	113.90	1031.928
			1037.619
Mg II	0.35	7.65	2795.528
			2802.705
Si II	0.35	8.15	1526.707
			1533.431
Si III	0.35	16.35	1206.500
Si IV	0.35	33.49	1393.755
			1402.770
Fe II	0.25	7.87	2585.876
			2598.370
			2599.396

Table 2.2: Typical wind parameters for main sequence O stars. Taken from Prinja and Howarth (1986).

Star	Spectral type	$T_{\text{eff}}$ (K)	$R/R_{\odot}$	$M/M_{\odot}$	$v_{\text{esc}}$	$v_{\infty}$
HD 199579	O6 V((f))	38000	12	38	990	3300
15 Mon	O7 V((f))	35000	12	30	890	2600
HD 48099	O7 V	35000	10	33	1030	3300
10 Lac	O9 V	35000	7	23	1070	1375
HD 93521	O9 V	34500	8	24	1020	1075
$\zeta$ Oph	O9.5 V	32000	10	23	880	1640

Typical wind parameters of OB main sequence stars are shown in Table 2.2 (see Prinja and Howarth, 1986). Mass loss rates are of the order of  $10^{-6}$ – $10^{-8} M_{\odot} \text{ y}^{-1}$  in hot stars (it can reach up to  $10^{-5} M_{\odot} \text{ y}^{-1}$ ).

### 2.2.2 Be phenomenon

A Be star is a hot star, with an O or B spectral type, non supergiant, whose spectrum has, or had at some time, one or more Balmer lines in emission. They are fast rotators and have high mass loss rates. In addition, infrared excess, with respect to normal B stars of the same spectral type, is observed in all Be stars. Both the emission lines and the infrared excess are believed to be formed in a circumstellar envelope with a higher concentration of mass around the star's equator. Depending on the angle of view with respect to the observer, this circumstellar envelope shows pure emission superimposed on the photospheric absorption or shows the so-called *shell profile*, with an absorption core dividing the emission in *blue* (*V*) and *red* (*R*) peaks. These geometrical effects are illustrated in Fig. 2.1. For a description of the large variety of geometrical configurations and related observed profiles see Slettebak (1988).

The Be phenomenon is commonly found in O and B stars. About 20% of known B stars are Be. This percentage increases considerably when considering young star clusters. In some star clusters up to 60% of B stars are Be stars. Although it is a phenomenon known for a very long time the *why* and *when* it is produced are still unknown. The first identified

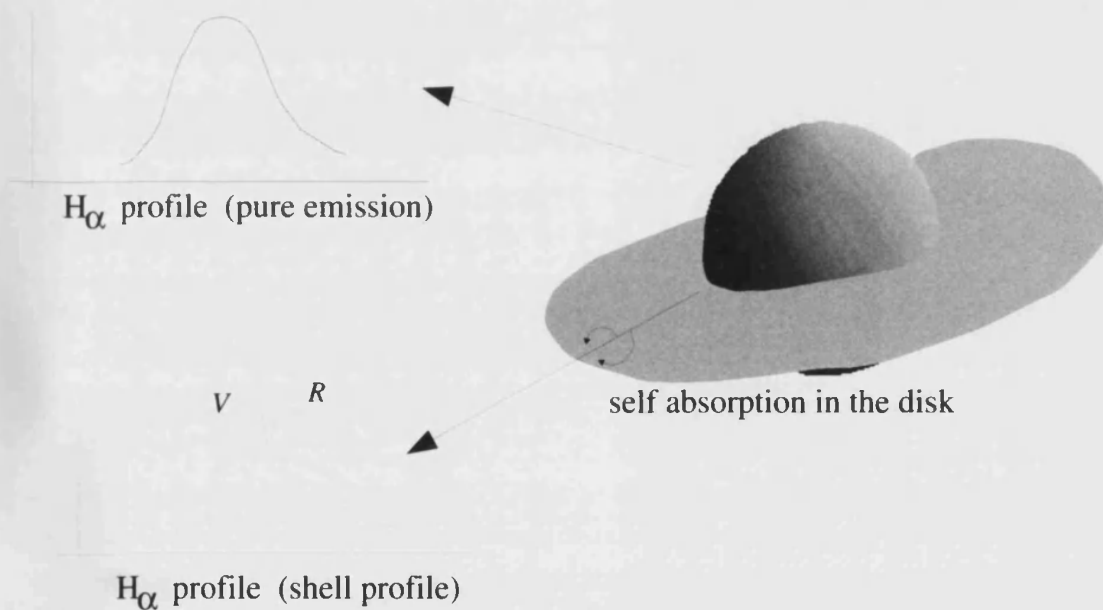


Figure 2.1: Schematic representation of the effects of the angle of view to the observer on the observed profile of the H $\alpha$  line in a Be star. When viewed pole-on the emission from the disk is superimposed over the photospheric absorption. However, when viewed more equator-on the effect of self absorption in the disk results in the characteristic shell profile, with blue ( $V$ ) and red ( $R$ ) peaks.

Be star was  $\gamma$  Cas when Angelo Secchi noticed that it showed prominent emission lines at the end of the XIX century. But it was only after Struve's (1931) work that the group of B stars showing emission lines started to be analysed as a class of stars.

Linked to the mass loss, fast rotation, and stellar pulsations, in some moment of their lifetime B stars can exhibit the set of peculiarities which led to its addition to the group of Be stars. In some Be stars the phenomenon has been observed only once, while in others this phenomenon can be recurrent (with losses and re-formations of the circumstellar envelope).

While displaying the Be phenomenon, Be stars can show variability on several timescales. Short term variability, on the order of a few minutes up to a few days can be observed in the shape of photospheric lines (see Hubert et al., 1997). One of the proposed explanations for this variability is the presence of non-radial oscillations. Medium term variability (months to years) can be seen in the  $H\alpha$  line shell profile, with a modulated variation of the relative intensity of the red and blue peaks. A satisfactory explanation of these variations is given by the Okazaki's one-armed oscillation model (Okazaki, 2000). The way in which a density wave, propagating through the disk according to Okazaki's model, can produce the shell profile variability is illustrated in Fig. 2.2. Important changes in photometry and spectroscopy can occur on time scales on the order of few decades, showing the star going through B to Be and possibly also developing shell profiles. These long term changes are not well understood.

Many models have been proposed to explain the formation of such a peculiar circumstellar environment in Be stars (the wind compressed disk model of Bjorkman & Cassinelli 1993, axi-symmetric radiative wind models by Stee et al. 1994, non-radial pulsations in combination with fast rotation, etc.). Observations of Be stars support the idea of the presence of two quite distinct zones in their circumstellar envelopes. A fast, low density, polar wind (see Marlborough 1987) and a very slow radial expansion of dense matter concentrated towards the equators (see, for example, Poekert & Marlborough 1978)

The presence of correlations between different  $H\alpha$  profile parameters indicate that the Be disks are rotationally dominated ( $H\alpha$  equivalent width versus Full Width at Half Maximum –FWHM– or versus  $V-R$  peak separa-

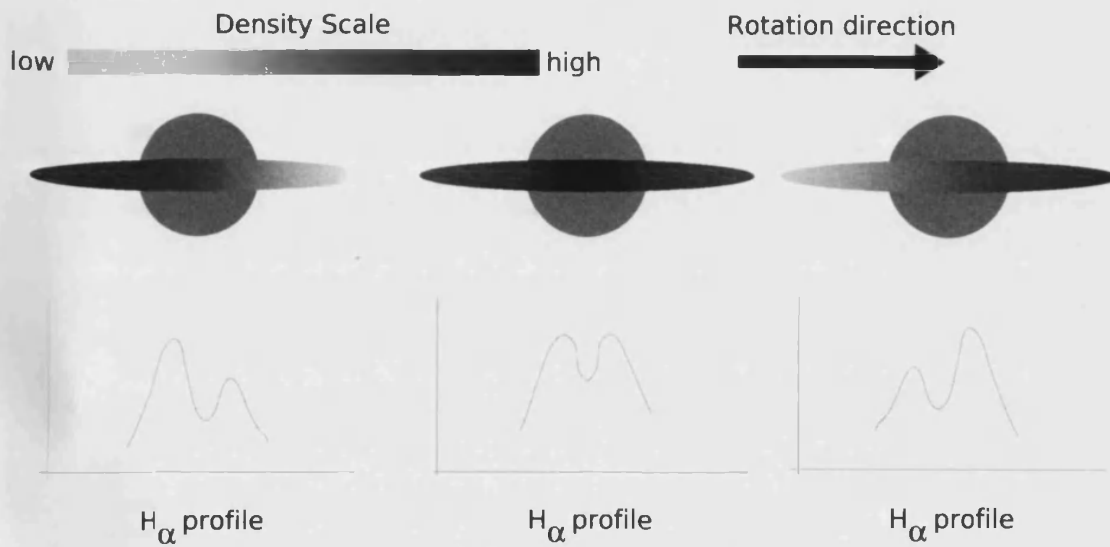


Figure 2.2: Schematic representation of the effects of a one armed oscillation in a Be star disk on the observed H $\alpha$  profile. When the oscillation brings a higher density of matter to the part of the disk approaching the observer (due to the rotational movement) the blue peak (V) becomes higher. If the oscillation, instead, brings matter to the side of the disk which is moving away from the observer, then the red peak (R) is enhanced.



tion) and that both infrared excess and Balmer lines emission are produced in the disk (due to the correlation between  $H\alpha$  emission line strength and the infrared magnitudes).

The viscous accretion model (see Lee et al., 1991; Porter, 1999; Okazaki, 2001) has proven to describe successfully these observational facts. In this model the B star transfers angular momentum to the innermost parts of the disk through some still unknown mechanism (which could be related to fast rotation, pulsation, magnetic fields, or a combination of some of them). Inner disk matter would find, in this way, its angular momentum increased and viscosity would be in charge of transferring this angular momentum outwards. Matter flows in a quasi-Keplerian regime, producing a rotationally dominated disk, governed by viscosity and pressure. Millar and Marlborough (1998, 1999) computed the temperature distribution of two Be stars' disk ( $\gamma$  Cas and 1 Del) up to a  $100 R_*$  radius and found that approximately the disk temperature is half of the star's effective temperature.

### 2.3 Compact objects

Black hole, neutron stars, and white dwarfs are commonly known as compact objects. They share one property: they all represent the final stage of stellar evolution.

Thermonuclear fusion in the core sustains a star against gravitational collapse during its life time. Massive stars (above eight solar masses) end their lives with supernova explosions, when there are not enough thermonuclear reactions to avoid the core collapse. The supernova remnant, that is, the core of the progenitor star, is heavy enough to become a neutron star, when the collapse is stopped by the nuclear interactions. At this stage, a very dense star of baryons (mainly neutrons) in a degenerate state will have formed. Typically, neutron star radii are of the order of 10 km and its densities of the order of  $10^{14} \text{ g cm}^{-3}$ . Neutron star masses are in the range  $1.2\text{--}1.5 M_\odot$  (the compact object in Vela X-1 is confirmed to have a mass greater than  $1.5 M_\odot$ , and there are theoretical models predicting possible stable structures up to  $2.5 M_\odot$ ). If the collapsing core is only a bit more massive than that, the gravitational collapse may not be stopped and eventually a black hole will be born. The inner structure of

neutron stars is still under debate, but it is believed to be formed by a inner core of quark matter and outer layers of superfluid hadronic matter and mixtures of barions.

White dwarfs, on the other hand, are born at the final stages in the life of low mass stars (below seven solar masses). Instead of finishing their lives violently, after a supernova explosion, low mass stars loose their envelopes quietly. As the remaining core of the progenitor cools down, it collapses progressively, until it reaches a density high enough to form a degenerate gas of electrons. The outwards pressure of this degenerate gas stops the collapse and a white dwarf is formed. Typical sizes and densities of white dwarfs are of the order of thousands of kilometers and  $10^9 \text{ g cm}^{-3}$ , respectively. White dwarfs can have masses in the range 1.0–1.44  $M_{\odot}$ , being the upper limit of the range the so-called Chandrasekar limit, and represents the maximum mass that a white dwarf can have to sustain a stable structure.

Although we refer to them all as compact objects, their natures and the kind of interaction with the surrounding matter are very different from one to another. In this thesis work we will concentrate on accretion of matter onto neutron stars, as they are the compact objects present in the two HMXRBs under study. However, in the case of 4U 2206+54, a discussion about the possibility that the source hosts a black hole or a white dwarf is included.

## 2.4 Accretion onto compact objects

As mentioned above, we will concentrate in this section on accretion onto a neutron star.

### 2.4.1 Spherical accretion (and wind-fed accretion)

Inter-stellar matter or the stellar wind from a companion in a binary system is caught by the gravitational potential of the compact object. In both cases the accreted matter possesses very little angular momentum and, hence, is unable to form an accretion disk. Matter free-falls, gaining mechanical energy until it reaches the neutron star surface. There the matter is decelerated and all the available energy is thermally emitted.

The energy rate (luminosity) emitted when accreting matter from infinity collides with the neutron star surface is:

$$\dot{E}_{\text{acc}} = \frac{GM_{\text{NS}}\dot{M}_{\text{acc}}}{R_{\text{NS}}} = L$$

where  $G$  is the universal constant of gravitation,  $M_{\text{NS}}$  is the compact object mass,  $R_{\text{NS}}$  is the neutron star radius and  $\dot{M}_{\text{acc}}$  is the mass accretion rate.

In the case of accretion from stellar wind, we can define the accretion radius ( $r_{\text{acc}}$ ) as the distance from the compact object at which its gravitational potential equals the mechanical energy of the stellar wind matter. Only matter within this radius is accreted, that is, only matter from a cone which subtends a solid angle of  $\frac{\pi r_{\text{acc}}^2}{a^2}$  (with  $a$  the distance from the OB star to the compact object) from the center of the companion OB star is accreted. This supposes a reduction of a factor of  $\frac{a^2}{r_{\text{acc}}^2}$  with respect to spherical accretion. A representative scenario is shown in Fig. 2.3 Therefore, the accretion rate is only a small fraction of the mass loss rate. This mechanism seems to be very ineffective in producing X-ray emission, but when the high mass loss rates of early type stars are taken into account, the process can lead to luminosities high enough to be detected.

The resulting spectrum corresponds to a black body. Interactions of the outgoing radiation with infalling matter can extend the spectrum to other energies, and can result in other interesting effects, like the Eddington limiting luminosity. If the accretion rate increases, the luminosity increases as well. As a consequence the outwards radiation pressure is also raised. It can happen that this pressure becomes so high as to stop the accretion of matter. The luminosity at which the accretion is inhibited by the resulting radiation pressure is called Eddington Luminosity ( $L_{\text{Edd}}$ ).

The picture described above, dealing with a spherically symmetric steady flow, although it helps to understand the way the process occurs, is far to be realistic. Stellar winds are more likely to be affected by turbulences, asymmetries, tidal forces (if in presence of a binary companion), etc. which will result in a clumpy wind with strong inhomogeneities (instead of the steady outflow considered above) which will affect the way accretion takes place. The result will be a variable accretion rate. The

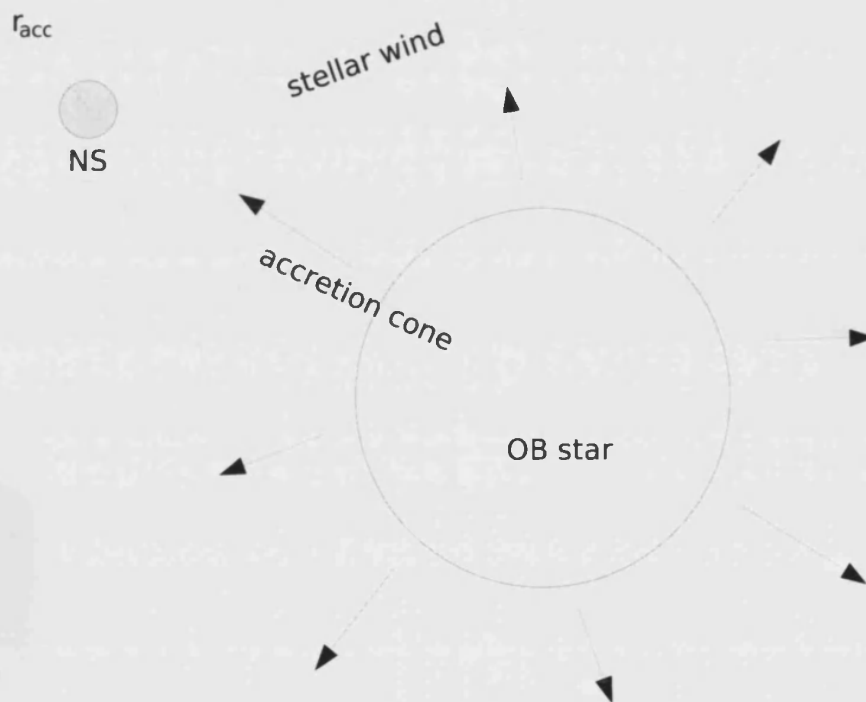


Figure 2.3: Schematic representation of the accretion by stellar wind onto a neutron star. Only matter subtending a solid angle of  $d\frac{\pi r_{\text{acc}}^2}{a^2}$  from the OB star center towards the neutron star is accreted.

accretion process itself will be highly unstable (see Benensohn and Lamb, 1996; Benensohn et al., 1997, and references therein). For a recent review including 3D hydrodynamical calculations see Nagae et al. (2004) and Jahanara et al. (2005).

### 2.4.2 Accretion through a disk

The modeling of accretion disks has been one of the most difficult tasks in the field of theoretical astrophysics. The first model proposed was that of a geometrically thin-optically thick disk described in detail in Pringle (1981) and Frank et al. (1992). We will discuss it here only briefly. A geometrically thin disk must conform the following properties: **a)** the total mass of the disk must be very small compared to the compact object mass; **b)** the characteristic half-height of the disk ( $H$ ) must be much smaller than the distance to the compact object. One of the key points of this model is the realization that the introduction of a turbulent viscosity of the form  $\nu = \alpha\mu H$  (where  $\mu$  is the mechanical viscosity) was needed to explain the transfer of angular momentum within the disk. These models are also called  $\alpha$ -disk models. Infalling matter occupies Keplerian orbits, but because of friction, angular momentum is transferred outwards while matter spirals inwards because of angular momentum loss. Another effect of viscosity is the dissipation of energy, which is emitted thermally. Half of the initially available potential energy is dissipated by friction.

The accretion disk forms, close to the compact object surface, an inner boundary layer of certain thickness which co-rotates with the compact object as a rigid body. This boundary layer carries the net energy available to be emitted when matter reaches the compact object surface. It will be only the remaining half of the initial potential energy.

One of the main problems faced by this model is the difficulty to explain the presence of the viscosity term. Furthermore, the radiation emitted by the colliding matter exerts some outwards pressure which destabilizes the accretion disk. Sunyaev & Shakura (1975) developed an  $\alpha$ -disk model which tried to avoid this problem. In their model the disk was divided in to three regions (with respect to the normal of the disk  $-z$  direction-):

1. **Outer region:** in this zone the gas pressure dominates over the

radiation pressure and the opacity is dominated by free-free interactions.

2. **Middle region:** in this zone the radiation pressure becomes important compared to gas pressure but the opacity is still dominated by free-free transitions.
3. **Inner region:** this zone is optically thick, radiation pressure dominates, and the opacity is dominated by scattering with electrons.

In this model the temperature raises towards the inner parts. The spectrum emitted is almost independent of the frequency (flat spectrum) except for the innermost zone, where an exponential decay is present. The steepness of the decay depends mainly on the increase in temperature, but also on the effects of scattering of the emitted photons by electrons.

As an attempt to overcome the problems of the thin disk models, a set of models were constructed on the basis of thick disk models, but all of them will be unstable. A way out came with the Advection Dominated Accretions Flow (ADAF) models (see Abramowicz et al., 1995a). In these models the dispersed heat is not radiated locally as a black body but transmitted inwards by advection. Abramowicz et al. (1995b) succeeded in explaining, for example, the different states at which black hole candidates are observed (quiescence, the low state, and the high state) as changes in the model parameters of ADAFs.

### 2.4.3 In the presence of magnetic fields

Compact objects (such neutron stars or white dwarfs) can possess strong magnetic fields. The presence of magnetic fields changes the way accretion onto the compact object takes place. The Alfvén radius is the distance at which the pressure exerted by infalling matter onto the magnetic field lines (called ram pressure) equals the outwards pressure exerted by the magnetic field itself. For the case of spherical accretion this can be written:

$$\rho v^2 = \frac{B_s^2}{\mu_0} \left( \frac{R_{\text{co}}}{r_{\text{alfvén}}} \right)^6$$

with  $\rho v^2$ ,  $B_s$ ,  $\mu_0$ , and  $R_{\text{co}}$ , being the mechanical pressure exerted by accreting matter, the magnetic field at the compact object surface, the magnetic dipole moment, and the radius of the compact object. From this equation and the one describing the accretion rate ( $\dot{M} = 4\pi r^2 \rho v$ ) an expression for the Alfvén radius can be derived:

$$r_{\text{alfvén}} = \left( \frac{2\pi^2}{G\mu_0^2} \right)^{\frac{1}{7}} \left( \frac{B_s^4 R_{\text{co}}^{12}}{M_{\text{co}} \dot{M}} \right)^{\frac{1}{7}}$$

For typical values of neutron star  $r_{\text{alfvén}} = \left( \frac{2\pi^2}{G\mu_0^2} \right)^{\frac{1}{7}} \left( \frac{B_s^4 R_{\text{co}}^{12}}{M_{\text{co}} \dot{M}} \right)^{\frac{1}{7}} \sim 10^3$  km (larger than the neutron star radius). A similar calculus for the case of accretion through a disk yields the same order of magnitude for the Alfvén radius (this is because of the strong dependence on the magnetic field at the surface of the compact object,  $B_s$ ). This approximation is telling us that the surroundings of the compact object are magnetically dominated and that the only way to reach the surface is through the magnetic poles. Infalling matter is driven along the magnetic field lines onto the magnetic poles of the compact object. The presence of a magnetic field causes the formation of an accretion column above both magnetic poles.

The magnetic field is in co-rotation with the compact object. Infalling matter at a certain distance from the compact object will also be co-rotating. This distance is called the co-rotation radius ( $r_{\text{cr}}$ ). On the one hand, if the Alfvén radius is smaller than the co-rotation radius ( $r_{\text{alfvén}} < r_{\text{cr}}$ ), then there will be a lot of matter, with a rotational velocity higher than that of the compact object, interacting with the magnetic field lines. This matter pulls the magnetic field lines and introduces a positive torque which accelerates the neutron star. This can explain the spin up observed in many X-ray binary systems. On the other hand, if  $r_{\text{alfvén}} > r_{\text{cr}}$  infalling matter is stopped at the magnetosphere before reaching the co-rotation radius. In this case the magnetic field lines interact with a bulk of matter moving slower than the rotation velocity of the compact object. This produces the opposite effect, slow infalling matter produces a braking of the magnetic field lines and that results in a negative torque applied to the compact object. This is called a spin-down process. If we are close to the limiting case ( $r_{\text{alfvén}} \sim r_{\text{cr}}$ ), variations in the accretion rate can lead to the accretion disk producing alternate positive or negative torques

on the compact object. When the amount of accreting matter increases, the Alfvén radius shrinks and a positive torque is exerted on the compact object. If the mass accretion rate diminishes, the ram pressure decreases and the Alfvén radius increases, resulting in a negative torque exerted on the compact object. This picture has been explained here in a quite intuitive manner which can explain the observed behavior, in terms of pulse period history, of many X-ray binaries, which undergo both spin up and spin down processes, but it is treated in a quantitative way by Nagase (1989) and Gosh & Lamb (1979).

Fig. 2.4 summarises all the types of accretion onto a compact object reviewed in this introduction.

An interesting effect which can be produced when matter is accreting onto a neutron star in the presence of magnetic fields is the inhibition of the accretion, due to a combination of the interaction of the plasma with the magnetosphere and the neutron star fast rotation. This effect is called *propeller effect*. It can take place when the magnetospheric radius is larger than the co-rotation radius. In this situation the matter will be spelled away by the magnetic field lines, which will rotate faster than the infalling matter. For a quantitative picture see Illarionov and Sunyaev (1975).

## 2.5 BeX systems

A binary system composed by a Be star as optical counterpart, and a neutron star as compact counterpart, will be called a BeX system. In these systems a very interesting interaction takes place between the neutron star and the Be star. On the one hand the neutron star affects the formation-disruption cycles of the Be star envelope. On the other hand the Be star envelope releases matter which is accreted onto the neutron star. This transport of matter is not produced in a constant manner, but it is of transient nature. In most cases, therefore, an interesting succession of positive and negative torques can be produced on the neutron star (depending on the quantity of matter available for accretion).

From an observational point of view, BeX systems can be classified as persistent or transient X-Ray sources. Some BeX systems show persistent X-Ray low luminosity ( $\sim 10^{34}$  erg s<sup>-1</sup>) which may be interrupted by transient brighter outbursts. Transient sources, in contrast, show high



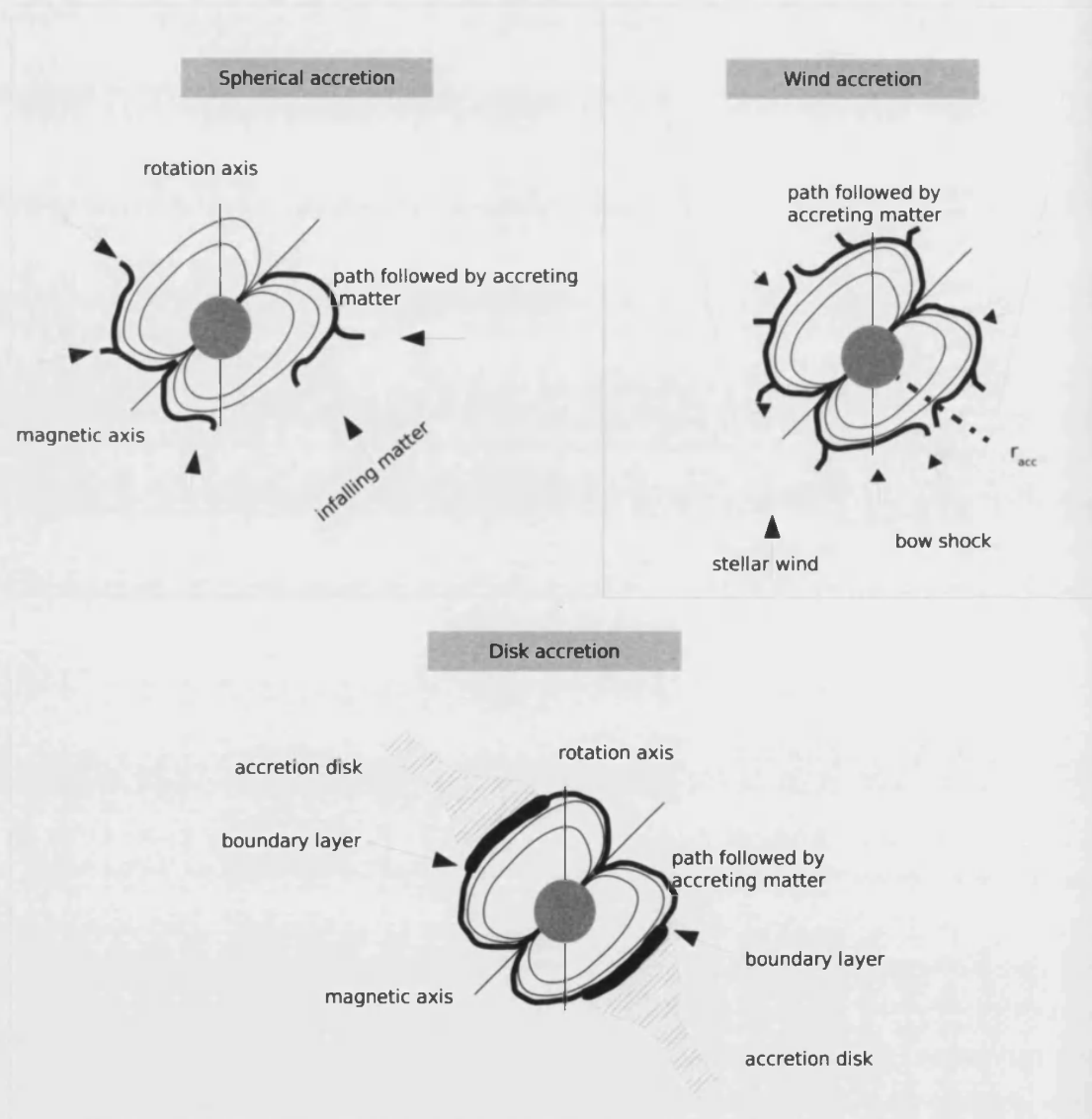


Figure 2.4: Schematic representation of the three different accretion processes reviewed in this introduction.

luminosity ( $>10^{36}$  erg s $^{-1}$ ) outbursts, which can be of two types:

- Type I outbursts: these are moderate luminosity outbursts which are recurrent with the orbital period of the system, not necessarily in coincidence with the periastron passage of the neutron star in its orbit around the Be star.
- Type II outbursts: high luminosity outbursts ( $>10^{37}$  erg s $^{-1}$ ) which can last from weeks to months and which do not show modulation with the orbital period of the system.

The model that has been put forwards to explain this behaviour is the disk truncation model. In this model, the outflowing disk matter is under the action of several torques which add or remove angular momentum to it, depending on which one dominates in a particular physical state of the disk. Basically we can reduce this torque to the sum of all torques due to viscosity within the disk (which mainly brings angular momentum outwards) and the resonant torque exerted as a result of the tidal interaction with the neutron star (which removes angular momentum from the outflowing matter). The truncation radius is that distance from the central B star at which the resonant torques are bigger than the viscous torques. At this radius disk matter loses angular momentum and falls again towards the Be star refueling the disk. A number of situations can happen:

1. If the truncation radius falls well within the B star Roche lobe, this results in the formation of a very dense disk which grows as matter is stopped at the truncation radius. It can happen that the disk becomes unstable and disrupted. When disruption takes place the matter is expelled away from the B star and it is available to be accreted onto the neutron star. These processes can account for Type II outbursts.
2. If the truncation radius is close to the first Lagrangian point at periastron, then some Roche lobe overflow of disk matter can take place. The runaway matter possesses enough angular momentum to form an accreting disk around the neutron star. Type I outbursts can be explained by this picture.

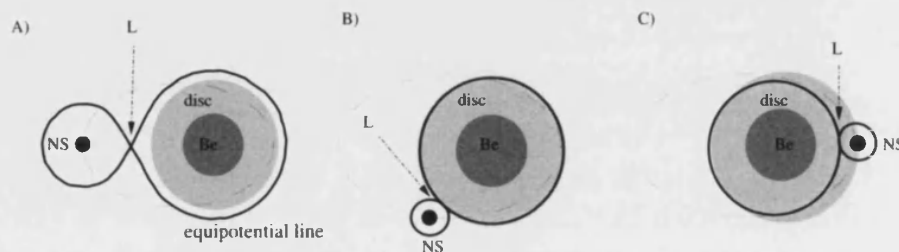


Figure 2.5: In an eccentric binary system composed by a Be star and a neutron star (NS), mass transfer can happen by stellar wind but also by Roche lobe overflow under some circumstances. (A) When the NS is at apastron, the only way matter can be transferred into its potential well is through stellar wind or some mass ejection mechanism. (B) Before the NS approaches the periastron, some disk matter can already be transferred through Roche lobe overflow (at the first lagrangian point L). The orbital phase of Roche lobe overflow onset depends on the eccentricity of the orbit and the size of the disk. (C) At periastron the NS can be immersed in the Be disk. The size of the disk and the mass transfer mechanism depend on the particular orbital parameters and/or disk dynamics of the system.

Truncation is not always 100% effective, as the presence of persistent low luminosity BeX systems requires some constant outflow of matter which is accreted onto the neutron star. The truncation radius depends on the orbital parameters of the system. This model successfully explains the behavior of low eccentricity ( $e < 0.25$ ) and high eccentricity ( $e > 0.6$ ) systems (see Okazaki & Negueruela 2001), but its application to moderate eccentricity systems is more subtle and depends on many details of each particular system. Low eccentricity systems have a small truncation radius and therefore generally show only Type II outbursts. High eccentricity systems have large truncation radius and show most of the time Type I outbursts. Systems with moderate eccentricity show a rich variety of phenomena, indicating successive disruptions and reformations of the Be disk. This last assumption applies to SAX J2103.5+4545, one of the systems analyzed in this thesis work.

There exists a correlation between the orbital period of the system and the pulse period of the compact object in the BeX systems, see Corbet (1986).

## Chapter 3

# INTEGRAL

The *INTEGRAL* satellite was launched on October 17, 2002. It is an ESA mission with collaborations from Russia and NASA. It is orbiting the Earth in a highly eccentric orbit with a revolution period of 3 sidereal days. It has a perigee height of 10000 km and an apogee height of 152600 km with an inclination of 51.6 deg with respect to the equatorial plane. These orbit parameters were chosen to minimize the background noise due to charged particles trapped in the radiation belt and to allow for long periods of continuous observation. The *INTEGRAL* objective is to perform  $\gamma$ -ray astronomy (in the 15 keV–10 MeV range) using high-resolution spectroscopy and fine imaging, with simultaneous monitoring in X-ray (3–35 keV) and optical (5000–6000 Å) bands.

There are three high energy instruments on board *INTEGRAL*:

- **1)** The Imager on Board INTEGRAL Spacecraft (IBIS), which is composed of two detector layers: INTEGRAL Spacecraft Gamma-Ray Imager (ISGRI), working in the 15–1000 keV energy range; and the PIXellated CsI Telescope (PICsIT), working in the 0.175–10.0 MeV energy range.
- **2)** The SPectrometer on board INTEGRAL (SPI), working in the 18 keV–8 MeV energy range.
- **3)** The Joint European Monitor-X (JEM-X), working in the softer X-ray bands (3–35 keV).

Giving support to the high energy observations, the Optical Monitoring Camera (OMC) provides  $V$  magnitudes of the targets of interest. All instruments are described in more detail below.

### 3.1 Coded Mask aperture systems

The high energy instruments aboard *INTEGRAL* are coded mask telescopes. This is due to the fact that focusing of high energy photons is very difficult. It requires techniques of very small angular incidence on special mirrors or crystals which, in turn, imply very large focusing lengths.

Coded mask systems were born with the idea of the pin hole camera in mind, i.e., just to block all radiation coming from the source with an opaque element except that passing through a small hole. As the number of photons coming from high energy sources is usually very low, instead of only one hole we need to perforate as many holes as possible in our opaque element. Now instead of an image we have one image per hole in our detector. The diffuse background will also contribute through all the holes. Fig. 3.1 illustrates this process.

The original image needs to be reconstructed. The quantity of holes and their pattern determines the *imaging* capabilities and the sensitivity of our system. An equilibrium must be found between the number of holes (the more holes we have the more photons we can detect) and the quality of the resulting image (the signal to noise ratio, the number of artifacts due to the reconstruction process, etc.)

The mask pattern must be chosen in a way that photons from a certain direction in the sky project the mask on the detector, shifted with respect to the central position, over a distance which corresponds uniquely to the direction of the incident photons. In addition, the signal-to-noise ratio of a reconstructed source position must be optimum. From the mathematical point of view, if the autocorrelation function of the mask pattern is a delta function, that makes the reconstruction process more reliable. Thus, we already have some restrictions on which kind of patterns are more appreciated by high energy astrophysicists.

Patterns based on cyclic difference sets demonstrated to be good candidates to accomplish the above requirements (see Gunson & Polychronopoulos 1976; Fenimore & Cannon 1978). Furthermore, their autocorrelation

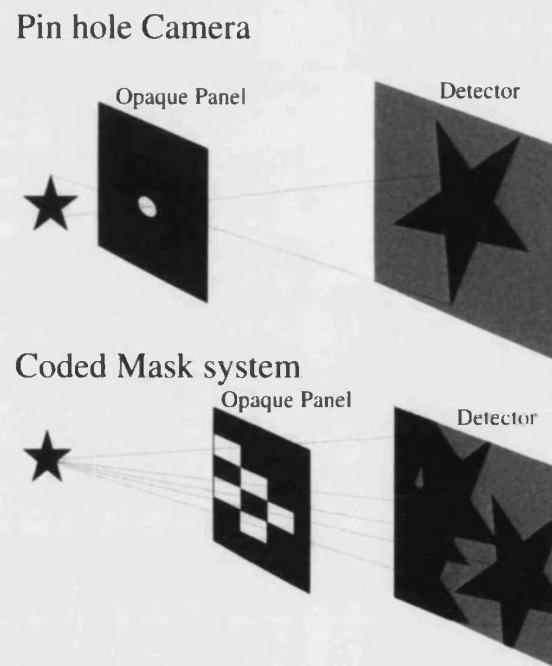


Figure 3.1: Comparison of the creation of an image in our detector plane by placing a pin hole camera as *imaging* system and by placing a coded mask system.

function can produce flat side lobes. Non-flat side lobes can introduce spikes in our image which can resemble true sky sources. Getting rid of these spikes (commonly called ghosts) is one of the more intriguing aspects of coded mask imaging.

A cyclic difference set  $D$ , characterized by the parameters  $n$ ,  $k$  and  $z$ , is a collection of  $k$  integers  $\{I_1, I_2, \dots, I_k\}$  with values  $I_i$  between 0 and  $n$  such that for any  $J \neq 0 \pmod{n}$  (that is, any  $J$  integer which is not divisible by  $n$ ) the congruence  $I_i - I_j = J \pmod{n}$  has exactly  $z$  solution pairs  $(I_i, I_j)$  within  $D$ <sup>1</sup>. A great advantage of cyclic difference sets is that they can be represented by a binary sequence  $a_i$  ( $i=0, \dots, n-1$ ) with  $a_i=1$  if  $i$  is a member of  $D$  and  $a_i=0$  otherwise. In this way the set of  $a_i$  can represent the discrete mask pattern if we assign a transparent element to  $a_i=1$  and an opaque element to  $a_i=0$ . If the condition  $n = p \times q$ , with  $p$  and  $q$  integers, is satisfied, then the sequence of  $a_i$ s can be transformed into a bi-dimensional array. Every difference  $i-j$  between a pair of  $a_i$  and  $a_j$  both equal to 1 is equally sampled. Therefore these arrays are also called Uniformly Redundant Arrays (URA, see Fenimore & Cannon 1978).

Which URA is chosen depends mainly on the existence of the inverse of the bi-dimensional array constructed from the set, and on its autocorrelation function. The cyclic autocorrelation  $c_l$  of  $a_i$  is:

$$c_l = \sum_{i=0}^{n-1} a_i a_{\text{mod}(i+l, n)} = \begin{cases} k & \text{if } \text{mod}(l, n) = 0 \\ z = \frac{k(k-1)}{n-1} & \text{if } \text{mod}(l, n) \neq 0 \end{cases}$$

From this relationship we can deduce that it is desirable to have a difference between  $k$  and  $z$  that is as large as possible, because  $k$  determines the signal and  $z$  the background level.

<sup>1</sup>A very important equivalence relation defined within the integers is called *congruence modulo  $n$* . It is important because of the kind of arithmetic that is associated with it. For example, if it is now 10 o'clock in the morning what time will it be in 7 hours? What you do is add 10 to 7 and get an answer of 5 since you replace the answer by the remainder on division by 12. That is we have  $10+7=5$ . Let  $n$  be a fixed positive integer. We define a relation between two integers  $i \equiv j \pmod{n}$  if and only if  $n$  divides  $i - j$ . This is an equivalence relation on the integers. An equivalence class consists of those integers which have the same remainder on division by  $n$ . Rather than saying the integers  $i$  and  $j$  are equivalent we say that they are *congruent modulo  $n$*  which, symbolically, is written as  $i \equiv j \pmod{n}$ . The set of class representatives is called a complete set of residues modulo  $n$  and a class representative is called a residue.

There are two kinds of cyclic sets which maximize the difference between  $k$  and  $z$ :

- **Singer sets** are characterized by  $n = \frac{t^{m+1}-1}{(t-1)}$ ,  $k = \frac{t^m-1}{(t-1)}$  and  $z = \frac{t^{m-1}-1}{(t-1)}$ , where  $t$  is a prime power.
- **Hartman sets** are characterized by  $n = 4t - 1$ ,  $k = 2t - 1$  and  $z = t - 1$ , if  $t$  is integer. According to the value of  $n$  they are classified in 3 classes: **a)** Quadratic residue sets when  $n$  is prime; **b)** Twin prime sets when  $n = p(p+2)$  for integer  $p$ , with  $p$  and  $p+2$  being prime; and **c)** Pseudo-noise sets:  $n = 2^m - 1$  ( $m > 1$  is integer).

From this sets the mask pattern can be obtained as mentioned above. Some tricks have been used to reduce the noise in the reconstructed image, such as substituting the 0s and 1s by some other numbers.

There are many available methods to reconstruct the original image from the codified one, we will enumerate only the most straightforward ones:

- **Inversion.** We can describe the pattern detected as  $D = M \times S + B$ , where  $M$  is the mask patter,  $S$  the sky in our field of view and  $B$  the background. The sky image ( $S$ ) is convolved by the mask pattern ( $M$ ), we represent this operation as  $M \times S$ . We can simply take the inverse of the mask pattern and multiply both sides of the equation, obtaining  $M^{-1}D - M^{-1}B = S$ . However, with this method the term  $M^{-1}B$  is likely going to dominate and the reconstructed noise can be very high.
- **Cross correlation.** This requires cross correlating the detector image  $D$  with the mask pattern via convolution with a matrix. The mask pattern, in practice, is modified in such a way that the matrix product  $MD$  evaluates directly  $S$  and cancels contributions from  $B$ .
- **Maximum Entropy Method (MEM) and Iterative Removal of Sources (IROS).** These two methods fall in the group that we may call *iterative methods*. They try to find the best solution through an iterative search for the solution that is most consistent





Figure 3.2: Mask patterns of the high energy instruments aboard *INTEGRAL* as used by the instruments software. Black zones denote those places with a zero value (i.e., transparent elements) while white zones correspond to elements with a value of 1 (opaque elements).

with the detector data. MEM has gained widespread favour in different areas as a tool to restore degraded data. Despite the good results that can be obtained with this method, a major drawback is the large amount of computer effort required, as compared to linear methods such as cross correlation. IROS is in fact an extension of the cross correlation method. First it performs a cross correlation and find the strongest source, then the expected detector counts corresponding to this source are subtracted from the observed ones and a new autocorrelation is performed. Every time a new source is located, the solutions of all the sources found are summed up and consistency with the observed image is checked.

IBIS mask is based in a MURA pattern (Modified Uniformly Redundant Array). It is a slight modification of an URA to improve its imaging capabilities. SPI and JEM-X masks are based in HURA patterns, that is, URA patterns mapped onto an hexagonal grid. *INTEGRAL* high energy instruments' mask patterns can be seen in Fig. 3.2

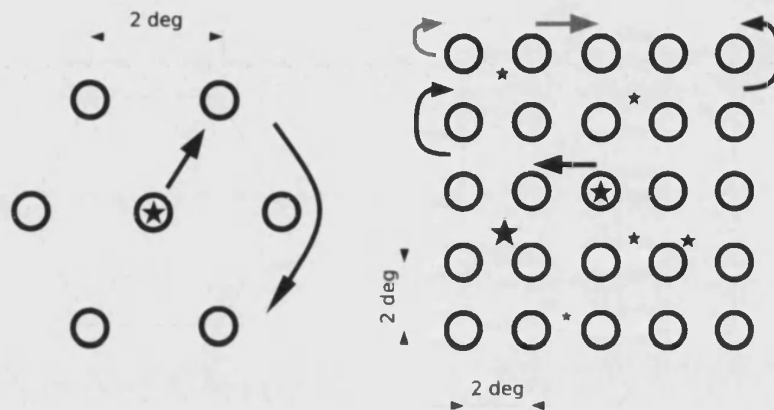


Figure 3.3: Hexagonal and  $5 \times 5$  dithering patterns used by *INTEGRAL* in open time observations. Hexagonal dithering is more adequate when only one source dominates in the FOV. In other cases it is more convenient to use the  $5 \times 5$ , otherwise SPI software may not be able to resolve the sources properly.

### 3.2 INTEGRAL observing time and observational strategy

*INTEGRAL* observing time is divided in *open time* (75% accessible to astronomers around the world) and *core program* (25%, which includes the Galactic Plane Survey –GPS– and the Galactic Center Deep Exposure –GCDE–, the science rights over the targets observed during the core program are distributed between the Institutes within the *INTEGRAL* collaboration).

Within the open time, the observational strategy is the so called *dithering pattern*. It consists on small (2 deg) displacements of the pointing from the target of interest which occupies the center of the FOV in the first pointing. *INTEGRAL* uses two kinds of dithering patterns,  $5 \times 5$  and hexagonal. They are illustrated in Fig. 3.3. The reason to perform such sort of observations is to minimize the systematic effects on spatial and temporal background variations in the spectrometer (SPI) detectors. The hexagonal dithering will be used when there is only one source in the FOV, the  $5 \times 5$  will be used in other cases.

The Galactic Plane, within 21 deg with respect to the galactic equator

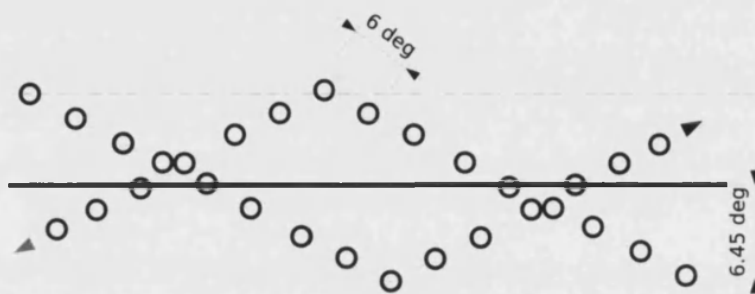


Figure 3.4: Representation of the observing strategy followed during GPS scans.

(taking into account the large FOV of SPI), is scanned by using a saw-like pattern, with individual exposures separated by 6 deg along the path. It is illustrated in Fig. 3.4. The exposure time of an individual pointing is typically of the order of  $\sim 2$  ks. These scans are performed once every two weeks.

The Galactic Center region, within galactic longitudes between  $-30$  and  $+30$  deg and galactic latitudes between  $-10$  and  $+10$  deg, is observed for a total of 46 days per year.

### 3.3 Instruments

#### 3.3.1 IBIS

The IBIS imaging system is based on two independent solid state detector arrays: ISGRI, optimized for low (15–1000 keV); and PICsIT, optimized for high (0.175–10.0 MeV) energies.

- ISGRI is composed by 16384 ( $128 \times 128$ ) CdTe detectors, covering a large sensitive area ( $\sim 2600$  cm<sup>2</sup>). It was doted with a very good imaging capability and fine spectral and timing resolutions. 8 identical modules, with 3264 pixels each one, compose the detector plane.
- PICsIT is made of 4096 ( $64 \times 64$ ) Caesium Iodide detectors (CsI) with a total sensitive area of  $\sim 2890$  cm<sup>2</sup>. The CsI(Tl) layer is divided into eight rectangular modules of  $16 \times 32$  pixels each.

Table 3.1: IBIS performance parameters.

Parameter	Value
Energy range	15 keV–10 MeV
Detector area	ISGRI: 2600 cm <sup>2</sup> (CdTe) PICsIT 2900 cm <sup>2</sup> (CsI)
Spectral resolution	7% @ 100 keV 9% @ 1 MeV
Field of view	9×9 deg Fully Coded (FCFOV)
Angular resolution	12 arcmin FWHM
Line sensitivity (3 $\sigma$ in 10 <sup>6</sup> s, @ 100 keV)	1.8×10 <sup>-5</sup> photon s <sup>-1</sup> cm <sup>-2</sup>
Continuum sensitivity (3 $\sigma$ in 10 <sup>5</sup> s, @ 100 keV, $\Delta E = \frac{E}{2}$ )	2.3×10 <sup>-6</sup> photon s <sup>-1</sup> cm <sup>-2</sup> keV <sup>-1</sup>
Timing accuracy	61 ms - 1 hr
Typical source location accuracy	30 arcsec @ 100 keV (5 $\sigma$ source) 3 arcmin @ 100 keV (5 $\sigma$ source)
Resources (following EID-A allocation):	Mass 677 kg Power (sun/eclipse) 240/0 W Data rate (solar max.) 59.8 kbps Data rate (solar min.) 56.8 kbps

Both detectors are surrounded by an active VETO System, which shields them from the bottom up to the ISGRI detector plane. The imaging system is a tungsten coded mask, which is 16 mm thick and  $\sim 1$  m<sup>2</sup> in dimension. The incident photons are collimated by a passive shielding covering the distance between mask and detection plane.

IBIS key performances are summarized in Table 3.1 and a view of the IBIS telescope and its detector layer is shown in Fig. 3.5.

ISGRI and PICsIT keep record of the spatial and time coordinates of each event produced in each detectors' plane. This collection of events and coordinates compose the shadowgram, projected from the mask down to the detection plane. Photons from the source and the background are distributed across the entire field of view, making necessary the use of cross-correlation techniques to recover the full image for the fully coded field of view (9×9 degrees). For the partially coded field of view (out to 29×29 degrees), special techniques must be applied to the data to properly reconstruct the image. The VETO system helps to discard events

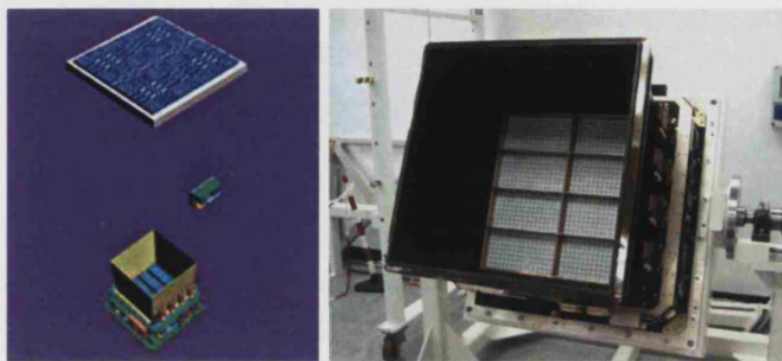


Figure 3.5: IBIS instrument schematic representation and view of its detector assembly.

attributed to the background.

The coded mask is optimized for high angular resolution, which is limited, then, by the spatial resolution of the detector array. The IBIS coded mask (together with SPI and JEM-X coded masks) can be seen in Fig 3.2. It is a square array with 9595 individual square cells, based on a cyclic replication of a MURA pattern of order 53. About half of the mask elements are opaque to photons in the operational energy range of the IBIS instrument.

ISGRI and PICsIT can be used simultaneously to work in *Compton* mode, however, this mode is not used yet. Photons scattered at ISGRI detector plane and detected in PICsIT detector layer help to recover information on the direction and energy of the incident photon. This helps to improve the instrument sensitivity by re-assigning the right energies to photons which may have lost energy by the scattering process.

All the instrument information can be found in the IBIS Analysis user Manual (see Chernyakova 2004a), available at the ISDC web pages<sup>1</sup>.

### 3.3.2 SPI

SPI is a coded-mask telescope with 19 hexagonal detector elements of Germanium, with a total of  $\sim 500$  cm<sup>2</sup> sensitive area. The spectral resolution is fine enough to resolve astrophysical lines and allow spectroscopy in the regime of gamma-rays. There are several methods to reduce the back-

<sup>1</sup><http://isdc.unige.ch/index.cgi?Support+documents>

Table 3.2: SPI performance parameters.

Parameter	Value
Energy range	18 keV–8 MeV
Detector area	500 cm <sup>2</sup> (Germanium)
Spectral resolution (E/ΔE @ 1 MeV)	~450. (2.2 keV FWHM @ 1.33 MeV)
Field of view (corner to corner)	16 deg fully coded
Angular resolution (point sources)	2.5 deg FWHM
Narrow-line sensitivity	
3σ in 10 <sup>6</sup> s, @ 1 MeV	2.4×10 <sup>5</sup> photon s <sup>-1</sup> cm <sup>2</sup>
3σ in 10 <sup>6</sup> s, @ 511 keV	4.6×10 <sup>5</sup> photon s <sup>-1</sup> cm <sup>2</sup>
Continuum sensitivity (3σ in 10 <sup>6</sup> s, @ 1 MeV)	8.8×10 <sup>4</sup> photon s <sup>-1</sup> cm <sup>2</sup> MeV <sup>-1</sup>
Timing accuracy (3σ)	0.129 ms
Resources (following EID-A allocation):	Mass 1309 kg Power (sun/eclipse) 385/110 W Data rate 45 kbps

ground counts: **a**) a Pulse Shape Discriminator system (PSD) reduces the decay background in the Germanium; **b**) an Anti-Coincidence Shield (ACS) which collimates the incident photons; and **c**) a plastic scintillator (PSAC) below the coded mask stops charged particles. The main SPI performance parameters are summarized in Table 3.2 and a view of the SPI telescope and its detector layer is shown in Fig. 3.6.

The SPI coded mask provides imaging at moderate resolution, and it can be seen (together with IBIS and JEM-X coded masks) in Fig 3.2.

The SPI mask is located 171 cm above the detector plane. It consists of a coded pattern made of 127 hexagonal elements of tungsten inscribed in a 78 cm diameter circle. 63 of them are opaque and 64 are transparent. The SPI mask pattern is symmetric against 120 deg rotation. The tungsten elements stop the gamma ray radiation in the range 20 keV to 8 MeV with an absorption efficiency greater than 95% at 1 MeV. The holes in the mask have a gamma ray transparency of 60% at 20 keV and 80% at 50 keV.

A deeper description of the instrument can be found in the *SPI Analysis User Manual* (see Dubath et al. 2004).



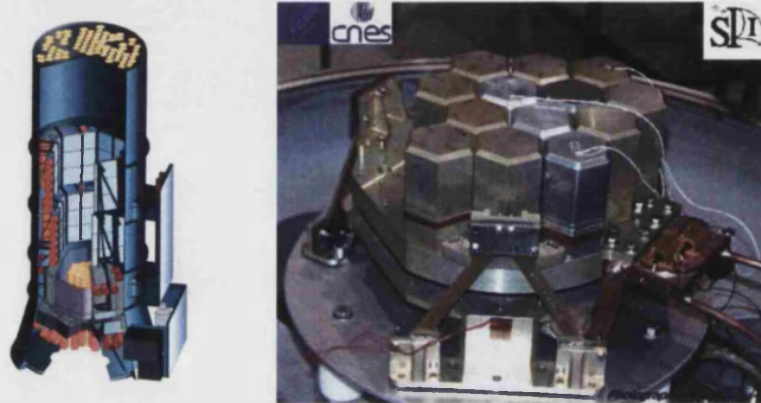


Figure 3.6: SPI instrument schematic representation and view of its detector assembly.

### 3.3.3 JEM-X

The Joint European X-Ray Monitor JEM-X gives support in softer energy bands (3–35 keV) to the main Integral instruments (the Spectrometer, SPI, and the Imager, IBIS). JEM-X can also provide scientific results concerning soft sources.

JEM-X consists of two identical coded-aperture mask telescopes co-aligned with the other instruments on INTEGRAL. Each one contains a detector which consists of a high pressure imaging microstrip gas chamber (at a pressure of 1.5 bar, and with a composition of 90% Xenon + 10% Methane), at nominal gas gain of 1500. Each detector unit views the sky through its coded aperture mask located at a distance of  $\sim 3.2$  m above the detection plane. The incoming photons are collimated by a structure with square-shaped cells placed on top of the detector entrance window. Table 3.3 summarizes the performance parameters of JEM-X and a view of the JEM-X telescope and its detector layer is shown in Fig. 3.7.

The JEM-X coded mask (together with IBIS and SPI ones) can be seen in Fig 3.2. The mask is based on a Hexagonal Uniformly Redundant Array (HURA). A pattern composed of 22501 elements with only 25% open area was chosen. The mask height above the detector ( $\sim 3.2$  m) and the mask element dimension (3.3 mm) define together the angular resolution of the instrument, in this case 3 arcmin.

A detailed description of the instrument can be found in the *JEM-X*

Table 3.3: JEM-X performance parameters.

Parameter	Value
Energy range	3–35 keV
Detector area	500 cm <sup>2</sup> (1 unit)
Energy resolution	1.3 keV @ 10 keV
Field of view	4.8 deg (dia) fully coded FOV
Angular resolution	3 arcmin
Continuum sensitivity (3 $\sigma$ in 10 <sup>5</sup> s, @ 6 keV, $\Delta E=0.5E$ )	$1.2 \times 10^{-4}$ photon s <sup>-1</sup> cm <sup>-2</sup> keV <sup>-1</sup>
Line sensitivity (3 $\sigma$ in 10 <sup>5</sup> s, @ 6 keV)	$1.6 \times 10^{-4}$ photon s <sup>-1</sup> cm <sup>-2</sup>
Timing accuracy	(3 $\sigma$ ) 122 $\mu$ s
Source location (15 $\sigma$ isolated source)	<1 arcmin (90% confidence)

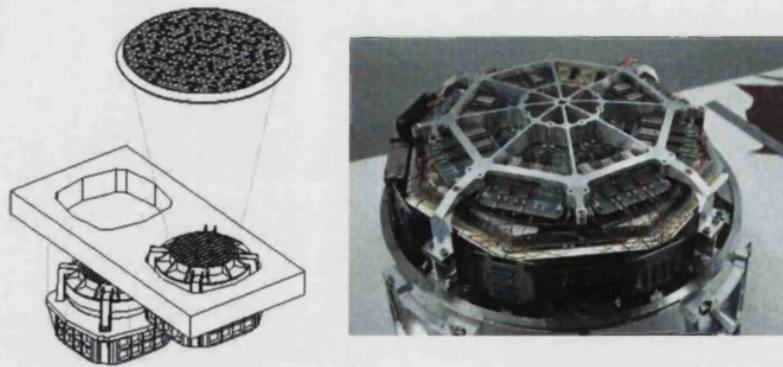


Figure 3.7: JEM-X instrument schematic representation and view of its detector assembly.



Table 3.4: OMC performance parameters.

Parameter	Value
Wavelength range	5000–6000 Å (Johnson <i>V</i> -filter)
Detector	50 mm lens + CCD (2055 x 1056 pixels) imaging area = 1024 x 1024 pixels
Pixel size	$(13 \times 13) \mu\text{m}^2 = (17.5 \times 17.5) \text{ arcsec}^2$
Field of view	5×5 deg
Angular resolution	23 arcsec
Typical integration times	10 s – 50 s – 200 s
Sensitivity ( $3\sigma$ in 10×200 s)	18.1 mag (V)
Photometric accuracy	<0.3 mag for <16 mag and >300 s
Typical source location accuracy	6 arcsec

*Analysis User Manual* (see Chernyakova & Kretschmar 2004a).

### 3.3.4 OMC

The Optical Monitoring Camera OMC consists of a CCD with 2055×1056 pixels, and an imaging area of 1024×1024 pixels, working in frame transfer mode. The frame transfer time is 2 ms. This design allows continuous measurements and makes it unnecessary to have a mechanical shutter. The CCD is at the focal plane of a 50 mm diameter optical telescope working with a Johnson *V*-filter. The OMC covers the 5000–6000 Å wavelength range. It gives support to the other *INTEGRAL* instruments by observing the high energy targets in the optical band. 2 light emitting diodes located at the CCD cavity of the camera allow flat field calibrations.

The OMC performance parameters are shown in Table 3.4 and a view of the OMC telescope is shown in Fig. 3.8.

The whole CCD image is not transmitted to ground, only a number of windows (of typically 11×11 pixels, or 30×30 arcmin) are extracted around each object of interest.

A detailed description of the instrument can be found in the *OMC Analysis User Manual* (see Chernyakova & Kretschmar 2004b).

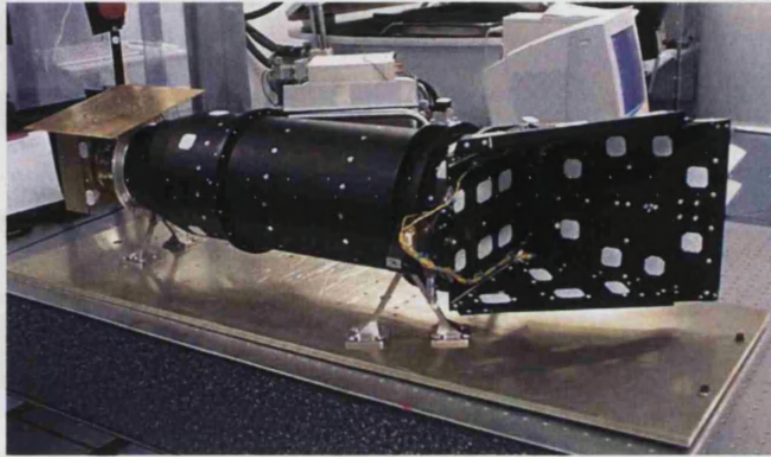


Figure 3.8: OMC FM before integration in the *INTEGRAL* payload.

## 3.4 Software.

### 3.4.1 INTEGRAL data repository

The Integral Science Data Center (ISDC) is in charge of storing, pre-processing, organising, and making available to users all the *INTEGRAL* data and analysis software. *INTEGRAL* data is organized in a quite logical way.

The first thing to keep in mind is the way the software access the data. The data format chosen to store *INTEGRAL* data is the FITS (Flexible Image Transport System) format. FITS files can store information in different extensions. This permits to have just one file agglutinating all the interesting information in the different extensions, instead of having multiple files to care for. A view of the extensions of a FITS file is shown in Fig. 3.9. In this case, the FITS file contains 4 extensions, numbered starting from 0. Each extension is accompanied by a HEADER, where we find information about what kind of data contains the extension, date of creation, as well as all useful information to analyse the data.

Thus, when accessing a FITS file, we need to specify which particular extension we want to access. In *INTEGRAL* terminology, when we specify both the FITS file and the extension, we say we are specifying the DOL object we want to access. DOL stands for Data Object Locator. In the example shown in Fig. 3.9, if we want to access the 4th extension, we

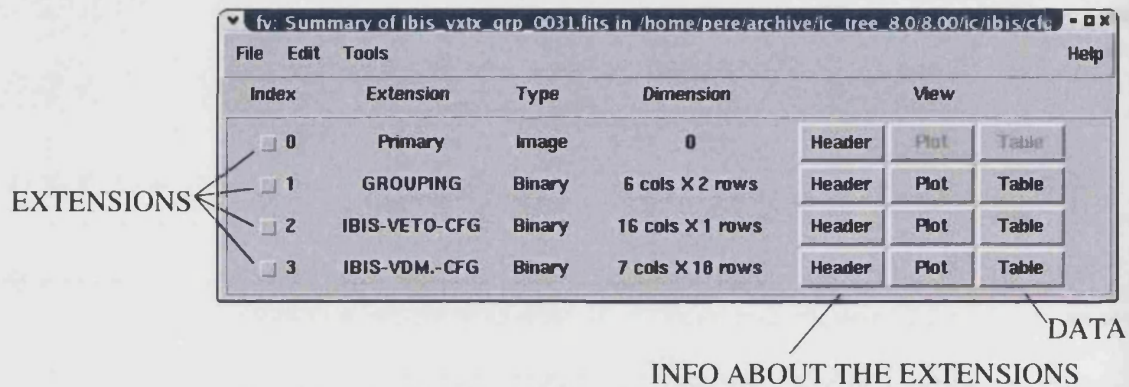


Figure 3.9: FITS file with four extensions. In particular, it is the *ibis\_vrtx\_grp\_0031.fits* file from the IBIS instrument characteristics.

will specify the DOL: *ibis\_vrtx\_grp\_0031.fits[3]*. For dealing with DOL specifications *INTEGRAL* software supplies a Data Access Library (DAL).

Instead of data, one extension can contain information about where data is stored, i.e., information about the path needed to find other files. In this case the FITS file is called an INDEX.

We could divide the repository of *INTEGRAL* data into those files concerning instrument calibrations, configurations and models, and those files concerning the scientific data themselves. Some of the data are stored in general folders which change very little in time (mask patterns, response matrix functions, etc) and some other data are stored in folders which contain information variable on time, like how the temperatures, voltage (and all house keeping parameters) change with time, the different pointing observations (scientific data), etc. This second group of time dependent data are organized by revolutions, that is, all the data collected during one *INTEGRAL* orbit will be stored in the same folder.

In the first group we can find the configuration files for the instruments, their mask models, their calibration files, good limits (referring to housekeeping data), etc. These files hang in a folder called *ic*, which stands for **in**struments **ch**aracteristics. Within this folder we can find one sub-folder per instrument. A view into this folder may look like this:

```
ibis  irem  jmx1  jmx2  omc  sc  spi
```

The *sc* (space craft) folder contains information about the whole payload

which can affect the data analysis. The *irem* folder contains data from the **INTEGRAL Radiation Environment Monitor**.

Another folder containing instrumental information is *aux*. It contains information about each particular time of observation. We can find there files like *time\_correlation.fits* which indicates the delay between *INTEGRAL* internal clock and an on ground clock (this delay is changing over time). The final true pointings and attitude information, and all the house keeping time dependent data (measurements of temperature and voltages, etc) are contained in this folder as well. In this folder data are organized by revolutions.

The last folder containing information of the instruments is the *idx* folder. Instead of real data, here we can find indexes, grouping the data into categories, in a way that when the software needs some kind of data it will search within the appropriate index and there it will find the real location of the data. This is very useful for programming purposes because in this way the software only needs to worry about where the indexes are located, DAL libraries will search the data for them.

All the scientific data are organized by revolution and within a revolution by pointing number. We have already seen that the *INTEGRAL* observational strategy divides observations into individual pointings within a dithering pattern or within the GPS. From all revolutions and science windows available we prepare our observation group, which contains indexes pointing to all the scientific data of our interest as well as indexes pointing to the instrument characteristics files. Within a folder called *obs* we store all the observation groups we prepare and analyse. There, the science products resulting from our analysis are stored.

As a summary, we can find in Fig. 3.10 how our data are organized in our working directory. Fig. 3.10 also exemplifies the naming rules to folders and sub-folders. When data is organized into folders according to science windows, the folder will be named as follows: the 4 first digits make reference to the revolution to which the folder belongs, the 4 next digits make difference to the science window number, the following 3 digits indicate the sub-science window division if the same pointing has been divided in several observations, the next digit make reference to the kind of observation (0 if it is science exposure, 1 if it is slew, and 2 in case it is some other kind of observation) and the last 3 digits after the dot

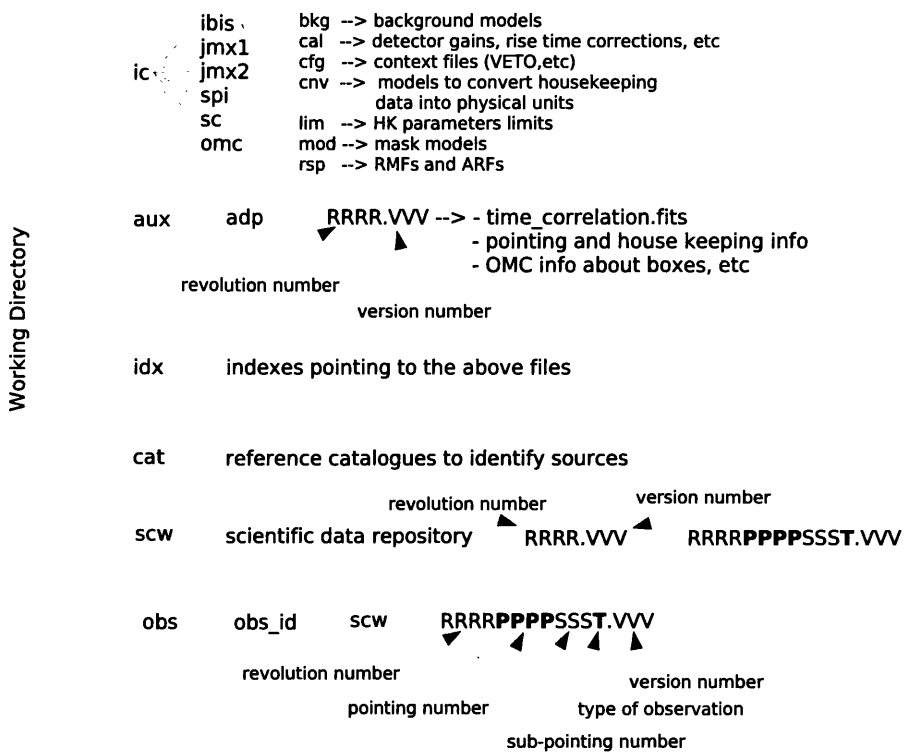


Figure 3.10: Schematic view of the organization of *INTEGRAL* data in a working directory.

indicate the data repository version number. This version change when the pre-processing software version changes and the whole data repository is re-pre-processed again.

### 3.4.2 INTEGRAL Data Analysis Software

The standard software to reduce *INTEGRAL* data and to extract light curves and spectra (that is, science products) is maintained at the Integral Science Data Center (ISDC) and it is called Offline Scientific Analysis (OSA) software. Software developers from all the instrument teams must deliver their software packages to the ISDC. In the ISDC all this software

is plugged together in a standard pipeline.

Although each *INTEGRAL* instrument has its own peculiarities, there are some general steps which are performed in all the instrument pipelines (with a dedicated specific software in each case, as the nature of the instruments is very diverse and requires treatment of the data in different ways). We can divide the data processing in two sets of operations. The first set is in charge of performing all necessary instrumental corrections on the data, i.e., gain corrections, time shifts corrections, calculate good time intervals according to house keeping limits, etc. The second set of operations is directed to obtaining the science products, through the deconvolution of the image, the extraction of events, etc.

The general correction steps defined by the ISDC are:

- **COR** In this step data is corrected of instrumental effects (gains, energy, position and time corrections, etc.).
- **POIN** (Only for SPI) The time periods during which the pointing can be considered to be constant.
- **GTI** (Good Time Intervals) The intervals in which there were telemetry gaps, anomalous high background, or improper behavior.
- **DEAD** Within the GTIs those intervals in which the instrument detectors are not capable to register photons are excluded (for instance the lapse between one detection, the reaction of the electronics and the time the detector needs to recover to be able to detect a new photon).

The set of steps which result in science products, as defined by the ISDC, are the following ones:

- **BIN\_I** Prepares the list of events binned in energies as required by the user.
- **BKG, BKG\_I, BKG\_S** Estimates the background from models for general use (BKG) for Imaging (BKG\_I) or for spectral extraction (BKG\_S).
- **CAT, CAT\_I, CAT\_S** From the reference catalog, selects the sources which fall in the FOV of the instrument for all the observing group.

This list of sources is used to identify the sources detected or tag them as NEW if no source from the catalog is coincident with the detected position.

- **IMA** In this step the deconvolution is performed and images of the sky are generated. A list of sources detected, with fluxes and positions, is also generated. For IBIS, only ISGRI image reconstruction is performed. Also a mosaic image of all the pointings in the observation group is generated.
- **IMA2** (Only IBIS and JEM-X) For IBIS, PICsIT image reconstruction is performed in this step (ISGRI image reconstruction was performed in the previous step). For JEM-X, the mosaicking of images is performed in this step.
- **BIN\_S** In this step the events are rebinned in the proper energy bins to perform spectral extraction.
- **SPE** Extracts the spectra of selected sources within the FOV of the instrument. In the case of JEM-X a set of ARFs are also created.
- **BIN\_T** (Only JEM-X) Performs a binning of the events in time, for the light curve analysis.
- **LCR** (Only IBIS and JEM-X) This step produces light curves with the desired time binning.

Each one of these steps is performed by one or more executables. These executables are the lower end responsible of the data reduction process. Their behaviour can be controlled by a set of parameter files which can be modified by the user.

In general the first set of operations are performed over the whole set of science windows in a particular observation group. When all corrections are finished, the next set of operations until imaging are performed again over the whole set of science windows in our observation group. At this point the user will have a look to the imaging results and the list of detected sources, as well as the quality of the detection. With this information at hand it will be time to decide for which sources to extract spectra and with which energy binning and also which light curves are of

interest (for long term analysis or pulse period analysis). Then the last steps are run over a selected set of science windows and/or sources.

All the above described steps make reference to the high energy instruments aboard *INTEGRAL*. The OMC, because of the very different nature of the instrument, presents some important differences in the data reduction process. In this case only the steps COR, GTI, IMA and IMA2 are carried out. The IMA2 step for the OMC consists of the creation of the list of detections with indication of times, position and magnitudes.

Extended information about the data analysis can be found in each instrument data analysis manual or at *Introduction to the INTEGRAL Data Analysis* (Chernyakova 2004b).

From the list of known software issues distributed together with the ISDC OSA software version 4.2, a set of limitations, considered of special interest, have been extracted:

**ISGRI software limitations:** In the image reconstruction, secondary lobes of strong very-off-axis sources are sometimes not fully corrected or cleaned in reconstructed images.

Addition of many spectra of a weak source obtained for the different science windows with `ii_spectra_extract` (standard ISGRI spectral extraction package) may give a bad total spectrum, because spectral reconstruction is very sensitive to the background correction. In certain cases, running the imaging procedure on several (large) energy bands can provide a better spectrum. It must also be noted that below 20 keV the spectrum is not properly extracted.

**SPI software limitations:** SPI is almost always dominated by background contributions. The scientific validation of the SPI data analysis going on at the ISDC and at different instrument teams is still incomplete. The results obtained with the ISDC software must be treated carefully. Spurious results can be derived, for example, when using a wrong set of parameters or an incorrect background modeling.

**JEMX software limitations:** Vignetting modeling still needs further development. Sources at the edge of the field of view must be treated very carefully, the systematics introduced by the incomplete vignetting correction can be of the order of  $\sim 30\%$ . Also, at this moment mosaicking has been disabled from the JEM-X standard pipeline, as there was a strong systematic noise structure because the significance information for



individual images was not yet used.

More information about the software and downloads can be found at ISDC web pages<sup>2</sup>.

## 3.5 Analysis Tools

Once we have all the science products coming from a standard OSA pipeline analysis, what can we do with the count rates, spectra and light curves obtained? In this section we try to introduce the basics of the standard analysis performed with high energy data.

### 3.5.1 High Energy Astrophysics software

The NASA's High Energy Astrophysics Science Archive Research Center (HEASARC<sup>3</sup>) develops and maintains a set of software applications destined to help high energy astrophysicist around the world to perform spatial, spectral, and timing analysis on their data. It consists on a series of general FITS file manipulation tools (FTOOLS), from which we highlight:

- Calibration tools: destined to work with each mission specific calibration data, mainly with the Response Matrix Functions (RMFs) and the Ancillary Response Files (ARFs).
- FITS utilities: a set of utilities to create and modify FITS files (add or modify headers, display data, operate with rows and columns, etc)
- FITS image tools: set of packages with the aim to manipulate FITS binary extensions which are images, as well as extract information from them, combine them, etc.
- Xronos: a set of utilities directed to the timing analysis (generation of light curves, Fourier transforms and epoch folding techniques, etc)

HEASARC software (HEASoft) has been widely adopted as a standard for high energy data manipulation.

<sup>2</sup><http://isdc.unige.ch/index.cgi?Soft+info>

<sup>3</sup><http://heasarc.gsfc.nasa.gov/>

### 3.5.2 Imaging

An important achievement with *INTEGRAL* mission is the possibility to combine high accuracy in imaging and spectroscopy at the same time. Imaging with ISGRI and JEM-X will allow us to determine with high precision the coordinates of high energy sources. The source location accuracy will depend on the signal to noise ratio. ISGRI can locate a source detected with a signal to noise ratio of 20 with a  $<1$  arcmin error (see Gros et al. 2003). JEM-X can locate a bright source with an error of the order of  $\sim 30$  arcsec (for a  $10\sigma$  source, see Lund et al. 2003 and Martínez Núñez et al. 2003).

Apart from source location, imaging will provide count rates integrated over the typical *INTEGRAL* pointing time scales (i.e. of the order of 2 ks). Furthermore, the possibility of computing mosaics can increase the instruments sensitivities and that will allow us to detect very weak sources (see Bird et al. 2004, 2006).

### 3.5.3 Timing analysis

Once we have extracted a light curve with a given binning in time from our list of events, we want to investigate the presence of variability. Most of the time a visual inspection of the events list will give us clues about the kind of variability we can expect, but in some cases the noise present in the data will hide variability from visual inspection.

To confirm the presence of some coherent variability (modulated at a certain period) in our light curve, Fourier transform techniques can be applied. The data will be transformed into a frequency domain and for each frequency a *power* will be estimated (as the square sum of the imaginary and real parts of the transformation). This power will give an indication of the relative importance of the given frequency with respect to the others in the modulation of the data. If one frequency dominates the modulation, a clear peak will be visible in the power versus frequency plot (the periodogram). The frequency at which this peak happens will give us an idea of the period of such modulation. In this work Discrete Fourier Transform (DFT) and Fast Fourier Transform (FFT) techniques have been used. The DFT can be applied to any light curve, but it requires a big amount of computing resources. FFT is a much faster method than the DFT but has

a limitation, it must be applied to a data set in which the total number of data is a power of 2. Both methods can be troublesome when dealing with large time gaps in the data set. To take care of such a problem a number of algorithms were created, like the Lomb-Scargle algorithm, or the Clean algorithm. The Lomb-Scargle Algorithm provides a method to treat gaps and unevenly spaced time points (Lomb 1976, Scargle 1982). The Clean algorithm is an adaptation of an aperture synthesis algorithm to treat one dimensional data and is suitable to study data unevenly distributed on time (see Roberts 1987).

After a periodic modulation is detected, a finer search of the period can be performed with epoch folding techniques. A set of periodic variations are fitted to the data in a given range of periods and the  $\chi^2$  of each fit is calculated. The period yielding the fit with the best  $\chi^2$  will be the most likely period modulating the time series under study.

The shape of the pulse profile obtained by folding the light curve on the measured period, and its changes with time and/or energy, will provide an important source of information about the accretion process onto compact objects (see section 2.4).

### 3.5.4 Spectral analysis

The most widely used software package for spectral analysis of high energy sources is XSPEC, provided by HEASARC. XSPEC will not only allow to display and visually inspect our spectra (by re-binning, cutting-off bad data, etc), but it will let the user fit a great variety of models to the data. One of the most powerful aspects of XSPEC is the possibility to introduce the users' own models to fit the data.

The model chosen to compare our results with previously published ones will be that of a power law modified by a high energy cut-off. This is an empirical fit which will not give us information about the physical processes taking place in the source under study. However, it will give us important information about the source variability (in particular, about the changes in the slope of the continuum). A power law model takes the form:

$$F(E) = KE^{-\Gamma}$$

where  $F(E)$  is the flux at a given energy,  $E$ , measured in photons  $cm^{-2} keV^{-1}$ .  $K$  is a normalization factor, and  $\Gamma$  is called photon index.  $\Gamma$  will give us information about the slope of the continuum.

When the slope of the continuum changes at certain energy (called the cut-off energy), the power law model is modified accordingly and the model used to fit the spectrum will be:

$$\begin{aligned} F(E) &= KE^{-\Gamma} e^{-(E_{\text{cut}}-E)/E_{\text{fold}}} & \text{for } E > E_{\text{cut}} \\ F(E) &= KE^{-\Gamma} & \text{for } E < E_{\text{cut}} \end{aligned}$$

where  $F(E)$ ,  $K$ , and  $\Gamma$  stand as above,  $E_{\text{cut}}$  is the energy at which the cut-off (the change in slope of the continuum) is produced, and  $E_{\text{fold}}$  is the factor which determines how much the slope changes (called the folding energy).

Two other models also used along this thesis work are the *compTT* and *bmc* models (in XSPEC notation). The *compTT* model describes the Comptonisation of soft x-ray photons produced in the surroundings of a neutron star into which matter is accreting. It was developed by Titarchuk (1994). The *bmc* model is an analytic model describing Comptonisation of soft photons by matter undergoing relativistic bulk-motion. The typical scenario involves thermal X-rays from the inner region of an accretion disk in a compact object illuminating in-falling matter. For a detailed description of the model, refer to Titarchuk et al. (1997). Although these two models imply a physical interpretation of the scenario in a given system, we only used them to obtain an acceptable fit to the spectral continuum.

Hardness ratios offer a model-independent way to study spectral variability. These are ratios of count rates in different energy ranges. They will give us information about the slope of the spectral continuum and how it changes with time. We can find two definitions for the hardness ratios in the literature. Let us call  $C_L$  the count rate (or flux) in the lower energy band and  $C_H$  the count rate (or flux) in the higher energy band used to build the hardness ratio. Then the two definitions will be as follows:

1.  $\frac{C_H}{C_L}$
2.  $\frac{C_H - C_L}{C_H + C_L}$

Along this thesis work we will indicate which form of the hardness ratio is used in the analysis carried on in that particular moment.

### 3.5.5 Alternative methods

#### PIF based methods

Timing analysis, in principle, can be more straightforward than having to go through all the OSA pipeline, as light curve production is one of the latest steps in all instruments pipelines. A set of methods based on the calculation of the Pixel Illumination Fraction (PIF) have been developed by ISDC and some individuals.

In these methods only the first steps of the standard pipeline are run, that is, those performing the instruments calibrations and corrections. After that, taking into account the position of the source of interest in the field of view of the instrument and the mask pattern, a PIF for that particular source and observation is calculated. The fraction of pixels containing photons from the source are extracted and a list of events is created from them. When there are other bright sources in the FOV they must be taken into account when calculating the PIF and extracting the photons which come from our source.

#### A. Segreto & C. Ferrigno Software

Segreto & Ferrigno<sup>4</sup> have developed a method to analyze *INTEGRAL*/ISGI data in a more straightforward way than it is done by the standard pipeline. It is a PIF based method. Once the source events are selected they can be binned in time (for timing analysis) or energies (for spectral analysis). This last procedure makes use of a new calibration (LUT tables, RMF and ARF) performed by A. Segreto & C. Ferrigno.

The OSA analysis presented in this thesis work has been complemented by the use of this software.

---

<sup>4</sup><http://www.pa.iasf.cnr.it/ferrigno/INTEGRALsoftware.html>

## Bibliography

- Abramowicz, M. A., Chen, X., Kato, S., Lasota, J., and Regev, O.: 1995a, *ApJL* **438**, L37
- Abramowicz, M. A., Chen, X., and Taam, R. E.: 1995b, *ApJ* **452**, 379
- Benensohn, J. S. and Lamb, D. Q.: 1996, *Bulletin of the American Astronomical Society*, *astro-ph/9610245* **28**, 960
- Benensohn, J. S., Lamb, D. Q., and Taam, R. E.: 1997, *ApJ* **478**, 723
- Bird, A. J., Barlow, E. J., Bassani, L., Bazzano, A., Bélanger, G., Bodaghee, A., Capitanio, F., Dean, A. J., Fiocchi, M., Hill, A. B., Lebrun, F., Malizia, A., Mas-Hesse, J. M., Molina, M., Moran, L., Renaud, M., Sguera, V., Shaw, S. E., Stephen, J. B., Terrier, R., Ubertini, P., Walter, R., Willis, D. R., and Winkler, C.: 2006, *ApJ* **636**, 765
- Bird, A. J., Barlow, E. J., Bassani, L., Bazzano, A., Bodaghee, A., Capitanio, F., Cocchi, M., Del Santo, M., Dean, A. J., Hill, A. B., Lebrun, F., Malaguti, G., Malizia, A., Much, R., Shaw, S. E., Stephen, J. B., Terrier, R., Ubertini, P., and Walter, R.: 2004, *apJL* **607**, L33
- Bjorkman, J. E. and Cassinelli, J. P.: 1993, *ApJ* **409**, 429
- Braes, L. L. E. and Miley, G. K.: 1972, *Nature* **235**, 273
- Butler, C. J. and Byrne, P. B.: 1973, *Nature* **243**, 136
- Castor, J. I., Abbott, D. C., and Klein, R. I.: 1975, *ApJ* **195**, 157
- Chernyakova, M.: 2004a, *IBIS Analysis User Manual*, INTEGRAL Science Data Center
- Chernyakova, M.: 2004b, *Introduction to the INTEGRAL Data Analysis*, INTEGRAL Science Data Center
- Chernyakova, M. and Kretschmar, P.: 2004a, *JEM-X Analysis User Manual*, INTEGRAL Science Data Center

- Chernyakova, M. and Kretschmar, P.: 2004b, *OMC Analysis User Manual*, INTEGRAL Science Data Center
- Corbet, R. H. D.: 1986, *MNRAS* **220**, 1047
- Crampton, D. and Hutchings, J. B.: 1972, *ApJL* **178**, L65
- De Loore, B. C.: 2001, in *AIP Conf. Proc. 308: The Evolution of X-ray Binaries*, pp 203–276
- Dubath, P., Kreykenbohm, I., Chernyakova, M., and Beckmann, V.: 2004, *SPI Analysis User Manual*, INTEGRAL Science Data Center
- Fenimore, E. E. and Cannon, T. M.: 1978, *Applied Optics* **17**, 337
- Frank, J., King, A., and Raine, D.: 1992, *Accretion Power in Astrophysics*, ISBN 0521408636, Cambridge University Press, Cambridge
- Frontera, F., dal Fiume, D., Robba, N. R., Manzo, G., Re, S., and Costa, E.: 1987, *ApJL* **320**, L127
- Ghosh, P. and Lamb, F. K.: 1979, *ApJ* **234**, 296
- Gros, A., Goldwurm, A., Cadolle-Bel, M., Goldoni, P., Rodriguez, J., Foschini, L., Del Santo, M., and Blay, P.: 2003, *A&A* **411**, L179
- Gunson, J. and Polychronopoulos, B.: 1976, *MNRAS* **177**, 485
- Hubert, A. M., Floquet, M., Hao, J. X., Caillet, S., Catala, C., Foing, B. H., Neff, J. E., Huang, L., Hubert, H., Barban, C., Baudrand, J., Cao, H., Char, S., Chatzichristou, H., Cuby, J. G., Czarny, J., Dreux, M., Felenbok, P., Guerin, J., Hron, J., Huovelin, J., Jankov, S., Jiang, S., Le Contel, J. M., Maitzen, H. M., Petrov, P., Savanov, I., Shcherbakov, A., Simon, T., Stee, P., Tuominen, I., and Zhai, D.: 1997, *A&A* **324**, 929
- Hutchings, J. B. and Crampton, D.: 1981, *ApJ* **247**, 222
- Illarionov, A. F. and Sunyaev, R. A.: 1975, *A&A* **39**, 185
- Jahanara, B., Mitsumoto, M., Oka, K., Matsuda, T., Hachisu, I., and Boffin, H. M. J.: 2005, *A&A* **441**, 589

- Joss, P. C., Avni, Y., and Rappaport, S.: 1978, *ApJ* **221**, 645
- Karttunen, H., Kröger, P., Oja, H., Poutanen, M., and Donner, K. J.: 1987, *Fundamental Astronomy*, XIII., Springer-Verlag, Berlin
- Kudritzki, R. and Puls, J.: 2000, *ARA&A* **38**, 613
- Lamers, H. and Cassinelli, J.: 1999, *Introduction to stellar winds*, ISBN 0521595657, Cambridge University Press, Cambridge
- Lee, U., Osaki, Y., and Saio, H.: 1991, *MNRAS* **250**, 432
- Lomb, N. R.: 1976, *ApSS* **39**, 447
- Longair, M.: 1981, *High Energy Astrophysics, Vol I & II*, ISBN 0521383749, Cambridge University Press, Cambridge
- Lucy, L. B. and Solomon, P. M.: 1970, *ApJ* **159**, 879
- Lund, N., Budtz-Jørgensen, C., Westergaard, N. J., Brandt, S., Rasmussen, I. L., Hornstrup, A., Oxborrow, C. A., Chenevez, J., Jensen, P. A., Laursen, S., Andersen, K. H., Mogensen, P. B., Rasmussen, I., Omø, K., Pedersen, S. M., Polny, J., Andersson, H., Andersson, T., Kämäräinen, V., Vilhu, O., Huovelin, J., Maisala, S., Morawski, M., Juchnikowski, G., Costa, E., Feroci, M., Rubini, A., Rapisarda, M., Morelli, E., Carassiti, V., Frontera, F., Pellicciari, C., Loffredo, G., Martínez Núñez, S., Reglero, V., Velasco, T., Larsson, S., Svensson, R., Zdziarski, A. A., Castro-Tirado, A., Attina, P., Gorla, M., Giulianielli, G., Cordero, F., Rezazad, M., Schmidt, M., Carli, R., Gomez, C., Jensen, P. L., Sarri, G., Tiemon, A., Orr, A., Much, R., Kretschmar, P., and Schnopper, H. W.: 2003, *A&A* **411**, L231
- Marlborough, J. M.: 1987, in *IAU Colloq. 92: Physics of Be Stars*, pp 316–335
- Marshall, N. and Ricketts, M. J.: 1980, *MNRAS* **193**, 7P
- Martínez Núñez, S., Reig, P., Blay, P., Kretschmar, P., Lund, N., and Reglero, V.: 2003, *A&A* **411**, L411
- Millar, C. E. and Marlborough, J. M.: 1998, *ApJ* **494**, 715



- Millar, C. E. and Marlborough, J. M.: 1999, *ApJ* **516**, 280
- Nagae, T., Oka, K., Matsuda, T., Fujiwara, H., Hachisu, I., and Boffin, H. M. J.: 2004, *A&A* **419**, 335
- Nagase, F.: 1989, *PASJ* **41**, 1
- Okazaki, A. T.: 2000, in *ASP Conf. Ser. 214: IAU Colloq. 175: The Be Phenomenon in Early-Type Stars*, p. 409
- Okazaki, A. T.: 2001, *PASJ* **53**, 119
- Okazaki, A. T. and Negueruela, I.: 2001, *A&A* **377**, 161
- Pakull, M.: 1982, in *Accreting Neutron Stars*, pp 53–56
- Peterson, B. A.: 1972, *Nature* **236**, 449
- Poekert, R. and Marlborough, J. M.: 1978, *ApJS* **38**, 229
- Porter, J. M.: 1999, *A&A* **348**, 512
- Pringle, J. E.: 1981, *ARA&A* **19**, 137
- Prinja, R. K. and Howarth, I. D.: 1986, *ApJS* **61**, 357
- Rappaport, S., Bradt, H., Clark, G. W., Jernigan, J. G., and Joss, P. C.: 1976, *ApJL* **208**, L119
- Rappaport, S., Clark, G. W., Cominsky, L., Li, F., and Joss, P. C.: 1978, *ApJL* **224**, L1
- Roberts, D. H., Lehar, J., and Dreher, J. W.: 1987, *AJ* **93**, 968
- Rossiger, S.: 1976, *Zentralinstitut fuer Astrophysik Sternwarte Sonneberg Mitteilungen ueber Veraenderliche Sterne* **7**, 105
- Scargle, J. D.: 1982, *ApJ* **263**, 835
- Schönfelder, V. E.: 2001, *The Universe in GammaRays*, Astronomy & Astrophysics Library, ISBN 0941-7834, Springer-Verlag, Berlin

- Schreier, E., Giacconi, R., Gursky, H., Kellogg, E., and Tananbaum, H.: 1972, *ApJL* **178**, L71
- Shklovsky, J. S., Cherepashchuk, A. M., and Efremov, Y. N.: 1972, *Nature* **236**, 448
- Slettebak, A.: 1988, *PASP* **100**, 770
- Stee, P. and de Araujo, F. X.: 1994, *A&A* **292**, 221
- Struve, O.: 1931, *ApJ* **73**, 94
- Sunyaev, R. A. and Shakura, N. I.: 1975, *Soviet Astronomy Letters* **1**, 158
- Titarchuk, L.: 1994, *ApJ* **434**, 570
- Titarchuk, L., Mastichiadis, A., and Kylafis, N. D.: 1997, *apJ* **487**, 834
- Townsend, R. H. D. and Owocki, S. P.: 2005, *MNRAS* **357**, 251
- Trümper, J., Kahabka, P., Oegelman, H., Pietsch, W., and Voges, W.: 1986, *ApJL* **300**, L63
- wan den Bergh, S.: 1972, *Nature* **235**, 273
- wan den Heuvel, E. P. J.: 1993, *Space Science Reviews* **66**, 309
- Weigert, A. and Kippenhahn, R.: 1967, in *On the Evolution of Double Stars*, p. 122
- Wilson, C. A., Fabregat, J., and Coburn, W.: 2005, *ApJ* **620**, L99



## Part II

# The High Mass X-Ray Binary system 4U 2206+54



## Chapter 4

# Introduction

The discovery of 4U 2206+54 as an X-ray emitter is reported in Giacconi et al. (1972). It was given the identification 2U 2208+54 (where "2U" means "2nd *UHURU* catalogue). The discovery was done with *UHURU* data. *UHURU* was the first X-ray astronomy satellite mission ever sent to space. See Giacconi et al. (1971) for a review of the *UHURU* mission. At this first detection the source showed a count rate of  $5.1 \text{ count s}^{-1}$ , which would roughly correspond to a flux of  $5.4 \text{ mCrab}^1$  (2–20 keV). In the subsequent third and fourth *UHURU* catalogues (Giacconi et al., 1974; Forman et al., 1978), the detection of the source is reported as 3U 2208+54 and 4U 2206+54, respectively, with mean fluxes of 4.7 mCrab in the former case and 3.1 mCrab in the latter (both in the 2–20 keV energy range).

In the mean time, Villa et al. (1976) reported the detection of this system with the *Ariel V* satellite data, with the name of A2204+54, and a mean count rate of  $1.1 \text{ counts s}^{-1}$ , which represents a flux of  $2.3 \text{ mCrab}^2$  (0.3–40 keV). The source was included in the third *Ariel V* catalogue as 3A2206+54 and the flux reported there reached a maximum of 6.2 mCrab with an average of 2 mCrab (both in the 0.3–40 keV energy range).

The source was also included in the the *X-Ray Source Catalogue* of Amnuel et al. (1979), with the identification XRS22063+544.

---

<sup>1</sup>Assuming that for the *UHURU* detectors  $1 \text{ count s}^{-1}$  corresponds to 1.06 mCrab, see Forman et al. (1978)

<sup>2</sup>A Crab count rate of  $403 \text{ count s}^{-1}$  was measured with *Ariel V*, see Warwick et al. (1981)

From these early detections two of the main peculiarities of this source started to emerge: **a)** *the source is variable on many timescales*, **b)** however, *as an overall long term averaged behaviour, it looks quite stable*.

In 1984, Wood et al. (1984) published the High Energy Astronomical Observatory 1 (HEAO-1) catalogue. In this catalogue the source was given the identification 1H2205+538 and a mean flux of 1.3 mCrab was reported (Wood et al., 1984).

An important achievement of the HEAO-1 mission was to refine the position of many known X-ray emitters. Based on this new refined position, (R.A. 22h 05' 18"; DEC. 53° 53' 48" ) Steiner et al. (1984) located the optical counterpart to 4U 2206+54. They found that the early type star BD +53°2790 fell within the error box of the location provided by the scanning Modulation Collimator (MC) on board HEAO-1. Through *UBV* photometry they estimated a spectral type of B1 for BD +53°2790, and a distance between 3.5 and 1.5 kpc (for an absolute magnitude between -4.2 and -2.5 –according to the uncertainty in their estimate of spectral type–). Because in the red spectrum of BD +53°2790 the H $\alpha$  line showed a shell-like profile, they proposed this system to be a HMXBR/BeX system. They failed to realise that previous observations of BD +53°2790 existed, with a spectral classification of O9III by Hiltner (1956). This constituted the first classification of 4U 2206+54.

Steiner et al. (1984) analysed MC data during December 1977 and June 1978, and *Ariel V* data from a wider period between November 1974 and June 1978. From these observations they deduced that the observed high energy behaviour of 4U 2206+54 most probably was explained by the presence of a compact object accreting from the wind of a Be star. They also outlined another of the main properties of this high energy source: **c)** *the amplitude of variability in the X-ray flux changes by a factor of 10 on timescales of the order of months and by a factor of 3 on shorter timescales*.

First measurements of position and magnitude of BD +53°2790 appear in the Bonner Durchmusterung catalogue (BD) of A. F. W. Argelander (Argelander, 1995, first published in 1903). A visual (*V*) magnitude of 9.8, measured from photographic plates, is reported there. The Tycho-2 catalogue (Høg et al., 2000) identified this star as TYC 3973 812 1. The measurements reported are shown in Table 4.1.

Table 4.1: Data about BD +53°2790 reported in the Tycho-2 catalogue.

RA (J2000) (degrees)	DEC (J2000) (degrees)	RA proper motion milli-arcsecond year <sup>-1</sup>	DEC proper motion milli-arcsecond year <sup>-1</sup>
331.98432206	54.51844498	-4.3	-3.1

B magnitude	V magnitude
10.197±0.027	9.898±0.028

A complete study of BD +53°2790 appeared in the work of Hiltner (1956). Hiltner gives a  $V$  magnitude of 9.86 for BD +53°2790, and proposes a spectral classification of O9.5p. He was probably not very sure about the luminosity classification, as he reports a III classification but marked it with a question tag. The distance modulus reported there for BD +53°2790 was  $m - M = 13.9$  (with  $m$  the observed magnitude and  $M$  the absolute magnitude, assumed to be -5.7 –that of a late O type star of luminosity class III–), which implies a distance of 6 kpc. This distance is much larger than the one derived by Steiner et al. (1984).

Saraswat and Apparao (1992) reported on dedicated observations of 4U 2206+54 with the Medium Energy (ME) detector on board the *EXOSAT* mission during 1983–1985. They confirm the high variability of the system, increasing from  $\sim 3.5$  mCrab up to  $\sim 10.5$  mCrab on timescales of the order of  $\sim 1000$  s. See Reynolds et al. (1999) for a short description of the ME on *EXOSAT* and the count rate of the Crab. The flux from 4U 2206+54 reported in the *ME Slew Survey Catalogue* is  $\sim 9$  mCrab (see Reynolds et al., 1999).

Subsequently, all high energy missions which have pointed to the region around 4U 2206+54 have reported its detection, like *ROSAT* (for which an average flux of 2.7 mCrab is found, see Voges et al., 1999) or *RXTE*.

From *RXTE* data, two extensive studies of the system were performed. Corbet and Peele (2001) used *RXTE*/ASM data and found a modulation of  $\sim 9.6$  days in the count rate, attributed to the orbital period of the system. Negueruela and Reig (2001) analysed the X-ray spectra and light curves of 4U 2206+54 from *RXTE*/PCA and included a detailed analysis of the



properties of BD +53°2790, the optical companion to the system. They concluded that the system does not seem to be a classical BeX system, but a HMXRB with a late and peculiar O type star. They suggested an spectral classification of O9.5V for BD +53°2790; closer to the original spectral classification of Hiltner (1956) than that of Steiner et al. (1984).

The most recent analysis on the source start to give some hints about the actual nature of the source: Torrejón et al. (2004) with a combined analysis of *RXTE* and *BeppoSAX* data; Masetti et al. (2004) with *BeppoSAX* data; Blay et al. (2005,2006) with *INTEGRAL*, VLA and optical data (included in this thesis work); and Ribó et al. (2005) with *RXTE* and IUE data (partially included in this thesis work).

Only when a complete multiwavelength approach is adopted, the system starts to unveil its secrets. Each energy range will give a bit of information about what is happening in a particular location of the binary system. Putting them all together we can obtain the whole picture of the physical processes going on, from stellar material flowing away from the outer shells of BD +53°2790, down to the compact object in 4U 2206+54, where the high energy emission is produced.

As a starting point, a summary of the main properties outlined in this introduction, as a "this is what we know" statement, follows:

- High energy emission:
  1. The source is persistent, as it has been detected by every mission pointing at it.
  2. As an overall behaviour, on short timescales random variability dominates, while on longer timescales orbital variability dominates.
  3. There is a range of variabilities present in the system, from short timescale *fllickering-like* variability, going through variations of a factor of 3 on timescales of hours, up to a 9.6 periodicity associated with the orbital period and longer timescale variability which can produce variations in flux by a factor of 10.
  4. No pulsations have been detected so far.
- Optical counterpart:

1. The  $V$  magnitude shows some degree of variability, but is very stable over very long timescales (from a value of  $\sim 9.8$  was reported in 1956, to a value of  $\sim 9.9$  reported in 2000 (Tycho-2 catalogue), and values of  $\sim 9.8$  reported in recent works).
2. The spectrum in the classification region (4000–5000 Å) is complex, resembling that of a O9.5V star but with variable lines that would correspond to cooler types.
3.  $H_\alpha$  shows a *shell-like* spectrum which resembles that of the BeX systems undergoing global disc oscillations in the envelope of the Be star, but with the peculiarity that the  $R$  peak always dominates over the  $V$  peak and no obvious periodicity is present.
4. The infrared spectrum ( $K$ -band) shows, also, some degree of variability.
5. The UV spectrum shows indications of a stellar wind and supports the spectral and luminosity classification found from the optical spectra.

With all those characteristics, the natural conclusion is that the system most likely consists of a compact object accreting from the wind of the early type star (sometimes called wind-fed systems, see Chapter 1). However, non definitive proof about what is the nature of the system, and in particular of the compact companion, has been found until now.

The vast majority of High Mass X-ray Binaries (HMXBs) harbour X-ray pulsars (c.f. Bildsten et al. 1997), believed to be young neutron stars with relatively strong magnetic fields ( $B \sim 10^{12}$  G). An important fraction of them are wind-fed systems.

Among the handful of HMXBs not displaying X-ray pulsations, only three show the typical characteristics of accreting black holes (LMC X-1, LMC X-3 and Cyg X-1). In four other HMXBs, pulsations have not been discovered in spite of intensive searches, but there is no strong evidence identifying the accreting object as a black hole. In principle, there is no reason to attribute the lack of pulsations in all these systems to any particular characteristic and different models have indeed been proposed to explain some of them. There have been suggestions that 2E 0236.6+6101, whose counterpart is the B0 Ve star LS I +61°303, and RX J1826.2–1450,

identified with the O6.5 V((f)) star LS 5039, may not be accreting binaries after all, but X-ray sources powered by rotational energy from a young non-accreting neutron star (Maraschi & Treves 1981; Martocchia et al. 2005), although the presence of relativistic radio jets points towards the accretion scenario (Massi et al. 2004; Paredes et al. 2000). In the case of 4U 1700–37, optically identified with the O6.5 Iaf+ star HD 153919, a compact object of unknown nature and mass  $M_X = 2.4 \pm 0.3 M_\odot$  accretes material from the wind of the massive supergiant (Clark et al. 2002).

The fourth HMXRB not displaying pulsations is 4U 2206+54. Its relatively high X-ray luminosity of 4U 2206+54,  $L_X \sim 10^{35}$  erg s<sup>-1</sup> (at an estimated distance of 3 kpc; see Negueruela & Reig 2001), combined with its spectral shape, makes the presence of a neutron star or a black hole in the system almost unavoidable. Up to now the possibility of a black-hole has not been ruled out completely by previous observations.

Also, we would like to notice that many high-energy sources not showing pulsations are microquasars (containing either black holes or neutron stars), while pulsating sources do not show significant radio-emission (Fender & Hendry 2000). 4U 2206+54 shares many characteristics with the well-known microquasar LS 5039 (Paredes et al. 2000, 2002). Both systems contain a non-supergiant late O-type star (Clark et al. 2001a) and a compact object that does not show pulsations (Ribó et al. 1999; Reig et al. 2003) orbiting in a relatively close orbit when compared to the majority of HMXBs, and both systems show evidences of wind-fed accretion (Negueruela & Reig 2001; McSwain et al. 2004) with X-ray luminosities in the range  $10^{34}$ – $10^{35}$  erg s<sup>-1</sup>.

In the next sections data from the different energy ranges will be analysed:

- Radio wavelengths from VLA.
- UV from IUE.
- Optical spectroscopy and photometry from several telescopes.
- Infrared spectroscopy and photometry from TCS (Canary Islands) and UKIRT (Hawaii).
- X-rays and soft  $\gamma$ -rays from *RXTE* and *INTEGRAL*.

The details of each dataset and instrument will be given in each section (if not given already in the general introduction). In the last section we will put everything together and reach some conclusions about the nature of the system, to end up with the still unsolved problems and the forthcoming work related to this HMXRB.



## Chapter 5

# Radio Observations

Nelson & Spencer (1988), in an extensive survey to measure radio emission from known X-ray binary systems, took two sets of measurements from the position of 4U 2206+54. The measurements were performed during August-September 1986 and July 1987 from the Lowell-Mk II interferometer at Jodrell Bank Observatory. They found an upper limit for the radio flux density of 1.7 mJy for the first epoch and 2.9 mJy for the second.

The National Radio Astronomy Observatory (NRAO) is a facility of the National Science Foundation operated under cooperative agreement by Associated Universities, Inc. The Very Large Array (VLA) is a NRAO instrument consisting of 27 radio antennas in a Y-shaped configuration on the Plains of San Agustin, New Mexico. Each antenna is 25 meters wide in diameter. Images of the VLA can be seen in Fig. 5.1

The VLA works as an interferometer, that is, the signal from all the antennas is mixed to create interference patterns. From these patterns, and through Fourier Transform techniques, the structure of the radio emitting region can be deduced and images of the radio sky are created at a wide range of frequencies and resolutions. The antennas can be arranged in four basic configurations, which will give different resolutions. These basic configurations are named D,C,B and A. The resolutions on each mode are scaled as 1:3.2:10:32. More information about the VLA can be found at the *NRAO* web site <sup>1</sup>.

---

<sup>1</sup><http://www.vla.NRAO.edu/astro/guides/vlas/current/vlas.html>



Figure 5.1: Images of the NRAO/VLA facilities.

An inspection of the VLA Sky Survey (NVSS, Condon et al. 1998, VizieR cataloge VIII/65/nvss) reveals no radio emission up to a  $3\sigma$  upper limit of 1 mJy from 4U 2206+54.

During two observing campaigns granted to Felix Mirabel and Marc Ribó, both reduced by Marc Ribó, 4U 2206+54 was observed with the NRAO/VLA at 8.4 GHz (3.6 cm wavelength) on two different epochs:

1. On 2003 May 12, from 7:05 to 8:00 UT and from 11:40 to 12:52 UT. The average Modified Julian Date (MJD) of the observation is 52771.4. The VLA was in its D configuration.
2. On 2003 May 20 from 15:27 to 17:20 UT. The average MJD of the observation was 52779.7, and the VLA was in reconfiguration from D to A.

VLA data need to be calibrated both in phase and flux. Lists of phase and flux calibrators are available at NRAO. The primary flux density calibrator used was 1331+305 (3C 286). The phase calibration is complicated and depends on the distance between the source of interest and the phase calibrator, the frequency and the weather conditions among other factors. Because of the need of frequent measurements of the phase calibrator, it is advisable to choose a phase calibrator as close as possible to our source. For that reason the observations of 4U 2206+54 were conducted devoting 10 min scans on the source position, preceded and followed by 2 min scans

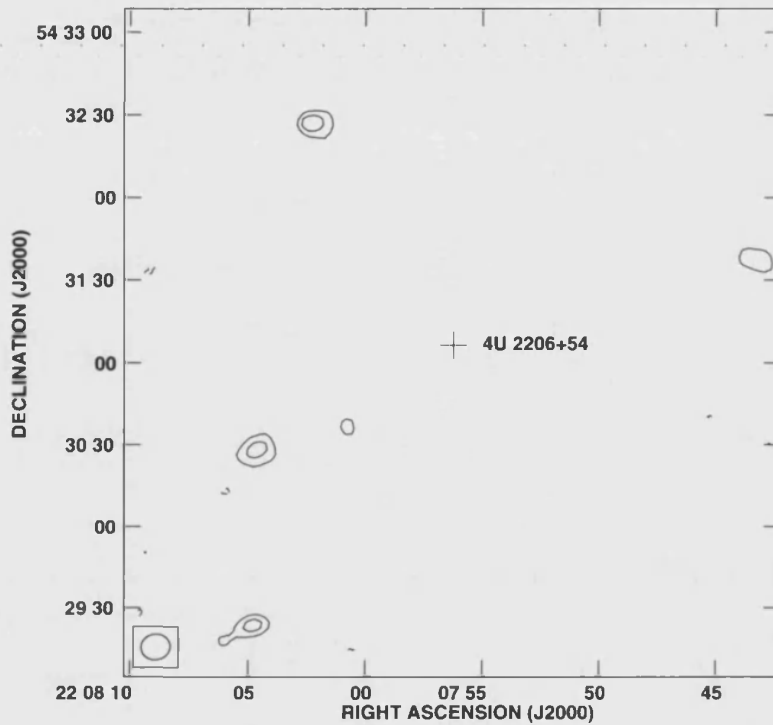


Figure 5.2: Image around 4U 2206+54, marked with a cross, obtained with the VLA at 8.4 GHz after concatenating data from 2003 May 12 and 20. The image size is  $4' \times 4'$ . Contours are  $-3$ ,  $3$ , and  $5$  times the rms noise level of  $0.013 \text{ mJy beam}^{-1}$ . The ellipse in the bottom left corner represents the Full Width Half Maximum of the synthesised beam obtained of  $10.6'' \times 9.4''$  in  $\text{PA} = -83.4^\circ$ .

on the VLA phase calibrator 2250+558. The data were reduced using standard procedures within the NRAO AIPS software package.

No radio emission at 8.4 GHz was detected, with a  $3\sigma$  upper limit of  $0.042 \text{ mJy}$  on 2003 May 12 (MJD 52771.4) and a  $3\sigma$  upper limit of  $0.066 \text{ mJy}$  on 2003 May 20 (MJD 52779.7). We concatenated all the data and obtained a final  $3\sigma$  upper limit of  $0.039 \text{ mJy}$ . The resulting image is shown in Fig. 5.2.

Thus, we can conclude that the system 4U 2206+54 produces no detectable radio emission. Only an upper limit for the expected radio flux can be given. This result adds more evidence to the presence of a neutron star in 4U 2206+54. If a black hole was present in the system, some radio emission would be expected (see the comments in chapter 4). From



radio observations we find a first indication about the possible nature of the system, later on we will see how this information combined with information from high energy bands will give us a clue about the nature of the compact object in 4U 2206+54. In chapter 10 we will argue in favour of the neutron star candidate on the basis of the expected radio emission derived from the X-ray flux measured from the system.

## Chapter 6

# The Infra-Red region

### 6.1 Infrared Spectroscopy

*K*-band spectroscopy of BD +53°2790 was obtained on July 7–8, 1994, with the Cooled Grating Spectrometer (CGS4) on the United Kingdom InfraRed Telescope (UKIRT), Hawaii. The instrumental configuration consisted of the long focal station (300 mm) camera and the 75 lines mm<sup>-1</sup> grating, which gives a nominal velocity resolution of 445 km s<sup>-1</sup> at 2 μm ( $\lambda/\Delta\lambda \approx 700$ ). The data were reduced by Chris Everall according to the procedure outlined by Everall et al. (1993).

*K*-band spectra are shown in Fig. 6.1. Unlike the optical components of several Be/X-ray binaries observed by Everall et al. (1993; see also Everall, 1995), BD +53°2790 shows no emission in He I  $\lambda 2.058 \mu\text{m}$  (though the higher resolution spectrum suggests a weak shell profile). Br $\gamma$  may have some emission component, but is certainly not in emission. The situation differs considerably from that seen in the *K*-band spectrum of BD +53°2790 presented by Clark et al. (1999), taken on 1996 October. There, Br $\gamma$  displays a clear shell profile with two emission peaks and He I  $\lambda 2.112 \mu\text{m}$  is in absorption. This shows that the shell-like behaviour and variability extends into the IR.

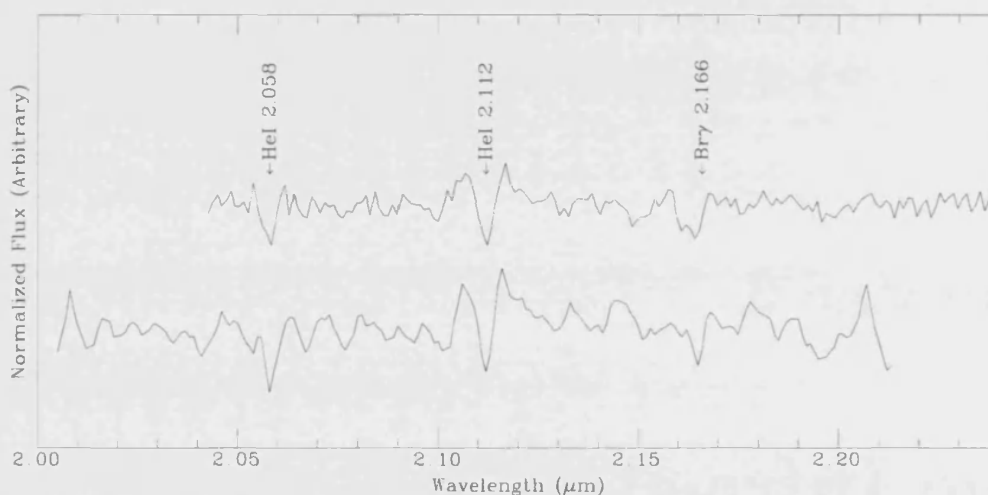


Figure 6.1: *K*-band spectra of BD +53°2790.

## 6.2 Infrared Photometry

Infrared observations of BD +53°2790 have been obtained with the Continuously Variable Filter (CVF) on the 1.5-m. Carlos Sánchez Telescope (TCS) at the Teide Observatory, Tenerife, Spain and the UKT9 detector at the 3.9-m UK Infrared Telescope (UKIRT) on Hawaii. All the observations are listed in Table 6.1. The errors are much smaller after 1993, when we started implementing the multi-campaign reduction procedure described by Manfroid (1993).

Table 6.1: Observational details, IR photometry.

Date	J	H	K	L'	Telescope
Sep 06, 1987	9.37±0.03	9.26±0.03	9.09±0.03	9.0±0.4	TCS
Sep 11, 1987	9.70±0.04	9.48±0.04	9.28±0.04		TCS
Nov 24, 1987	9.16±0.03	9.08±0.03	8.92±0.03	8.71±0.06	UKIRT
Dec 28, 1987	9.26±0.03	9.16±0.03	9.06±0.03		TCS
Jan 01, 1988	9.28±0.04	9.10±0.04	8.99±0.04	8.8±0.4	TCS
Jan 03, 1988	9.24±0.03	9.08±0.03	8.97±0.03	8.8±0.3	TCS
Jun 23, 1988	9.28±0.04	9.17±0.04	9.01±0.04		TCS
Jun 24, 1988	9.25±0.03	9.15±0.03	8.98±0.03		TCS

*Continued...*

Table 6.1: Continued.

Date	J	H	K	L'	Telescope
Jun 28, 1988	9.16±0.04	9.11±0.04	9.00±0.04		TCS
Apr 14, 1991	9.25±0.02	9.12±0.03	9.05±0.02		TCS
Apr 17, 1991	9.26±0.06	9.12±0.03	9.03±0.02		TCS
Aug 23, 1991	9.22±0.03	9.08±0.02	9.01±0.02		TCS
Aug 24, 1991	9.16±0.09	9.04±0.05	9.00±0.05		TCS
Aug 25, 1991	9.18±0.04	9.05±0.03	8.95±0.03		TCS
Aug 27, 1991	9.17±0.03	9.06±0.02	9.00±0.03		TCS
Aug 28, 1991	9.19±0.04	9.05±0.03	8.98±0.05		TCS
Nov 29, 1991	9.30±0.10	9.10±0.10	9.00±0.10		TCS
Dec 01, 1991	9.24±0.05	9.08±0.04	9.01±0.04		TCS
Jul 20, 1992	9.22±0.03	9.11±0.03	8.98±0.05		TCS
Aug 04, 1992	9.33±0.09	9.09±0.04	8.93±0.05		TCS
Aug 21, 1992	9.29±0.04	9.07±0.03	9.03±0.06		TCS
Aug 21, 1992	9.25±0.05	9.07±0.03	8.94±0.06		TCS
Aug 22, 1992	9.14±0.06	9.04±0.04	9.07±0.04		TCS
Aug 23, 1992	9.29±0.07	9.16±0.09	9.11±0.06		TCS
Jan 12, 1993	9.20±0.03	9.07±0.01	8.98±0.02		TCS
Jun 22, 1993	9.23±0.01	9.17±0.01	9.09±0.01	8.91±0.03	UKIRT
Jun 30, 1993	9.27±0.03	9.14±0.02	9.02±0.02	8.9±0.3	UKIRT
Jul 06, 1993	9.26±0.02	9.14±0.03	9.03±0.02	8.9±0.2	UKIRT
Jul 07, 1993	9.26±0.03	9.15±0.02	9.05±0.03		UKIRT
Dec 20, 1993	9.11±0.01	9.11±0.01	8.95±0.02		TCS
Dec 20, 1993	9.11±0.01	9.08±0.01	8.93±0.01		TCS
Dec 20, 1993	9.18±0.03	9.06±0.01	8.99±0.06		TCS
Dec 21, 1993	9.26±0.02	9.18±0.01	9.09±0.03		TCS
Dec 21, 1993	9.27±0.03	9.13±0.01	9.13±0.01		TCS
Jun 08, 1994	9.16±0.02	9.16±0.01	9.01±0.01		TCS
Jun 09, 1994	9.28±0.01	9.13±0.02	9.06±0.03		TCS
Jun 10, 1994	9.16±0.03	9.07±0.01	9.04±0.03		TCS
Jun 11, 1994	9.24±0.06	9.28±0.04	9.17±0.05		TCS
Jun 21, 1994	9.22±0.01	9.12±0.01	9.03±0.01		TCS
Jun 26, 1994	9.22±0.02	9.14±0.01	9.06±0.03		TCS
Jun 28, 1994	9.22±0.01	9.15±0.01	9.03±0.01		TCS
Jun 30, 1994	9.24±0.01	9.09±0.02	9.08±0.02		TCS
Jul 01, 1994	9.17±0.01	9.12±0.01	8.99±0.00		TCS
Jul 02, 1994	9.26±0.02	9.20±0.01	9.09±0.01		TCS
Jul 03, 1994	9.27±0.02	9.17±0.01	9.12±0.01		TCS
Nov 05, 1994	9.16±0.01	9.09±0.01	9.06±0.01		TCS

*Continued...*

Table 6.1: Continued.

Date	J	H	K	L'	Telescope
Nov 06, 1994	9.01±0.01	8.94±0.01	8.90±0.01		TCS
Nov 07, 1994	9.28±0.02	9.21±0.01	9.14±0.02		TCS
Nov 08, 1994	9.29±0.02	9.18±0.01	9.08±0.00		TCS
Nov 09, 1994	9.21±0.01	9.11±0.01	9.08±0.01		TCS
Jan 02, 1995	9.23±0.01	9.15±0.01	9.03±0.01		TCS
Jan 03, 1995	9.12±0.01	9.07±0.01	9.00±0.01		TCS
Jan 05, 1995	9.14±0.02	9.09±0.01	8.99±0.01		TCS
Apr 24, 1995	9.16±0.01	9.07±0.01	9.02±0.02		TCS
Apr 25, 1995	9.21±0.01	9.12±0.01	9.07±0.00		TCS
Apr 26, 1995	9.25±0.01	9.13±0.01	9.03±0.01		TCS
Apr 28, 1995	9.23±0.01	9.14±0.01	9.05±0.01		TCS
Apr 29, 1995	9.20±0.01	9.08±0.01	9.04±0.01		TCS
Jul 28, 1995	9.22±0.02	9.12±0.01	9.09±0.15		TCS
Jul 28, 1995	9.23±0.01	9.04±0.01	9.60±0.13		TCS
Jul 29, 1995	9.18±0.01	9.06±0.01	8.94±0.06		TCS
Jul 29, 1995	9.19±0.01	9.04±0.01	9.09±0.11		TCS
Jul 31, 1995	9.27±0.01	9.10±0.01	8.95±0.01		TCS
Oct 11, 1995	9.36±0.01	9.17±0.01	9.00±0.00		TCS
Oct 14, 1995	9.15±0.01	9.03±0.01	8.90±0.01		TCS
Jul 27, 1996	9.40±0.01	9.25±0.01	9.07±0.00		TCS
Jul 28, 1996	9.14±0.01	9.03±0.01	8.92±0.01		TCS
Jul 16, 1997	9.20±0.01	9.09±0.01	8.98±0.01		TCS
Jul 17, 1997	9.18±0.01	9.06±0.01	8.96±0.01		TCS
Jul 19, 1997	9.17±0.01	9.07±0.01	8.99±0.00		TCS
Jun 15, 1998	9.16±0.01	9.09±0.01	8.98±0.01		TCS
Jun 16, 1998	9.12±0.01	9.07±0.01	8.98±0.01		TCS
Jun 17, 1998	9.19±0.01	9.10±0.01	8.99±0.00		TCS
Oct 27, 1998	9.29±0.01	9.17±0.01	9.13±0.00		TCS
Jul 26, 1999	9.23±0.02	9.12±0.02	9.09±0.02		TCS
Jul 28, 1999	9.20±0.02	9.13±0.02	9.05±0.02		TCS
Jul 31, 1999	9.22±0.02	9.13±0.02	9.06±0.02		TCS
Oct 02, 1999	9.18±0.02	9.08±0.02	8.98±0.02		TCS
Oct 04, 1999	9.20±0.02	9.10±0.02	9.03±0.02		TCS
Oct 05, 1999	9.20±0.02	9.13±0.01	9.02±0.02		TCS
Jan 15, 2001	9.20±0.02	9.08±0.02	8.96±0.02		TCS

Our infrared photometry coverage extends for  $\approx 13$  years and is much more comprehensive than our optical photometry. The IR long-term lightcurve is shown in Fig. 6.2. Data have been binned so that every point represents the average of all the nights in a single run (excluding those with unacceptably large photometric errors).

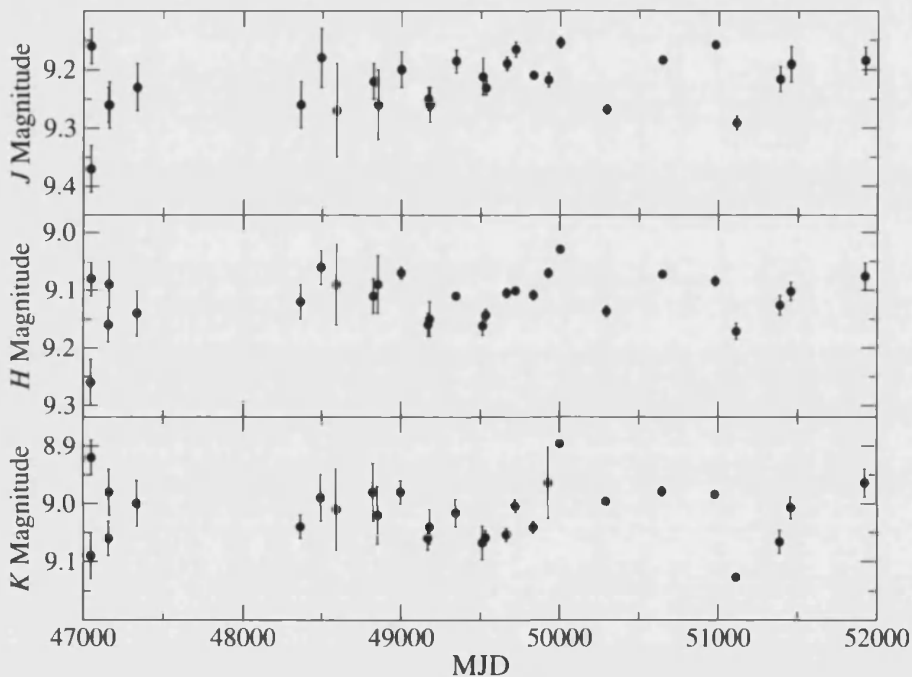


Figure 6.2: Infrared lightcurves of BD +53°2790, 1987–1999.

As can be seen in Fig. 6.2, the range of variability is not very large, with extreme values differing by  $\approx 0.2$  mag in all three bands. Variability seems to be relatively random, in the sense that there are no obvious long-term trends. The light curves for the three infrared magnitudes are rather similar in shape, suggesting that the three bands do not vary independently.

In spite of this, all colour-magnitude plots are dominated by scatter. Moreover, an analysis of the temporal behaviour shows that there is no obvious pattern in the evolution of the source on the  $H/(H - K)$  and  $K/(H - K)$  planes, with frequent jumps between very distant points and no tendency to remain in any particular region for any length of time.

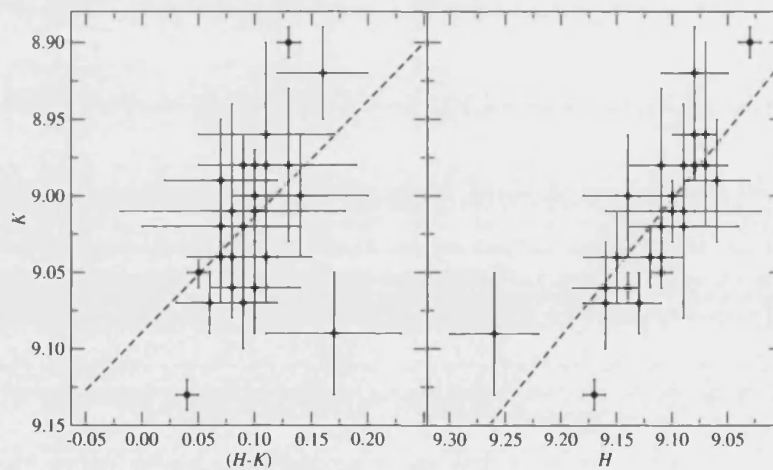


Figure 6.3: Colour-magnitude plots showing the evolution of the infrared magnitudes. The strong correlation seen in the  $K/(H - K)$  plane is not a simple reflection of the fact that a fainter  $K$  means a smaller  $(H - K)$ , as the correlation between  $H$  and  $K$  is also strong. In the first case the correlation coefficient is  $r_{(H-K),K} = -0.46$  and the correlation is significant in a 98% confidence level. In the latter case the correlation coefficient is  $r_{H,K} = 0.80$  and the correlation is also significant at a 98% confidence level.

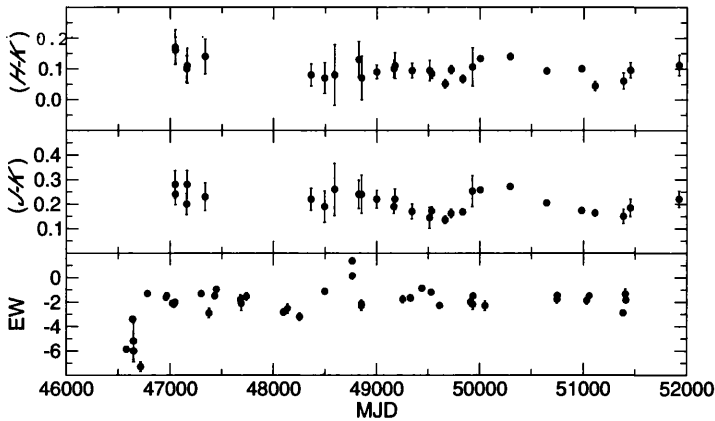


Figure 6.4: Evolution of the infrared colours in BD +53°2790 during 1987–1999 compared to that of the EW of  $H\alpha$ . Since simultaneous measurements are rare, we cannot properly search for correlations. The lack of any obvious correlated trends could be caused by the lack of long-term trends.

The only plot in which a clear correlation stands out is the  $K/(H - K)$  diagram (see Fig. 6.3). In principle, one would be tempted to dismiss this correlation as the simple reflection of stronger variability in  $K$  than in  $H$ , since  $(H - K)$  would necessarily be smaller for larger values of  $K$ . However, a linear regression of  $H$  against  $K$  also shows a clear correlation. We find  $a = 0.89$ ,  $b = 0.93$  and a correlation coefficient of  $r = 0.80$  for  $K = aH + b$ . Suspecting, then, that a linear correlation must be present in the  $H/(H - K)$  plot as well, we also performed a linear regression. In this case we found a very poor correlation.

Equally disappointing is the search for correlations between the EW of  $H\alpha$  and the  $(J - K)$  color. Even though our measurements of these two quantities are not simultaneous, a look at their respective evolutions (Fig. 6.4) shows no clear correlation.





## Chapter 7

# Optical Band

### 7.1 Optical Spectroscopy

#### 7.1.1 Observations

We have collected data from BD +53°2790 from 1986 up to the present time. Part of the dataset comes from archives and part of it has been obtained by different observers, including myself, at several telescopes:

- From 1986 up to 1990 data were retrieved from the Isaac Newton Group (ING) *La Palma data archive* (Zuiderwijk et al., 1994). These data consist of a total of 21 spectroscopic H $\alpha$  observations of BD +53°2790 performed with the 2.5 m Isaac Newton Telescope (INT), operated by the ING at the *Observatorio del Roque de los Muchachos*, La Palma, Spain. All observations were taken with the Intermediate Dispersion Spectrograph (IDS) and either the Image Photon Counting System (IPCS) or a CCD camera.
- From 1991 to 1999 we gathered a series of observations taken by different collaborator observers. This second data set was obtained at the INT and the 1.0 m Jacobus Kapteyn Telescope (JKT), also located at the *Observatorio del Roque de los Muchachos*. At the INT the combination of the IDS and a CCD camera was used. At the JKT the observations were obtained using the St Andrew's Richardson-Brealey Spectrograph (RBS) with the R1200Y grating, the red optics and either the EEV7 or TEK4 CCD cameras.

- Although the main bulk of data comes from INT and JKT telescopes, in the long term 1986–1999 monitoring campaign, data from a few other observatories have been used: **a)** A total of 8  $H\alpha$  observations were retrieved from the 1.5 m telescope at Palomar Mountain (PAL), located at San Diego County California, owned and operated by the California Institute of Technology. It was operated using the f/8.75 Cassegrain echelle spectrograph in regular grating mode. **b)** One  $H\alpha$  observation from the 2.6 m telescope at the Crimean Astrophysical Observatory (CRAO) located in Nauchny, Ukraine. **c)** We have also used one observation from the 1.3 m Telescope at Skinakas Observatory (SKI), located at the top of the Skinakas mountain, in Crete, Greece. The telescope is an f/7.7 Ritchey-Cretien, which was equipped with a  $2000 \times 800$  ISA SITE chip CCD. **d)** Two sets of the  $H\alpha$  spectroscopic range observations from the 1.52 m G. D. Cassini Telescope at the Loiano Observatory (BOL), Italy, equipped with the Bologna Faint Object Spectrograph and Camera (BFOSC) are included also in the long term monitoring of BD +53°2790.
- Apart from this long term monitoring, during 2000, 2002, 2003 and 2004 four intensive campaigns were dedicated to the follow-up of BD +53°2790: **1)** The one in 2000 was a combined campaign from the 1.3 m Telescope at Skinakas Observatory and the 1.52 m G. D. Cassini Telescope at the Loiano Observatory. From Sinakas, data were obtained between 17 and 22 July 2000 and from Loiano the source was observed between 25 and 30 July 2000 (plus a series of observations from Skinakas during October 2000). **2)** The one in 2002 was performed entirely at the INT in La Palma. It consists of 9 nights of observations, from 23 to 31 July 2002. **3)** The next intensive campaign was also carried out with the INT, from 1 to 10 July 2003, covering 10 nights of good weather and optimum observations of BD +53°2790 **4)** The last intensive campaign took place during late August–early October, 2004. A total of 8 non-consecutive observing nights (due to weather restrictions) were conducted at Skinakas observatory.

The variety of instruments and configurations used is large. Thus, care must be taken in the treatment of the data, as this represents an extra

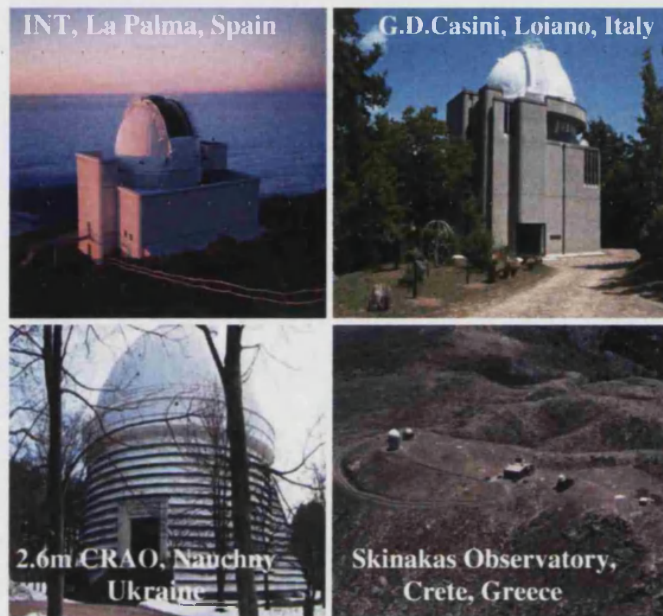


Figure 7.1: Images of some of the telescopes where data of BD +53°2790 was retrieved for our analysis.

difficulty in the analysis and interpretation of the results. In most of the cases the observations were conducted only in the red region of the spectrum, that is, where the  $H\alpha$  line is located, but in some of the observations, and specially during the intensive campaigns, blue-end spectra were also obtained. The configuration of the telescope is usually the same for red or blue-end spectra, but changing the optics according to the wavelength range of interest. From Loiano, several echelle spectra were also acquired, usually covering the red and near infra-red wavelength ranges. A list of all observations used in the long term monitoring is shown in Table 7.1. The case of the intensive campaigns will be explained in dedicated sections below.

This complete set of data allowed us to develop an exhaustive and complete analysis of the optical spectrum of BD +53°2790. Spectral classification, line variability and radial velocity analysis were performed. A picture of some of the observation sites participating in this campaign is shown in Fig. 7.1.

### 7.1.2 Data Reduction

We will outline briefly the basic steps followed to obtain a spectrum from a CCD image acquired in the telescope:

1. The act of adding a potential difference on the CCD detector implies that there will be some electrons piling up at the electrode, even with no incident light. Thus, all images of interest must be corrected for this extra number of counts (extra number of electrons gathering at the electrodes of the CCD chips). The number of extra counts produced by this effect is called *bias level*. Every science exposure must be corrected of this effect by a series of *bias* images taken along the night. A second effect producing an extra number of counts is the *dark current*, due to thermal movements of the electrons within the detector. This last effect is controlled by cooling down the CCD with liquid Nitrogen.
2. To take into account the possible difference in sensitivity of different zones of the CCD, images of an uniformly illuminated panel are taken. The sky light at twilight is also quite uniform and used very often for the same purpose. The differences of intensity in the CCD image of this uniformly illuminated area will give us a measurement of the sensitivity differences along the CCD and a way to correct our science images from this effect. The images of the uniformly illuminated area are called *flat fields*. Several of these images are taken usually before and after the observing time every night. Generally, sky flats are more suited for photometry, while flat lamp are more adequate for spectroscopy observations.
3. During the exposure time needed to achieve a good signal to noise for our science data, it is possible that some cosmic rays hit our CCD. These hits are seen as traces or spikes in our CCD images. It is important, and sometimes quite difficult, to clean our image of these hits.
4. The CCD area illuminated by the spectrum of our source (usually parallel to one of the CCD axes) is used to extract all the counts due to photons coming from it. The extracted list of counts per

detector along the illuminated area is then transformed into flux units according to the CCD properties.

5. To correct from atmospheric emission that can introduce fake counts in the spectra of our source, areas of the CCD parallel to that one where the spectrum of our source has been imaged, are extracted to produce a sky spectrum. This sky spectrum will be subtracted from the source spectrum in order to clean it from atmospheric effects.
6. Whenever a science image is taken, at least one of the so called *arc images* must be acquired as well. An *arc* is an image of a laboratory lamp, with some gas (usually mixtures of Thorium and Argon, or Copper and Neon, Copper and Argon, etc) which will produce series of known emission lines. These known emission lines are used to translate our 'per pixel' scale to a 'wavelength' scale, by measuring in which pixels these emission lines fall. Ideally a couple of these *arc images* must be acquired with each science exposure, right before and after it, as movements of the telescope will affect the conversion between pixel and wavelength scales.

All spectra in the optical band used in this thesis work have been reduced using these procedures. The software packages used for this purpose are FIGARO and KAPPA from the STARLINK project (see <http://star-www.rl.ac.uk>; Shortridge et al. 1997; Currie and Berry 2004). For echelle spectra the package ECHOMOP from STARLINK (Mills et al., 1997) and the Image Reduction and Analysis Facility (IRAF) were used (see <http://iraf.noao.edu>).

Table 7.1: Log of spectroscopic observations during the long monitoring campaign (1986–1999).

Date	Tel	Configuration	Detector	$\lambda$ Range
May 28, 1986	INT	IDS + 500 mm	GEC1	6450 – 6830
Jul 26, 1986	INT	IDS + 500 mm	GEC1	6495 – 6695
Aug 03, 1986	INT	IDS + 235 mm	IPCS	6010 – 7020
Aug 04, 1986	INT	IDS + 235 mm	IPCS	6010 – 7020

*Continued...*

Table 7.1: Continued.

Date	Tel	Configuration	Detector	$\lambda$ Range
Sep 07, 1986	INT	IDS + 235 mm	GEC1	4000 – 8000
Oct 09, 1986	INT	IDS + 500 mm	GEC1	6465 – 6665
Dec 24, 1986	INT	IDS + 500 mm	GEC1	6250 – 6875
Jun 12, 1987	INT	IDS + 235 mm	GEC1	6330 – 6770
Jun 20, 1987	INT	IDS + 235 mm	GEC1	6080 – 6900
Aug 13, 1987	INT	IDS + 500 mm	GEC1	6375 – 6765
Aug 28, 1987	INT	IDS + 235 mm	GEC1	6340 – 6770
Sep 08, 1987	INT	IDS + 500 mm	GEC1	6340 – 6730
May 19, 1988	INT	IDS + 500 mm	IPCS	6240 – 6720
Aug 02, 1988	INT	IDS + 235 mm	GEC4	6230 – 6860
Sep 26, 1988	INT	IDS + 500 mm	GEC4	6455 – 6655
Oct 12, 1988	INT	IDS + 500 mm	GEC4	6325 – 6950
Jun 02, 1989	INT	IDS + 235 mm	IPCS	6230 – 6875
Jun 11, 1989	INT	IDS + 235 mm	IPCS	5970 – 7010
Jul 31, 1989	INT	IDS + 235 mm	IPCS	6205 – 6870
Jul 24, 1990	INT	IDS + 235 mm	GEC6	6350 – 6780
Sep 02, 1990	INT	IDS + 235 mm	GEC6	6345 – 6775
Dec 27, 1990	INT	IDS + 500 mm	GEC6	6470 – 6670
Aug 28, 1991	INT	IDS + 500 mm	GEC6	6480 – 6680
May 18, 1992	PAL	f/8.75 Cass	CCD9	6255 – 6938
May 19, 1992	PAL	f/8.75 Cass	CCD9	6522 – 6663
Aug 16, 1992	PAL	f/8.75 Cass	CCD9	6255 – 6930
Aug 17, 1992	PAL	f/8.75 Cass	CCD9	6255 – 6930
Aug 18, 1992	PAL	f/8.75 Cass	CCD9	6255 – 6930
Sep 23, 1993	PAL	f/8.75 Cass	CCD9	6280 – 6960
Dec 05, 1993	PAL	f/8.75 Cass	CCD9	6259 – 6936
Dec 06, 1993	PAL	f/8.75 Cass	CCD9	4300 – 5000
Dec 07, 1993	PAL	f/8.75 Cass	CCD9	6260 – 6940
Mar 26, 1994	JKT	RBS	EEV7	5700 – 6710
Mar 27, 1994	JKT	RBS	EEV7	5700 – 6710
Jun 25, 1994	JKT	RBS	EEV7	4200 – 5200
Jun 26, 1994	JKT	RBS	EEV7	6070 – 7040
Jun 27, 1994	JKT	RBS	EEV7	4200 – 5200
Sep 16, 1994	JKT	RBS	EEV7	5825 – 6890
Sep 16, 1994	JKT	RBS	EEV7	8100 – 9100
Sep 17, 1994	JKT	RBS	EEV7	3900 – 4950
Jul 11, 1995	INT	IDS + 235 mm	TEK3	4080 – 4940

*Continued...*

Table 7.1: Continued.

Date	Tel	Configuration	Detector	$\lambda$ Range
Jul 12, 1995	INT	IDS + 235 mm	TEK3	6430 – 7286
Aug 04, 1995	JKT	RBS	TEK4	6360 – 7265
Aug 04, 1995	JKT	RBS	TEK4	8200 – 9000
Aug 05, 1995	JKT	RBS	TEK4	4100 – 5050
Aug 06, 1995	JKT	RBS	TEK4	6420 – 6755
Aug 07, 1995	JKT	RBS	TEK4	4000 – 4450
Sep 22, 1995	CRAO	Coude	EEV15–11	4400 – 4950
Nov 29, 1995	JKT	RBS	TEK4	6100 – 6900
Jun 30, 1997	CRAO	Coude	EEV15–11	4200 – 5100
Oct 26, 1997	JKT	RBS	TEK4	5904 – 6818
Oct 27, 1997	JKT	RBS	TEK4	8200 – 9000
Oct 28, 1997	JKT	RBS	TEK4	6380 – 6720
Aug 03, 1998	INT	IDS + 235 mm	EEV42	3700 – 5050
Aug 04, 1998	INT	IDS + 235 mm	EEV42	5800 – 7100
Aug 31, 1998	CRAO	Coude	EEV15–11	6530 – 6600
Aug 31, 1998	CRAO	Coude	EEV15–11	6645 – 6620
Jul 26, 1999	SKI	1201 line mm <sup>-1</sup> grating	ISA SITe CCD	5520 – 7560
Aug 17, 1999	BOL	BFOSC + gr#9+#12	Loral	5300 – 9000
Aug 17, 1999	BOL	BFOSC + gr#7	Loral	4200 – 6700
Aug 22, 1999	BOL	BFOSC + gr#8	Loral	6100 – 8200
Aug 22, 1999	BOL	BFOSC + gr#7	Loral	4200 – 6700

### 7.1.3 Analysis

#### ★ Blue Zone:

Spectra in the classification region show all Balmer and He I lines in absorption. Several spectra of BD +53°2790 at moderately high resolution were presented in Negueruela and Reig (2001), together with a detailed discussion of its spectral peculiarities. A representative spectrum covering a wider spectral range is given in Fig. 7.2. The rather strong He II  $\lambda 5412\text{\AA}$  line represents further confirmation that the underlying spectrum is that of an O-type star.



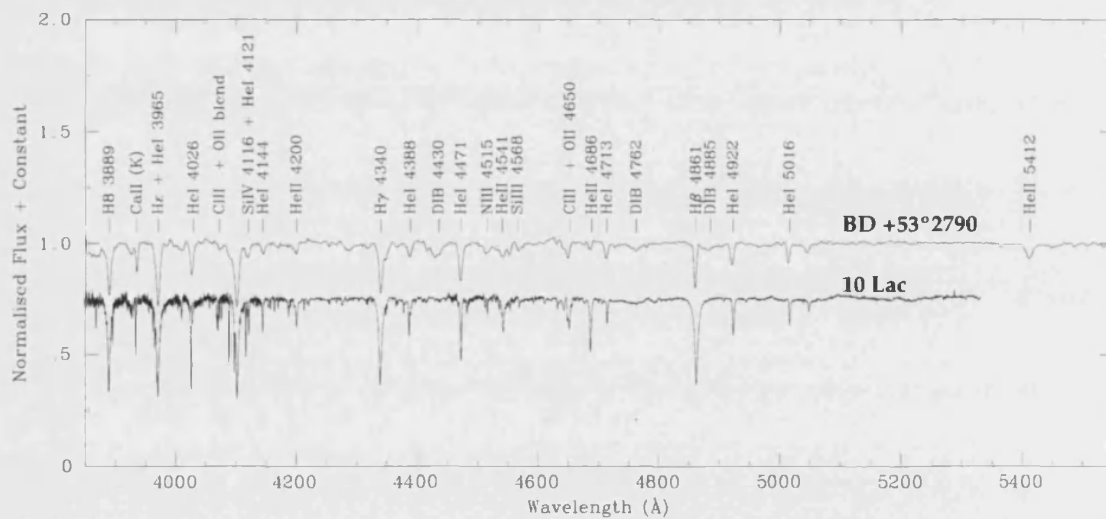


Figure 7.2: Blue/green spectrum of BD +53°2790, taken on July 21, 2000 with the 1.3-m telescope at Skinakas. Only the strongest features have been indicated. For a more complete list of photospheric features visible in the spectrum, see Negueruela and Reig (2001). The spectrum has been normalised by dividing the continuum with a spline fit. A normalised spectrum of 10 Lac (09V), shifted down for plotting purposes, is also shown for comparison.

Table 7.2: Measurement of the equivalent width of strong absorption lines (without obvious variability and presumably of photospheric origin) in the spectrum of BD +53°2790.

Line	EW (Å)
He II $\lambda$ 4200Å	0.4
H $\gamma$	2.2
He II $\lambda$ 4471Å	1.3
He II $\lambda$ 4541Å	0.4
He I $\lambda$ 4713Å	0.5
He I $\lambda$ 4923Å	0.7

The strong He II lines, specially He II  $\lambda$ 4200Å, indicates that the spectral type of BD +53°2790 O. However, Negueruela and Reig (2001) report about a variable component of O II and Si III lines. These lines are typically seen in B-type stars. The O-type classification is supported by the strong N III  $\lambda$ 4515Å as well.

There is no evidence for variability in what can be considered with certainty photospheric features (i.e., the Balmer lines from H $\gamma$  and higher and all He I and He II lines in the blue). However, it must be noted that the Equivalent Width (EW) of H $\gamma$  is  $\approx 2.2$  Å in all our spectra (and this value should also include the blended O II  $\lambda$ 4350 Å line), which is too low for any main sequence or giant star in the OB spectral range (Balona and Crampton, 1974). Average values of EWs for different lines are indicated in Table 7.2. The main spectral type discriminant for O-type stars is the ratio He II 4541Å/He I 4471Å. The quantitative criteria of Conti and Alschuler (1971), revised by Mathys (1988), indicate that BD +53°2790 is an O9.5 V star, close to the limit with O9 V.

In order to obtain a measurement of the rotational velocity of the star BD +53°2790, we have created a grid of artificially rotationally broadened spectra from that of the standard O9V star 10 Lac. We have chosen 10 Lac because of its very low projected rotational velocity and because the spectrum of BD +53°2790 is close to that of a O9V star. In Fig. 7.3 normalised profiles of a set of selected helium lines (namely, He I  $\lambda$ 4026,

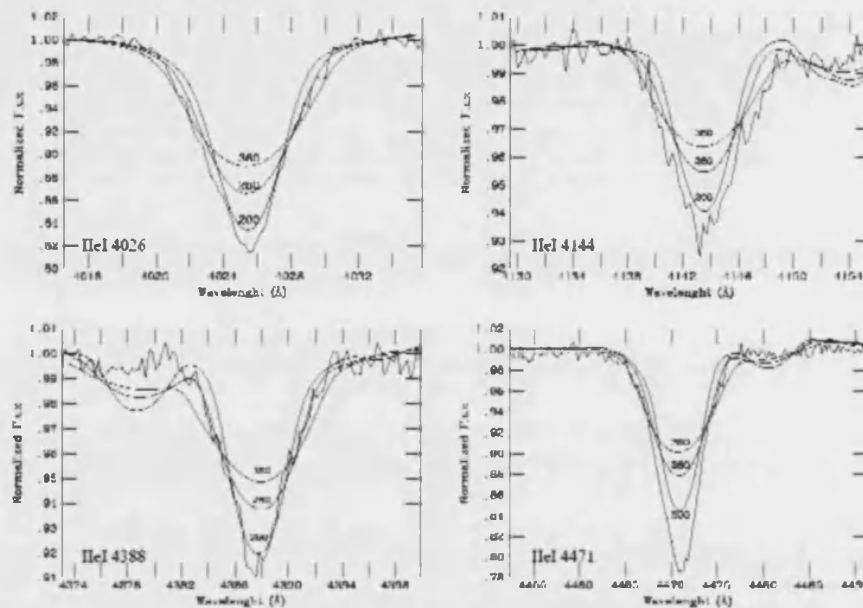


Figure 7.3: Normalised profiles of selected He I lines (namely, He I  $\lambda 4026$ ,  $\lambda 4144$ ,  $\lambda 4388$ , and  $\lambda 4471$  Å) from BD +53°2790 together with those of the same lines from 10 Lac but rotationally broadened to  $200 \text{ km s}^{-1}$  and to those rotational velocities yielding upper and lower envelopes to the width of the BD +53°2790 lines. In all cases rotational velocities above  $200 \text{ km s}^{-1}$  are needed to reproduce the line widths.

$\lambda 4144$ ,  $\lambda 4388$ , and  $\lambda 4471$  Å) are shown together with the rotationally broadened profiles from 10 Lac, at  $200 \text{ km s}^{-1}$  and those rotational velocities producing upper and lower envelopes to the widths of the observed profiles of BD +53°2790. The rotational velocity of BD +53°2790 must be above  $200 \text{ km s}^{-1}$ . For each line, the average of the rotational velocities yielding the upper and lower envelopes were taken as a representative measurement of the rotational velocity derived from that line. The results of these measurements are summarised in Table 7.3. We estimated the averaged rotational velocity of BD +53°2790 to be  $315 \pm 70 \text{ km s}^{-1}$ .

Table 7.3: Summary of the measured rotational velocities for the selected Helium lines shown in Fig. 7.3.

Line (Å)	Rot. Vel. (km s <sup>-1</sup> )	Average (km s <sup>-1</sup> )
HeIλ4026	280	320±40
	360	
HeIλ4144	320	350±30
	380	
HeIλ4388	260	290±30
	320	
HeIλ4471	260	300±40
	340	

★ **Red zone:**

Most of the spectra obtained cover the area around H $\alpha$ . For this reason, the evolution of H $\alpha$  can be studied in detail. In Table 7.4 we list all the H $\alpha$  observations used in this analysis.

Table 7.4: Details of the red spectroscopy monitoring for the period 1986–1999. Some representative spectra are displayed in Fig. 7.4 (marked with ‘\*’)

Date of Observation(s)	JD	Telescope	EW of H $\alpha$ (Å)
May 28, 1986 (*)	46578.5	INT	-5.87 ± 0.17
Jul 26, 1986 (*)	46637.5	INT	-3.40 ± 0.20
Aug 03, 1986	46645.5	INT	-5.20 ± 1.50
Aug 04, 1986	46646.5	INT	-6.00 ± 0.90
Oct 09, 1986 (*)	46712.5	INT	-7.30 ± 0.40
Dec 24, 1986 (*)	46778.5	INT	-1.30 ± 0.11
Jun 12, 1987	46958.5	INT	-1.62 ± 0.18

*Continued...*

Table 7.4: Continued.

Date of Observation(s)	JD	Telescope	EW of H $\alpha$ ( $\text{\AA}$ )
Jun 20, 1987	46966.5	INT	$-1.47 \pm 0.21$
Aug 13, 1987 (*)	47020.5	INT	$-2.10 \pm 0.21$
Aug 28, 1987	47035.5	INT	$-2.19 \pm 0.22$
Sep 08, 1987	47046.5	INT	$-2.01 \pm 0.12$
May 19, 1988	47300.5	INT	$-1.31 \pm 0.19$
Aug 02, 1988 (*)	47375.5	INT	$-2.90 \pm 0.40$
Sep 26, 1988	47430.5	INT	$-1.49 \pm 0.25$
Oct 12, 1988	47446.5	INT	$-0.96 \pm 0.17$
Jun 02, 1989	47679.5	INT	$-1.80 \pm 0.40$
Jun 11, 1989	47688.5	INT	$-2.10 \pm 0.60$
Jul 31, 1989 (*)	47738.5	INT	$-1.54 \pm 0.30$
Jul 24, 1990	48096.5	INT	$-2.83 \pm 0.26$
Sep 02, 1990	48136.5	INT	$-2.55 \pm 0.38$
Dec 27, 1990	48252.5	INT	$-3.20 \pm 0.30$
Aug 28, 1991 (*)	48496.5	INT	$-1.12 \pm 0.18$
May 18, 1992 (*)	48760.5	PAL	$+1.38 \pm 0.13$
May 19, 1992	48761.5	PAL	$+0.13 \pm 0.05$
Aug 16, 1992 (*)	48850.5	PAL	$-2.30 \pm 0.40$
Aug 17, 1992	48851.5	PAL	$-2.14 \pm 0.30$
Aug 18, 1992	48852.5	PAL	$-2.23 \pm 0.30$
Sep 23, 1993 (*)	49253.5	PAL	$-1.78 \pm 0.30$
Dec 05, 1993	49326.5	PAL	$-1.64 \pm 0.19$
Dec 07, 1993	49328.5	PAL	$-1.69 \pm 0.15$
Mar 26, 1994	49437.5	JKT	$-0.88 \pm 0.18$
Mar 27, 1994	49438.5	JKT	$-0.87 \pm 0.15$
Jun 26, 1994	49529.5	JKT	$-1.19 \pm 0.21$
Sep 16, 1994 (*)	49611.5	JKT	$-2.28 \pm 0.24$
Jul 12, 1995 (*)	49910.5	INT	$-2.00 \pm 0.30$
Aug 04, 1995	49933.5	JKT	$-2.20 \pm 0.40$
Aug 06, 1995	49935.5	JKT	$-1.51 \pm 0.25$
Nov 29, 1995	50050.5	JKT	$-2.30 \pm 0.40$
Oct 26, 1997	50747.5	JKT	$-1.77 \pm 0.32$

*Continued...*

Table 7.4: Continued.

Date of Observation(s)	JD	Telescope	EW of H $\alpha$ ( $\text{\AA}$ )
Oct 28, 1997 (*)	50749.5	JKT	$-1.47 \pm 0.25$
Aug 04, 1998 (*)	51030.5	INT	$-1.87 \pm 0.30$
Aug 31, 1998	51056.5	CRAO	$-1.49 \pm 0.02$
Jul 26, 1999	51385.5	SKI	$-2.89 \pm 0.07$
Aug 17, 1999 (*)	51407.5	BOL	$-1.35 \pm 0.40$
Aug 22, 1999	51412.5	BOL	$-1.85 \pm 0.10$

Representative shapes of the H $\alpha$  line in BD +53°2790 are shown in Fig. 7.4. In all the spectra, two emission components appear clearly separated by a deep narrow central reversal. The absorption component normally extends well below the local continuum level – which is usually referred to as a *shell* spectrum – but in some spectra, it does not reach the continuum. The red (*R*) peak is always stronger than the blue (*V*) peak, but the *V/R* ratio is variable.

The first case of observed strong variability happened during 1986, when the profile seems to have changed repeatedly over a few months from a shell structure to a double-peaked feature, with the central absorption not reaching the continuum level. It represents the largest Equivalent Width (EW) ever measured. The second one took place in 1992, when the strength of the emission peaks decreased considerably to about the continuum level. We will show later on in this section that during the summer of 2000, we again saw line profiles in which the central absorption hardly reached the continuum level alternating with more shell-like profiles.

Figure 7.5 displays a plot of the EW of the H $\alpha$  against its Full Width at Half Maximum (FWHM), *V/R* (ratio between maximum flux at the blue –*V*– peak and that at the red –*R*– peak of the H $\alpha$  line) and  $\Delta V$  (distance in wavelength between red and blue peaks), for all the data from the INT. H $\alpha$  parameters (EW, FWHM, *V/R* and  $\Delta V$ ) have been obtained for all the datasets shown in Table 7.1. Given the very diverse origins of the spectra and their very different spectral resolutions, it is difficult to compare them all, as there are some effects which introduce some artificial

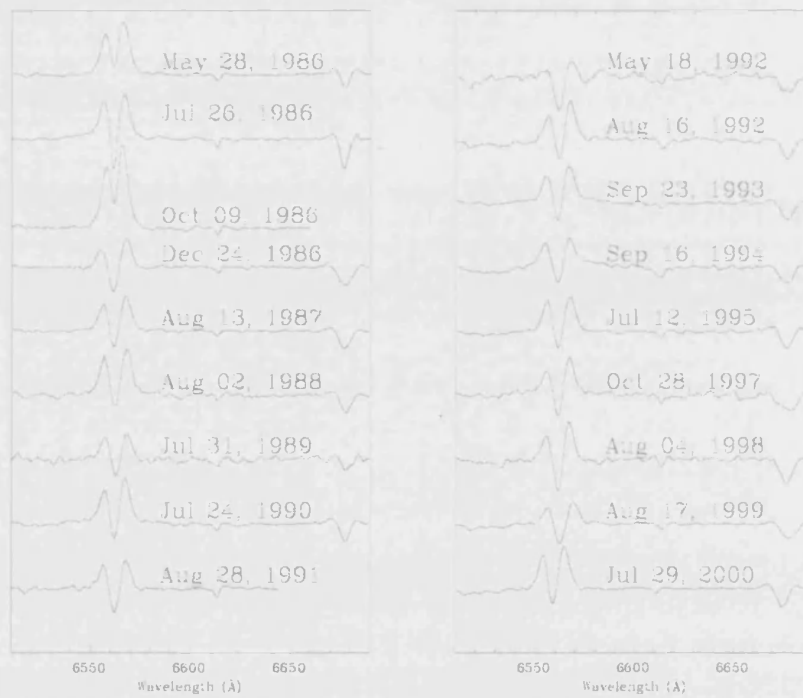


Figure 7.4: Evolution of the  $H\alpha$  line profile of BD +53°2790 during 1986–2000. All spectra have had the continuum level normalised and are offset vertically to allow direct comparison.

scattering in the data. This is the case of the instrumental broadening affecting the FWHM. At a first approximation we considered that it was not necessary to account for it. Taking into account the typical spectral resolutions of our dataset –better than 3 Å in most cases– and the fact that for the majority of our spectra  $\text{FWHM} > 11 \text{ \AA}$  (and generally  $\approx 14 \text{ \AA}$ ), the instrumental broadening, a priori, can be considered negligible. Dachs et al. (1986) found a correlation between  $\text{H}\alpha$  parameters (FWHM, peak separation, EW) in Be stars. We fail to see these correlations when the entire set of spectra is used but they are present when we restrict the analysis to those spectra taken with the same instrument, see Fig. 7.5. There is, however, a big spread in the case of the V/R ratio. Most of the scatter in FWHM may be related to the larger uncertainties involved when the emission components are small and the profile split.

Red spectra covering a larger wavelength range (such as that in Fig. 7.6) show the  $\text{He I } \lambda 6678$  and  $\text{He I } \lambda 7065 \text{ \AA}$  lines displaying characteristic shell profiles. Since most of our  $\text{H}\alpha$  spectra include the  $\text{He I } \lambda 6678 \text{ \AA}$  line (as can be seen in Fig. 7.4), we can also study its evolution. Like  $\text{H}\alpha$ , this line typically displays a shell profile, but the emission peaks are weaker than those of  $\text{H}\alpha$ , while the central absorption component is normally very deep. Variability in this line is also more frequent than in  $\text{H}\alpha$ . The V peak is generally dominant, but the two peaks can be of approximately equal intensities and sometimes so weak that they cannot be distinguished from the continuum. Given the apparent different behaviour of  $\text{H}\alpha$  and  $\text{He I } \lambda 6678 \text{ \AA}$  lines, it is surprising to find that there is some degree of correlation between their parameters, as can be seen in Fig. 7.7, where EW of both lines from INT observations are shown. The correlation coefficient of the regression is  $r=0.62$  and the correlation is significant at a 98% confidence level.

#### ★ Far Red/Near Infrared:

The upper Paschen series lines are always seen in absorption and no variability is obvious (see Fig. 7.6). The Paschen lines are much deeper and narrower than those observed in main-sequence OB stars by Andrillat et al. (1995) and rather resemble their early B-type supergiant stars. This is clearly shown in Fig. 7.8, where the near IR spectra of some OB supergiant stars, together with some OB main sequence stars, from Caron



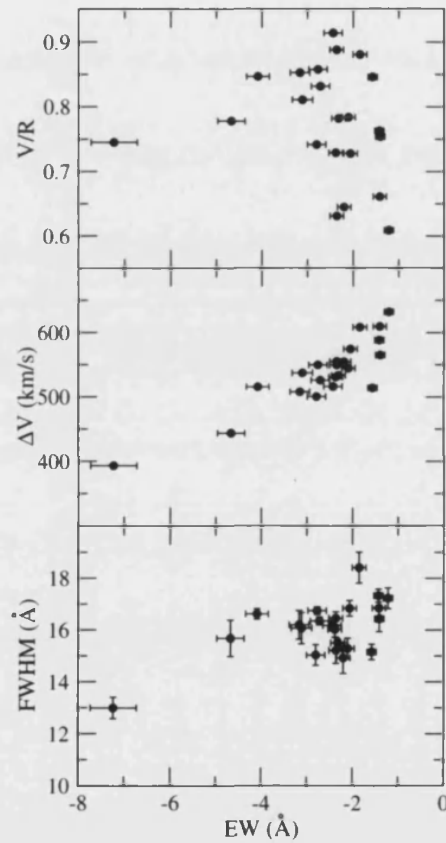


Figure 7.5: Parameters of the  $H\alpha$  emission line for all spectra taken from INT in the long-term, 1986–1999, monitoring campaign.

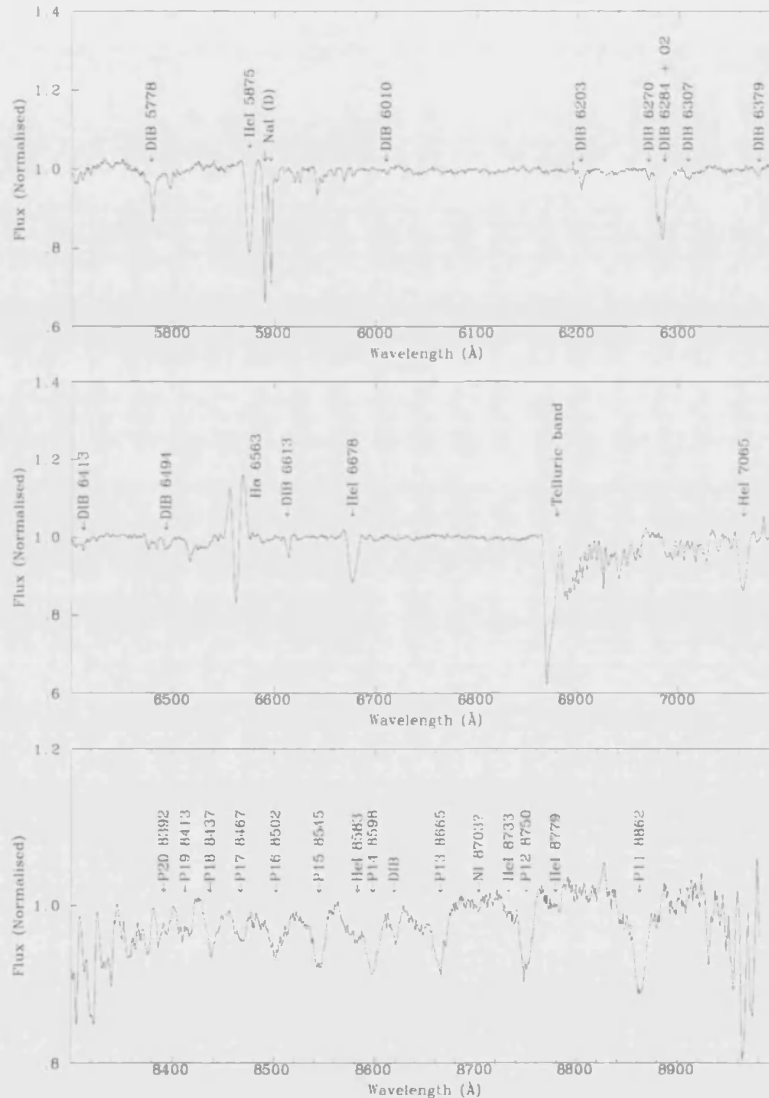


Figure 7.6: The spectrum of BD +53°2790 in the yellow/red/near-IR. Echelle spectrum taken on 17th August 1999 using the 1.52-m G. D. Cassini Telescope equipped with BFOSC and gratings #9 (echelle) and #13 (cross-disperser). All the orders have been flattened by division into a spline fit to the continuum.

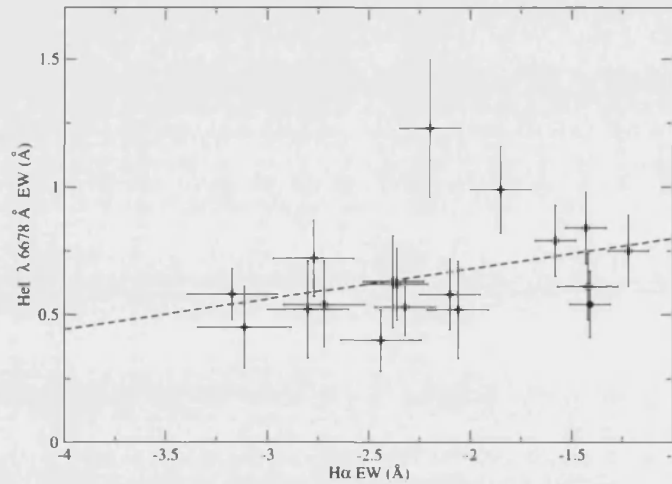


Figure 7.7: EW of the He I  $\lambda 6678\text{\AA}$  line versus that of the H $\alpha$  line. There seems to be some degree of correlation between both quantities. Only data from INT spectra where both lines were visible are shown. A linear regression fit to the data is shown as a dashed line. The correlation coefficient of the regression is  $r=0.62$  and the correlation is significant at a 98% confidence level.

et al. (2003), and that of BD +53°2790, are displayed. This is one of the most striking properties of BD +53°2790. The near IR spectrum of BD +53°2790 looks like those of supergiant stars, while the rest of spectral ranges are compatible with a main-sequence classification.

#### 7.1.4 Intensive monitoring campaigns

##### ★ July 2000:

Considering the possibility that the lack of detectable periodicities and correlations between spectral parameters in our dataset was due to the varying resolutions and irregular time coverage, we carried out a more intensive spectroscopic monitoring of BD +53°2790 during July 2000. Observations were made from Skinakas (Crete) and Loiano (Italy). We collected a set of 2 to 5 spectra per night in two runs: from 17th to 20th July in Skinakas and from 26th to 31st July in Loiano. The instrumental configurations were identical to those described in Section 2.

We fear that one of our objectives, the study of possible orbital vari-

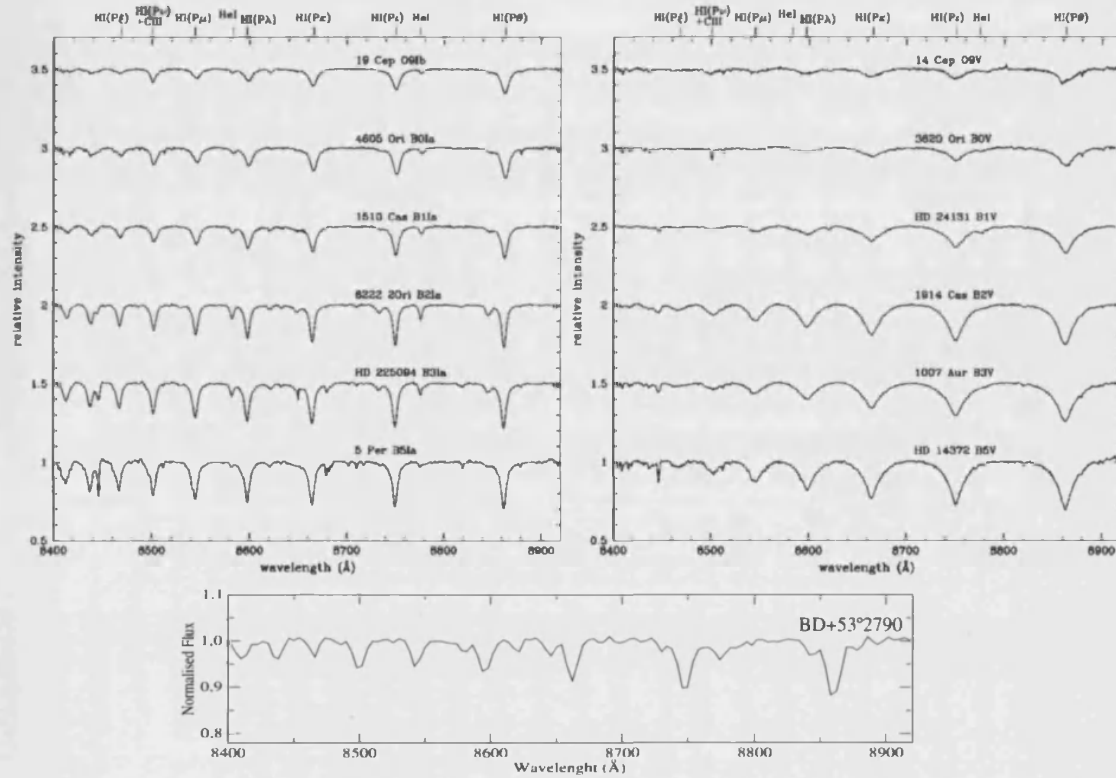


Figure 7.8: Comparison of the near IR spectrum of BD +53°2790 (lower panel) with the supergiant (upper left panel) and main sequence (upper right panel) stars shown in Caron et al. (2003). The upper panel figures were extracted from the given reference.

ations, may have been affected by an observational bias. The presumed orbital period of the source is  $\sim 9.6$  days, probably too close to the time lag (10 days) between the first observing night at Skinakas and the first observing night at Loiano. Therefore we have not been able to cover the whole orbital period. For this reason, our coverage of the orbital period extends to only  $\approx 60\%$ , which is probably insufficient to effectively detect any sort of modulation of any parameters with the orbital period.

Again, we measured all parameters of the  $H\alpha$  line, which are shown in Fig 7.9. Contrary to what we saw when considering the dataset for the 13 previous years, we find some degree of correlation between EW, FWHM and  $\Delta V$ , while V/R seems to vary independently. Since this correlation between the different line parameters seems natural, we assign the lack of correlations within the larger dataset to the use of data of very uneven resolution and quality.

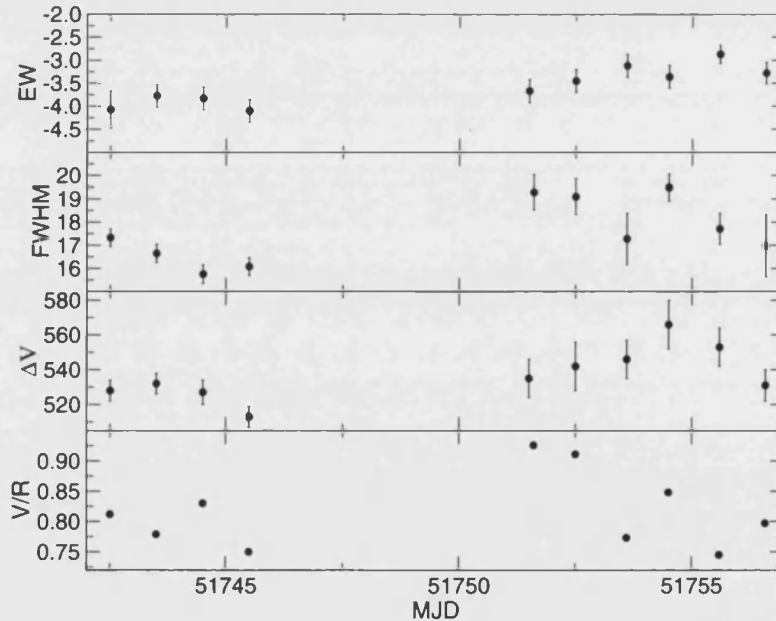


Figure 7.9:  $H\alpha$  parameters – EW (in  $\text{\AA}$ ), FWHM (in  $\text{\AA}$ ), peak separation (in  $\text{km s}^{-1}$ ) and V/R ratio– for the monitoring campaign in July 2000. There seems to be a high degree of correlation in the evolution of EW, FWHM and peak separation, which is not shared by the V/R ratio.

We observe obvious changes in the depth of the central absorption

core in the  $H\alpha$  line, which is seen sometimes reaching below the continuum level, while in other occasions is above the continuum (see Fig 7.10). Similar behaviour had already been observed in 1986 (see Fig. 7.4, but no further examples are found in our data sample). Lines in the blue are much more stable, as is also the case when the longer term data set is considered. The spectra resemble closely those obtained at other epochs, with weak emission components visible in He II  $\lambda 4686\text{\AA}$  and  $H\beta$ .

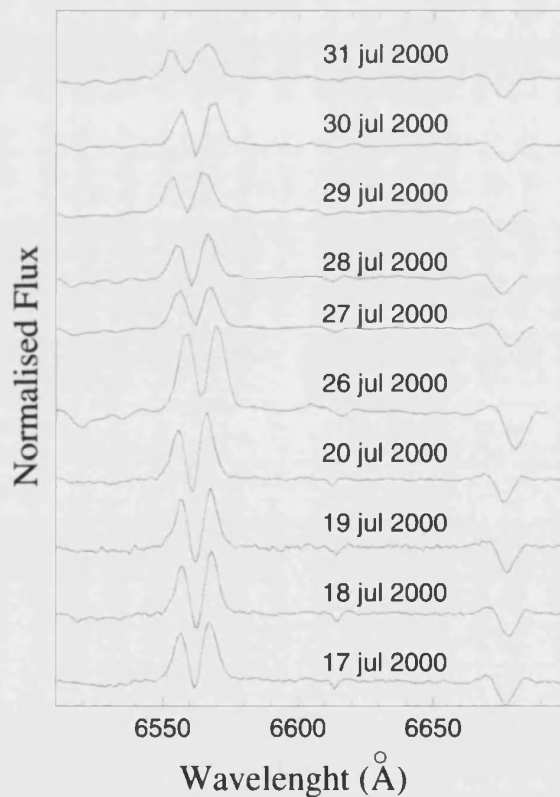


Figure 7.10: Evolution of  $H\alpha$  line in BD +53°2790 during the monitoring campaign in July 2000. Note the moderate night-to-night changes of the line profile and the important difference between the spectra from the first and second week.

★ July 2002:

Due to the unsuccessful approach on covering a whole orbital period in the 2000 campaign, two more campaigns were dedicated to a follow up of BD +53°2790 during at least an orbital cycle. From 23 to 31 July 2002 a set of red and blue regions spectroscopic observations were carried out from the INT. One red spectrum for the whole campaign and one or more blue spectra per night were acquired. In Fig. 7.11 average spectra per night are shown. Apparently there is no clear variability detected by visual inspection.

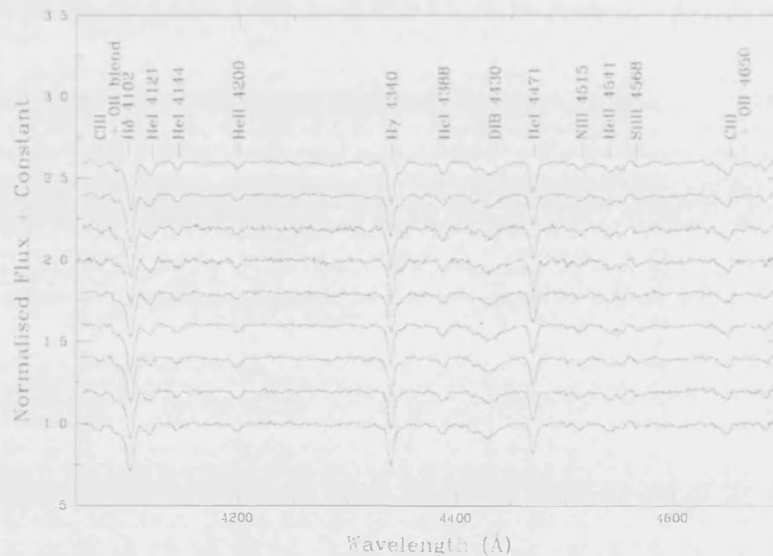


Figure 7.11: Blue spectra averaged in a per night basis of the INT July 2002 campaign. All the lines look quite stable over the whole observing period.

During the observing nights of July 30 2002 and July 31 2002 we have a set of eleven to twelve blue spectra spread along the whole night. We performed a more detailed analysis of possible variability of the order of hours with these two sets of spectra. We obtained EW for several He and H lines. The result for July 30 can be seen in Fig. 7.12. Average values are indicated with a dashed line. We find that all the EW are compatible with a constant value and with those values shown in Table 7.2 for the long term monitoring of BD +53°2790.

Furthermore, if we perform the same check for the whole INT July 2002 campaign we find the same result (see Fig. 7.13). The blue spectrum of BD +53°2790 is quite stable. The variations in O II and Si III lines described in Negueruela and Reig (2001) must be of transient nature. These sets of lines are visible in all our blue spectra (see Fig 7.11).

#### ★ July 2003:

During the period 1–10 July 2003 BD +53°2790 was observed from the INT. In this case a full orbital period was covered. As we will see below, once more, we cannot find any variation of the spectral shape or parameters modulated by the orbital period.

The results in the blue range of the electromagnetic spectrum for this campaign mimic those during July 2002. However, during July 2003 we have a more complete set of observations of the spectrum around the H $\alpha$  line. This will allow us to cross-check the results we found on the intensive campaign of July 2000 for the H $\alpha$  line parameters. We can see a history of H $\alpha$  profiles during the period July 1–July 7 2003 in Fig. 7.14. The plot in Fig. 7.14 resembles that of the July 2000 campaign. The H $\alpha$  line absorption core can be seen at the level of continuum for July 1 2003, but going down below the continuum level in the following days. It seems that by July 7 2003, it was approaching again the continuum level. The He I  $\lambda$ 6678 Å line shows all the time the characteristic shell-like profile. Contrary to the H $\alpha$  line, it shows the blue peak always higher than the red peak in the whole set of spectra shown in Fig. 7.14.

We have measured EW, FWHM,  $\Delta V$  and the V/R ratio, as well as we did with the 2000 data, for H $\alpha$  and for the close-by He I  $\lambda$ 6678 Å lines. Fig. 7.15 summarises the results for the H $\alpha$  line. We see that the EW, the FWHM and the  $\Delta V$  parameters are nicely correlated. Again, the FWHM suffers more spread, as we face the same difficulties explained in previous sections. We can also check that the V/R ratio does not correlate with any of the other parameters. We fail to detect periodic variations with the  $\sim$ 9.6 d orbital period. For the case of the EW *vs.* FWHM and EW *vs.*  $\Delta V$  correlations, linear regression fits are shown as dashed lines in the two lower plots of the left panel of Fig. 7.15.



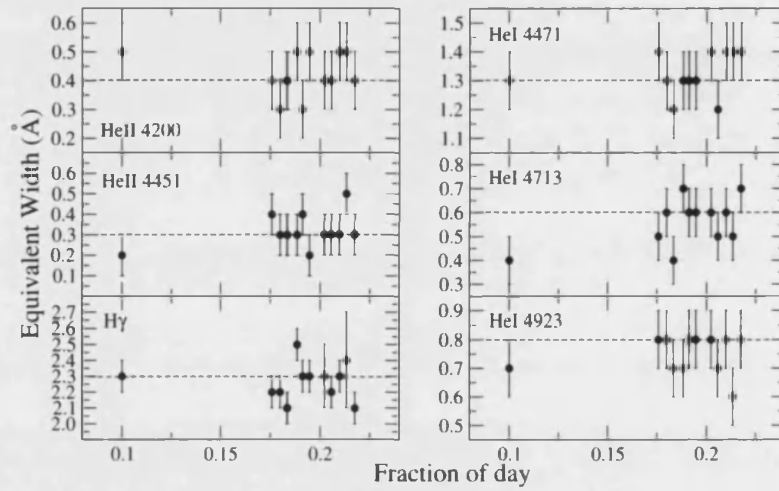


Figure 7.12: Measurements of the EW for He II, He I lines and H $\gamma$  during the night of July 30, 2002. Their values remain constant and compatible within errors with those given in Table 7.2 for the long-term monitoring. Dashed lines represent the mean values for each case.

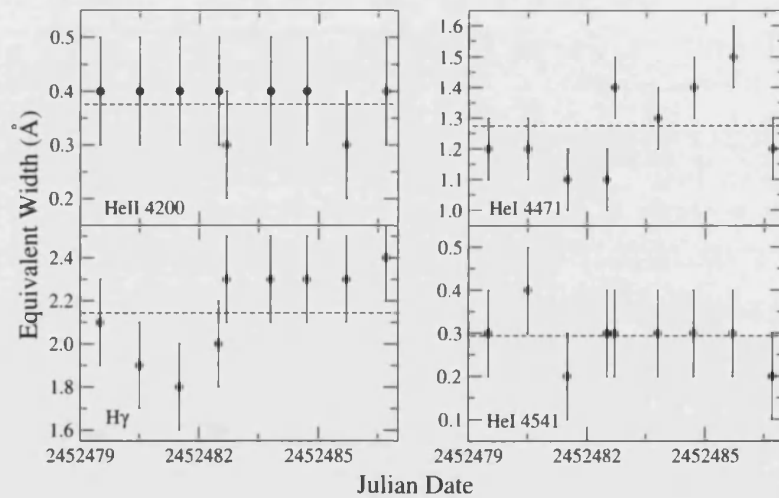


Figure 7.13: EW of He II  $\lambda$ 4200 Å, H $\gamma$  and He I  $\lambda$ 4471 Å and  $\lambda$ 4541 Å lines along the INT July 2002 campaign. Values are compatible with no variability (within errors) and with those in Table 7.2 for the long-term monitoring. The spread is due to the uncertainties in the determination of the continuum.

A summary of measurements of the HeI  $\lambda 6678$  Å line parameters is shown in Fig. 7.16. They follow the same relationships of correlation/uncorrelation as in the case of the H $\alpha$  line parameters. Again we fail to detect modulation with the orbital period of the system.

We have also checked for possible correlations between the H $\alpha$  and the HeI  $\lambda 6678$  Å lines parameters. Our aim was to check whether the two lines are affected by the same physical mechanism. Fig. 7.17 shows the EW of the HeI  $\lambda 6678$  Å line as a function of the EW of the H $\alpha$  line. A dashed-styled regression line fitted to the data shows a fair correlation (the correlation coefficient is  $r=0.50$ ). We cannot discard or confirm the possibility of a correlation, we need to investigate it further with a more extensive dataset .

#### ★ May–October 2004:

The last intensive monitoring campaign was performed intermittently during the period from May to October, 2004. This campaign took place at the Skinakas Observatory, in Crete (Greece). One to two red and blue spectra per night were acquired for a total of 8 nights. A summary of observations can be found in Table 7.5.

Blue spectra resemble those of preceding campaigns. One night averaged spectra can be found in Fig. 7.18. Helium lines parameters mimic the results from the July 2002 campaign. Metallic lines (O II and Si III) are visible during the whole monitoring campaign. It must be noted that in some cases (for example, during October 3rd, 2004) the Si III line is stronger than the He II  $\lambda 4541$  Å line, indicative of spectral classification close to O9.

A detailed view of the H $\alpha$  and HeI  $\lambda 6678$  Å line profiles is shown in Fig. 7.19. We find less dramatic changes in these profiles when compared to prior campaigns, but the central core and the double peak of the H $\alpha$  line are clearly variable, still maintaining the  $V/R$  asymmetry, with the red peak higher than the blue one. The HeI  $\lambda 6678$  Å line shows clearly variable emission only in the blue wing, as in the red wing the possible emission is at the level of the spectral noise.

The evolution of the H $\alpha$  line parameters and the correlation of all of them with respect the EW, are shown in Fig. 7.20. We find the kind of behaviour expected from previous campaigns, however, in this case the

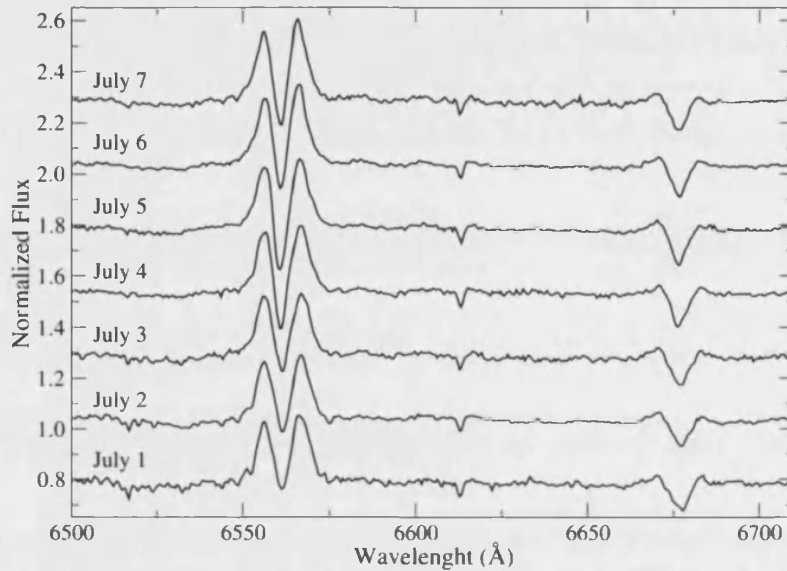


Figure 7.14:  $H\alpha$  and  $He\ I\ \lambda 6678\ \text{\AA}$  line profiles along the July 2003 campaign.

Table 7.5: Summary of spectroscopic observations during the period May–October 2004 from Skinakas Observatory.

Date	Red spectral range coverage ( $\text{\AA}$ )	Blue spectral range coverage ( $\text{\AA}$ )
21/05/2004	6400–6700	—
06/07/2004	6400–6700	—
25/08/2004	6400–6700	3600–5725
26/08/2004	—	3600–5725
27/08/2004	—	3600–5725
03/09/2004	6400–6700	3650–5700
04/09/2004	6400–6700	3650–5700
12/09/2004	6400–6700	3600–5725
13/09/2004	—	3600–5725
03/10/2004	—	3600–5750

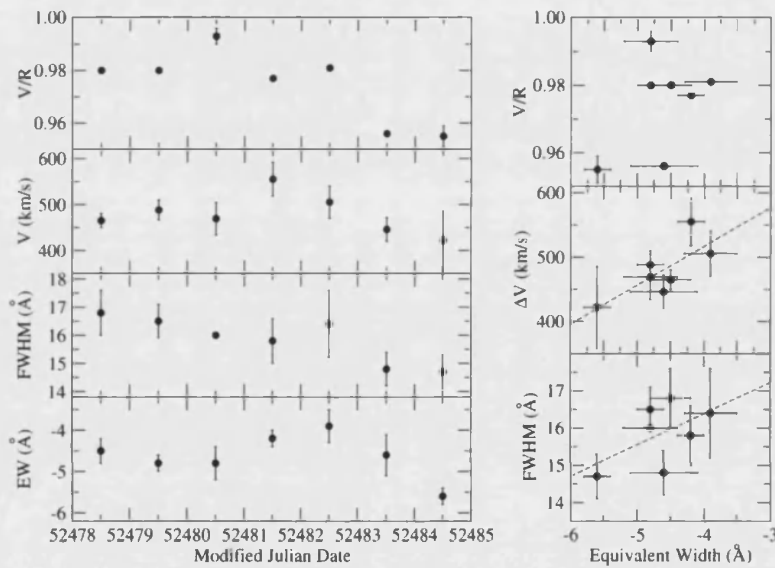


Figure 7.15: Summary of the H $\alpha$  line measurements for the July 2003 campaign. In the left panel the variations of the parameters with time are shown. In the right panel the FWHM,  $\Delta V$  and V/R ratio are plotted vs. the EW. H $\alpha$  parameters follow the expected tendency, with EW, FWHM and  $\Delta V$  correlated but all of them uncorrelated with the V/R ratio. Regression analysis tendencies are shown in the FWHM *vs.* EW and  $\Delta$  *vs.* EW plots as dashed lines. In the former case the correlation coefficient is  $r=0.75$  and in the latter case  $r=0.54$ .

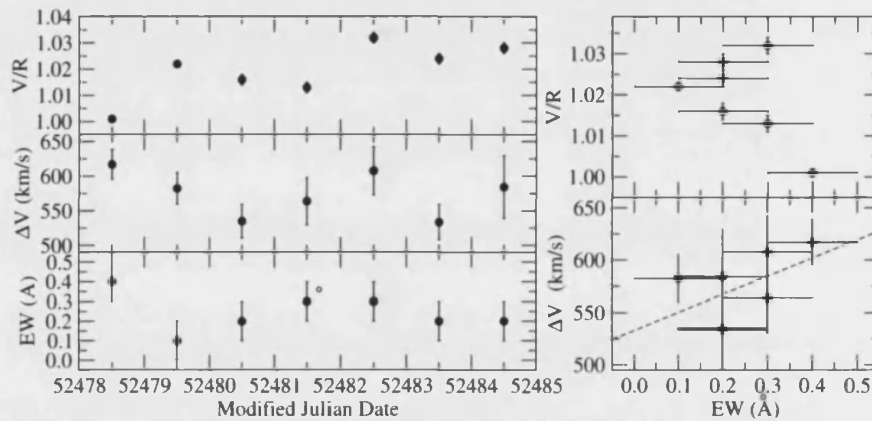


Figure 7.16: Summary of the He I  $\lambda$  6678 Å line measurements for the July 2003 campaign. In the left panel we see the evolution of the parameters measured. In the right panel the correlation plots among the  $\Delta V$  and  $V/R$  ratio vs the  $EW$  of the line are shown. The parameters behave as those from the  $H\alpha$  line. A Regression line fit is shown in the  $\Delta V$  vs.  $EW$  plot as a dashed line. The correlation coefficient of the fit is  $r=0.51$ .

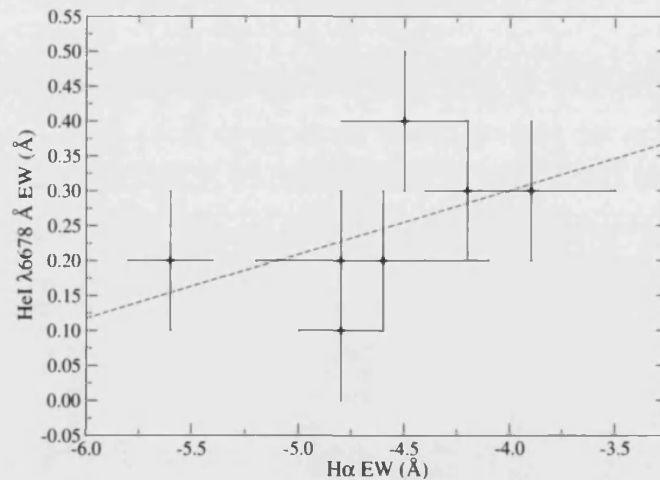


Figure 7.17:  $EW$  of the He I  $\lambda$ 6678 Å line as a function of the  $EW$  of the  $H\alpha$  line. We can find traces of a possible correlation between the two datasets (the correlation coefficient is  $r=0.50$ ).

Table 7.6: Summary of He I  $\lambda 6678$  Å line EW measurements during the May-October 2004 monitoring campaign.

Julian Date	He I $\lambda 6678$ Å EW(Å)
2453147.5	0.9±0.2
2453193.5	0.7±0.2
2453242.5	0.8±0.2
2453251.5	0.7±0.2
2453252.5	0.7±0.2
2453260.5	0.7±0.2
2453281.5	0.7±0.2

errors are larger.

The behaviour of the He I  $\lambda 6678$  Å line is summarised in Table 7.6. We find a very stable He I  $\lambda 6678$  Å line.

Fig. 7.21 shows the He I  $\lambda 6678$  Å line EW vs. that of the H $\alpha$  line. Like in the July 2003 campaign, there is a poor correlation between both parameters (the correlation coefficient of the linear regression shown as a dashed line in Fig. 7.21 is  $r=0.54$ ). However, when we put both campaigns together in the same plot, we find a very nice correlation (see Fig. 7.22) like the one shown in the long monitoring campaign (see Fig. 7.7).

### 7.1.5 Radial Velocities and Orbital Parameters

The most important result from the intensive campaigns during 2002, 2003 and 2004 has been the radial velocity analysis performed. None of the three campaigns by itself gave us sufficient coverage of a complete orbital cycle (expected to be  $\sim 9.6$  days), but all sets together can be used to set some constraints on the orbital parameters of the HMXRB system 4U 2206+54.

The spectral range coverage of the July 2002 campaign was narrower than that of the July 2003 and 2004 runs. Therefore, for the sake of uniformity, the spectral range 4050–4750 Å was chosen to perform the radial velocity analysis in all datasets (adjusted to the observed spectral

range during the July 2002 campaign).

Radial velocity measurements were done by cross-correlation techniques, with the software package MOLLY. For periodograms and best-fit periods the package RVANAL<sup>1</sup> and a Discrete Fourier Transform (DFT) FORTRAN code were used.

The following steps were performed in order to measure the radial velocity of BD +53°2790:

1. One averaged spectrum per night was obtained.
2. The nightly-averaged spectra were rebinned to a uniform wavelength range, ensuring that all have the same resolution. The spectral coverage chosen was 4050–4750 Å. A requirement of the cross-correlation techniques was that the rebinning had to be done in a logarithmic scale.
3. A Diffuse Interstellar Band (DIB) in absorption was chosen to align all the spectra.
4. The data were corrected to a heliocentric frame of reference.
5. All the spectra were normalised to the continuum. The continuum level was brought down to zero. That was required by the cross-correlation techniques used.
6. An averaged spectrum was used as a template to cross-correlate all the spectra.

Radial velocities for the three periods of observations can be seen in Fig. 7.23.

A broad peak can be seen in the periodogram computed, by a DFT code, over the complete set of radial velocity measurements (see Fig. 7.24). The most significant peak is located at a frequency of  $\sim 0.067 \text{ d}^{-1}$ , which corresponds to a period of  $14.89 \pm 0.07 \text{ d}$ . The software package RVANAL also gave us the smallest value of  $\chi^2$  for a period of 14.89 days. We cannot find a clear peak of the expected  $9.5591 \pm 0.0007$  orbital period derived from X-ray measurements (see Ribó et al. 2005).

---

<sup>1</sup>MOLLY and RVANAL are available at Tom Marsh's web pages: <http://quetzal.csc.warwick.ac.uk/phsaap/software/>

Fig. 7.25 shows the radial velocity measurements folded by both, the 14.89 d period found by Fourier Transform (FT) techniques, and the expected 9.5591 d period of the system, in both cases the orbital epoch used has been  $t_0 = \text{MJD } 51856.6$ , as in Ribó et al. (2005). The 14.89 d period is likely to be an artifact of the DFT. In these techniques very noisy data points can affect dramatically the behaviour of the transformation. Furthermore, in Fig. 7.25 we see that the data folded with the 14.89 d is gathered at certain phases, which is unlikely due to the number of data points (namely, 27) and the distribution of data during the July 2002 and July 2003 campaigns, which extent close to 10 days and should cover almost a whole phase. In view of the well distributed data when folding with the 9.5591 d period, we can discard the 14.89 d period and attribute its detection to some artifact of the DFT technique.

We have written a code which calculates a grid of radial velocity curves for a wide set of orbital configurations. The radial velocity curve follows the general relationship:

$$v = V_{sys} + K_1(\cos(w + \nu) + e\cos w)$$

Where  $V_{sys}$  represents the systemic velocity of the target, that is, its velocity relative to the heliocentric frame of reference. As a first approximation, we have not taken into account this term.  $K_1$  is the semi-amplitude of the radial velocity curve variation,  $\nu$  is the true anomaly (related to the orbital phase by a transcendental equation which must be solved by an iteration procedure),  $e$  is the eccentricity of the orbital motion, and  $w$  is the periastron anomaly. Once we have a grid of models, we compare them to the observed radial velocity curve. Eccentricities of 0.2, 0.3 and 0.4 had to be used to reproduce the observed radial velocity curve, see Fig. 7.26. Eccentricities above (i.e. 0.5) and below (i.e. 0.1) deviated appreciably from the measurements.

We have also prepared a code which reads in the measured radial velocities and the grid of models and calculates  $\chi^2$  for each model in the grid. This will let us select the statistically best-fit periods. The models with lowest values of  $\chi_{\text{RED}}^2$  are shown in Table 7.7, while the models which give best match against observed radial velocity light curve (see Fig. 7.26) are shown in Table 7.8.



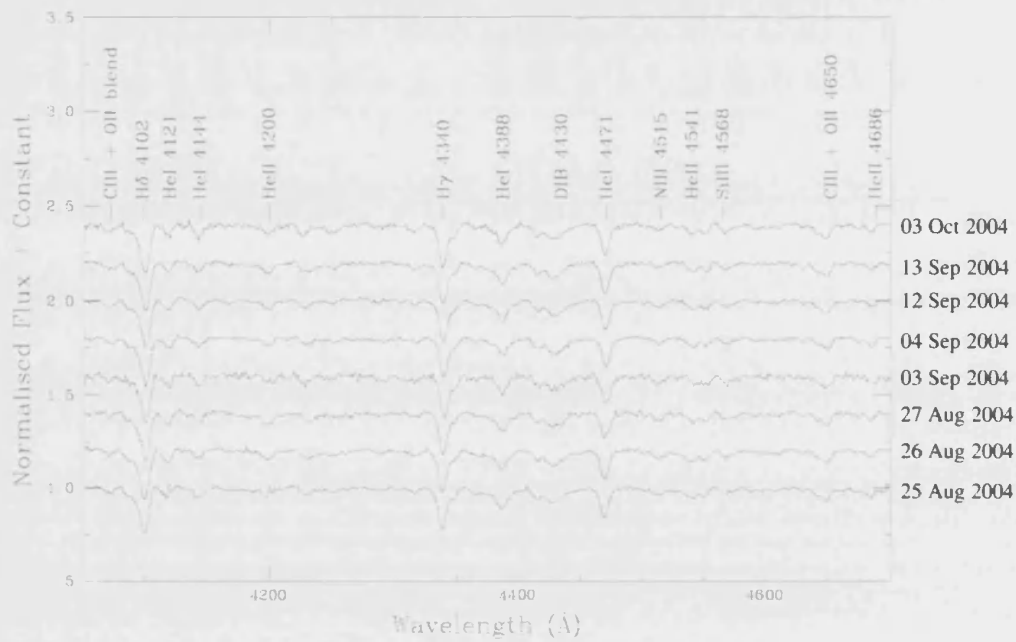


Figure 7.18: Blue spectra of BD+53°2790 during the monitoring campaign of August-October 2004 from Skinakas Observatory, Crete, Greece.

Table 7.7: Lowest values of the computed  $\chi_{\text{RED}}^2$  by comparing the observed values of the radial velocity with the calculated theoretical profiles for a wide range of orbital parameters.

<b>P=9.5591 d</b>					
$e$	$\omega$	$K_1$ (km s $^{-1}$ )	$\chi_{\text{RED}}^2$	DOF	
0.2	0.2	10	11.437	47	
0.3	0.2	10	11.525	47	

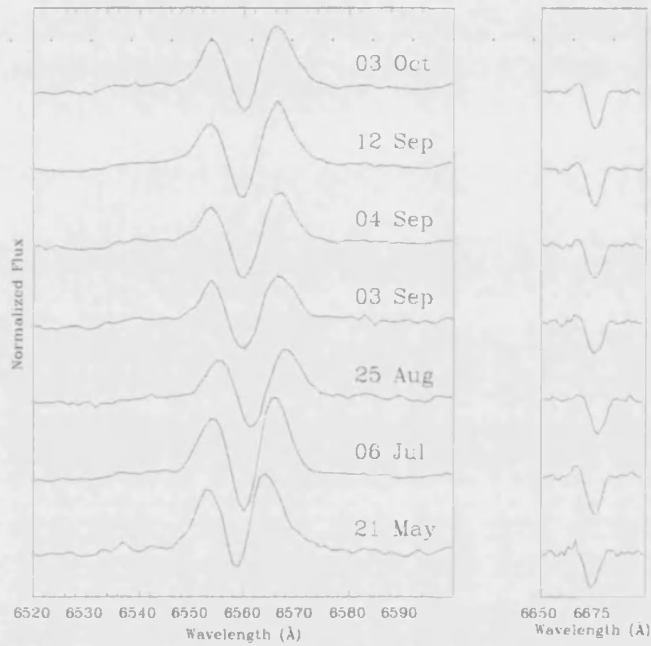


Figure 7.19: Evolution of the H $\alpha$  and He I  $\lambda 6678 \text{ \AA}$  line profiles during the period May-October 2004, as observed from Skinakas Observatory.

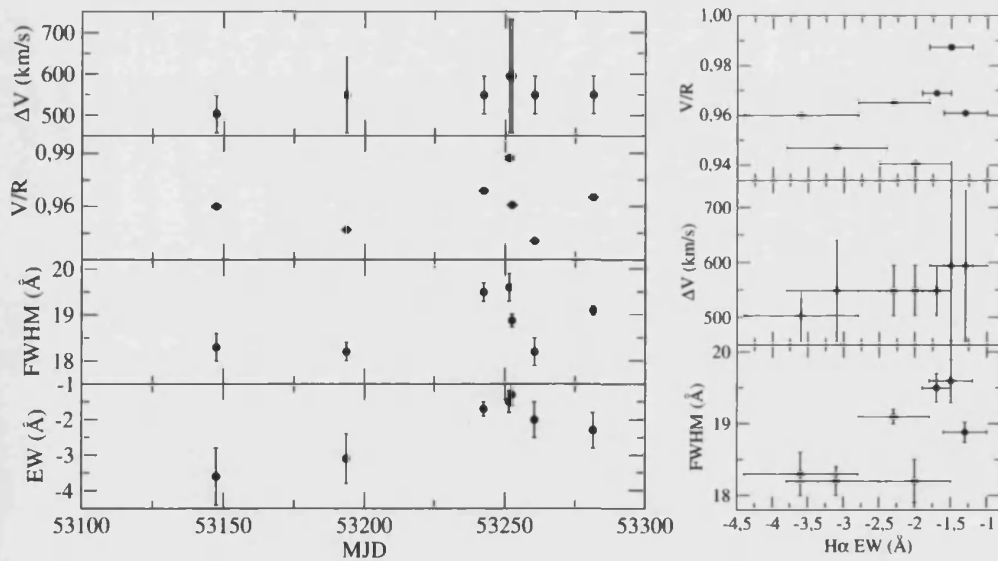


Figure 7.20: In the left panel we the evolution of H $\alpha$  parameters during August-October 2004 is shown. In the right panel FWHM,  $\Delta V$ , and V/R ratio versus EW of the H $\alpha$  line during August-October 2004 are plotted.

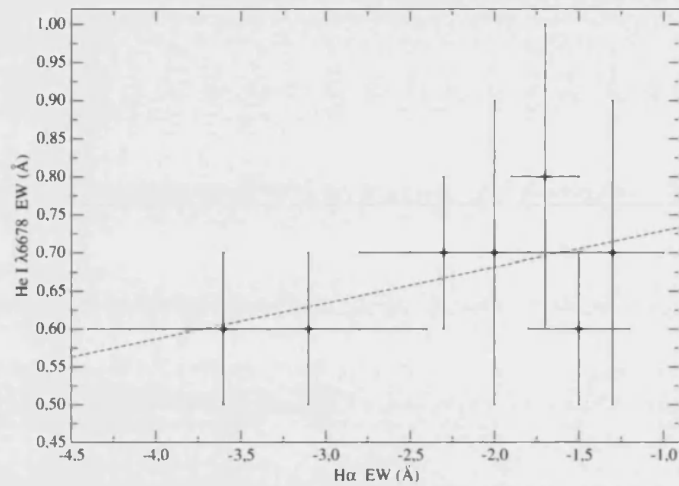


Figure 7.21: EW of the He I  $\lambda 6678$  Å line vs. that of the H $\alpha$  line for the August-October 2004 spectra. The correlation coefficient of the linear regression shown as a dashed line is  $r=0.54$ .

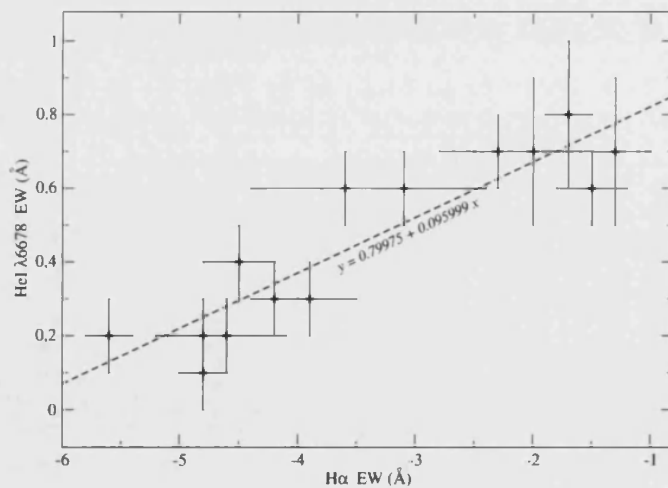


Figure 7.22: EW of the He I  $\lambda 6678$  Å line vs. that of the H $\alpha$  line for the 2003 and 2004 monitoring campaigns.

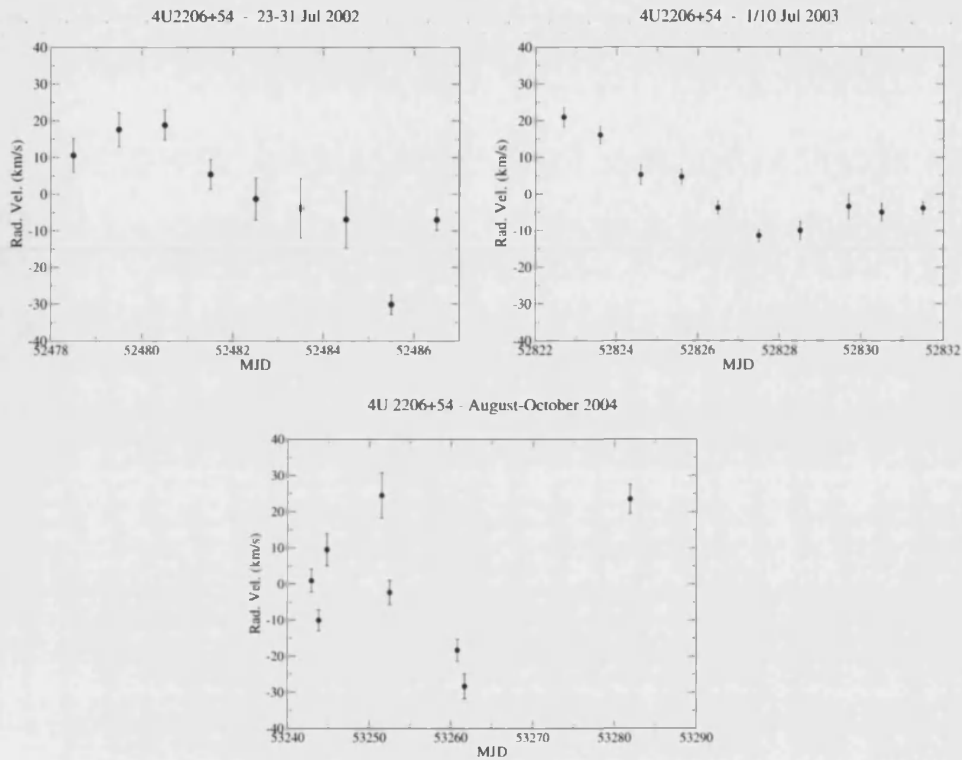


Figure 7.23: Radial velocity measurements for the INT campaign during July 2002, July 2003 and the period August-October 2004.

Table 7.8: Computed values of  $\chi_{red}^2$  for the models used in the visual fitting shown in Fig. 7.26.

<b>P=9.5591 d</b>				
$e$	$\omega$	$K_1$ (km s $^{-1}$ )	$\chi_{RED}^2$	DOF
0.2	0.1	18	18.411	47
0.2	0.2	18	14.498	47
0.3	0.1	18	18.251	47
0.3	0.2	18	14.242	47
0.4	0.1	18	18.003	47
0.4	0.2	18	14.114	47

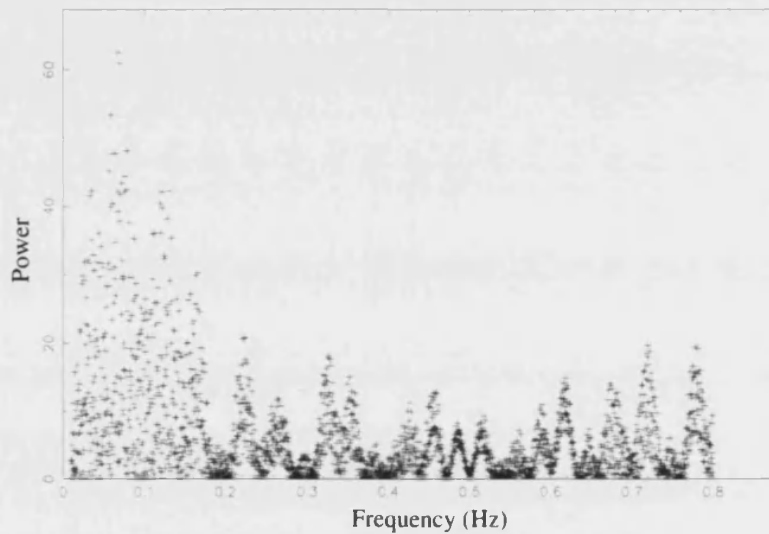


Figure 7.24: Periodogram computed from all the radial velocity measurements of BD+53° 2790.

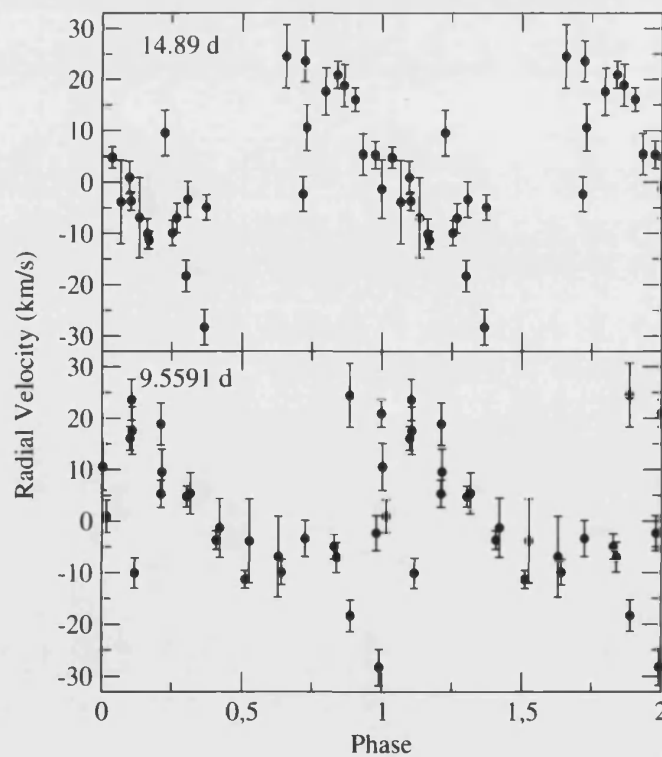


Figure 7.25: Radial velocity measurements folded with the 14.89 d period derived from FT techniques, and the 9.5591 d period found by Ribó et al. (2005). In both cases  $t_0$ =MJD 51856.6.

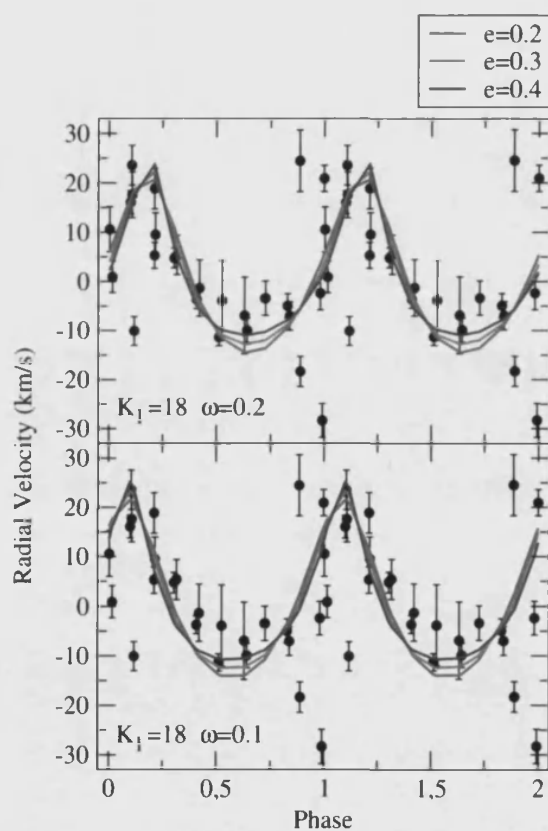


Figure 7.26: Radial velocity measurements folded with the 9.5591 d period. Different eccentricities have been used to compute radial velocity curves which are compared to the measurements. Eccentricities above (i.e. 0.5) and below (i.e. 0.1) deviated significantly from the observed radial velocity curve.

A radial velocity analysis has been carried out for the first time using optical data from the HMXRB 4U 2206+54. Although no definitive value of the orbital parameters can be given, some restrictions to its possible values can be deduced. Eccentricity must be between 0.2 and below 0.4, while the periastron anomaly will lie close to phase  $\sim 0.15$  (when  $t_0 = \text{MJD } 51856.6$  is considered). We know from X-ray measurements (see Corbet and Peele, 2001; Ribó et al., 2005) that the orbital period of the system is  $\sim 9.6$  d, our set of radial velocity measurements is compatible with an orbital modulation of this period. It must be noticed that we have not made use of the term  $V_{\text{sys}}$ . This radial velocity analysis is far from complete. We need more data in order to have enough statistics to derive a definitive orbital solution with optical data.

## 7.2 Optical Photometry

We took one set of *UBVRI* photometry of the source on August 18, 1994, using the JKT. The observations were made using the TEK#4 CCD Camera and the Harris filter set. The data have been calibrated with observations of photometric standards from Landolt (1992) and the resulting magnitudes are on the Cousins system.

We also obtained several sets of Strömgren *uvby $\beta$*  photometry. The first observations were taken at the 1.5 m Spanish telescope at the German-Spanish Calar Alto Observatory, Almería, Spain, using the *UBVRI* photometer with the *uvby* filters, in single-channel mode, attached to the Cassegrain focus. Three other sets were obtained with the 1.23 m telescope at Calar Alto, using the TEK#6 CCD equipment. One further set was taken with the 1.5 m Spanish telescope equipped with the single-channel multipurpose photoelectric photometer. Finally, one set was obtained with the 1.3-m Telescope at Skinakas, equipped with a Tektronik  $1024 \times 1024$  CCD.

The *UBVRI* photometric values we obtain are  $U = 9.49$ ,  $B = 10.16$ ,  $V = 9.89$ ,  $R = 9.88$  and  $I = 9.55$ . The photometric errors are typically 0.05 mag, derived from the estimated uncertainties in the zero-point calibration and colour correction of our data. Table 7.9 lists our Strömgren *uvby $\beta$*  measurements.

From the OMC on board *INTEGRAL*, we have collected a few values

Table 7.9: Strömgren photometry of the optical counterpart to 4U 2206+54. The last column indicates the telescope used. a stands for the 1.5-m Spanish telescope at Calar Alto. b represents the 1.23-m German telescope. c is the Skinakas 1.3-m telescope.

Date	$V$	$(b - y)$	$m_1$	$c_1$	$\beta$	T
1988, Jan 7	$9.909 \pm 0.013$	$0.257 \pm 0.005$	$-0.083 \pm 0.007$	$0.011 \pm 0.007$	$2.543 \pm 0.040$	a
1989, Jan 4	$9.845 \pm 0.015$	$0.257 \pm 0.007$	$-0.042 \pm 0.010$	$-0.117 \pm 0.017$	$2.543 \pm 0.007$	a
1991, Nov 16	$9.960 \pm 0.034$	$0.268 \pm 0.005$	$-0.040 \pm 0.012$	$-0.041 \pm 0.033$	—	b
1991, Dec 19	$9.969 \pm 0.038$	$0.271 \pm 0.021$	$-0.322 \pm 0.006$	$-0.010 \pm 0.018$	$2.489 \pm 0.024$	b
1994, Jun 21	$9.835 \pm 0.019$	$0.258 \pm 0.013$	$-0.032 \pm 0.021$	$0.053 \pm 0.030$	$2.617 \pm 0.020$	b
1996, May 26	$9.845 \pm 0.012$	$0.267 \pm 0.007$	$-0.052 \pm 0.012$	$-0.074 \pm 0.013$	$2.553 \pm 0.006$	a
1999, Aug 16	$9.883 \pm 0.031$	$0.255 \pm 0.044$	$-0.226 \pm 0.074$	$0.298 \pm 0.094$	—	c

of the  $V$  magnitude of BD +53°2790 during the last three years. Table 7.10 shows these measurements.

$V$  measurements in the literature are scarce and consistent with no changes (see references in NR01). However, our more accurate set of measurements of the  $V$  magnitude (or Strömgren  $y$ ) show variability, with a difference between the most extreme values of  $0.13 \pm 0.05$  mag (see Table 7.9), 0.05 mag being also the standard deviation of all 7 measurements. From the OMC on board *INTEGRAL*, we have collected a few values of the  $V$  magnitude of BD +53°2790 during the last three years. Table 7.10 shows these measurements.

From our  $UBV$  photometry, we find that the reddening-free  $Q$  parameter is  $Q = -0.86 \pm 0.10$ . This value corresponds, according to the revised  $Q$  values for Be and shell stars calculated by Halbedel (1993), to a B1 star.

We have derived the intrinsic parameters of BD +53°2790 from our Strömgren photometry by applying the iterative procedure of Shobbrook (1983) for de-reddening. Though the values obtained for the reddening from the different measurements agree quite well to  $E(b - y) = 0.38 \pm 0.02$  (one standard deviation), the intrinsic parameters derived are rather inconsistent, except for  $(b - y)_0$ , which averages to  $-0.12 \pm 0.02$ . This value corresponds to a B1V star according to the calibrations of Perry et al. (1987) and Popper (1980).

We can use this very stable value of the  $V$  magnitude, and the reddening measured, to estimate the distance to the source, as outlined in



Table 7.10:  $V$  magnitude measurements from the OMC on board *INTEGRAL*.

MJD	V
52638.524	9.819±0.007
52761.357	9.897±0.010
52806.032	9.865±0.008
52820.985	9.896±0.010

Negueruela and Reig (2001). The reddening to BD +53°2790 can be estimated in several different ways. Photometrically, from our value of  $E(b - y) = 0.38 \pm 0.02$ , using the correlation from Shobbrook (1983), we derive  $E(B - V) = 0.54 \pm 0.05$ . An independent estimation can be made by using the standard relations between the strength of Diffuse Interstellar Bands (DIBs) in the spectra and reddening (Herbig, 1975). Using all the spectra obtained from the Cassini telescope (for consistency), we derived  $E(B - V) = 0.57 \pm 0.06$  from the  $\lambda 6613\text{\AA}$  DIB and  $E(B - V) = 0.62 \pm 0.05$  from the  $\lambda 4430\text{\AA}$  DIB. All these values are consistent among themselves within their errors and therefore we take the photometric value as representative, as it is a more reliable measurement of the reddening. From five  $UBV$  measurements available in the literature (including the one presented in this work), we find  $(B - V) = 0.28 \pm 0.02$ . With the  $E(B - V)$  derived, this indicates an intrinsic colour  $(B - V)_0 = -0.26 \pm 0.05$ , typical of an early-type star, confirming the validity of the reddening determination. As discussed in Negueruela and Reig (2001), the value of the absorption column derived from *RXTE* X-ray observations is one order of magnitude larger than what is expected from the interstellar reddening.

Even when we consider the more accurate measurement of the absorption column (i.e.,  $\sim 1.0 \times 10^{22} \text{ atoms cm}^{-2}$ ) from *BeppoSAX* data (see Torrejón et al., 2004; Masetti et al., 2004) we obtain higher values for the the absorption column than those calculated from photometric data.

Averaging our 7 measurements of  $y$  with the 5  $V$  measurements, we find a mean value for BD +53°2790 of  $V = 9.88 \pm 0.04$ . Assuming a standard reddening law ( $R = 3.1$ ), we find  $V_0 = 8.21$ . If the star has the

typical luminosity of an O9.5V star ( $M_V = -3.9$ , see Martins et al. 2005), it is situated at  $d \approx 2.6$  kpc, closer than previous estimates (cf. NR01), because the absolute magnitudes of O-type stars have been lowered down in the most recent calibrations.

The photometric behaviour of BD +53°2790 is quite stable over long and short timescales, the visual magnitude has been stable around  $\sim 9.88$  ever since the first reported measurements. It must be noticed that the spectral classification through photometry leads to later spectral types (B1) than with spectroscopy (O9.5).



## Chapter 8

# Ultra-Violet Spectrum

The stellar wind phenomenon is known to be especially dramatic in massive early-type stars. The theory of radiative driven winds has successfully explained the physics behind many astrophysical scenarios (see subsection 2.2.1 in the Introduction of this thesis). Far from being complete, it has been updated continuously as new approaches, mathematical methods, recalculations of opacities, etc., have come into light.

Although the underlying physics of momentum transfer from the outgoing photons to the photospheric matter in the radiative driven wind model is quite intuitive, the modelling of the processes involved is not an easy task, as it requires tools from non-LTE radiative transfer theories and hydrodynamics (even including magnetohydrodynamics). There are many effects to take into account (cross sections of the different ionisation states, turbulent movements within the photosphere and within the wind structure, interaction of the outgoing plasma with magnetic field lines, shearing forces and frictions, etc). At present there is no complete model accounting for all possible cases, but great advances have been achieved especially in the field of computational analysis and predicted profiles match the observed ones quite well .

There are some methods available for modelling the wind process and structure, like the Co-Moving Frame method (CMF) (Mihalas et al., 1975), or the so called Sobolev-method of Sobolev (1947), or more recent methods including non-laminar effects in the winds (Owocki et al., 1988), among others. There are, as well, different methods used to compare modelled

and observed line profiles. However the basics of all the comparing-fitting methods are the creation of a grid of theoretical models corresponding to a great variety of wind velocities and plasma properties and the comparison of these models to the observed profile, with the goal of selecting the one best matching the observation. The parameters corresponding to this best-matched model are the ones accepted as representing the physical conditions and structure of the stellar wind of the star under study.

There are also attempts to measure directly the terminal velocity of the wind on the observed profile. Traditionally the point at which the blue end of the line touches the continuum was taken as a good estimator of the terminal wind velocity ( $v_{\text{edge}}$ ). There are studies, however, which show that this measurement overestimates the wind terminal velocity (Prinja et al., 1990), but we will come to that later in this section.

The International Ultraviolet Explorer satellite (*IUE*) was a joint project between NASA, ESA and PPARC. It was launched into geosynchronous orbit on January 26 1978 from Kennedy Space Centre, and was turned off on 30 September 1996, after 18 years of successful operations. Its aim was to study the ultra-violet radiation locked by the atmosphere's ozone and invisible from ground based telescopes. An image of the *IUE* satellite can be seen in Fig. 8.1. The *IUE* was a 45 cm telescope with UV optics driving the light into the cameras attached to two spectrographs. The *IUE* could perform spectrophotometry at high ( $\sim 0.2 \text{ \AA}$ ) and low ( $\sim 6 \text{ \AA}$ ) spectral resolution covering short (between 1150 and 1900  $\text{\AA}$ ) and long (from 1800 up to 3200  $\text{\AA}$ ) spectral ranges. The data cover a dynamic range of approximately 17 astronomical magnitudes.

The *IUE* archive is very extensive (with more than 100000 spectra) and still used by many astronomers. It is named INES, standing for *IUE* Newly Extracted Spectra, and can be accessed through its web site<sup>1</sup>.

*IUE* observed BD +53°2790 in both the high and low resolution modes. We have analysed in detail the high resolution *IUE* spectrum SWP39112M, from BD +53°2790 which was described in Negueruela and Reig (2001). Our goal was to investigate the stellar wind in BD +53°2790 from the resonance ultra-violet lines, in particular the C IV  $\lambda\lambda$  1548.19 1550.76  $\text{\AA}$  doublet, N IV  $\lambda$  1718.55  $\text{\AA}$  singlet, N V  $\lambda\lambda$  1238.80 1242.78  $\text{\AA}$  doublet and Si IV  $\lambda\lambda$  1393.76 1402.77  $\text{\AA}$  doublet. The 1200-1900  $\text{\AA}$  *IUE* spectrum

---

<sup>1</sup><http://iuearc.vilspa.esa.es>

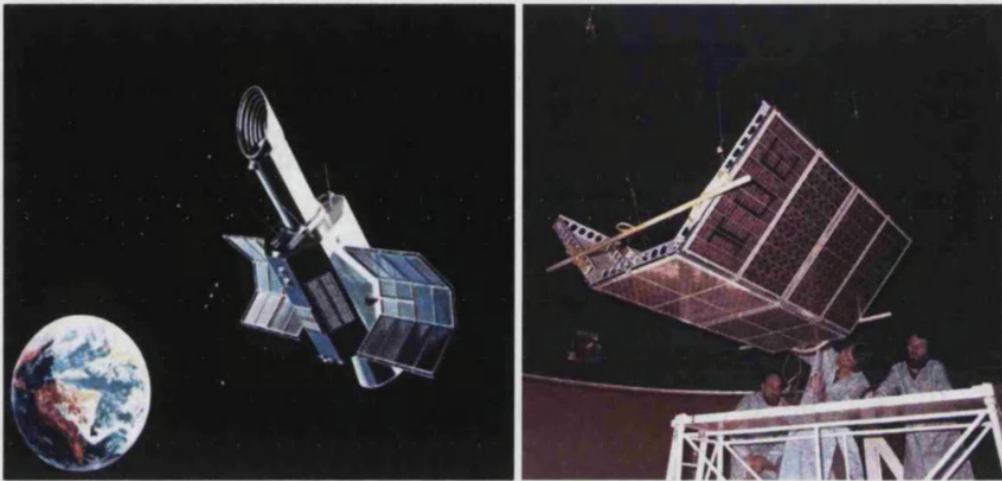


Figure 8.1: **Left:** Artist Impression of the *IUE* satellite orbiting the Earth. **Right:** Image of the solar panel of the satellite during testing.

can be seen in Fig. 8.2. The original spectrum had a resolution of  $0.05\text{\AA}$ , but it was rebinned to a resolution of  $0.1\text{\AA}$  for plotting purposes. The *IUE* spectrum of the O9V standard 10 Lac is also plotted for comparison. It must be noticed that the Si IV line presents very little or no star wind signatures, just like the standard 10 Lac. Walborn and Panek (1984) discuss the luminosity dependence of the Si IV line and reach the conclusion that this line is a very good luminosity indicator. In their analysis they show that main sequence stars show no evidence of wind features at the Si IV line position, which is purely photospheric, on the other hand supergiant stars will show strong P-Cygn profiles at this line. In contrast, the C IV  $\lambda\lambda$  1548.19 1550.76  $\text{\AA}$  and N V  $\lambda\lambda$  1548.19 1550.76  $\text{\AA}$  lines show clear indication of the presence of a strong wind.

Our analysis followed the SEI (Sobolev with Exact Integration of the transfer equation) method, as outlined in Lamers et al. (1987). This method is a modification of the Sobolev approximation to the star wind problem (Sobolev, 1947). As a confirmation of our method we have also made use of a genetic algorithm developed to fit UV lines, based also on the SEI method, and kindly supplied by Leonid Georgiev and Xavier Hernández. They describe the method in Georgiev and Hernández (2005). In all cases the velocity law used was of the form:

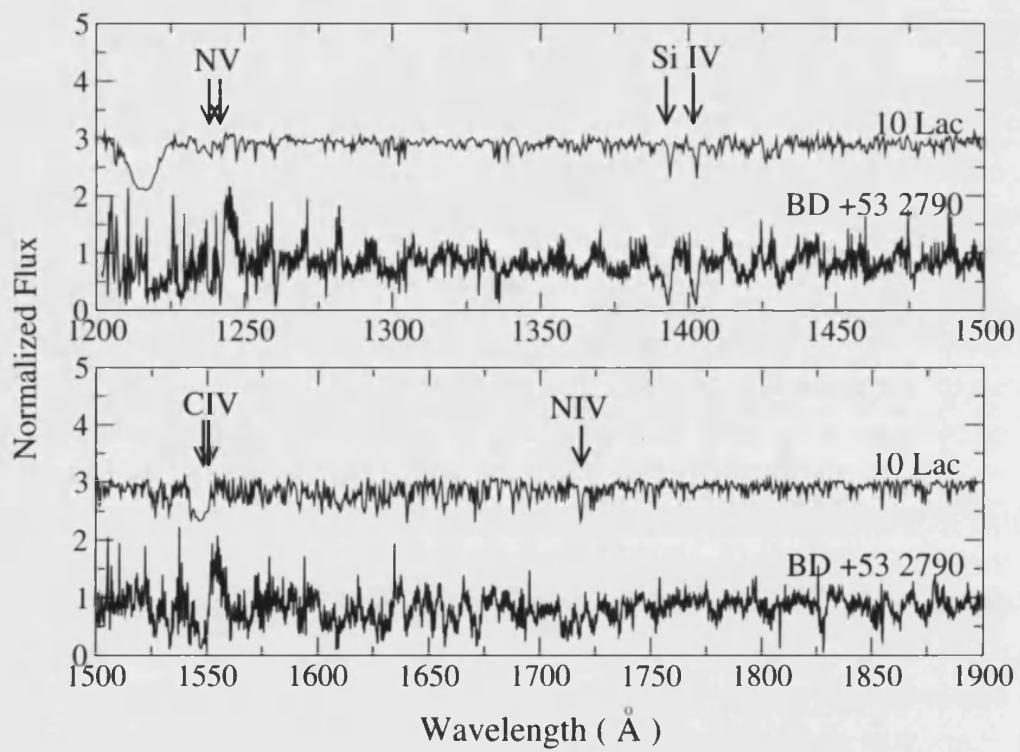


Figure 8.2: UV spectra of BD +53°2790 from 1200 up to 1900  $\text{\AA}$ . The wind resonance lines used in the analysis are marked with arrows.

$$w(x) = w_0 + (1 - w_0) \left(1 - \frac{1}{x}\right)^\beta$$

where  $w$  represents the wind velocity normalised to the terminal velocity ( $v/v_\infty$ ),  $x$  the distance from the photosphere normalised to the stellar radius ( $r/R$ ),  $w_0$  the velocity with which the wind plasma leaves the photosphere normalized to  $v_\infty$  (generally taken as  $w_0 = 0.01$ ) and  $\beta$  is the so-called velocity-law-index.  $\beta$  lies in the range 0.6–1.0 for early-type stars. And the opacity law takes the form:

$$T = \frac{T_{\text{total}}}{I} \left(\frac{w}{w_1}\right)^{\alpha_1} \left\{1 - \left(\frac{w}{w_1}\right)^{\frac{1}{\beta}}\right\}^{\alpha_2}$$

where  $T_{\text{total}}$  represents the integrated opacity at the line position at the photosphere,  $I$  the integrated photospheric spectrum,  $w$  and  $\beta$  have the same meaning as in the velocity law,  $\alpha_1$  and  $\alpha_2$  are the opacity-law indexes, and  $w_1$  is the velocity at which the photons will escape freely without interaction with the stellar wind matter (i.e. represents the point where the opacity goes to zero). Note that in the case of doublets we have two opacities, one for the blue-side line and one for the red-side line.

We created a grid of theoretical profiles with different wind and photospheric parameters and then matched them all against the observed profile. The *IUE* spectrum was previously transformed to a heliocentric frame of reference. The indications from the extensive study of stellar winds by Groenewegen and Lamers (1989) were followed and the parameters listed there were chosen as initial parameters to build our grid of models, though no O9.5V type star is analysed there. The set of parameters which produce a profile as close as possible to the observed one from BD +53°2790 will be the parameters most likely describing the physical conditions of its stellar wind. We found that, in general, terminal velocities above 500 km s<sup>-1</sup> could not produce a theoretical model with a set of parameters consistent with a late O type star. Terminal velocities in the range 300–350 km s<sup>-1</sup> and a turbulent motion with a mean velocity in the range 20–100 km s<sup>-1</sup> yielded line profiles which resulted in the best match against the observed profiles. We show in Fig. 8.3 an example of two UV lines from BD +53°2790, C IV  $\lambda\lambda$  1548.19 1550.76 Å



and N V  $\lambda\lambda$  1238.80 1242.78 Å doublets, matched against two theoretical profiles, calculated for 300 and 350 km s<sup>-1</sup>. For the C IV doublet an upper limit for the turbulent velocity of 80 km s<sup>-1</sup> was found, while for the N V  $\lambda\lambda$  1238.80 1242.78 Å doublet an upper limit of 100 km s<sup>-1</sup> for the turbulent velocity could be set. The other line analysed is the N IV  $\lambda$ 1718.55 Å singlet. All line positions are shown in Fig. 8.2 and all results are summarised in Table 8.1.

Prinja et al (1990) defined  $v_{\text{black}}$  as the point where saturated wind lines turn upwards towards the continuum level. They showed that  $v_{\text{black}}$  is a very good terminal velocity estimator for such lines. They derived a relationship between  $v_{\text{edge}}$  and  $v_{\text{black}}$  for late O and early B-type stars for terminal velocities greater than 600 km s<sup>-1</sup>. They show that  $v_{\text{edge}}$  over-estimates the value of the wind terminal velocity. In Fig. 8.3 we find the approximate position of  $v_{\text{black}}$  for two saturated doublet lines in the UV spectrum of BD +53°2790. Their values are  $\sim$ 260 km s<sup>-1</sup> for the N V doublet and  $\sim$ 290 km s<sup>-1</sup> for the C IV doublet. Within the errors implicit in the procedure followed to fit the line profiles, these values are in very good agreement with the derived 300–350 km s<sup>-1</sup>.

As a cross check to our method, we also tried the automatic fitting procedure of (Georgiev and Hernández, 2005). The fits resulting from their genetic algorithm are shown in Fig. 8.3. For the case of the C IV doublet, a fit yielding a terminal velocity of  $\sim$ 450 km s<sup>-1</sup> and turbulent velocities of  $\sim$ 80 km s<sup>-1</sup> resulted in a good approximation to the observed profile. For the N V line the best fit was found for a terminal velocity of  $\sim$ 300 km s<sup>-1</sup> and a turbulent velocity of  $\sim$ 115 km s<sup>-1</sup>. All the results are summarised in Table 8.1.

Our estimate of the wind terminal velocity is tied to many uncertainties. One of them, as an example, is the determination of the continuum, which is quite critical in the case of the C IV doublet. The normalisation of this spectral range is quite ambiguous, as there can be absorption features produced in the wind material and which do not reflect the actual photospheric continuum. In Fig. 8.3 two continuum normalisations are shown. In the first one (left panels) normalisation was performed by placing the continuum on the top-most data points of the spectrum. In the second one, a set of continuum regions were selected and normalisation was performed through a continuum fit to these regions. As shown in Fig. 8.3 in

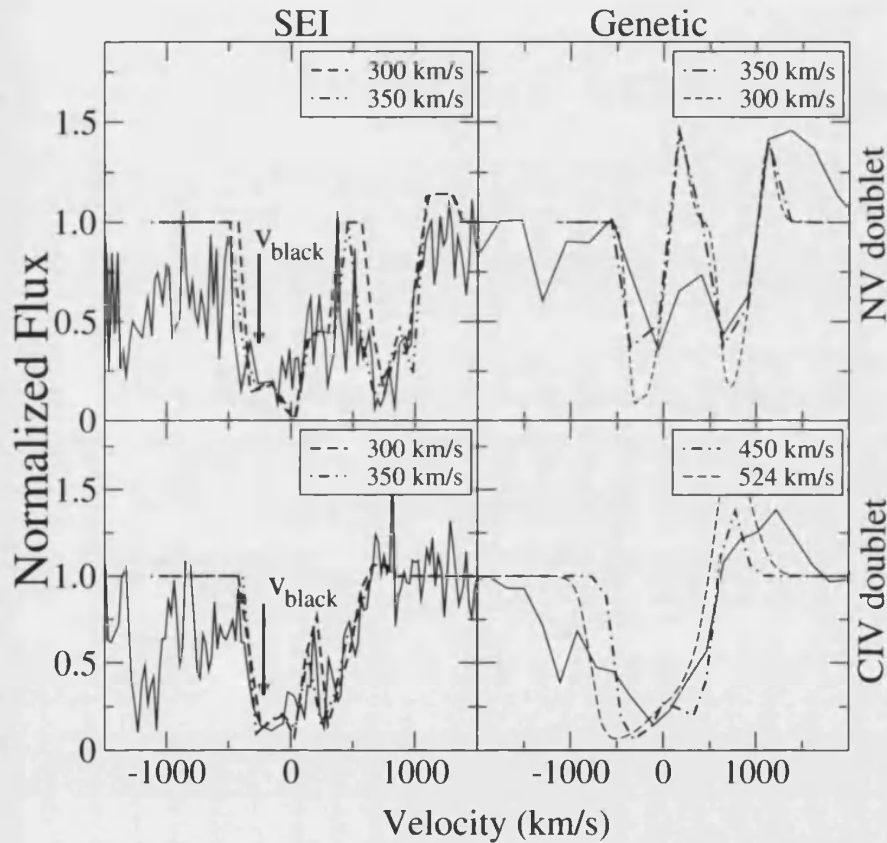


Figure 8.3: **Left panels:** Examples of fits of our models for terminal wind velocities of 300 and 350 km s<sup>-1</sup>, for the two resonance doublets C IV  $\lambda\lambda$  1548.19 1550.76 Å and N V  $\lambda\lambda$  1238.80 1242.78 Å **Right panels:** Fit to the same two doublets by using the genetic algorithm of Georgiev and Hernández (2005). A different normalisation has been used for C IV in both cases to stress its influence on the result, it is one of the main sources of uncertainty. In the case of the genetic algorithm, the resolution of the spectrum was degraded in order to ease and speed up the convergence of the fit.

Table 8.1: Comparison of the best fit parameters obtained by all the methods used to analyse the UV lines.  $v_\infty$  and  $v_{\text{turb}}$  are both given in units of  $\text{km s}^{-1}$ . For the case of doublets the opacity given is that of the red component.

	SEI			Genetic		$v_{\text{black}}$	
	C IV	N IV	N V	C IV	N V	C IV	N V
$v_\infty$	300	300	300	452.74	300	290	260
$v_{\text{turb}}$	80	100	20	80	115.88	–	–
$\beta$	1.0	1.0	1.0	1.5	0.7	–	–
$T_{\text{total}}$	4.5	0.9	18	14.0	8.0	–	–
$\alpha_1$	0.9	1.9	1.8	2.9	0.2	–	–
$\alpha_2$	0.7	0.1	1.5	0.9	0.22	–	–

both cases a similar line width is achieved. Therefore, we are confident that fits to the line width will yield reliable results.

In both sets of fits (SEI and genetic algorithm) terminal wind velocities below  $500 \text{ km s}^{-1}$  are needed to reproduce the observed line widths and positions. An accurate measurement of the terminal wind velocity cannot be given due to the many uncertainties in the procedure and to the poor signal to noise ratio of the *IUE* spectrum.

If the second normalisation is the most appropriate one, it must be noticed that the low wind velocities derived cannot account for the big red excess shown by both C IV and N V doublet lines. It was not possible to fit this excess neither by increasing the wind terminal velocity in the models nor by forcing different wind structure parameters (opacity law). This observational fact can be interpreted as the possible presence of a second wind component of higher velocity. A high velocity polar wind component plus a low velocity equatorial wind component succeeded to explain the observed wind lines in HD 93521 (see Bjorkman et al., 1994). If this excess of red-shifted emission in wind lines is not due to a second velocity component, this would add evidence to the connection of BD +53°2790 with the He-strong class of stars (see the conclusions below in this part).

We can conclude that the terminal wind velocity in BD +53°2790 is

much smaller than expected for an early type star. The mass loss rate expected for BD +53°2790 will be on the order of  $\dot{M} \sim 5 \times 10^{-8}$ , as calculated by the genetic algorithm, taking into account both the velocity and opacity laws, and assuming solar abundances for C IV and N V (on the order of  $\frac{\text{C IV}}{\text{H}} \sim \frac{\text{N V}}{\text{H}} \sim 10^{-4}$ ).

As shown in Ribó et al. (2005), this results is in excellent agreement with the expected wind properties needed to explain the X-ray behaviour of the system, assuming it is composed by a neutron star accreting from the wind of a peculiar late O type star (see the discussion, below in this part).



## Chapter 9

# X-Rays and $\gamma$ -Rays

### 9.1 *INTEGRAL* data.

*INTEGRAL* observed the region around 4U 2206+54 on several occasions during its first year of Galactic Plan Survey scans (GPSs), i.e., from 2002 December to 2004 February. We present in Table 9.1 a summary of all the *INTEGRAL* revolutions during which the source was inside the Field Of View (FOV) of ISGRI. In total, the source was inside the FOV of ISGRI for  $\sim 204$  ks, but it was detected only for 38.2 ks. It must be remembered from the Introduction that a detection is considered good for ISGRI when the detection level, lies above a value of 8. For the typical exposure times of GPS pointings ( $\sim 2$  ks), the sensitivity limit of ISGRI lies around  $2 \text{ count s}^{-1}$  at 40 keV. For revolutions 70, 74, 145 and 189 only an upper limit is given because the source had quite a marginal position in the FOV of ISGRI and the detection is not significant enough. The JEM-X FOV is smaller and thus data were only collected during those revolutions when *INTEGRAL* pointed close enough to the source (marked in Table 9.1 with the † symbol). Only a few pointings in 2003 May and June fulfil this requirement. Although SPI has the largest FOV, it cannot acquire enough information with one exposure due to the detector design. To achieve a  $S/N \sim 10$  for a source like 4U 2206+54, SPI would need around 300 ks. Nevertheless, using SPIROS in TIMING mode (see Skinner and Connell, 2003) a light curve has been obtained in the 20–40 keV energy range. The obtained flux values are in good agreement with the ISGRI data, but they

have larger uncertainties. Therefore, no data from SPI have been used in this analysis. Data reduction has been performed as outlined in Chapter 2.

## 9.2 *RXTE* data

The Rossi X-ray Timing Explorer (*RXTE*) combines a very good time resolution with a moderate spectral resolution to explore the variability of X-ray sources. Time scales from microseconds to months are covered in an instantaneous spectral range from 2 to 200 keV. The mission carries two pointed instruments, the Proportional Counter Array (PCA) which covers the lower part of the energy range (2–60 keV), and the High Energy X-ray Timing Experiment (HEXTE) covering the upper energy range (20–200 keV). In addition, *RXTE* carries an All-Sky Monitor (ASM) that scans about 80% of the sky every orbit, allowing monitoring on timescales of 90 minutes or longer. For a complete description of the instrument see Bradt et al. (1993).

*RXTE*/ASM data of 4U 2206+54 was retrieved from the online archive<sup>1</sup>. Archival *RXTE*/PCA data from March 11–12 1997 and October 12–20 2001 were also retrieved. The durations of these observations range from 17.7 to 29.8 ks and the complete integration time spans  $\sim 100$  ks. A more detailed description of these observations is given in Torrejón et al. (2004).

## 9.3 Timing

Analysis of the X-ray lightcurves clearly shows that the source is variable on all timescales. However, except from the 9.6 d modulation observed in *RXTE*/ASM data (see Corbet and Peele, 2001; Ribó et al., 2005, and subsection 7.1.5) and believed to be the orbital period, no periodic variability has been detected so far. Unfortunately, the *INTEGRAL* coverage of the source is not long enough to test the presence of this periodicity. Ribó et al. (2005) performed a very detailed timing analysis of *RXTE*/ASM data and refined the orbital period to a value of  $9.5591 \pm 0.0007$  d.

---

<sup>1</sup><http://xte.mit.edu/asmlc/>

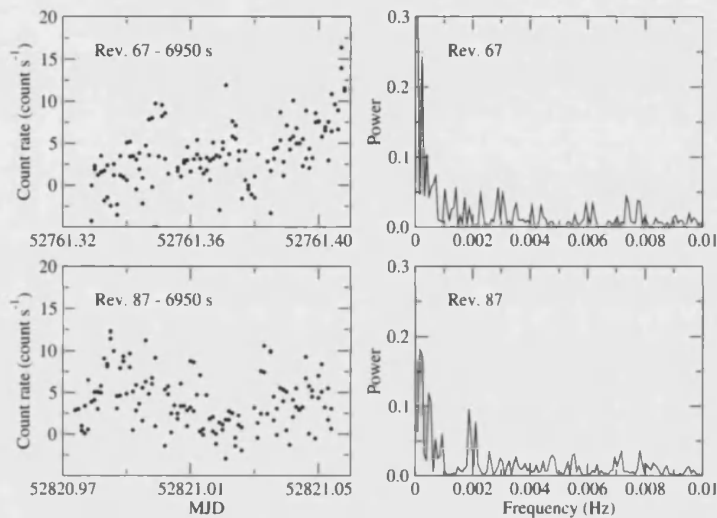


Figure 9.1: ISGRI lightcurves of 4U 2206+54 in the energy range 20–40 keV binned to 50 s (left) and associated power spectra (right) for a time span equivalent to 3 *INTEGRAL* science windows (around 6950 s) during revolutions 67 (top panels) and 87 (bottom panels).

Pulse period analysis gave negative results for both our ISGRI and JEM-X datasets. This was expected, as previous searches on similar timescales had also failed (see Negueruela and Reig, 2001; Corbet and Peele, 2001; Torrejón et al., 2004; Masetti et al., 2004).

ISGRI data from consecutive pointings were joined together when possible and rebinned to 50 s to search for possible longer periods. Nothing was found up to timescales of  $\sim 1$  h. The 20–40 keV lightcurve and power spectrum for a time-span of 6950 seconds during revolutions 67 and 87 can be seen in Fig. 9.1. The difference between the two lightcurves and between the corresponding power spectra is apparent. A quasi-periodic feature at  $\sim 0.002$  Hz ( $\sim 500$  s) can be seen in data from revolution 87, but it is not present at other epochs. The timing behaviour of the source seems to be different in every pointing.

Little attention has been paid so far to intermediate periods (of the order of hours), perhaps because intermediate periods would be difficult to detect in the *RXTE*/ASM data, especially when points are filtered and rebinned as one day averages to keep statistical significance. We therefore searched the *RXTE*/PCA lightcurves described in the previous



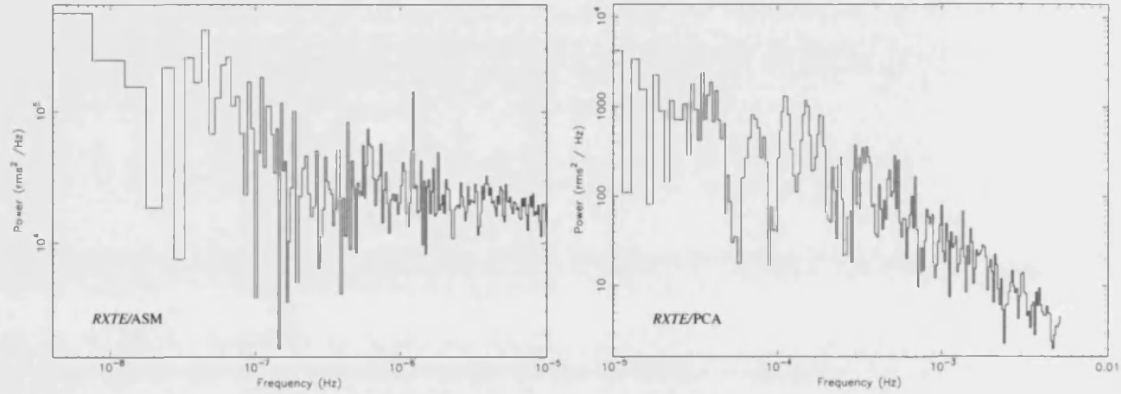


Figure 9.2: **Left:** Power spectrum of the *RXTE*/ASM lightcurve, binned to 25 ks intervals. Note the feature detected at a frequency of  $\simeq 1.2 \times 10^{-6}$  Hz, which corresponds to the orbital period (see Corbet & Peele 2001). No other period is found at the limit of the lightcurve resolution. **Right:** Power spectrum of the 100 ks *RXTE*/PCA lightcurve, binned to 96 s intervals. No significant period is detected in the interval  $[0.95-5.5] \times 10^{-4}$  Hz, which corresponds approximately to the interval from 3 hours to 30 minutes. The slope of the power spectrum is  $\sim \nu^{-0.8}$ , where  $\nu$  is the frequency.

section for intermediate period pulsations to test the possible presence of a slowly rotating neutron star. Unfortunately, the gaps due to the satellite low-Earth orbit are rather large in comparison to the periods searched, which certainly hampers somewhat the search. We used epoch folding and Lomb-Scargle periodogram techniques with negative results. We show in Fig. 9.2 the power spectrum analysis of the whole time span. Apart from the orbital period No significant period is detected, particularly in the interval  $[0.95-5.5] \times 10^{-4}$  Hz, which corresponds to periods from 3 hours to 30 minutes, approximately.

We found some periodicities searching inside individual observations, although with low significance. Inside the *RXTE*/PCA 60071-01-03 observation we find a possible period of 6895.902 s while in observation 60071-01-04 we find 8619.858 s. Folding the entire lightcurve on either of these periods results in no pulsed signal. We conclude therefore that the analysis of the entire lightcurve does not deliver any significant period in the range explored. This result leaves only the possibility of a period in the

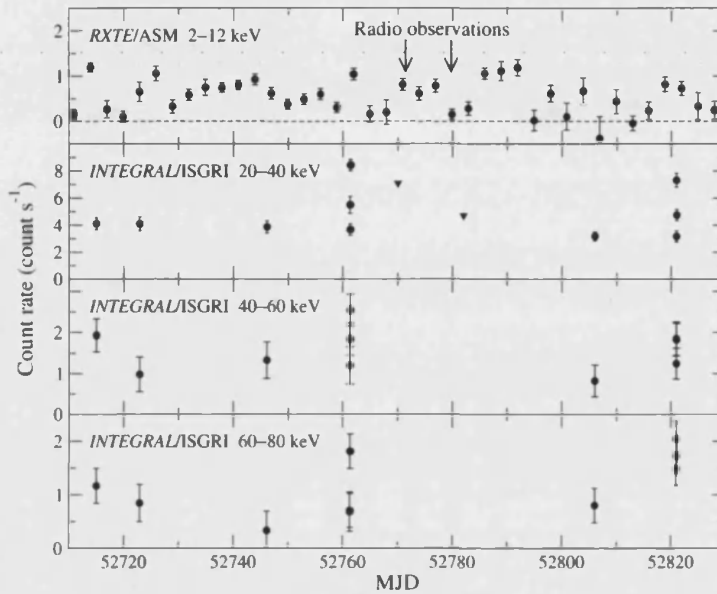


Figure 9.3: Lightcurves of 4U 2206+54 in different energy bands (quoted inside the different panels). The top panel is for the 3-day average of the *RXTE*/*ASM* data, where the arrows indicate the epochs of the radio observations. The three bottom panels are for the *INTEGRAL*/*ISGRI* data in intervals of  $\sim 2$  ks. Error bars represent the mean of the 1-day average data errors for *RXTE*/*ASM* data and the formal errors for *INTEGRAL*/*ISGRI* data. The two triangles in the 20–40 keV lightcurve indicate  $3\sigma$  upper limits.

range from some hours to 1 d to be explored. In order to do this, a long observation with a high Earth orbit satellite, like *INTEGRAL*, would be required.

We show in Fig. 9.3 the long-term lightcurves of 4U 2206+54 in different energy ranges, from the 2–12 keV of the *RXTE*/*ASM* data up to 80 keV for the *ISGRI* data, spanning 120 d. As can be seen in the 20–40 keV lightcurve, an increase in brightness occurred during revolution 67 (MJD 52761.36). The source brightness increased threefold over a time span of the order of half an hour (see also the top left panel in Fig. 9.1).

## 9.4 Spectral Analysis

From the whole time span during which ISGRI collected data from the HMXRB 4U 2206+54, the source was inside both, the Fully Coded Field Of View (FCFOV) of ISGRI and the JEM-X FOV, only during one pointing in revolution 67 and 3 pointings in revolution 87. Therefore, the available spectrum from revolution 67 and the mean spectrum from revolution 87 were used for the spectral analysis. Systematic errors of 10% for ISGRI and 5% for JEM-X were added to our data sets<sup>2</sup>. The software package used was XSPEC 11.2 (Arnaud 1996).

With the aim of comparing with previously published data, the comptonisation model of Sunyaev & Titarchuk (1980), improved by Titarchuk (1994) including relativistic effects, implemented in XSPEC as `compTT`, and a powerlaw model, modified to include photon absorption and a high energy cut-off, were chosen to fit the data. For the comptonisation model, the emitting region temperatures derived were  $10 \pm 3$  and  $13 \pm 8$  keV for the data of revolutions 67 and 87, respectively. The fits were acceptable, with corresponding  $\chi^2_{\text{Red}}$  of 1.3 for 173 degrees of freedom (DOF) in the first case, and  $\chi^2_{\text{Red}}$  of 1.2 for 176 DOF in the second one. The powerlaw parameters of both observations are listed in Table 9.2.

Both models yield a 4–150 keV flux of  $\sim 16 \times 10^{-10}$  erg s<sup>-1</sup> cm<sup>-2</sup> for revolution 67 and  $\sim 8 \times 10^{-10}$  erg s<sup>-1</sup> cm<sup>-2</sup> for revolution 87. Assuming a distance to the source of 2.6 kpc, its luminosity amounts to  $\sim 1.1 \times 10^{36}$  erg s<sup>-1</sup> and  $\sim 0.6 \times 10^{36}$  erg s<sup>-1</sup>, respectively. Around  $\sim 50\%$  of the total flux lies in the 4–12 keV energy band, that is  $\sim 5.5 \times 10^{35}$  erg s<sup>-1</sup> for revolution 67 and  $\sim 3.0 \times 10^{35}$  erg s<sup>-1</sup> for revolution 87. We notice that during these observations the source appears brighter than in any previous observation. The *RXTE*/ASM lightcurve confirms that the flux was high in the 2–12 keV band as well.

We show in Fig. 9.4 the *INTEGRAL* spectra of 4U 2206+54 for revolutions 67 and 87. Both spectra suggest the presence of an absorption feature around  $\sim 30$  keV, as already noticed by Torrejón et al. (2004) and Masetti et al. (2004) in *RXTE* and *BeppoSAX* data. An absorption fea-

<sup>2</sup>Private communication from instruments teams, see also each instrument *Scientific Validation Report* at ISDC web pages: <http://isdc.unige.ch/index.cgi?Support+documents>

ture through the `cyclabs` model (in XSPEC notation) was added to the powerlaw model. In the revolution 67 spectrum, the absorption feature was fitted at an energy of  $32\pm 5$  keV for a fixed line width of 3 keV (see Torrejón et al., 2004; Masetti et al., 2004). The same feature is apparent in the spectrum from revolution 87, where it was fitted at  $32\pm 3$  keV. These values are in agreement with those of the absorption features already proposed by Torrejón et al. (2004) and Masetti et al. (2004), see Table 9.2. An F-test was applied to the spectral fits of revolution 87, which has a better signal to noise ratio than that of revolution 67. The improvement of the  $\chi^2$  by the inclusion of a `cyclabs` component has a 12% probability of occurring by chance (this is an indication that the inclusion of the `cyclabs` component to the model does not yield a significant improvement in the fit, i.e., the detection of the absorption feature is not significant enough). One should take into account the limitations of this test when applied to lines (Protasov et al. 2002). The significance of the Cyclotron Resonance Scattering Feature (CRSF) detection cannot be derived from the individual analysis of revolutions 67 and 87, due to the poor improvement of the statistics obtained when adding the CRSF component in both cases. We can only state the significance of the detection after the improvement in the signal-to-noise ratio achieved with the mosaicking of *INTEGRAL*/ISGRI images, this will be shown later on in this section.

Except for the normalisation factors, the fitted parameters to the datasets of both revolutions are compatible within the errors (see Table 9.2).

Table 9.1: Summary of ISGRI observations of the field around 4U 2206+54 during the *INTEGRAL* GPS. We list the revolution number, the intervals of time when the source was in the FOV of ISGRI during these revolutions in Modified Julian Days, the total on-source time within these intervals, the amount of time in which the source was detected, the mean count rate and its formal error obtained in the 20–40 keV energy range and the detection level value given by the software package. For revolutions 70, 74, 145 and 189 (with significances between  $1\sigma$  and  $3\sigma$ ), we give  $3\sigma$  upper limits. The † symbol indicates JEM-X detections.

Rev.	MJD	On-source time (ks)	Mean count rate (count s <sup>-1</sup> )	Detection level
26	52638.43–52640.07	14	—	—
31	52653.32–52655.90	12	—	—
47	52701.15–52701.27	8	—	—
51	52714.85–52714.96	8	4.1±0.4	9.0
54	52722.85–52722.93	6	4.1±0.4	8.0
55	52727.64–52727.67	4	—	—
59	52737.03–52737.10	4	—	—
62	52746.01–52746.04	10	3.9±0.4	8.6
67†	52761.26–52762.45	8	5.9±0.5	12.6
70	52769.93–52770.10	12	< 7.1	4.1
74	52781.92–52782.12	14	< 4.7	2.7
79	52796.88–52797.07	14	—	—
82	52805.94–52806.15	14	3.2±0.3	9.5
87†	52820.92–52821.08	12	5.1±0.4	11.2
92	52835.84–52836.00	12	—	—
142	52985.44–52985.60	12	—	—
145	52994.41–52994.62	12	< 7.6	2.9
153	53019.25–53019.45	14	—	—
162	53045.49–53045.69	14	—	—
177	53090.55–53091.48	16	—	—
181	53102.88–53103.05	15	—	—
185	53114.56–53114.70	13	—	—
189	53126.47–53126.63	15	< 4.4	4.8
193	53138.39–53138.42	4	—	—
202	53165.48–53165.67	15	—	—
210	53189.33–53189.51	15	—	—
229	53246.96–53247.13	15	—	—
233	53258.01–53258.80	8	—	—
234	53260.99–53261.92	17	—	—

Table 9.2: Comparison of published powerlaw+high-energy cutoff parameters, adding photon absorption at lower energies, for 4U 2206+54. We remit the reader also to tables 2, 3, and 4 of Saraswat & Apparao (1992) for earlier *EXOSAT* data. All fluxes shown are unabsorbed in the quoted energy ranges. The errors are at 68% confidence level for the entry of Negueruela & Reig (2001) and at 90% confidence level for the rest of the data except for the entry of Corbet & Peele (2001), where significance levels were not reported. Flux is given in units of  $\times 10^{-10}$  erg s $^{-1}$  cm $^{-2}$

Ref. (Mission, year)	$\Gamma$	$E_{\text{cut}}$ (keV)	$E_{\text{fold}}$ (keV)	$N_{\text{H}} \times 10^{22}$ (atom cm $^{-2}$ )	$\chi_{\text{Red}}^2$ (DOF)	Flux	Energy range (keV)
Negueruela & Reig 2001 ( <i>RXTE</i> , 1997)	1.7 $\pm$ 0.3	7.4 $\pm$ 0.2	17.5 $\pm$ 0.8	4.7 $\pm$ 0.2	0.9(56)	4.8	2.5–30
Corbet & Peele 2001 ( <i>RXTE</i> , 1997-1)	1.71 $\pm$ 0.03	7.3 $\pm$ 0.1	17.3 $\pm$ 0.6	4.6 $\pm$ 0.2	0.82	3.1	2–10
( <i>RXTE</i> , 1997-2)	1.12 $\pm$ 0.12	5.3 $\pm$ 0.2	10.5 $\pm$ 1.2	2.7 $\pm$ 0.7	0.75 <sup>a</sup>	1.1	2–10
Torrej3n et al. 2004 ( <i>RXTE</i> , 1997)	1.6 $\pm$ 0.1	7.6 $\pm$ 0.4	16.3 $\pm$ 1.2	4.5 $\pm$ 0.4	0.71(52)	2.7	2–10
( <i>RXTE</i> , 2001)	1.6 $\pm$ 0.1	4.3 $\pm$ 0.3	20 $\pm$ 2	4.6 $\pm$ 0.1	1.27(49)	1.3	2–10
( <i>BeppoSAX</i> , 1998)	1.0 $\pm$ 0.2	7.8 $\pm$ 0.5	11 $\pm$ 3	1.1 $\pm$ 0.3	1.32(113)	0.4	2–10
Masetti et al. 2004 ( <i>BeppoSAX</i> , 1998)	0.95 $^{+0.11}_{-0.14}$	4.3 $^{+0.6}_{-0.5}$	10.6 $^{+2.7}_{-2.0}$	0.88 $^{+0.21}_{-0.19}$	1.1(219)	0.4	2–10
This work ( <i>INTEGRAL</i> , 2003, Rev. 67)	1.8 $\pm$ 0.7	13 $\pm$ 5	22 $\pm$ 6	1.0 (fixed)	1.2(154)	15.9	4–150
Rev. 87	1.7 $^{+0.3}_{-0.4}$	11 $\pm$ 5	29 $^{+8}_{-7}$	1.0 (fixed)	1.0(153)	8.3	4–150

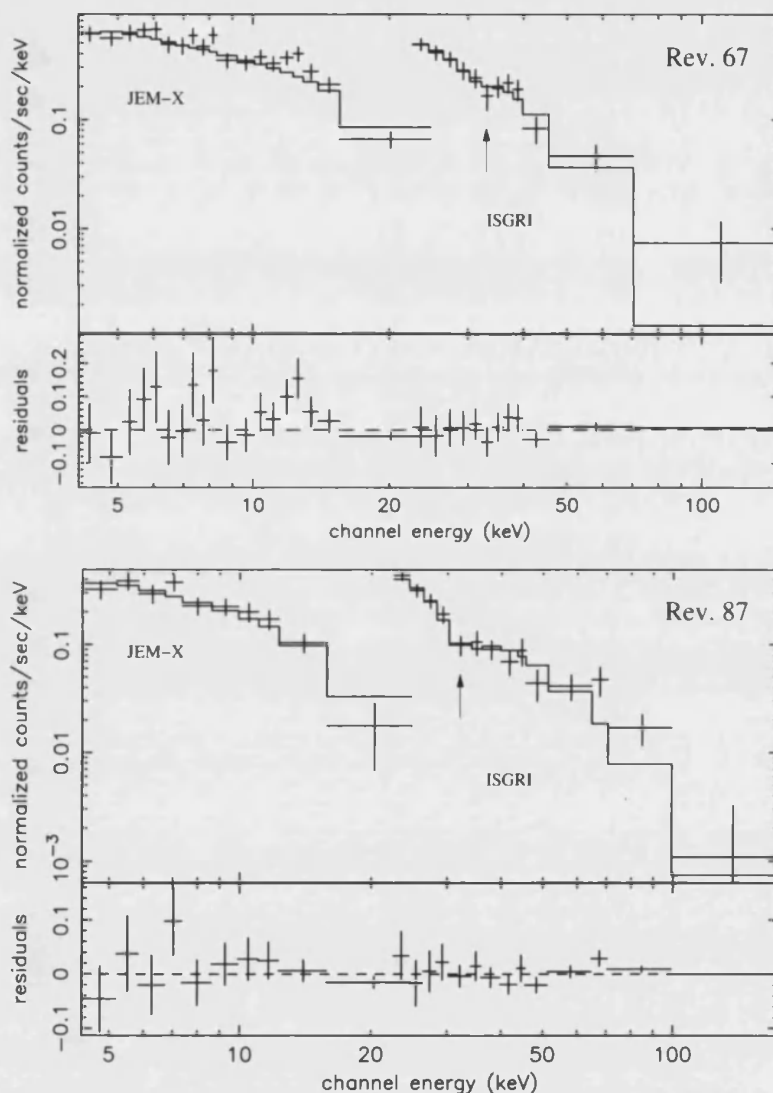


Figure 9.4: Spectra of 4U 2206+54 from JEM-X and ISGRI detectors. **Top:** The spectrum shown is for 2.2 ks of exposure time during revolution 67 (MJD 52761.36). **Bottom:** The spectrum shown is for 6.6 ks of exposure time during revolution 87 (MJD 52821.17). In both cases the spectral model shown in Table 9.2 (i.e. a powerlaw modified by a cutoff, with photo-absorption and the `cyclabs` component) is represented by the solid line, and the residuals to the model are displayed in the lower panels. The presence of an absorption feature around 32 keV, indicated by arrows, is suggested by the two datasets.

There are well known calibration problems in the ISGRI Response Matrix Function (RMF) that may cast some doubts about the reality of the absorption feature reported here. In order to investigate if this feature is an instrumental effect, we normalised the 20–60 keV spectra of 4U 2206+54 and the Crab to their respective continua modelled by a powerlaw, and then divided the normalised 4U 2206+54 spectrum over that of the Crab. We have chosen a Crab observation as close in time as possible to our data and with similar off-axis angles, to ensure that the RMF and off-axis effects are as much similar as possible. We show in Fig. 9.5 the observed spectra (top panel), their ratio to the powerlaw model (middle panel), and the ratio between the former ratios (bottom panel). The absorption feature around 32 keV is still seen. The quality of the data does not allow us to state that the detection is statistically significant, but the likely presence of a feature at this position had already been reported in the analysis of two other independent datasets obtained by two different satellites (see Table 9.2). As it has been seen by three different instruments at different times, the existence of this absorption feature is strongly suggested. Such features in X-ray spectra are generally attributed to CRSFs (see, e.g., Coburn et al. 2002 and references therein).

Motivated by the possible presence of this CRSF, we have summed up images from those *INTEGRAL* revolutions with positive ISGRI detections. The effective exposure time of this mosaic amounts to  $\sim 27$  ks, and we show its extracted spectrum in Fig. 9.6. We note that spectral shape changes with luminosity have been reported in Saraswat and Apparao (1992) and Negueruela and Reig (2001). Therefore, by summing up data taken on different epochs we might be losing spectral shape information. However, our goal is not to study the shape of the continuum, but to achieve an improved signal to noise ratio at the CRSF position, which is suggested by both the revolution 67 and revolution 87 spectra to be at  $\sim 32$  keV. The best fit to the continuum of the new spectrum was a comptonisation model of soft photons by matter undergoing relativistic bulk-motion, i.e. `bmc` in XSPEC notation (Shrader and Titarchuk, 1999), which provided a  $\chi^2_{\text{Red}}$  of 1.7 for 6 degrees of freedom (see top panel in Fig. 9.6). We fitted a `cyclabs` absorption feature (representing a CRSF) at  $32 \pm 2$  keV to the `bmc` model, and obtained a slightly improved fit with  $\chi^2_{\text{Red}}$  of 1.3 for 5 degrees of freedom. Finally, we also fitted the data by adding a



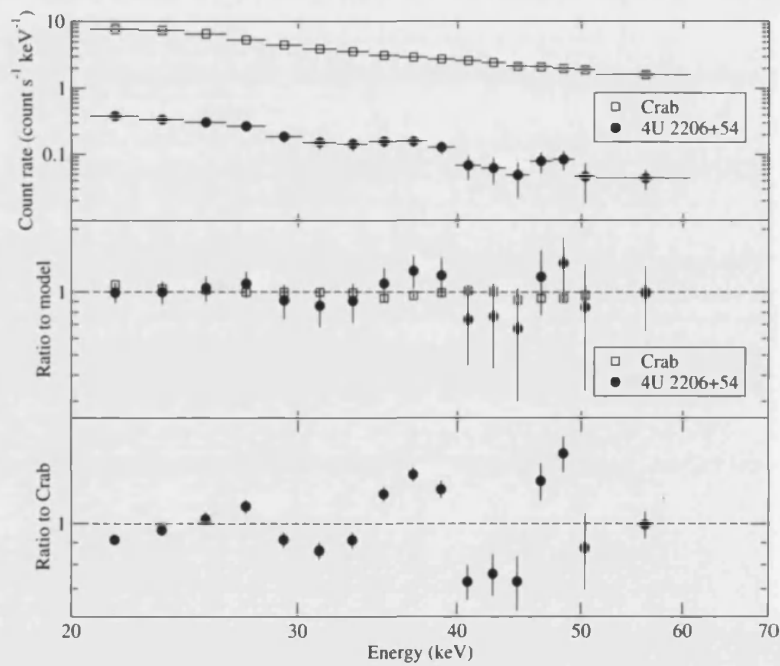


Figure 9.5: Observed ISGRI spectra of the Crab and 4U 2206+54 (top panel), their ratio to the powerlaw model (middle panel), and the ratio of 4U 2206+54 to that of the Crab for the former ratios. The variations above 40 keV are not smooth, but random, and show large errors, indicating that they reflect most likely extraction problems due to the fact that we are approaching the sensitivity limit of ISGRI (around  $\sim 0.04$  count  $s^{-1}$  keV $^{-1}$  for 2 ks exposures and  $3\sigma$  level detection at 45 keV).

Lorentzian profile in absorption to the *bmc* model. In this case the  $\chi^2_{\text{Red}}$  went down to 1.1 for 5 degrees of freedom (see bottom panel in Fig. 9.6). The centre of the line was located at  $31.5 \pm 0.5$  keV and its FWHM was found to be  $0.015 \pm 0.005$  keV. The normalisation of the line,  $1.5^{+0.7}_{-0.8} \times 10^{-3}$  count  $\text{s}^{-1}$  keV $^{-1}$  at a 68% confidence level ( $1\sigma$ ), yields a significance of the line of  $\sim 2\sigma$ . Thus we can conclude that the presence of a CRSF is strongly suggested by our data. In our opinion, this result, when combined with the previous claims after *BeppoSAX* and *RXTE* data (Torrejón et al., 2004; Masetti et al., 2004) gives evidence for the presence of this CRSF in 4U 2206+54.

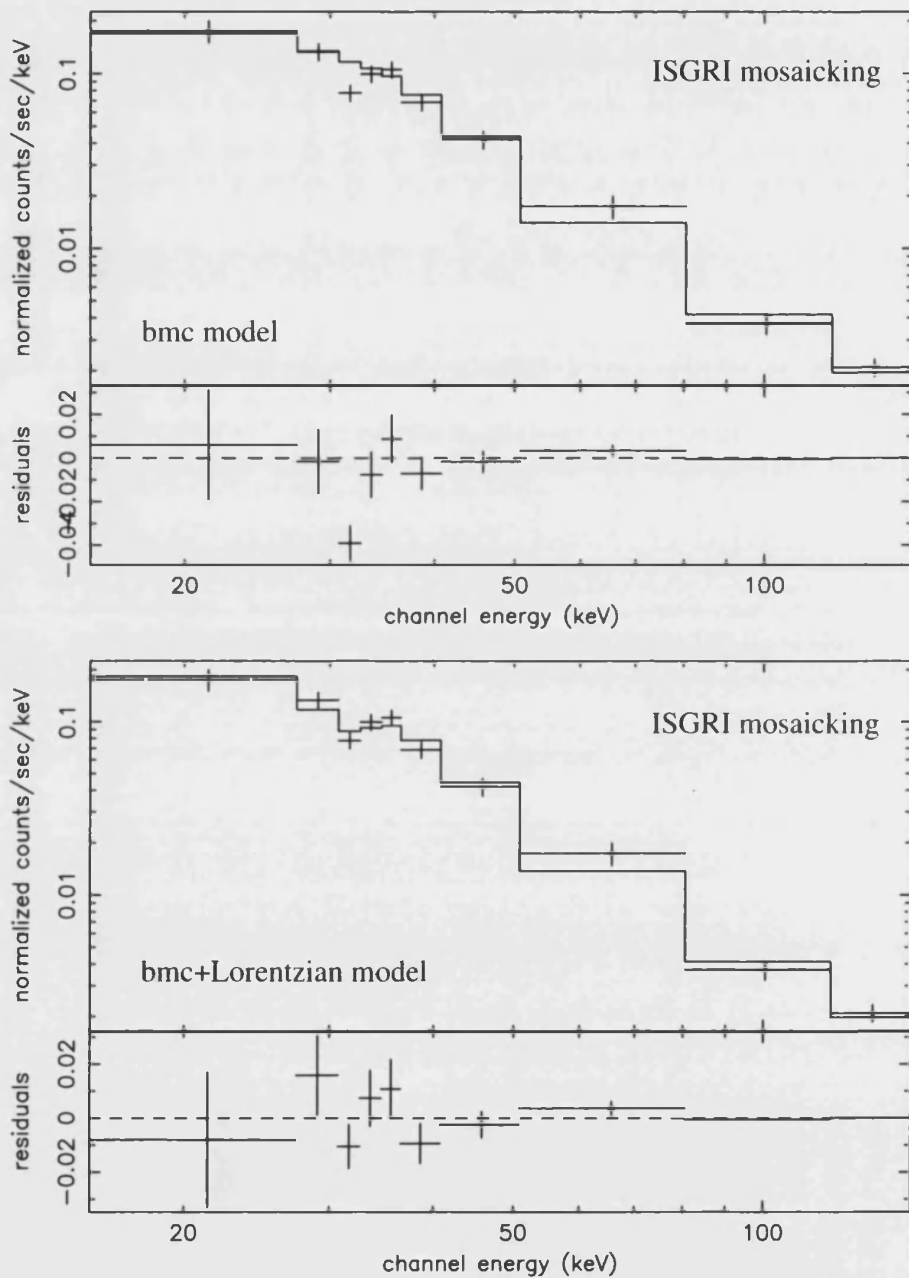


Figure 9.6: Spectrum of 4U 2206+54 extracted from the mosaicking of all images with positive detections from ISGRI. **Top:** The solid line represents the **bmc** model (in XSPEC notation) fitted to the data. An absorption feature around 32 keV is seen in the residuals. **Bottom:** The solid line represents the **bmc** model plus a Lorentzian feature in absorption, yielding a line position of  $31.5 \pm 0.5$  keV.

# Chapter 10

## Discussion

### 10.1 The optical counterpart to 4U 2206+54

#### 10.1.1 Why BD +53°2790 is not a classical Be star

Since its identification with 4U 2206+54, BD +53°2790 has always been considered a classical Be star, because of the presence of shell-like emission lines in the red part of its spectrum. However, the main observational characteristics of BD +53°2790 differ considerably from those of a classical Be star:

- The H $\alpha$  emission line presents a permanent (at least stable during 15 years)  $V < R$  asymmetry. Changes in the  $V/R$  ratio are not cyclical, as in classical Be stars undergoing  $V/R$  variability because of the presence of global one-armed oscillations (see Okazaki, 2000). Moreover, the asymmetry survives large changes in all the other parameters of the emission line and is also present when there is basically no emission, which in a classical Be star would correspond to a disc-less state. This behaviour is fundamentally different from that seen in Be/X-ray binaries, where discs undergo processes of dispersion and reformation during which they develop instabilities that lead to long-term quasi-cyclical  $V/R$  variability (e.g., Negueruela et al. 2001 and Reig et al. 2000).
- In BD +53°2790 we observe strong night-to-night variability in both the shape and intensity of the H $\alpha$  emission line. These variations

affect both the strength of the emission peaks and the depth of the central absorption component. If the emission line did arise from an extended quasi-Keplerian disc (as in Be stars), such variations would imply global structural changes of the disc on timescales of a few hours and/or major changes in the intrinsic luminosity of the O star. Such behaviour is unprecedented in a Be star, where the circumstellar disc is believed to evolve on viscous timescales, on the order of months (Lee et al. 1991; Porter 1999).

- Be stars display a clear correlation between the EW of  $H\alpha$  and the infrared excess and between the infrared magnitudes and infrared colours, which reflect the fact that emission lines and infrared excess are produced in an envelope that adds its emission to that of the star, e.g., Dachs and Wamsteker (1982). Such correlations are not readily detected in BD +53°2790. The evolution of observables (both IR magnitudes and  $H\alpha$  line parameters) lacks any clear long-term trends. The star's properties may be described to be very variable on short timescales and very stable on longer timescales, without obvious long-term variations (except for, perhaps, the  $(J - K)$  colour).
- Photometrically, Be/X-ray systems are characterised by large variations in both magnitudes and (to a lesser extent) colours (e.g., Negueruela et al. 2001; Clark et al. 1999 and Clark et al. 2001b), associated with the periods of structural changes in their circumstellar discs. In contrast, the magnitudes and colours of BD +53°2790 remain basically stable, with small random fluctuations, as is typical of isolated O-type stars.

As a matter of fact, the only High-Mass X-ray Binary presenting some similarities to BD +53°2790 in its photometric behaviour is LS 5039 (RX J1826.2–1450). As BD +53°2790, it displays little variability in  $UBV$  and moderate variability in the infrared magnitudes, see Clark et al. (2001a). RX J1826.2–1450 is believed to be, like 4U 2206+54, powered by accretion from the wind of a main-sequence O-type star, see McSwain and Gies (2002), Ribó et al (1999), Reig et al. (2003) and Casares et al. (2005).

### 10.1.2 What is BD +53°2790?

We estimate that the most likely spectral classification of BD +53°2790 is O9.5Vp. However some remarkable peculiarities have been noticed: while the blue spectrum of BD +53°2790 suggests an O9.5 spectral type, there are a few metallic lines reminding of a later type spectrum (see NR01); the UV lines support the main sequence luminosity classification, but the Paschen lines resemble those of a supergiant.

Comparison of the helium profiles with those artificially broadened from 10 Lac shows that the observed helium profiles in BD +53°2790 are stronger than what is expected for a normal O9.5V star. The strength of the He lines suggests the possibility that BD +53°2790 may be related to the He-strong stars. These are a small group of stars, with spectral types gathered around B2 V, that show anomalously strong helium lines. A well known O-type star believed to be related to He-strong stars is  $\theta^1$  Ori C, which is known to vary in spectral type from O4 to O7 (Donati et al. 2002, Smith & Fullerton 2005). BD +53°2790 could be the second representative of this kind of objects among O-type stars. He-strong stars display a remarkable set of peculiarities: oblique dipolar magnetic fields, magnetically controlled winds, and chemical surface anomalies, among others. Usually this kind of stars are distributed along the ZAMS (Pedersen & Thomsen, 1977; Walborn, 1982; Bohlender et al. 1987; Smith & Groote 2001).

A rich variety of phenomena have been observed in these objects:

- UV:
  1. Red shifted emission of the C IV and Si IV resonance lines (sometimes variable).
- Optical:
  1. Periodically modulated H $\alpha$  emission.
  2. High level Balmer lines appear at certain rotational phases.
  3. Periodically modulated variability in He lines, sometimes emission at He II  $\lambda$ 4686 Å.
- Photometric variability:

### 1. Eclipse-like light and colour curves.

Except for the periodic modulation of the variations, BD +53°2790 shares many of these peculiarities. In particular, together with the apparent high helium abundance, BD +53°2790 shows variable H $\alpha$  emission and He II  $\lambda$ 4686 Å emission, the UV spectrum shows apparently prominent P-Cygni profiles at C IV and Si IV resonance lines (see NR01) but in contrast a wind slower than expected is found (see chapter 8), which can be an indication of some red-shifted excess of emission at these lines. In He-strong stars the wind is conducted along the magnetic field lines into a torus-like envelope located at the magnetic equator. This configuration can lead to the presence of double emission peaks in H $\alpha$ , which resemble those seen in BD +53°2790, but which usually show modulation with the rotational period. The complexity and shape of the double peak will depend on the angle between magnetic and rotational axes and the line of sight to the observer (see Townsend and Owocki, 2005).

A rotationally dominated circumstellar envelope is clearly present in BD +53°2790, as indicated by the infrared magnitudes, the emission in Balmer and some helium lines and the correlations between H $\alpha$  line parameters. However the structure of this circumstellar envelope differs clearly from those seen in Be stars. Following the analogy with He-strong stars, the existence of a circumstellar disk-like structure is common to these type of objects also. The only difficulty to accept BD+53°2790 as a He-strong star is the apparent lack of rotational modulation of the emission lines parameters. Given the rotational velocities derived, we could expect a rotational period of a few days. In addition to the commented problems of the very diverse origin of our data, the sampling of our measurements is not adequate to find variations on timescales of a few days (modulated with the rotational period), thus we cannot discard yet the presence of rotational periodicity. The idea of a magnetically driven wind contributing to a dense disk-like structure is not strange even in the field of Be stars' circumstellar envelopes. The wind compressed disk of Bjorkman & Cassinelli (1993) was shown to be compatible with observations only with the presence of a magnetic field (on the order of tens of Gauss) driving the wind from the polar caps onto the equatorial zone (Porter 1999).

A careful inspection to the correlation seen in Fig. 7.7 between the He I  $\lambda$ 6678 and H $\alpha$  EWs shows that there is a common component to

the emission of both lines.  $H\alpha$  emission, then, will have at least two contributions: a P-Cygni like contribution (as seen in the 1992 spectra, see Fig. 7.4, where the double peak structure disappeared and only the red peak survives) and an additional variable double peaked structure. The relative variation of both components may be hiding whatever periodic modulations could be present.

Therefore, we can conclude that this is a very peculiar O9.5V star where most likely a global strong magnetic field may be responsible for most of the behaviour seen so far.

## 10.2 The compact object in 4U 2206+54

### 10.2.1 Conflicts in the neutron star scenario

The aperiodic variability of the X-ray emission from 4U 2206+54 favours the idea that the X-ray source is powered by wind-fed accretion onto a compact object. The luminosity of the source combined with its spectral shape likely excludes the possibility of a white dwarf (see, e.g., de Martino et al. 2004 for white dwarf spectra). The compact object must be, therefore, a neutron star or black hole.

There are two main difficulties for accepting 4U 2206+54 as a typical wind-accreting neutron star. The first one is the lack of pulsations, as most other wind-fed systems are X-ray pulsars. In principle, this might result from a geometrical effect: if the angle between the spin axis and the magnetic axis of the neutron star is close to zero or the whole system has a very low inclination angle, all the high-energy radiation seen could be coming from a single pole of the neutron star. The system inclination is unlikely to be very small, as the projected  $v \sin i$  for the optical companion is not particularly small (see Negueruela and Reig, 2001, and subsection 7.1.3 where we estimated  $v \sin i \sim 315 \pm 70 \text{ km s}^{-1}$ ), unless there is a very strong misalignment between the rotation axis of the optical star and the orbit. However, if the angles between the spin and magnetic axes of neutron stars are drawn from a random distribution, there is a non-negligible chance that for some systems they will be aligned. Similar scenarios have been proposed to explain the absence of pulsations from 4U 1700–37 (White et al. 1983) and also from the low-mass X-ray bi-



nary 4U 1700+24 (Masetti et al. 2002), though in the latter case, there is no conclusive evidence that this system is sufficiently young to show pulsations.

The second, stronger argument is the expected X-ray luminosity. The average  $L_X$  of 4U 2206+54 is much higher than expected for a neutron star in a 9.6 d orbit accreting from the wind of a low-luminosity O9 star. The X-ray luminosity of 4U 2206+54 is comparable to those of HMXBs with OB supergiant donors, which are believed to have mass-loss rates 2 orders of magnitude higher than the O9III–V companion to 4U 2206+54. To make things worse, most of these systems have smaller orbits than 4U 2206+54.

### 10.2.2 Excluding the black hole scenario

If a black hole was present in the system, the photon index and luminosities of our *INTEGRAL* observations would indicate that the source is in a low/hard state (see McClintock & Remillard 2006 and references therein). Our radio observations took place on 2003 May 12 and 20, or during *INTEGRAL* revolutions 70 and 73, i.e., right between *INTEGRAL* observations at revolutions 67 (2003 May 01–04) and 87 (2003 Jun 30–Jul 03).

Gallo et al. (2003) found an empirical correlation between the soft X-ray flux (in the range 2–11 keV) and the centimetre radio emission (with a flat spectrum in the range 4.9–15 GHz) for black hole binary systems in the low/hard state, of the form:  $S_{\text{radio}} = (223 \pm 156) \times (S_X)^{+0.7}$ , where  $S_{\text{radio}}$  is the radio flux density scaled to 1 kpc,  $S_X$  is the X-ray flux in Crab units scaled to 1 kpc, and the uncertainty in the multiplying factor is the non-linear  $1\sigma$  error of their fit. Therefore, by using a measured X-ray flux we can compute the expected radio emission of a source in case it is a black hole.

We obtained the flux from 4U 2206+54 in the 2–11 keV band from our JEM-X data, being  $7.2$  and  $4.0 \times 10^{-10}$  erg s $^{-1}$  cm $^{-2}$  for the 2003 May and June observations, respectively. This flux was translated to Crab units by measuring the flux from the Crab in the 2–11 keV band, using JEM-X data from an *INTEGRAL* observation close in time to our 4U 2206+54 pointings. The Crab flux was found to be  $1.8 \times 10^{-8}$  erg s $^{-1}$  cm $^{-2}$ , leading to fluxes of 40 and 22 mCrab for 4U 2206+54 during revolutions 67 and 87,

respectively. From this, and using  $N_{\text{H}} = 1.0 \times 10^{22}$  atom  $\text{cm}^{-2}$  (derived by Torrejón et al. (2004) and Masetti et al. (2004) from *BeppoSAX* data) we computed the unabsorbed corrected flux following equation (1) of Gallo et al. (2003), and then the resulting flux in Crab units scaled to 1 kpc distance (assuming a distance of 2.6 kpc to 4U 2206+54). The relation discussed above then predicts a radio flux density, already scaled to 2.6 kpc, of  $13.7 \pm 9.6$  mJy at the time of revolution 67 and of  $9.1 \pm 6.4$  mJy for revolution 87 (where the errors come directly from the  $1\sigma$  uncertainties given in Gallo et al. 2003 for the parameters of their fit). Thus, for revolution 67 the expected radio emission would be in the range 4.1–23.3 mJy, and for revolution 87 in the range 2.7–15.5 mJy.

We note that the lower expected radio flux density of 2.7 mJy is already more than 60 times greater than the 0.039 mJy  $3\sigma$  upper limit found with our VLA observations (see chapter 5). Obviously, it can be argued that our observations are not simultaneous. During revolution 70 (which was in coincidence with the first radio observations) the flux found from ISGRI data is not significant enough and, unfortunately, the source was outside the FOV of JEM-X, which could have provided an X-ray flux suitable for this analysis. Nevertheless, we point out that the *RXTE*/ASM count rate during our first radio observation is very similar to that measured during revolution 87, so it is reasonable to compare the obtained 2.7 mJy limit with our measured 0.042 mJy  $3\sigma$  upper limit on that day, giving again a difference with a factor of  $\sim 60$ . It could also be argued that the source could have experienced a transition to the high/soft state, that would naturally prevent the detection of radio emission. However, in such a case the *RXTE*/ASM count rates should increase considerably, while during both radio observations the count rates are similar or lower than during revolutions 67 and 87, when the photon indexes are typical of low/hard states. In summary, if the correlation between X-ray emission and radio emission reflects indeed a general property of black hole systems, we conclude that most likely there is not a black hole in 4U 2206+54.

Moreover, Fender & Hendry (2000) show that all Galactic persistent black holes have detectable radio emission. As 4U 2206+54 is a persistent source and does not show any detectable radio emission, most probably it does not host a black hole. Systems containing magnetised neutron stars ( $B \gtrsim 10^{11}$  G), on the other hand, do not show detectable radio emission.

### 10.2.3 The cyclotron feature

The presence of a likely cyclotron feature centred at 32 keV strongly suggests that there is a magnetic neutron star in 4U 2206+54, in good agreement with the lack of radio emission. *INTEGRAL* is the third mission reporting the likely detection of this absorption feature (see Table 9.2) and, even though none of the detections can be considered statistically very significant, the fact that it appears in three independent datasets cannot be ignored.

If the line is indeed a CRSF we can compute the value of the magnetic field in the scattering region by means of the equation  $[B/10^{12} \text{ G}] = [E_{\text{cycl}}/\text{keV}] (1 + z)/11.6$ , with  $z$  being the gravitational redshift at which we see the region. Considering that the line is produced at the surface of a canonical neutron star of  $1.4 M_{\odot}$  with a radius of 10 km, the gravitational redshift amounts to  $z=0.3$  (see, e.g., Kreykenbohm et al. 2004), and from the position of the line centre at 32 keV we obtain a magnetic field of  $3.6 \times 10^{12} \text{ G}$ . This value, in agreement with those found by Torrejón et al. (2004) and Masetti et al. (2004), is typical of magnetic neutron stars, and well within the range of  $1.3\text{--}4.8 \times 10^{12} \text{ G}$  obtained by Coburn et al. (2002) for a sample of ten X-ray pulsars displaying CRSFs (see their table 7).

One is led to the conclusion that 4U 2206+54 is the first system known in which an accreting magnetic neutron star does not appear as an X-ray pulsar. In principle, the possibility of very slow pulsations cannot be discarded. The wind-accreting X-ray source 2S 0114+650, with a B1 supergiant donor (Reig et al. 1996), shows pulsations with a period of  $\sim 2.8 \text{ h}$  (Finley et al. 1994). The orbital period of the system is  $\sim 12 \text{ d}$ , similar to that of 4U 2206+54. Our timing analysis rules out the possibility of significant pulsations from 4U 2206+54 in the range 0.5–3.0 h. A modulation at a period of several hours is still possible, as existing datasets do not constrain strongly this period range. However, it seems more logical to conclude that geometrical effects are responsible for the lack of pulsations (see discussion in subsection 10.2.1). Ribó et al. (2005) set a lower limit of 470 s in the spin period of the compact object in 4U 2206+54 in order to avoid the propeller effect (which would yield the absence of pulsations).

### 10.3 Conclusions and Future Work

We have been able to give evidence for the nature of both, the optical and compact counterparts to 4U 2206+54, through a complete multiwavelength analysis.

Concerning the optical counterpart, for the first time, clues about the likely connection of BD+53°2790 with the He-strong stars are given, after a detailed analysis of a large amount of optical and infrared data. Important conclusions about the wind properties were outlined, with the striking finding of a very slow and high density wind present in the system. The presence of this wind is compatible with the He-strong classification. Its connection to the X-ray behaviour of the system was discussed briefly.

The finding of rotationally modulated photometric magnitudes would confirm the classification of BD+53°2790 as a He-strong star. This will be possible through extensive photometric campaigns. We intend to organise such campaigns from Skinakas Observatory.

For the first time, orbital parameters have been constrained through optical observations, in very good agreement with the orbital period found with high-energy data. The derived constraints are in agreement with those derived from the X-ray properties by Ribó et al. (2005). A complete orbital solution from optical data will be possible after the forthcoming observing campaigns (as is the case of the 10 nights of consecutive observations during August, 2005, from the Observatory of Haute Provence, France, or the continuous monitoring from Skinakas Observatory, Greece) provide further measurements of radial velocities. With a more statistically complete set of data, the determination of the systemic velocity of the system ( $V_{\text{sys}}$ ) will also be possible.

Concerning the compact companion, further evidence for its neutron-star nature was shown. The presence of a cyclotron line feature and the absence of radio emission point towards this interpretation. More high energy observations are needed to study in detail the properties of the cyclotron feature. A dedicated high energy observation would help also to discard or confirm the possibility of slow pulsations (on the order of a few hours).

The picture that emerges from BD +53°2790/4U 2206+54 is that of a system composed by a young peculiar active early type star (O9.5Vp) and a neutron star. Both are orbiting each other with a period of  $\sim 9.6$  d

in an eccentric orbit ( $e \sim 0.2-0.4$ ). The high energy radiation is produced by direct accretion of matter from a slow dense wind.

We have demonstrated how multiwavelength analysis are very useful to perform a complete study of high energy sources. Optical and UV data gave us information about BD +53°2790. We could relate the information extracted from the UV bands (stellar wind) to the accretion onto the neutron star. Infrared measurements also gave us information about this dense and slow wind. In addition, we have seen that high energy and radio emissions are also related, giving important information about the nature of the source.

This all was possible due to the fact that all the physical processes going on in these kind of systems are linked by one simple idea: all of them are produced by matter on its journey from the outer shells of the optical companion down to the polar caps of the neutron star.



## Bibliography

- Amnuel, P. R., Guseinov, O. K., and Rakhamimov, S. I.: 1979, *ApJS* **41**, 327
- Andrillat, Y., Jaschek, C., and Jaschek, M.: 1995, *A&AS* **112**, 475
- Argelander, A. F. W.: 1995, *VizieR Online Data Catalog* **1122**, 0
- Arnaud, K. A.: 1996, in *ASP Conf. Ser. 101: Astronomical Data Analysis Software and Systems V*, p. 17
- Balona, L. and Crampton, D.: 1974, *MNRAS* **166**, 203
- Bildsten, L., Chakrabarty, D., Chiu, J., Finger, M. H., Koh, D. T., Nelson, R. W., Prince, T. A., Rubin, B. C., Scott, D. M., Stollberg, M., Vaughan, B. A., Wilson, C. A., and Wilson, R. B.: 1997, *ApJS* **113**, 367
- Bjorkman, J. E. and Cassinelli, J. P.: 1993, *ApJ* **409**, 429
- Bjorkman, J. E., Ignace, R., Tripp, T. M., and Cassinelli, J. P.: 1994, *ApJ* **435**, 416
- Blay, P., Negueruela, I., Reig, P., Coe, M. J., Corbet, R. H. D., Fabregat, J., and Tarasov, A. E.: 2006, *A&A* **446**, 1095
- Blay, P., Ribó, M., Negueruela, I., Torrejón, J. M., Reig, P., Camero, A., Mirabel, I. F., and Reglero, V.: 2005, *A&A* **438**, 963
- Bohlender, D. A., Landstreet, J. D., Brown, D. N., and Thompson, I. B.: 1987, *ApJ* **323**, 325
- Bradt, H. V., Rothschild, R. E., and Swank, J. H.: 1993, *A&AS* **97**, 355
- Caron, G., Moffat, A. F. J., St-Louis, N., Wade, G. A., and Lester, J. B.: 2003, *AJ* **126**, 1415
- Casares, J., Ribó, M., Ribas, I., Paredes, J. M., Martí, J., and Herrero, A.: 2005, *MNRAS* **364**, 899

- Clark, J. S., Goodwin, S. P., Crowther, P. A., Kaper, L., Fairbairn, M., Langer, N., and Brocksopp, C.: 2002, *A&A* **392**, 909
- Clark, J. S., Reig, P., Goodwin, S. P., Larionov, V. M., Blay, P., Coe, M. J., Fabregat, J., Negueruela, I., Papadakis, I., and Steele, I. A.: 2001a, *A&A* **376**, 476
- Clark, J. S., Steele, I. A., Fender, R. P., and Coe, M. J.: 1999, *A&A* **348**, 888
- Clark, J. S., Tarasov, A. E., Okazaki, A. T., Roche, P., and Lyuty, V. M.: 2001b, *A&A* **380**, 615
- Coburn, W., Heindl, W. A., Rothschild, R. E., Gruber, D. E., Kreykenbohm, I., Wilms, J., Kretschmar, P., and Staubert, R.: 2002, *ApJ* **580**, 394
- Condon, J. J., Cotton, W. D., Greisen, E. W., Yin, Q. F., Perley, R. A., Taylor, G. B., and Broderick, J. J.: 1998, *AJ* **115**, 1693
- Conti, P. S. and Alschuler, W. R.: 1971, *ApJ* **170**, 325
- Corbet, R. H. D. and Peele, A. G.: 2001, *ApJ* **562**, 936
- Currie, M. and Berry, D.: 2004, *KAPPA – Kernel Application Package – Starlink User Note 95.28*, Rutherford Appleton Laboratory
- Dachs, J., Hanuschik, R., Kaiser, D., and Rohe, D.: 1986, *A&A* **159**, 276
- Dachs, J. and Wamsteker, W.: 1982, *A&A* **107**, 240
- de Martino, D., Matt, G., Belloni, T., Haberl, F., and Mukai, K.: 2004, *A&A* **415**, 1009
- Donati, J.-F., Babel, J., Harries, T. J., Howarth, I. D., Petit, P., and Semel, M.: 2002, *MNRAS* **333**, 55
- Everall, C.: 1995, *Ph.D. thesis*, University of Southampton
- Everall, C., Coe, M. J., Norton, A. J., Roche, P., and Unger, S. J.: 1993, *MNRAS* **262**, 57



- Fender, R. P. and Hendry, M. A.: 2000, *MNRAS* **317**, 1
- Finley, J. P., Taylor, M., and Belloni, T.: 1994, *ApJ* **429**, 356
- Forman, W., Jones, C., Cominsky, L., Julien, P., Murray, S., Peters, G., Tananbaum, H., and Giacconi, R.: 1978, *ApJS* **38**, 357
- Gallo, E., Fender, R. P., and Pooley, G. G.: 2003, *MNRAS* **344**, 60
- Georgiev, L. and Hernández, X.: 2005, *Revista Mexicana de Astronomía y Astrofísica* **41**, 121
- Giacconi, R., Kellogg, E., Gorenstein, P., Gursky, H., and Tananbaum, H.: 1971, *ApJL* **165**, L27
- Giacconi, R., Murray, S., Gursky, H., Kellogg, E., Schreier, E., Matilsky, T., Koch, D., and Tananbaum, H.: 1974, *ApJS* **27**, 37
- Giacconi, R., Murray, S., Gursky, H., Kellogg, E., Schreier, E., and Tananbaum, H.: 1972, *ApJ* **178**, 281
- Groenewegen, M. A. T. and Lamers, H. J. G. L. M.: 1989, *Astronomy and Astrophysics Supplement Series* **79**, 359
- Halbedel, E. M.: 1993, *PASP* **105**, 465
- Herbig, G. H.: 1975, *ApJ* **196**, 129
- Hiltner, W. A.: 1956, *ApJS* **2**, 389
- Høg, E., Fabricius, C., Makarov, V. V., Urban, S., Corbin, T., Wycoff, G., Bastian, U., Schwkendiek, P., and Wicenec, A.: 2000, *A&A* **355**, L27
- Kreykenbohm, I., Wilms, J., Coburn, W., Kuster, M., Rothschild, R. E., Heindl, W. A., Kretschmar, P., and Staubert, R.: 2004, *A&A* **427**, 975
- Lamers, H. J. G. L. M., Cerruti-Sola, M., and Perinotto, M.: 1987, *ApJ* **314**, 726
- Landolt, A. U.: 1992, *AJ* **104**, 340
- Lee, U., Osaki, Y., and Saio, H.: 1991, *MNRAS* **250**, 432

- Manfroid, J.: 1993, *A&A* **271**, 714
- Maraschi, L. and Treves, A.: 1981, *MNRAS* **194**, 1P
- Martins, F., Schaerer, D., and Hillier, D. J.: 2005, *A&A* **436**, 1049
- Martocchia, A., Motch, C., and Negueruela, I.: 2005, *A&A* **430**, 245
- Masetti, N., Dal Fiume, D., Amati, L., Del Sordo, S., Frontera, F., Orlandini, M., and Palazzi, E.: 2004, *A&A* **423**, 311
- Masetti, N., Dal Fiume, D., Cusumano, G., Amati, L., Bartolini, C., Del Sordo, S., Frontera, F., Guarnieri, A., Orlandini, M., Palazzi, E., Parmar, A. N., Piccioni, A., and Santangelo, A.: 2002, *A&A* **382**, 104
- Massi, M., Ribó, M., Paredes, J. M., Garrington, S. T., Peracaula, M., and Martí, J.: 2004, *A&A* **414**, L1
- Mathys, G.: 1988, *A&AS* **76**, 427
- McClintock, J. E. and Remillard, R. A.: 2006, *to appear as Chapter 4 in Compact Stellar X-ray Sources*, eds. W.H.G. Lewin and M. van der Klis, Cambridge University Press, astro-ph/0306213
- McSwain, M. V. and Gies, D. R.: 2002, *ApJL* **568**, L27
- McSwain, M. V., Gies, D. R., Huang, W., Wiita, P. J., Wingert, D. W., and Kaper, L.: 2004, *ApJ* **600**, 927
- Mihalas, D., Kunasz, P. B., and Hummer, D. G.: 1975, *ApJ* **202**, 465
- Mills, D., Webb, J., and Clayton, M.: 1997, *ECHOMOP-Echelle Data Reduction Package – Starlink User Note 152.4*, Rutherford Appleton Laboratory
- Negueruela, I. and Reig, P.: 2001, *A&A* **371**, 1056
- Nelson, R. F. and Spencer, R. E.: 1988, *MNRAS* **234**, 1105
- Okazaki, A. T.: 2000, in *ASP Conf. Ser. 214: IAU Colloq. 175: The Be Phenomenon in Early-Type Stars*, p. 409

- Owocki, S. P., Castor, J. I., and Rybicki, G. B.: 1988, *ApJ* **335**, 914
- Paredes, J. M., Martí, J., Ribó, M., and Massi, M.: 2000, *Science* **288**, 2340
- Paredes, J. M., Ribó, M., Ros, E., Martí, J., and Massi, M.: 2002, *A&A* **393**, L99
- Pedersen, H. and Thomsen, B.: 1977, *A&AS* **30**, 11
- Perry, C. L., Olsen, E. H., and Crawford, D. L.: 1987, *PASP* **99**, 1184
- Popper, D. M.: 1980, *ARA&A* **18**, 115
- Porter, J. M.: 1999, *A&A* **348**, 512
- Prinja, R. K., Barlow, M. J., and Howarth, I. D.: 1990, *ApJ* **361**, 607
- Protassov, R., van Dyk, D. A., Connors, A., Kashyap, V. L., and Siemiginowska, A.: 2002, *ApJ* **571**, 545
- Reig, P., Chakrabarty, D., Coe, M. J., Fabregat, J., Negueruela, I., Prince, T. A., Roche, P., and Steele, I. A.: 1996, *A&A* **311**, 879
- Reig, P., Negueruela, I., Coe, M. J., Fabregat, J., Tarasov, A. E., and Zamanov, R. K.: 2000, *MNRAS* **317**, 205
- Reig, P., Ribó, M., Paredes, J. M., and Martí, J.: 2003, *A&A* **405**, 285
- Reynolds, A. P., Parmar, A. N., Hakala, P. J., Pollock, A. M. T., Williams, O. R., Peacock, A., and Taylor, B. G.: 1999, *Astronomy and Astrophysics Supplement Series* **134**, 287
- Ribó, M., Reig, P., Martí, J., and Paredes, J. M.: 1999, *A&A* **347**, 518
- Ribó, M., Negueruela, I., Blay, P., Torrejón, J. M., and P, R.: 2005, *A&A* in press, astro-ph/0511408
- Saraswat, P. and Apparao, K. M. V.: 1992, *ApJ* **401**, 678
- Shobbrook, R. R.: 1983, *MNRAS* **205**, 1215

- Shortridge, K., Meyerdierks, H., Currie, M., Clayton, M., Lockley, J., Charles, A., Davenhall, C., Taylor, M., Ash, T., Wilkins, T., Axon, D., Palmer, J., Holloway, A., and Graffagnino, V.: 1997, *FIGARO – A general data reduction system – Starlink User Note 86.20*, Rutherford Appleton Laboratory
- Shrader, C. R. and Titarchuk, L.: 1999, *ApJL* **521**, L121
- Skinner, G. and Connell, P.: 2003, *A&A* **411**, L123
- Smith, M. A. and Fullerton, A. W.: 2005, *PASP* **117**, 13
- Smith, M. A. and Groote, D.: 2001, *A&A* **372**, 208
- Sobolev, V. V.: 1947, *Moving Envelopes of Stars*, Leningrad State University (Translated to English by Sergei Gaposchkin for Cambridge, MA: Harvard U. Press, 1960)
- Steiner, J. E., Ferrara, A., Garcia, M., Patterson, J., Schwartz, D. A., Warwick, R. S., Watson, M. G., and McClintock, J. E.: 1984, *ApJ* **280**, 688
- Sunyaev, R. A. and Titarchuk, L. G.: 1980, *A&A* **86**, 121
- Titarchuk, L.: 1994, *ApJ* **434**, 570
- Torrejón, J. M., Kreykenbohm, I., Orr, A., Titarchuk, L., and Negueruela, I.: 2004, *A&A* **423**, 301
- Townsend, R. H. D. and Owocki, S. P.: 2005, *MNRAS* **357**, 251
- Villa, G., Page, C. G., Turner, M. J. L., Cooke, B. A., Ricketts, M. J., Adams, D. J., and Pounds, K. A.: 1976, *MNRAS* **176**, 609
- Voges, W., Aschenbach, B., Boller, T., Bräuninger, H., Briel, U., Burkert, W., Dennerl, K., Englhauser, J., Gruber, R., Haberl, F., Hartner, G., Hasinger, G., Kürster, M., Pfeffermann, E., Pietsch, W., Predehl, P., Rosso, C., Schmitt, J. H. M. M., Trümper, J., and Zimmermann, H. U.: 1999, *A&A* **349**, 389
- Walborn, N. R.: 1982, *PASP* **94**, 322

Walborn, N. R. and Panek, R. J.: 1984, *ApJL* **280**, L27

Warwick, R. S., Marshall, N., Fraser, G. W., Watson, M. G., Lawrence, A., Page, C. G., Pounds, K. A., Ricketts, M. J., Sims, M. R., and Smith, A.: 1981, *MNRAS* **197**, 865

White, N. E., Swank, J. H., and Holt, S. S.: 1983, *ApJ* **270**, 711

Wood, K. S., Meekins, J. F., Yentis, D. J., Smathers, H. W., McNutt, D. P., Bleach, R. D., Friedman, H., Byram, E. T., Chubb, T. A., and Meidav, M.: 1984, *ApJS* **56**, 507

Zuiderwijk, E. J., Martin, R., Raimond, E., and van Diepen, G. N. J.: 1994, *PASP* **106**, 515

## **Part III**

# **The BeX system SAX J2103.5+4545**



## Chapter 11

# Introduction

SAX J2103.5+4545 was discovered with *BeppoSAX* in 1997, when the source underwent a bright state (Hulleman et al. 1998). The source reached a maximum flux of 20 mCrab and was found to be an X-ray pulsar with a 358.61 s pulse period. An absorbed power-law of index 1.27 gave the best fit to the spectrum. The modulated nature of the high energy emission plus the spectral shape of the source pointed to an accreting compact object in a binary system as the most likely nature of the source. The presence of pulsations indicated that probably the compact object was a neutron star or a white dwarf. However, the white dwarf model was discarded because of the behaviour of the pulsation fraction, which tends to increase at lower energies in white dwarfs but showed the opposite behaviour in SAX J2103.5+4545. The orbital modulation of the outbursts suggested that the system would likely be a BeX system. A close-by B8 star, HD 200709, was proposed as candidate to optical counterpart to the system, but with some doubts because the star was never reported to have shown emission and the spectral type fell outside the O9-B2 range (typical of BeX counterparts).

Two more X-ray active phases are reported in the literature, in October 1999 and March 2001 (Baykal et al. 2000, 2002). Pulse arrival time analysis allowed the determination of the orbital parameters of the system. The orbital period was calculated to be  $12.68 \pm 0.25$  days and the eccentricity  $0.4 \pm 0.2$  (Baykal et al. 2000). A summary of the orbital parameters of the source is shown in Table 11.1.



Based on the Ghosh & Lamb (1979) relationship, which relates the spin changes with the high energy luminosity of the source:

$$-\dot{P} = 2.2 \times 10^{-12} \mu_{30}^{2/7} m_X^{-3/7} R_6^{6/7} I_{45}^{-1} P^2 L_{37}^{6/7} \text{ s s}^{-1}$$

where  $\mu_{30}$ ,  $m_X$ ,  $R_6$ , and  $I_{45}$  are the magnetic dipole moment in units of  $10^{30}$  G cm<sup>3</sup>, the mass of the compact object in units of solar mass, the radius in units of  $10^6$  cm, and the moment of inertia in units of  $10^{45}$  g cm<sup>2</sup> and  $L_{37}$  represents the X-ray luminosity in units of  $10^{37}$  erg s<sup>-1</sup>, Baykal et al. (2000) estimated a distance to the source of 5 kpc (through the derived luminosity and the observed flux) and a magnetic field on the order of  $\sim 10^{12}$  G.

A bright state, with a luminosity of the order of  $10^{36}$  erg s<sup>-1</sup> and strong orbital modulation, and a faint state, with a luminosity of the order of  $10^{34}$  erg s<sup>-1</sup> and weak orbital modulation, have been reported by Baykal et al. (2002). In the faint state the spectral shape was harder while in the bright state it was softer. Fig. 11.1 shows a periodogram of both, faint and bright states of the source. A peak at a pulse frequency in agreement with the measured orbital period is found only in the bright state periodogram. Based on *RXTE*/ASM count rate, we can state that the limiting count rate between faint and bright states is around  $\sim 5$  count s<sup>-1</sup>.

Recently, Reig et al. (2004) reported the first optical and infrared observations of this system, leading to the identification of the optical counterpart with a B0 Ve star (different than HD 200709, the one initially

Table 11.1: Summary of orbital parameter determinations for the BeX system SAX J2103.5+4545.

Parameter	Author		
	Baykal (2000)	İnam (2004)	Sidoli (2005)
Orbital Epoch (MJD)	51519.3±0.2	52633.90±0.05	
$P_{orb}$ (d)	12.68±0.25		12.670±0.005
$a_x \sin i$ (lt-s)	72±6		
Eccentricity	0.4±0.2		
Periastron anomaly	240±30		

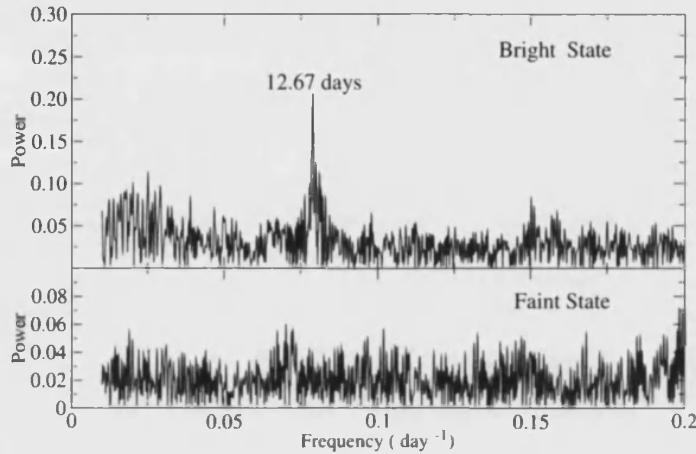


Figure 11.1: Power spectrum of *RXTE*/ASM SAX J2103.5+4545 data separated in two sets, one corresponding to the epochs of bright state of the system, and one where only faint state data is included. The frequency peak corresponding to the orbital period is detected only in the bright state data.

proposed) and identifying the system as a BeX.

*INTEGRAL* was able to observe the last bright state undergone by SAX J2103.5+4545. During November-December 2002, within the Performance and Verification phase (PV), the Cygnus X-1 region was intensively monitored with the aim of checking the performance of all the instruments and subsystems on board *INTEGRAL*, and to perform the first background studies. Lutovinov et al. (2003) and Del Santo et al. (2003) showed preliminary results from the first detections of SAX J2103.5+4545 during the PV phase and the first two Galactic Plane Survey (GPS) scans, respectively.

In coincidence with these first *INTEGRAL* observations, İnam et al. (2004) observed the source with XMM-Newton. They improved the spectral fit with a soft component and found a transient Quasi Periodic Oscillation (QPO) at a frequency of  $\sim 0.044$  Hz. Usually QPOs are attributed to processes in the inner parts of the accretion disc.

During 2003 and 2004, the source was repeatedly observed by *INTEGRAL*. The transient nature of the system and the observing strategy of

*INTEGRAL* spacecraft meant that the amount of data and the time coverage were not adequate to perform a deep analysis of the source. In spite of these difficulties, some work has been done. Falanga et al. (2005) developed the first attempt to carry out a detailed analysis of the pulse profile shape and energy dependence with *INTEGRAL* data from a private observation which took place in May 2003. Sidoli et al. (2005) reported on the spin-up rates measured during the bright state observed by *INTEGRAL*, between the end of 2002 and mid-2004.

During the subsequent faint state, only a few observations are available. As a matter of fact, the source is very weak and no spectral or timing information can be obtained. Actually, in most of the observations during the faint state, only upper limits to the source flux can be given.

The optical coverage of the source is scarce and mainly concentrated on its faint state. However, some very interesting properties of the source can be outlined through the analysis of the spectra of the optical counterpart to SAX J2103.5+4545.

In this chapter, we will present a comprehensive analysis of this source. The optical properties of the system will be reviewed and stellar parameters of the mass donor will be estimated. We will present a spectral, timing and spatial analysis of the X-ray transient pulsar SAX J2103.5+4545, using *INTEGRAL* observations from PV phase (where a detailed analysis of two type-I outbursts can be performed) and GPS (which will give us information about the long-term behaviour of the system). Hints about the nature of SAX J2103.5+4545 will be discussed based on correlations between optical and high energy emission. With this work, the capabilities of the *INTEGRAL* mission to perform a detailed study of this kind of sources are demonstrated.

## Chapter 12

# Optical band

Since the identification of the optical counterpart to SAX J2103.5+4545 (Reig et al. 2004), it has been monitored continuously, mainly from the Skinakas Observatory (Crete, Greece).

A total of 21 spectra were collected during 2003 and 2004, two of them in the classification region of the spectra ( $\sim 3900\text{--}5000\text{ \AA}$ ) and the rest cover a wide range including the  $H\alpha$  line. The dates of observations and wavelength covered are summarised in Table 12.1. Data were taken mainly from Skinakas Observatory, but also a couple of observations from the William Herschel Telescope (WHT, La Palma, Spain) and the Calar Alto Observatory (Almeria, Spain) were analysed.

Part of this spectral set is already described in Reig et al. (2004). There, a classification of B0V is reported for the optical counterpart to SAX J2103.5+4545. We have retrieved a classification spectra of the B0V standard  $\nu$  Ori, from the Walborn & Fitzpatrick (1990) digital spectral classification catalogue for OB stars. The spectrum of  $\nu$  Ori together with the two blue spectra of SAX J213.5+4545 are shown in Fig. 12.1. The intensity of O II  $\lambda 4415, \lambda 4650$  and the strength of the He II lines (in particular He II  $\lambda 4686$ ) give a direct visual classification of earlier than B1 (see Walborn & Fitzpatrick 1990). The strength of He I lines indicate also a spectral type later than O9. As outlined in Reig et al. (2004) the ratios He I  $\lambda 4026/\text{He II } \lambda 4200$  and He I  $\lambda 4713/\text{He II } \lambda 4686$  are very similar to those of  $\nu$  Ori, the equivalent widths of these lines and their ratios can be seen in Tables 12.2 and 12.3. Reig et al. (2004) state

Table 12.1: Spectroscopic observations of SAX J2103.5+4545 during 2003 and 2004.

Telescope	MJD	Wavelength range (Å)
Skinakas	52853.5	4750–6825
Skinakas	52869.5	5950–6850
Skinakas	52869.5	3925–4800
Skinakas	52897.5	5525–7550
Skinakas	52897.5	3600–5325
Skinakas	52919.5	5275–7325
Skinakas	52921.5	5275–7325
Calar Alto	52976.5	4200–8300
Skinakas	53149.5	4756–6832
Skinakas	53153.5	4749–6832
Skinakas	53154.5	4746–6824
Skinakas	53180.5	5498–6861
Skinakas	53182.5	5498–6860
Skinakas	53194.5	5498–6861
Skinakas	53243.5	4768–6840
Skinakas	53244.5	4762–6840
Skinakas	53245.5	4773–6839
WHT	53250.5	6040–6910
Skinakas	53251.5	4780–6830
Skinakas	53261.5	4762–6840
Skinakas	53262.5	4762–6841
Skinakas	53304.5	4773–6850

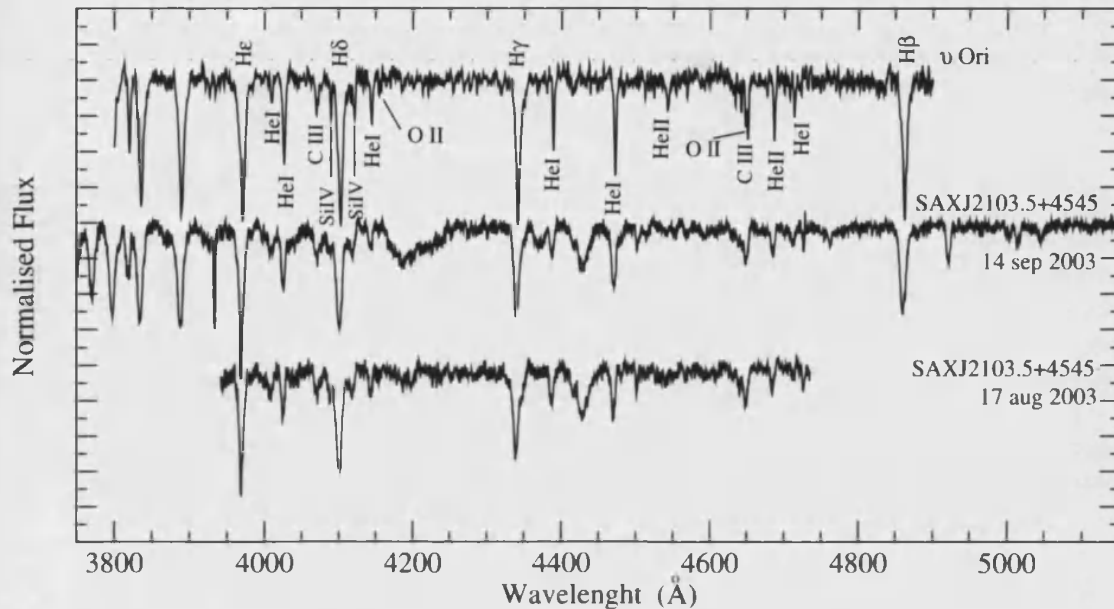


Figure 12.1: Spectrum of the standard B0V star  $\nu$  Ori together with the two blue spectra available of SAX J2103.5+4545.

that the optical counterpart to SAX J2103.5+4545 is most likely a main-sequence star. This is supported by the intensity of He II  $\lambda 4686$  relative to that of He I  $\lambda 4731$  Å and by the weakness of the Si III lines. The ratios He II  $\lambda 4686$ /C III  $\lambda 4650$  and He I  $\lambda 4145$ /Si IV  $\lambda 4089$  are very similar to those of  $\nu$  Ori, as shown in Table 12.3, giving support to the main-sequence classification.

Reig et al. (2004) reported a rotational velocity of  $240 \pm 20$  km s<sup>-1</sup> based on the measurement of the EW of some He I lines. Here we have taken a different approach. Fig. 12.2 shows the He I profiles in the September 14, 2003, spectrum. From these lines we have selected those showing the most symmetric wings, namely He I  $\lambda 4386$  Å and He I  $\lambda 4471$  Å. We have artificially broadened the same He I lines of  $\nu$  Ori at different rotational velocities. We have compared the broadened profiles of  $\nu$  Ori to the profiles of SAX J2103.5+4545. For each He I line we selected the two rotationally broadened He I profiles giving the upper and lower envelopes to the width of the SAX J2103.5+4545 He I line wings. We took the rotational velocity of these broadened profiles as the upper and lower limits to the rotational velocity of SAX J2103.5+4545. From these up-

Table 12.2: Equivalent width measurements of selected lines for spectral and luminosity classification purposes, as outlined in the main text.

Line (Å)	<i>v</i> Ori	SAX J2103.5+4545	
		17/08/2003	14/09/2003
He I $\lambda$ 4026	$1.2 \pm 0.3$	$1.1 \pm 0.3$	$0.81 \pm 0.18$
He I $\lambda$ 4144	$0.72 \pm 0.16$	$0.45 \pm 0.10$	$0.40 \pm 0.09$
He I $\lambda$ 4713	$0.40 \pm 0.09$	$0.32 \pm 0.07$	$0.22 \pm 0.05$
He II $\lambda$ 4200	$0.15 \pm 0.03$	$0.17 \pm 0.04$	$0.07 \pm 0.02$
He II $\lambda$ 4686	$0.67 \pm 0.15$	$0.53 \pm 0.12$	$0.41 \pm 0.09$
Si IV $\lambda$ 4089	$0.23 \pm 0.05$	$0.30 \pm 0.07$	$0.30 \pm 0.07$
C III $\lambda$ 4650	$0.65 \pm 0.14$	$0.47 \pm 0.10$	$0.31 \pm 0.08$

Table 12.3: Equivalent width ratios of selected lines from Table 12.2 for spectral and luminosity classification purposes, as outlined in the main text.

Ratio	<i>v</i> Ori	SAX J2103.5+4545
He I $\lambda$ 4026/He II $\lambda$ 4200	$8 \pm 3$	$8 \pm 4$
He I $\lambda$ 4713/He II $\lambda$ 4686	$0.60 \pm 0.16$	$0.6 \pm 0.2$
He II $\lambda$ 4686/C III $\lambda$ 4650	$1.0 \pm 0.3$	$1.2 \pm 0.4$
He I $\lambda$ 4144/Si IV $\lambda$ 4089	$3 \pm 2$	$1.4 \pm 0.5$

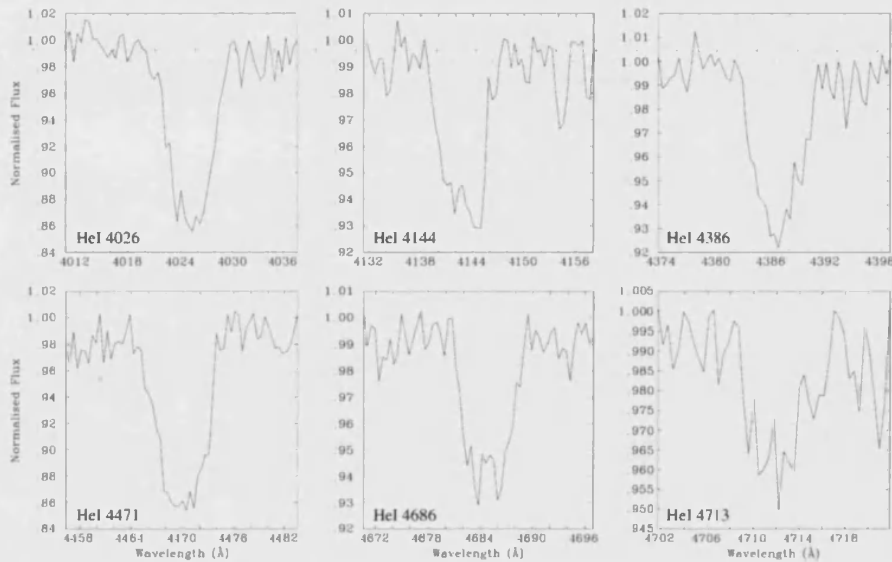


Figure 12.2: He I profiles of SAX J2103.4+4545 from the September 14, 2003, spectrum.

per and lower limits we have calculated the average rotational velocity of SAX J2103.5+4545, yielding a value of  $230 \pm 20 \text{ km s}^{-1}$ , in excellent agreement with the value derived by Reig et al. (2004). Fig. 12.3 shows the He I  $\lambda 4386 \text{ \AA}$  and He I  $\lambda 4471 \text{ \AA}$  lines of SAX J2103.5+4545 together with the rotationally broadened profiles of  $v$  Ori.

A detailed analysis of the  $H\alpha$  line behaviour can be performed with our set of data. The  $H\alpha$  line is the main indicator of the state of circumstellar envelope in BeX systems. Fig. 12.4 shows evolution of the  $H\alpha$  line profile (together with the He I  $\lambda 6678 \text{ \AA}$  line) in SAX J2103.5+4545. The high degree of variability in both lines is evident. The  $H\alpha$  line suffered a major change from August 2003 to September 2003, where a double emission peak feature (a shell spectrum), seen during August 2003, disappeared. Only pure absorption is seen in the spectrum from September 14, 2003, on. The double peak feature has not been observed yet again, though we notice the presence of variable absorption core components, indicative of the presence of some circumstellar emission. Despite the apparent variability in the core of the  $H\alpha$  line from September 2003 on, its equivalent width is quite constant. In contrast, the FWHM suffers a big spread, as can be seen in Figures 12.5 and 12.6.



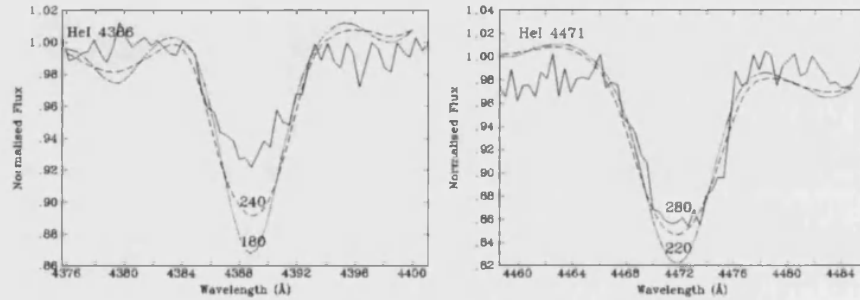


Figure 12.3: He I  $\lambda 4386 \text{ \AA}$  and He I  $\lambda 4471 \text{ \AA}$  profiles of SAX J2103.4+4545 together with the same lines rotationally broadened line profiles of  $\nu$  Ori.

We have very poor statistics and our data are not conclusive, but they suggest some degree of correlation between the FWHM and the EW of the  $H\alpha$  line while the spectrum still shows the shell profile. When the shell profile disappears we have a quite constant value of the EW and an important spread in the FWHM. It is also noticeable the fact that the EW of the He I  $\lambda 6678 \text{ \AA}$  line also suggests the same kind of correlation as with the EW of the  $H\alpha$  line. This may indicate that the He I  $\lambda 6678 \text{ \AA}$  line is affected as well to some extent by the circumstellar emission. As mentioned above, we have only two data points in the *shell state* and thus these suggestions must be taken with caution. From September 2003 on, the He I  $\lambda 6678 \text{ \AA}$  line also shows a high degree of variability, displaying, like the  $H\alpha$  line, some filling in the line core, most likely due to circumstellar emission. We searched for modulations in the  $H\alpha$  and He I  $\lambda 6678 \text{ \AA}$  line parameters, but the amount and distribution of data may not be very adequate for this analysis and we were not able to find any kind of periodicity. Fig. 12.7 shows the  $H\alpha$  EW and FWHM and the He I  $\lambda 6678 \text{ \AA}$  line EW folded in phase. The orbital solution of Baykal et al. (2002) with the improved orbital epoch of İnam et al. (2004) were used to fold the data.

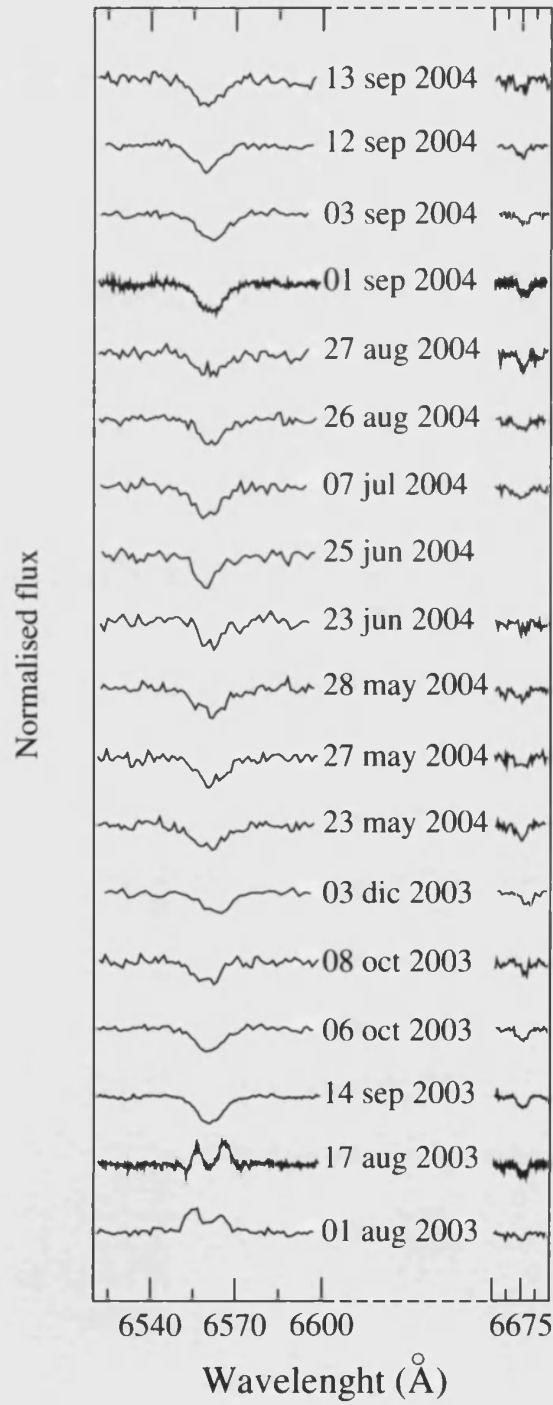


Figure 12.4: Evolution of the H $\alpha$  and He I  $\lambda 6678$  Å line profiles.

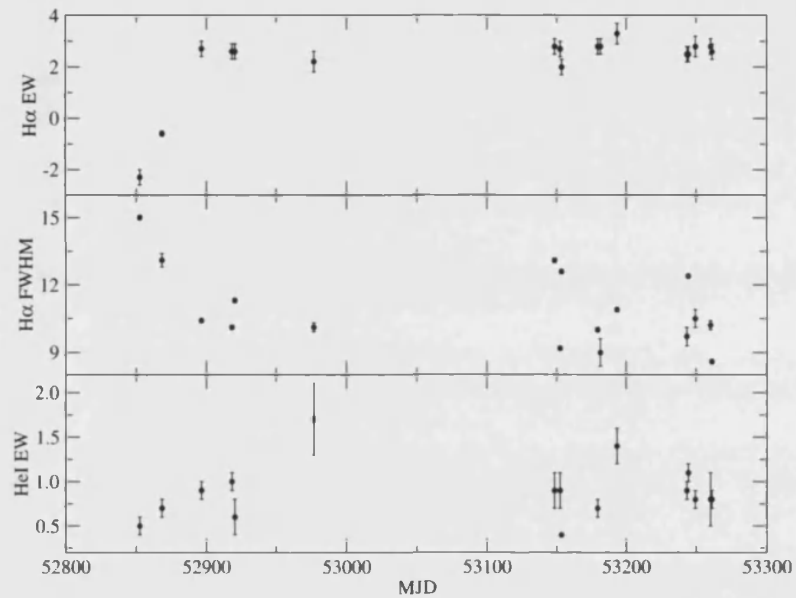


Figure 12.5: Evolution of the EW and the FWHM of the H $\alpha$  line and the EW of the He I  $\lambda$ 6678 Å line.

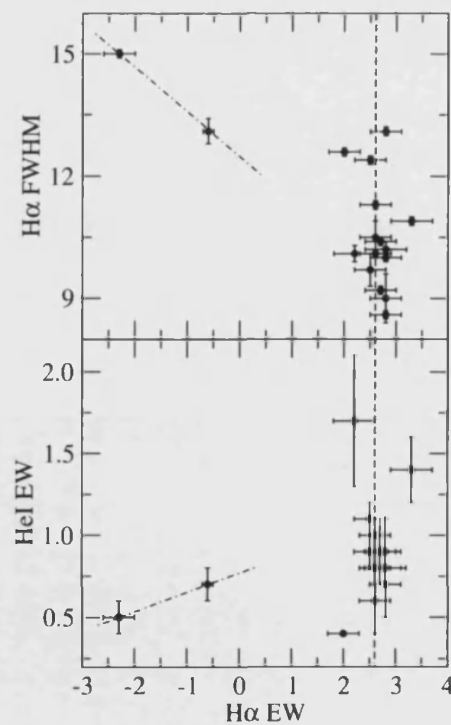


Figure 12.6: FWHM of the H $\alpha$  line and EW of the He I  $\lambda$ 6678 Å line versus the EW of the H $\alpha$  line. The average value of the H $\alpha$  EW is shown with a vertical dashed line.

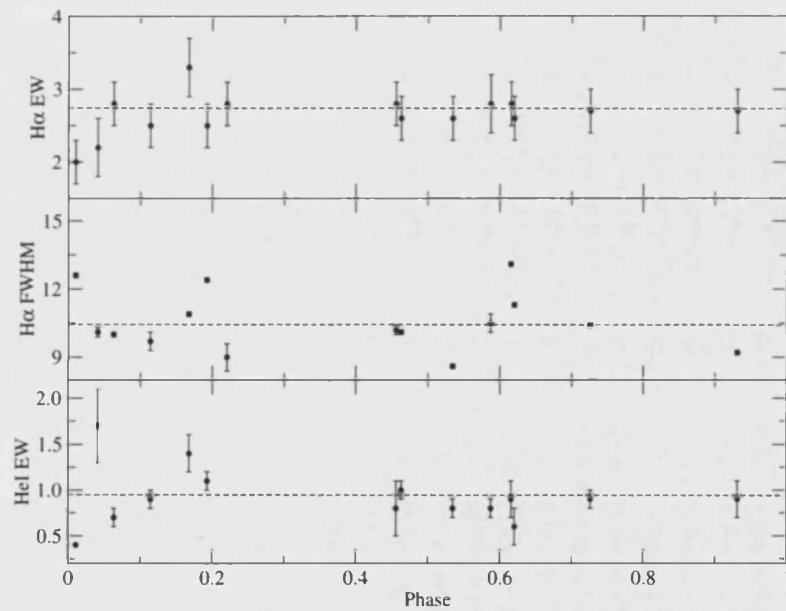


Figure 12.7: EW and FWHM of the H $\alpha$  line and EW of the He I  $\lambda$ 6678 folded at the orbital phase of SAX J2103.5+4545. The average value of each parameter is shown by a dashed horizontal line.



## Chapter 13

# X-Rays and $\gamma$ -Rays

From December 8 up to December 29, 2002 (*INTEGRAL* revolutions 19 to 25), SAX J2103.5+4545 was detected by all high energy instruments on board *INTEGRAL*. The total on-source time was approximately 500 ks for ISGRI, 730 ks for SPI and 20 ks for JEM-X. This represents a coverage of two type-I outbursts. Unfortunately, due to the observing strategy of *INTEGRAL* the source was not inside the FOV of all the instruments all the time. In addition, the software analysis restrictions limited our analysis and did not allow a deeper spectral and sub-science window timing analysis with data of those pointings where the source was out of the FCFOV of ISGRI or at distances larger than  $2.5^\circ$  from the centre of the FOV in the case of JEM-X. SPI coverage is better but its sensitivity is lower.

GPS observations up to revolution 181 (6–9 April, 2004) have also been included in this analysis. The observations from this period only give partial coverage of some type-I outbursts during the SAX J2103.5+4545 bright state, which lasted up to MJD  $\sim 52820$ . Most of the time the source lies in the FCFOV of ISGRI for only two to three consecutive science windows. More complete coverage happens during revolution 67, where we can follow the decline of a type-I outburst during a bit less than one day. In spite of these limitations, this set of data will allow us to study the long-term behaviour of SAX J2103.5+4545.

Table 13.1: Most significant SAX J2103.5+4545 detections.

Instrument	Mean MJD	Mean Flux phot cm <sup>-2</sup> s <sup>-1</sup> keV <sup>-1</sup>
JEM-X	52630.71	0.00088±0.00002
(5–20keV)	52636.69	0.00021±0.00001
ISGRI	52618.73	0.00037±0.00004
(20–40 keV)	52630.71	0.00025±0.00002
	52636.69	0.00009±0.00001
SPI	52618.73	0.000051±0.000016
(40–100 keV)	52621.72	0.000005±0.000019
	52630.71	0.000067±0.000010

## 13.1 PV phase, analysis of an outburst

### 13.1.1 Imaging

During the PV phase, ISGRI detected the source in a total of 280 pointings. Since each pointing had an integration time of around 30 minutes, the total ISGRI observing time was around 500 ks. However, only those detections with a detection level above 8 were included in the analysis. Thus, the total time used in our analysis amounts to about 108 ks.

Even though the source was inside the SPI field of view for all of December 2002, except during revolution 24 (when the satellite moved into an empty region to perform background measurements), the averaging of data over one revolution gave significant flux values only for revolutions 19, 20, and 23. Figure 13.1 depicts the evolution of the significance of the detection of SAX J2103.5+4545 with SPI. Flux maxima are separated by the orbital period of the system.

JEM-X only gave positive detections of the source (even forcing the software to find significant flux at the source position) for 10 pointings, spread over revolutions 23 and 25. This is due to the small field of view of JEM-X and the dithering pattern used.

The best ISGRI position is R.A.=21h 03m 31s and DEC=45° 45' 00", with  $\sim 1$  arcmin error radius. The best JEM-X source location is R.A.=21h

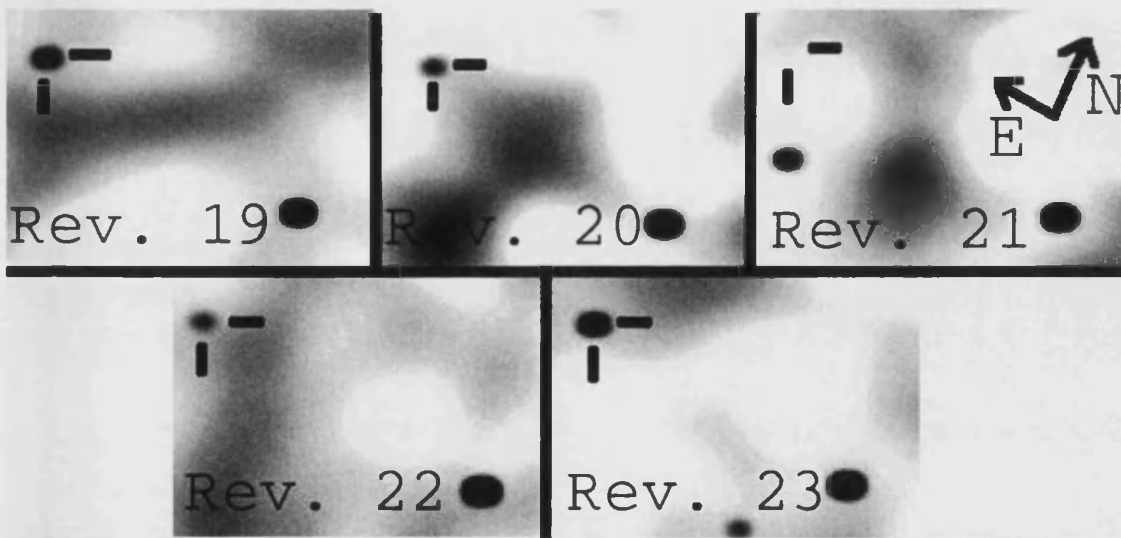


Figure 13.1: Evolution of the detections of SAX J2103.5+4545 with SPI during PV phase, averaged over a revolution. The location of SAX J2103.5+4545 is shown with two orthogonal lines at the top-left corner. The time elapsed between peaks coincides with the orbital period of the system. The source at the right bottom corner is Cyg X-3. A spurious source appears in the revolution 21 image (south-west from the indicated position of SAX J2103.5+4545), being very likely an artifact of the image reconstruction process.



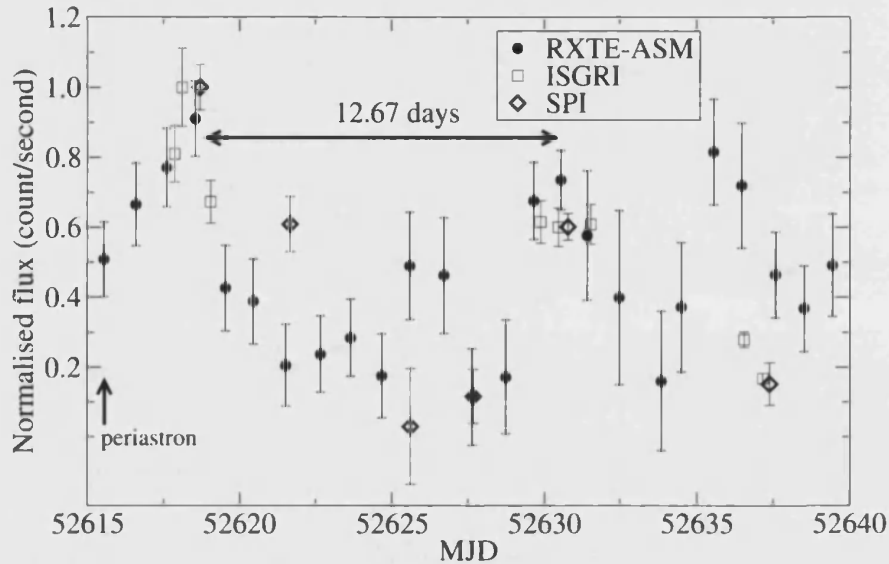


Figure 13.2: ISGRI, SPI and *RXTE*/ASM light curve during December 2002. Each data point represents an averaged one day flux for all the instruments. Units are normalised to the peak value.

03m 36.7s and DEC=45° 45' 02.7", with an error radius of 30 arcsec. These values represent a considerable improvement with respect to the  $\sim 2$  arcmin uncertainty radius of the *BeppoSAX* Wide Field Camera and confirm the identity of the optical counterpart.

### 13.1.2 Timing

In revolution 19 (December 8–12, 2002, MJD 52617.39–52620.06), ISGRI data showed the peak of an outburst. The source was active during previous revolutions (as shown by *RXTE*/ASM data) but not detected because it was only marginally inside the field of view (FOV) and the observing mode was set to *staring*, i.e., pointing continuously in the same direction. The detection of SAXJ 2103.5+4545 extends to revolution number 20, although the detection level is too low. Another outburst peak was detected at the end of revolution 22 and in revolution number 23 (December 20–23, 2002, MJD 52629.36–52632.05), but this time the source was well inside the FOV. In about a dozen pointings, it was inside the fully coded FOV (FCFOV) of ISGRI. During revolution 24 (December 23–26, 2002, MJD 52632.34–52635.00), the satellite moved again away from the source, and

only at the end of this revolution (December 26, 2003) and during revolution 25 (December 26–29, 2002, MJD between 52635.37 and 52638.00); the source appears again. Table 1 gives a summary of the detections for all three high-energy instruments.

The peaks of the two type-I outbursts detected take place in revolution 19 and 23, i.e., they are separated by about 12 days, which corresponds to the value of the system orbital period (Fig. 13.1). The source lies below the detection level of the instruments between outbursts. This is the typical behaviour of type I outbursts seen in most BeX-ray binaries.

In Fig. 13.2 one-day averaged fluxes from *RXTE*/ASM (2–12 keV), ISGRI (20–40 keV) and SPI (20–40 keV) are shown, with normalised units in counts per second. *INTEGRAL* detections coincide with peaks in the orbital-modulated *RXTE*/ASM light curve. A careful look at the maxima of the outbursts shows that the second outburst is weaker than the previous one. It is also worth noting that the flux seems to increase after apastron passage (around MJD 52626 and around MJD 52637).

### 13.1.3 Pulse Period

Pulse period analysis is hindered by the low S/N. ISGRI light curve extraction in sub-science window time-scales does not give very good results for off-axis and weak sources. Thus only data from pointings in revolution 23, for which the source was in the FCFOV, were used. This makes a total of 17 pointings. A power spectrum is shown in Fig. 13.3. This power spectrum was obtained by using an accumulated list of events for all the 17 pointings. The maximum power is found for the frequency 0.00281678 Hz, consistent with the known pulse period of the system.

Once we confirmed the presence of pulsations, we carried out an epoch folding analysis of the entire 1-s binned light curve of revolution 23. The time-span of these observations is almost 2 days. The resulting pulse period is  $355.0 \pm 0.5$  seconds, in excellent agreement with that reported by Inam et al. (2004) of 354.794 seconds.

### 13.1.4 Spectral Analysis

For ISGRI and JEM-X, spectral extraction works on a per-pointing basis, hence all our spectra were extracted for individual pointings and later on

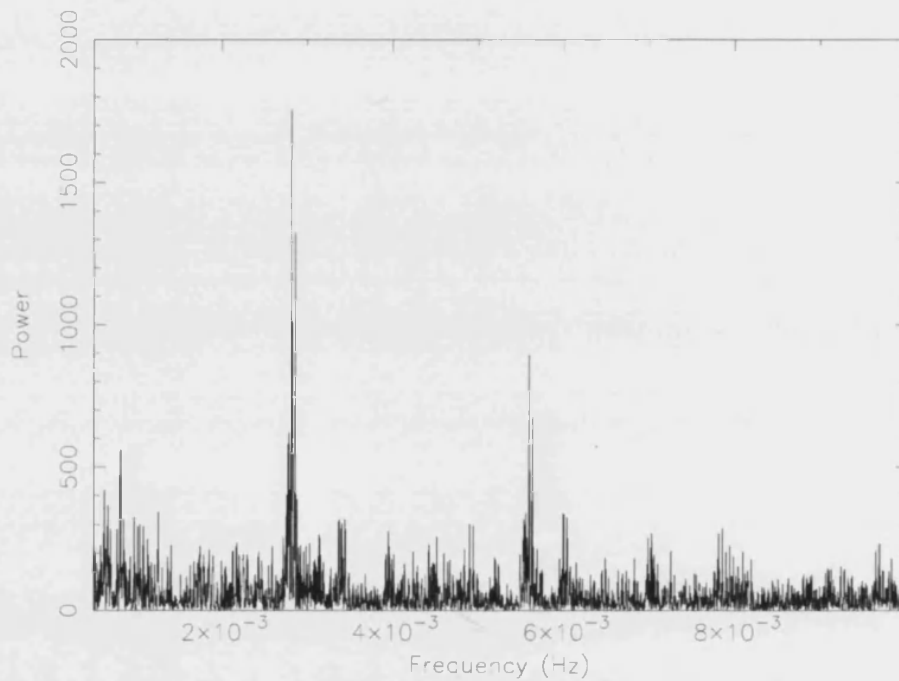


Figure 13.3: Power-spectrum for positive detections of SAX J2103.5+4545 inside the FCFOV of ISGRI during revolution number 23. The maximum power is achieved at  $\sim 0.00281678$  Hz.

Table 13.2: Spectral extraction summary. Values for a power-law fitting for all 3 instruments, JEM-X, ISGRI and SPI.  $\chi_{\text{red}}^2$  for a bremsstrahlung fit are also shown for comparison.

Instrument	Rev.	Energy Range (keV)	Flux ( $\times 10^{-10}$ ) erg cm $^{-2}$ s $^{-1}$	$\chi_{\text{red}}^2$ power law	$\chi_{\text{red}}^2$ bremsstrahlung
JEM-X	23	4–25	5.6	0.99	—
ISGRI	19	25–70	3.5	1.3	1.2
	23	20–150	5.3	1.1	1.1
	25	25–70	1.8	1.4	1.3
SPI	19	20–150	7.4	1.1	—
	23	20–150	8.3	1.3	—

summed up to build averages. In addition, ISGRI can provide reliable spectra only when the source is inside the fully coded field of view (FC-FOV). With SPI, for a source like SAX J2103.5+4545, in order to achieve a S/N of  $\sim 10$ , we need typically about 300 science windows, namely, a total integration time of around 550 ks. With these constraints, the number of "good" spectra reduces to 22 (17 from ISGRI, 1 from SPI and 4 from JEM-X). For SPI up to 2 can be obtained (averaged over a revolution and for revolutions 19 and 23) but in order to increase S/N we have used only the averaged spectrum for all December 2002. A summary of spectral extraction and flux values for a single power-law fit are presented in Table 13.2.

In order to search for medium-term spectral variability ( $\sim$ days) we obtained mean ISGRI spectra for revolutions 19, 23 and 25 (see Fig. 13.4 and Table 13.2). However, no significant changes were observed, within the errors. These spectra were equally well fitted by power law and bremsstrahlung models with photon index  $\Gamma = 2.5 \pm 0.1$  and  $kT = 36 \pm 4$  keV, respectively. A decrease in the 20–50 keV flux from revolution 23 to revolution 25 is apparent, though. We also searched for short-term spectral variability ( $\sim$ hours) by fitting a power-law model to each pointing of revolution 23 for which we could extract a spectrum (FCFOV observations). The photon spectral index remained constant, within the errors. A mean 20–100 keV flux of  $5.3 \times 10^{-10}$  erg cm $^2$  s $^{-1}$  was found. Table 13.3

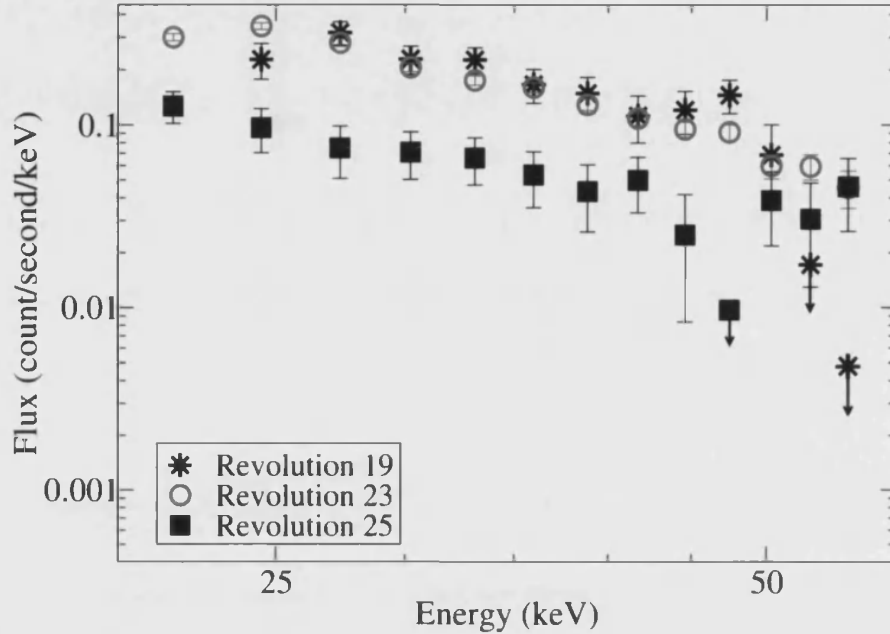


Figure 13.4: ISGRI SAX J2103.5+4545 spectra in revolutions 19 (stars), 23 (circles) and 25 (squares). Apart from a difference in flux no spectral variability is apparent. Downwards arrows denote upper limits.

gives the evolution of the power-law index during revolution 23.

A 4–150 keV combined spectrum from all three instruments is shown in Fig. 13.5, where the mean ISGRI and JEM-X spectra of revolution 23 and the mean SPI spectrum of the entire PV phase are shown. The spectrum was fitted with a power law plus an exponential cut-off, i.e., the photon flux density adopts the form,  $f(E) = KE^{-\Gamma}e^{(E_{\text{cut}}-E)/E_{\text{fold}}}$ , where  $K$  is a normalisation constant. No absorption was included because previously reported values of the hydrogen column density, namely ( $\sim 3.7 \times 10^{22} \text{ cm}^{-2}$ ), do not have any effect above 4 keV. The resulting best-fit parameters are  $\Gamma = 1.0 \pm 0.1$ ,  $E_{\text{fold}} = 30.9 \pm 2.5$  and  $E_{\text{cut}} = 7.6 \pm 2.0$  keV, consistent with previous published values (Baykal et al. 2002; İnam et al. 2004). The 4–150 keV X-ray flux,  $1.2 \times 10^{-9} \text{ erg cm}^{-2} \text{ s}^{-1}$  and the spectral photon index of  $1.0 \pm 0.1$  indicate that the source was in a bright state.

There seems to be some excess emission between 6 and 10 keV. The modest signal-to-noise ratio of the data, together with the moderate energy resolution of the instrument prevent us from identifying it as an iron line

Table 13.3: Time evolution of the spectral parameters (for a power-law fit) of SAX J2103.5+4545 using ISGRI data from revolution 23.

MJD	$\Gamma$	$\chi^2$	DOF
52629.91931	$2.4 \pm 0.3$	1.27	25
52630.13241	$2.3 \pm 0.3$	1.24	25
52630.15902	$2.6 \pm 0.3$	0.72	25
52630.18565	$1.9 \pm 0.5$	1.14	25
52630.21228	$1.9 \pm 0.3$	1.70	25
52630.37240	$2.1 \pm 0.5$	1.35	25
52630.39909	$2.2 \pm 0.2$	1.52	25
52630.42570	$2.5 \pm 0.3$	0.96	25
52630.45233	$2.2 \pm 0.3$	0.89	25
52631.25349	$2.4 \pm 0.5$	1.08	25
52631.46663	$2.6 \pm 0.4$	1.03	25
52631.49325	$2.4 \pm 0.4$	0.99	25
52631.51988	$2.3 \pm 0.4$	1.13	25
52631.54651	$2.2 \pm 0.3$	1.37	25
52631.79678	$2.5 \pm 0.4$	1.01	25
52631.82341	$2.6 \pm 0.4$	1.43	25
52631.85004	$2.3 \pm 0.4$	1.30	25

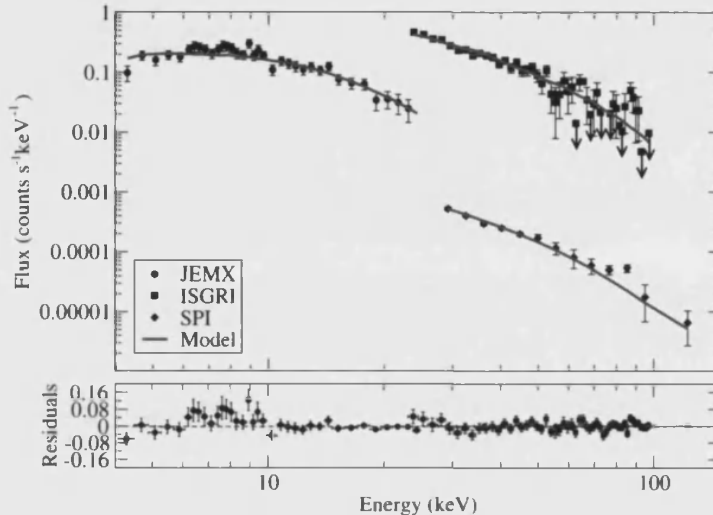


Figure 13.5: Fit to joint JEM-X, ISGRI and SPI spectra. JEM-X and ISGRI spectra are mean spectra for revolution 23. For SPI a mean spectrum for December 2002 is used.

feature or absorption edge. Nevertheless, although the presence of an iron line has been reported in the past (Baykal et al. 2002) the soft excess is likely to be an artifact of the reduction process. Sources in the outer field of view of JEM-X are more strongly affected by vignetting correction and error estimation since they only illuminate a small fraction of the detector. This applies to SAX J2103.5+4545, with the closest angular distance to on-axis position being  $\sim 2$  degrees.

## 13.2 GPS Long term analysis: the nature of the system

### 13.2.1 Imaging

We have made use of publicly available data from GPS revolution 31 up to revolution 181. The source coverage with *INTEGRAL* is not very extensive, due both to the *INTEGRAL* observing plan (GPS scans) and the transient nature of the source. There must be coincidence of a GPS

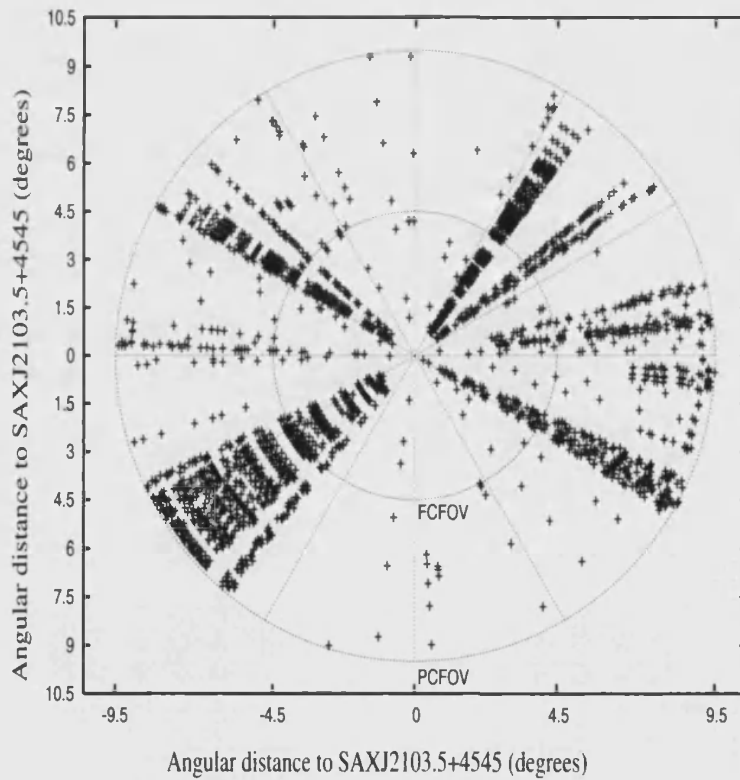


Figure 13.6: Representation of all the pointings in which the source (in the middle of the plot) lies within the field of view of the ISGRI instrument. The inner circle encloses those pointing in which the source lies within the FCFOV of the ISGRI instrument.



scan around the source location with the occurrence of an outburst in order to allow *INTEGRAL* detectors to collect photons from the source. In Fig. 13.6 we show the closest pointings to the source from which is very likely that *INTEGRAL* detectors can collect data from it. We have shown two circles, the inner one encloses all the *INTEGRAL* pointings for which the source is within  $4.5^\circ$  of the centre of the FOV (the FCFOV of ISGRI is a box of  $9^\circ \times 9^\circ$ ). The outer circle encloses all the pointings in which the source lies within the FOV of ISGRI ( $19^\circ \times 19^\circ$ ). The structure seen in the distribution of the pointings is related to the dithering patterns used during observations.

Table 13.4 summarises ISGRI and JEM-X detections of the source during GPS revolutions from 31 up to 181. We see that in most cases the source is not detected. This is due to the transient nature of the source. It will be detected by *INTEGRAL* only during the brightest moments of an outburst. As an example, ISGRI sensitivity at 25–40 keV is  $2.5 \text{ counts s}^{-1}$ . Up to revolution 87, the source was in the bright state; from revolution 88 on, the source flux went down to that typical of the faint state. This results in the decreasing number of detections of the source after revolution 87.

Due to the way in which SPIROS extracts fluxes, instead of detections per science window we have produced a list of SPI detections per revolution, see Table 13.5.

Table 13.4: Summary of ISGRI and JEM-X detections during GPS scans from revolution 31 up to revolution 181 (publicly available data). Bold face numbers indicate  $3\sigma$  upper limits of the count rate for those science windows where the detection level is very low or there are doubts about the detection of the source.

MJD	Exposure (s)	ISGRI (25-40 keV)		JEM-X (5-25 keV)	
		Count Rate (count s <sup>-1</sup> )	Detection Level	Count Rate (count s <sup>-1</sup> )	Off Axis angle (deg)
52653.3467	4090.0021	<b>2.8</b>	–		2.9
52653.3855	2200.0012	<b>1.4</b>	–		8.1
52722.8599	2199.0011	$2.7 \pm 0.3$	8.2		5.0
52722.8879	2201.0011	$3.3 \pm 0.3$	11.6	$3.4 \pm 0.2$	1.6
52722.9166	2312.0011	$2.6 \pm 0.3$	8.4		7.1

*Continued...*

Table 13.4: Continued.

MJD	Exposure (s)	ISGRI		JEM-X	Off Axis angle (deg)
		Count Rate (count s <sup>-1</sup> )	Detection Level	Count Rate (count s <sup>-1</sup> )	
52737.0515	2875.0014	<b>1.4</b>	–		9.0
52737.0833	2200.0011	2.6±0.3	8.0		5.0
52737.1113	2200.0011	<b>2.0</b>	–		6.4
52746.1105	2201.0011	3.9±0.3	12.1		6.0
52746.1385	2201.0010	3.7±0.3	12.6		5.7
52746.1664	2199.0010	3.8±0.4	9.4		7.4
52761.2734	2201.0012	3.0±0.3	9.5		5.1
52761.3012	2200.0012	3.4±0.3	10.7		5.1
52761.4247	2200.0011	<b>2.2</b>	–		9.3
52761.4517	2200.0011	<b>2.7</b>	–		8.7
52761.4786	2200.0011	<b>2.5</b>	–		8.5
52761.5055	2200.0011	3.6±0.5	7.8		8.8
52761.5324	2200.0011	<b>2.2</b>	–		6.9
52761.5593	2200.0010	2.6±0.4	7.1		6.5
52761.5863	2200.0010	2.8±0.4	7.9		6.7
52761.6132	2201.0010	<b>2.6</b>	–		7.5
52761.6669	2200.0010	3.6±0.3	10.5		7.3
52761.6938	2201.0010	3.8±0.3	12.4		5.8
52761.7208	2201.0010	3.4±0.3	11.2		4.8
52761.7477	2201.0010	4.0±0.3	12.6		4.5
52761.7746	2201.0010	<b>3.0</b>	–		5.1
52761.8015	2199.0010	3.8±0.3	12.0		3.4
52761.8284	2200.0010	2.8±0.3	9.1		2.5
52761.8554	2200.0010	2.9±0.3	9.6		3.0
52761.8823	2201.0010	3.2±0.3	10.8		4.5
52761.9092	2200.0010	2.5±0.3	7.6		6.2
52761.9361	2199.0010	2.4±0.3	7.4		5.7
52761.9630	2200.0010	2.8±0.3	9.9		3.7
52761.9900	2200.0010	3.8±0.3	13.1	3.4±0.2	1.8
52762.0169	2200.0010	3.4±0.3	11.8	3.9±0.2	0.6
52762.0438	2200.0010	3.0±0.3	9.3	2.9±0.2	2.4
52762.0707	2201.0010	2.5±0.3	8.6	3.5±0.2	0.6
52762.0977	2200.0010	2.8±0.3	9.9	3.5±0.2	1.8
52762.1246	2200.0011	2.6±0.3	9.2		3.7

*Continued...*

Table 13.4: Continued.

MJD	Exposure (s)	ISGRI		JEM-X	Off Axis angle (deg)
		Count Rate (count s <sup>-1</sup> )	Detection Level	Count Rate (count s <sup>-1</sup> )	
52762.1515	2200.0011	2.7±0.3	8.2		5.7
52762.1784	2199.0011	3.0±0.3	9.3		6.2
52762.2053	2201.0011	3.0±0.3	10.0		4.5
52762.2323	2200.0011	2.9±0.3	9.6		3.0
52762.2592	2200.0011	2.5±0.3	8.0		2.5
52762.2952	3780.0018	3.7±0.2	15.5		3.4
52762.3313	2199.0011	2.5±0.3	7.6		5.1
52762.3582	2200.0011	3.3±0.3	10.4		4.5
52762.3851	2201.0011	2.4±0.3	7.7		4.8
52762.4260	4602.0022	3.0±0.2	13.5		5.8
52770.0633	2201.0011	5.0±0.3	16.8		3.5
52770.0912	2200.0011	5.0±0.3	16.9		2.6
52770.1190	2201.0011	3.8±0.5	8.6		8.6
52782.0472	2201.0011	3.1±0.4	7.1		9.0
52782.0751	2201.0011	3.1±0.3	10.9		3.1
52782.1029	2201.0011	4.4±0.3	14.3		3.0
52782.1307	2200.0011	5.1±0.5	9.8		9.0
52797.0271	2201.0010	3.3±0.3	10.2		5.3
52797.0549	2200.0010	2.9±0.3	9.2		4.6
52797.0827	2201.0010	3.6±0.5	7.1		9.3
52801.4109	3450.0018	<b>1.1</b>	–		8.8
52801.4520	3449.0018	<b>1.0</b>	–		9.3
52801.7603	3450.0018	<b>1.1</b>	–		8.6
52801.8836	3450.0017	<b>2.3</b>	–		4.9
52801.9247	3449.0017	<b>1.4</b>	–		5.8
52801.9659	3450.0017	<b>1.9</b>	–		7.2
52802.1716	3449.0017	<b>2.3</b>	–		6.1
52802.2177	4308.0021	<b>2.2</b>	–		4.4
52802.2638	3449.0017	<b>2.1</b>	–		3.1
52802.3053	3518.0017	<b>8.5</b>	–	<b>1.8</b>	1.6
52802.3357	1747.0009	2.6±0.3	7.8		1.6
52802.3986	5438.0027	1.9±0.2	8.0		5.5
52805.9493	2200.0011	2.4±0.3	7.1		5.7
52805.9771	2200.0011	2.4±0.3	7.3		5.8

*Continued...*

Table 13.4: Continued.

MJD	Exposure (s)	ISGRI		JEM-X	Off Axis angle (deg)
		Count Rate (count s <sup>-1</sup> )	Detection Level	Count Rate (count s <sup>-1</sup> )	
52806.0049	2200.0011	<b>2.7</b>	–		7.8
52820.9019	2200.0011	<b>1.7</b>	–		8.6
52820.9297	2201.0011	2.5±0.3	8.1		5.0
52820.9576	2201.0011	<b>2.2</b>	–		6.9
52985.4499	2200.0011	–	–	1.6±2	1.2
52994.4126	2200.0011	–	–	<b>1.5</b>	2.3
53018.6935	1980.0012	–	–	<b>1.4</b>	2.3
53020.0327	2200.0011	–	–	<b>1.2</b>	2.4
53020.1938	2202.0011	–	–	<b>0.7</b>	1.8
53020.2206	2202.0011	–	–	<b>1.1</b>	0.5
53020.2475	4781.0025	–	–	<b>1.4</b>	2.3
53020.3039	2611.0014	–	–	<b>0.8</b>	1.8
53020.5817	3534.0018	–	–	<b>1.2</b>	2.3
53020.6226	2048.0011	–	–	<b>0.8</b>	2.3
53020.6646	2204.0011	–	–	<b>0.8</b>	0.5
53020.6915	2200.0011	–	–	<b>1.2</b>	1.8
53022.6964	540.0003	–	–	<b>1.5</b>	2.4
53023.5799	3055.0016	–	–	<b>1.2</b>	2.4
53023.7510	2203.0012	–	–	<b>1.0</b>	1.7
53036.2041	2201.0012	–	–	<b>1.0</b>	0.5
53036.2310	2201.0012	–	–	<b>1.5</b>	1.7
53036.3925	2199.0012	–	–	<b>1.6</b>	2.4
53037.2538	2200.0012	–	–	<b>1.1</b>	2.4
53037.4153	2201.0012	–	–	<b>1.2</b>	1.7
53037.4422	2201.0012	–	–	<b>0.8</b>	0.5
53037.4692	2202.0012	–	–	<b>1.8</b>	2.4
53037.4961	3780.0020	–	–	<b>0.9</b>	0.5
53037.5413	2199.0012	–	–	<b>1.2</b>	1.7
53037.7128	2200.0012	–	–	<b>1.4</b>	2.4
53039.2237	2201.0012	–	–	<b>1.9</b>	2.4
53039.2506	2202.0012	–	–	<b>0.9</b>	0.5
53039.2776	2199.0012	–	–	<b>1.7</b>	1.7
53039.4391	2200.0012	–	–	<b>1.7</b>	2.4
53040.3007	2200.0012	–	–	<b>1.6</b>	2.4

*Continued...*

Table 13.4: Continued.

MJD	Exposure (s)	ISGRI		JEM-X	
		Count Rate (count s <sup>-1</sup> )	Detection Level	Count Rate (count s <sup>-1</sup> )	Off Axis angle (deg)
53040.4623	2202.0012	–	–	<b>0.8</b>	1.7
53040.4892	2313.0012	–	–	<b>0.9</b>	0.5
53040.5344	2203.0012	–	–	<b>1.4</b>	2.4
53040.5613	2202.0012	–	–	<b>1.0</b>	0.5
53040.5883	2199.0012	–	–	<b>1.0</b>	1.7
53040.7598	2201.0012	–	–	<b>1.2</b>	2.4
53045.6337	2200.0012	–	–	<b>1.2</b>	1.3

### 13.2.2 Modulation of type-I outbursts

Light curves were built for all the instruments using the following energy ranges:

- *RXTE*/ASM: 2–12 keV
- JEM-X: 5–15 keV
- ISGRI: 15–25 keV, 25–40 keV, 40–60 keV, and 60–80 keV
- SPI: 20–44 keV

The SPI light curve in the 20–44 keV energy range is shown in Fig. 13.7. Within the uncertainty of the large errors, it seems to follow the same trend as in ISGRI and *RXTE*/ASM data.

The result for ISGRI and JEM-X is shown in Fig. 13.8. We notice there the high variability of the source in all energy ranges. When there is simultaneous coverage by *RXTE*/ASM and ISGRI of one of the type-I outbursts, the time of the maxima is coincident in both data sets. When the detection level of JEM-X or ISGRI was not enough for a reliable detection,  $3\sigma$  upper limits have been plotted with downwards triangles (for both instruments).

Something interesting revealed by this plot (Fig. 13.8) is the apparent variation of the intensity of the type-I outbursts. The intensity of the maxima of the type-I outburst increases until it reaches a maximum and

then decreases again until a faint phase is reached. This is evident also in Fig. 13.9, where *RXTE*/*ASM* data rebinned to 12.68 days (the duration of an orbit) are plotted. Each datum represents, thus, the integrated flux over an orbit. This modulation is clearly visible in *ISGRI* data in all energy ranges (from 15 up to 80 keV).

From a more detailed inspection of the last bright state of the source (seen almost in entirety by *INTEGRAL* instruments), we can corroborate the modulation of the outburst maxima. This can be seen in Fig. 13.10, where we have indicated by an horizontal dashed line the maxima of the outbursts of *RXTE*/*ASM* data, for the sake of clarity. The maximum flux is reached for the same outburst in both *ISGRI* and *RXTE*/*ASM* data. It can be argued that this conclusion cannot be derived from *ISGRI* data due to the partial coverage of the outburst. It is possible that we are observing the source only at the beginning or the very end of the outburst in our observations. This is partially true. We calculated the occurrence of the outburst taking as reference the maxima of the outburst during PV phase (i.e., MJD 50550.71, see previous section) and the updated orbital period of Sidoli et al. (2005). In Table 13.6 the averaged MJD of each *INTEGRAL* observation is compared with the predicted time of the outburst maxima. Only in one case, revolution 67, *ISGRI* seems to have missed the peak of the outburst. In this case we have detected the decay of the outburst.

Table 13.5: Summary of SPI detections from GPS core program observations between revolution 31 and revolution 181. The flux is given in mCrabs for the 20–44 keV energy range. Fluxes in bold-face indicate upper limits.

Rev.	MJD	Flux (mCrab)	Rev.	MJD	Flux (mCrab)
31	52653.3	$38.5 \pm 16.7$	82	52805.9	$39.0 \pm 10.4$
54	52722.8	$48.0 \pm 13.0$	87	52820.9	$52.5 \pm 9.2$
59	52737.1	$30.6 \pm 13.6$	92	52836.0	<b>10.0</b>
62	52746.2	$60.1 \pm 11.6$	153	53020.2	$8.6 \pm 4.2$
67	52761.8	$46.9 \pm 3.5$	154	53023.3	$10.9 \pm 3.6$
70	52770.1	$53.2 \pm 10.2$	159	53037.6	$7.1 \pm 4.0$
74	52782.1	$24.6 \pm 10.0$	160	53040.0	$13.1 \pm 4.0$
79	52798.1	$22.8 \pm 8.3$	162	53045.7	<b>6.0</b>
80	52801.4	<b>3.8</b>			

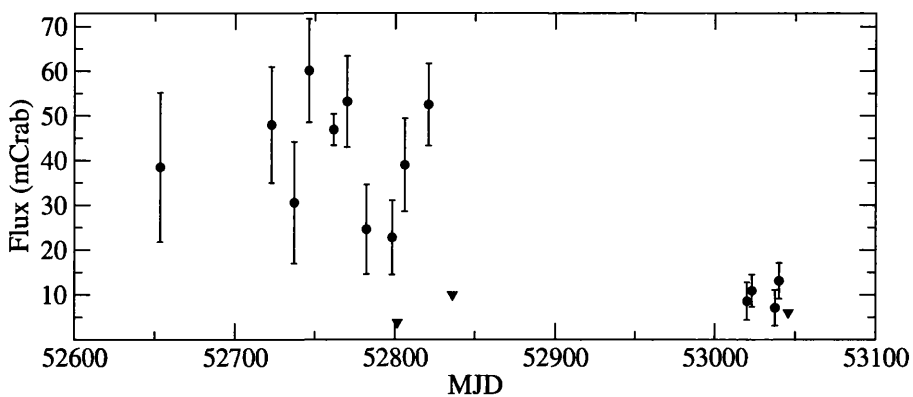


Figure 13.7: 20–44 keV SPI light curve of SAX J2103.5+4545 from GPS pointings, from revolution 31 up to revolution 162. Downwards triangles indicate upper-limits.

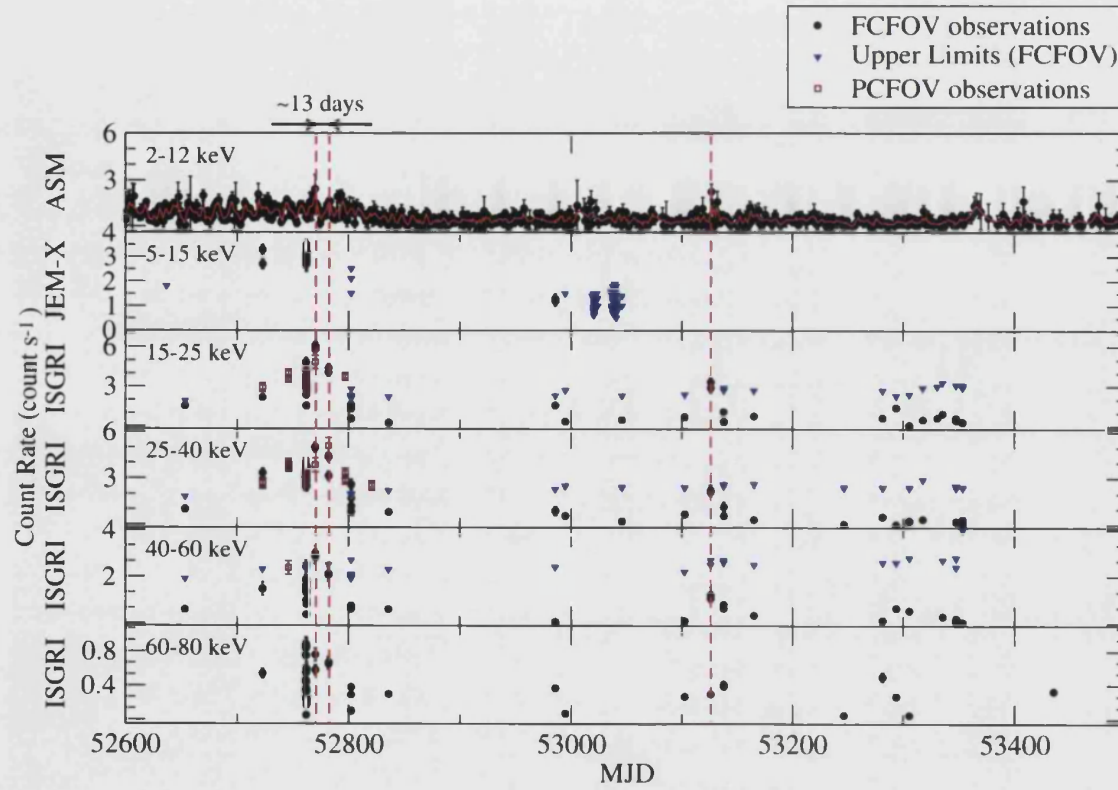


Figure 13.8: Long term light curves of JEM-X and ISGRI instruments, together with *RXTE*/ASM count rate for all the GPS scans from revolution 31 up to revolution 181. Upper limits are plotted (downwards triangles) when the detection was not significant enough to be considered reliable. For ISGRI data, FCFOV observations are differentiated from PCFOV observations.



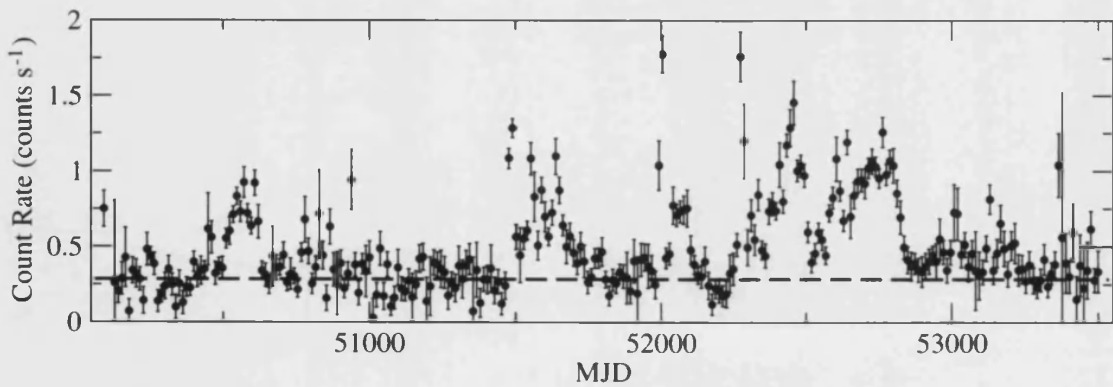


Figure 13.9: *RXTE*/ASM long-term light curve rebinned to 12.68 days (the orbital period of the system). We notice the modulation of the maximum flux achieved during each type-I outburst. The horizontal dashed line indicates the average flux while in the faint state.

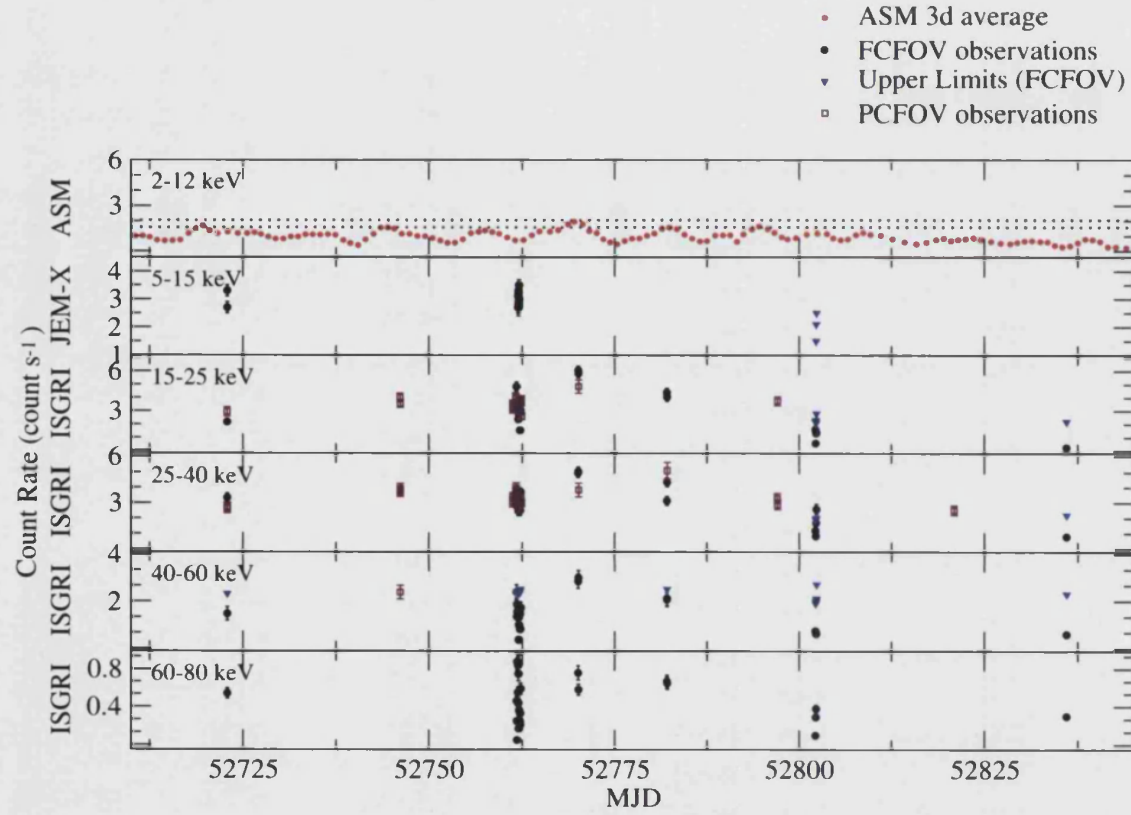


Figure 13.10: Detailed view of the bright state seen by ISGRI. *RXTE*/ASM data is also shown, with an horizontal dashed line indicating the top of orbital outburst at maximum emission, for the sake of clarity. The modulation of the maximum flux of type-I outbursts is clearly seen in both ISGRI and *RXTE*/ASM data.

Table 13.6: Comparison of the MJD of the maximum flux of the type-I outbursts detected by ISGRI to the MJD of the predicted occurrence of the outbursts' maxima, according to the refined orbital period of Sidoli et al. (2005) and the epoch of the maximum detected by ISGRI during PV phase (MJD 52618.73, during revolution 23).

Revolution	MJD of ISGRI peak	MJD of ASM peak	Predicted MJD of Type-I outburst peak
54	52720	52719	52719
62	52746	52745	52745
67	52761	52757	52757
70	52770	52770	52770
74	52782	52783	52783
79	52797	52795	52795
87	52821	52820	52821

One striking result is a possible modulation on the order of  $\sim 5$  hours which is seen in ISGRI data from revolution 67 specially in the 25–40 keV energy range (see Fig. 13.11). Unfortunately *RXTE*/ASM and JEM-X coverage are poor in this time interval, but the few data available from these two instruments seem to confirm this modulation. However, we must keep in mind that this modulation coincides just with the coverage of 10 pointings, which are one way up and one way down of the  $5 \times 5$  dithering pattern used by *INTEGRAL* during GPS scans. The possibility that systematics can introduce bigger error must also be taken into account. The finding of this modulation is not conclusive, but it is something which needs further investigation.

### 13.2.3 Orbital variability

Something interesting which deserves also a deeper analysis is the flux increase observed after apastron. In Fig. 13.12 data from ISGRI, SPI, and *RXTE*/ASM are folded in phase, using the orbital epoch of İnam et al. (2004) and the new determination of the orbital period of Sidoli et al. (2005). In Baykal et al. (2002) apastron is reported to be at phase  $\sim 0.40$ .

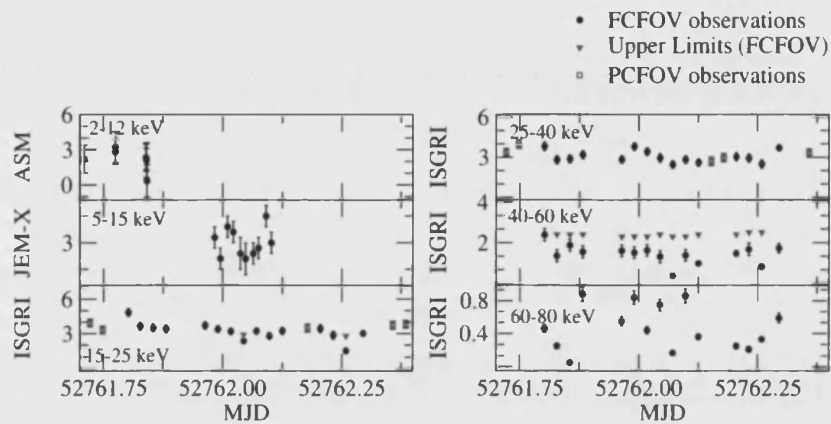


Figure 13.11: Light curve of *RXTE*/ASM data in dwell by dwell binning together with JEM-X and ISGRI data in the energy intervals indicated at the top left corner of each panel. A modulation of the order of  $\sim 5$  hours seems to be present in ISGRI data and supported by JEM-X and *RXTE*/ASM data.

Translating their apastron by imposing the orbital epoch and period considered here, we find that apastron will lie close to phase  $\sim 0.42$  in Fig. 13.12. We see that ISGRI and SPI data show an apparent second peak at phase close to  $\sim 0.1$ , i.e., roughly after apastron passage. This peak is not so evident in the *RXTE*/ASM data.

The dependence of the shape of the folded light curve, at the orbital period, with energy is shown in Fig. 13.13. While the shape of the profile remains unchanged, the amplitude decreases with energy, from 4.5 in the 15–25 keV energy range to 0.7 at the 60–70 keV energy range.

Periastron passage, as explained above, is indicated in Fig. 13.13 with a dashed vertical line. Caution must be taken in considering this as the real position of the periastron. Due to the error in the determination of the orbital epoch and the orbital period it is possible that periastron passage is displaced from the position marked in Fig. 13.13. Nevertheless, the marked position of periastron is in agreement with the onset of the outburst right after the neutron star passes through this position.

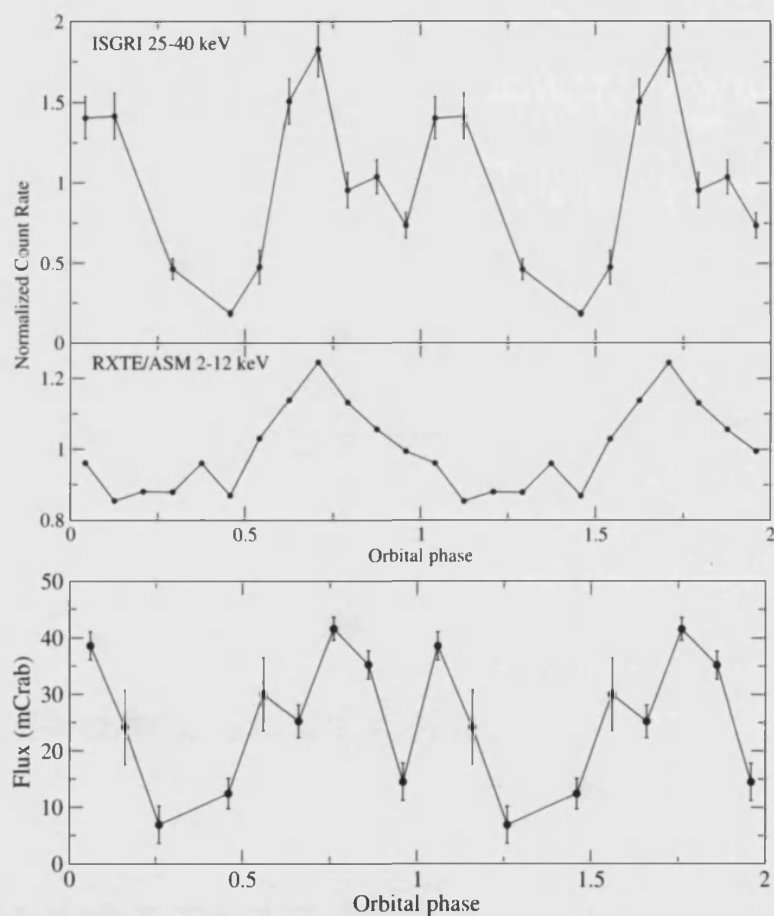


Figure 13.12: **Upper Panel:** Folded light curve of ISGRI data (25–40 keV) and *RXTE*/ASM data (2–12 keV). The orbital epoch was taken from 2004 but the orbital period is that of Sidoli et al. (2005). **Lower Panel:** Folded light curve of SPI data (20–44 keV) (with the same orbital period and epoch as in the upper panel).

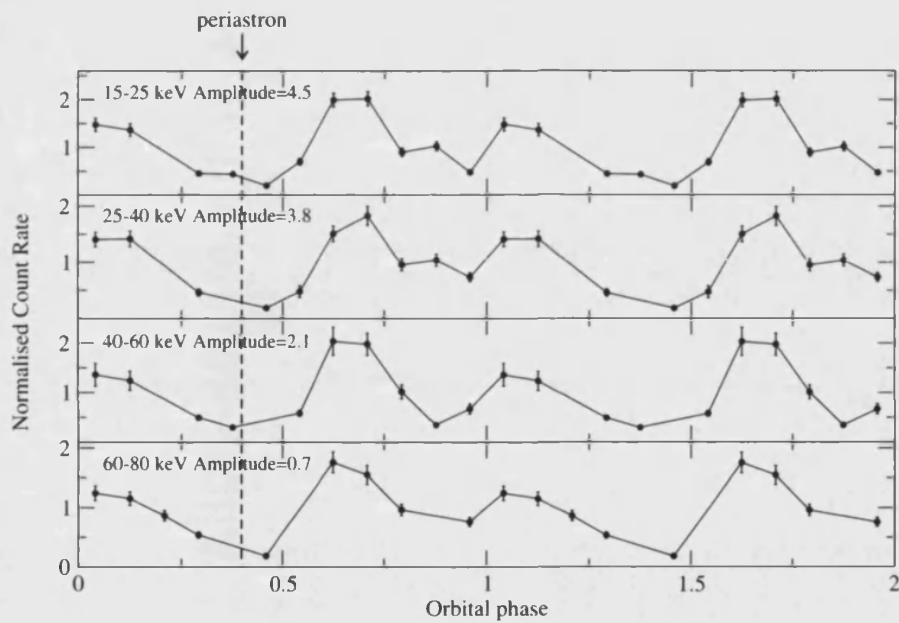


Figure 13.13: Folded light curve of ISGRI data in all energy ranges used in the analysis of this chapter. The ephemeris used are the same as in Fig. 13.12. Periastron passage, according to the estimate of Baykal et al. (2000) is indicated by a vertical dashed line.

### 13.2.4 Hardness ratios

All along this subsection the following definition of hardness ratio will be used:

$$HR = \frac{C_H - C_L}{C_H + C_L}$$

where  $C_H$  stands for the count rate of the higher energy band and  $C_L$  for the count rate of the lower energy band. The energy bands used are: 15–25 keV, 25–40 keV, 40–60 keV, and 60–80 keV.

In Fig. 13.14 the variation of several hardness ratios with time is shown. We see that the large variability seen in the count rate is not reflected in the hardness ratios. Dashed lines are indicating the average of each hardness ratio. We notice that the main bulk of measurements are gathered around this average. We find some positive points, which indicate that some measurements are dominated by background. The main background peaks for ISGRI are located at  $\sim 25$  keV (Ag activation and decay) and  $\sim 60$  keV (W activation and decay), and affect a range of  $\sim 10$  keV around the peak.

In Fig. 13.15 the hardness ratios as a function of the 25–40 keV count rate are shown. We can differentiate clearly 3 different zones in this plot. Data points to the left of the red vertical line represent measurements which are clearly affected by background (i.e. where the source count rate was not extracted properly). The zone between the red vertical line and the green vertical line is occupied by measurements where the source is suffering a process of softening. This process is very short in terms of count rate range. Finally, the zone to the right of the green vertical line contains measurements where the hardness ratio is nearly constant. The source suffers a process of softening when it increases count rate but, when a certain count rate is reached, the softening saturates and the hardness ratio keeps constant. Above a certain flux ( $>1.7$  count  $s^{-1}$ , in the ISGRI 25–40 keV energy range) the source keeps its spectral shape independently of the variations of the flux. This last fact is supported by the spectral observations (see the sections below) and by the results of Baykal et al. (2000), who found two spectral states, one characterised by a harder photon index when the source was in the faint state, and the other

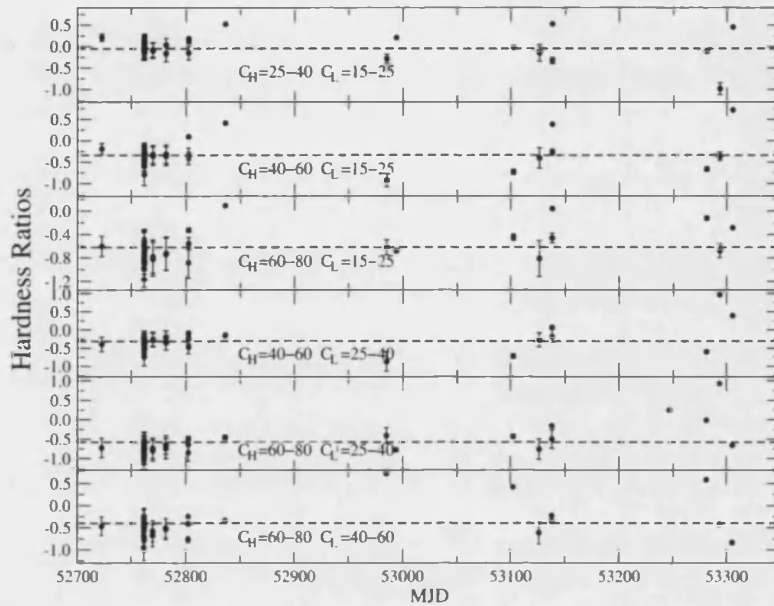


Figure 13.14: History of hardness ratios along *INTEGRAL* GPS scans observations from revolution 31 up to revolution 181.

characterised by a softer photon index when the source was in the bright state. Apart from these two spectral states, no other spectral change has been reported up to know in the literature.

### 13.2.5 Pulse Period

For JEM-X, only revolution 67 allows us to perform a timing analysis with a time resolution of  $\sim 1$  s. In revolution 54 only one science window is available and it was found not to produce reliable results. Initially a list of events in the JEM-X full energy range was obtained, but to optimise the S/N of the data, the 5–25 keV energy range was selected. A total of 5 consecutive science windows were joined, with a total time coverage amounting to 11.5 ks. The science windows used are those of revolution 67 shown in Table 13.4. Before performing the timing analysis, data were transformed to a heliocentric frame of reference and the arrival times were corrected for the orbital motion. Then a periodogram was obtained and once the presence of the pulse period was confirmed, epoch-folding techniques were used to find a more accurate value (using the



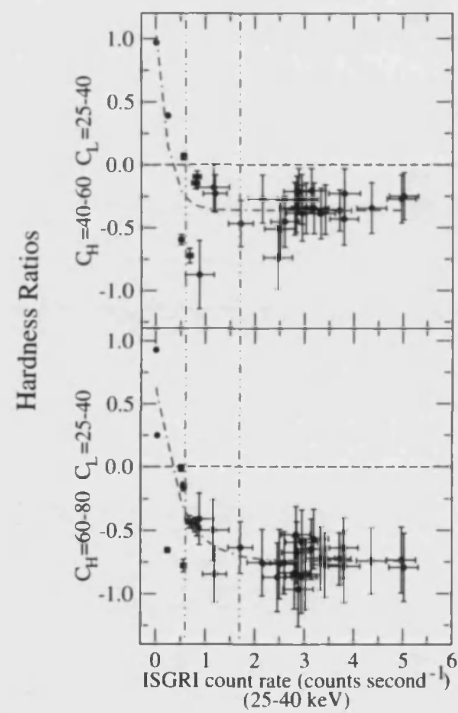


Figure 13.15: ISGRI hardness ratios along *INTEGRAL* GPS scans observations from revolution 31 up to revolution 181 versus ISGRI count rate in the 25–40 keV energy range.

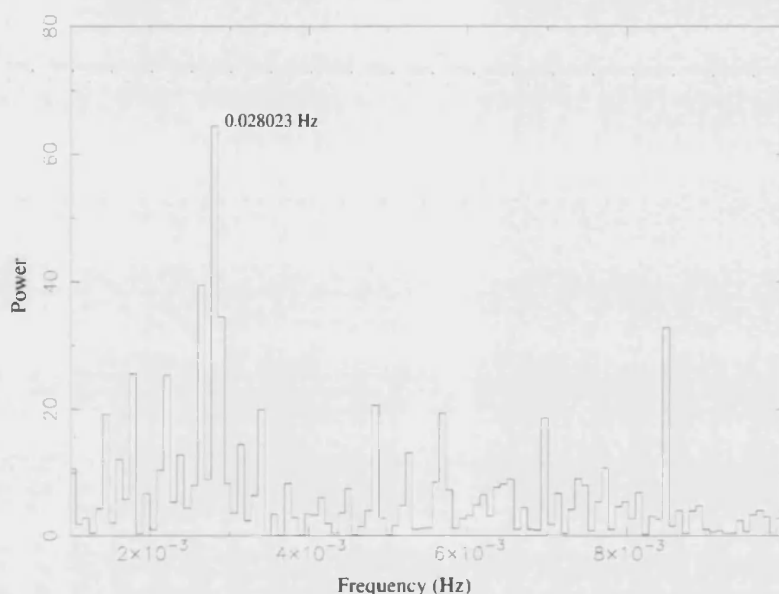


Figure 13.16: Power spectrum of the 11.5 ks long light curve obtained after joining JEM-X events extracted from 5 consecutive science windows during revolution 67 in the 5–25 keV energy range.

software package EFSEARCH within the FTOOLS). The power spectrum of the JEM-X revolution 67 time series is shown in Fig. 13.16.

A peak is seen at a frequency of 0.00280023 Hz. This frequency corresponds to a periodical variability on the order of  $\sim 356$  s. A deeper analysis with EFSEARCH yielded a pulse period of  $353.0 \pm 0.1$  s. Data were folded using this period and the result is shown in Fig. 13.17.

It must be noticed that the main peak of the pulsation lasts for about 60% for the orbital period (the so-called duty-cycle of the pulse period in HMXRBs). A secondary peak is also visible with a phase difference of  $\sim 0.4$  with respect to the main peak and a relative intensity of 0.95 (ratio of secondary peak intensity to the main peak intensity).

In order to obtain light curves in higher energy bands with ISGRI data, we used a PIF-based event extraction method. As a first step we grouped all the data per revolution and obtained a pulse period and pulse profile in the 25–45 keV energy range for each revolution. In Fig. 13.18 DFT and FFT periodograms are shown for revolutions 67 and 70 and Table 13.7 shows all the pulse periods measured.

The observations with larger errors are those where the amount of data

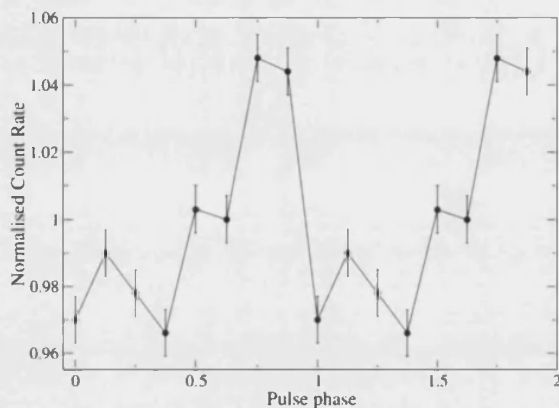


Figure 13.17: Folded light curve of JEM-X events list using the  $353.0 \pm 0.1$  s pulse period.

Table 13.7: Measurements of the pulse period with ISGRI data for all the GPS revolutions, from 31 up to 181, for which there was timing data available.

Rev.	MJD	Exposure (ks)	Pulse Period (s)
67	52762.53	34.6	$353.34 \pm 0.01$
70	52770.56	4.4	$354.6 \pm 0.5$
74	52782.58	4.4	$351.7 \pm 0.5$

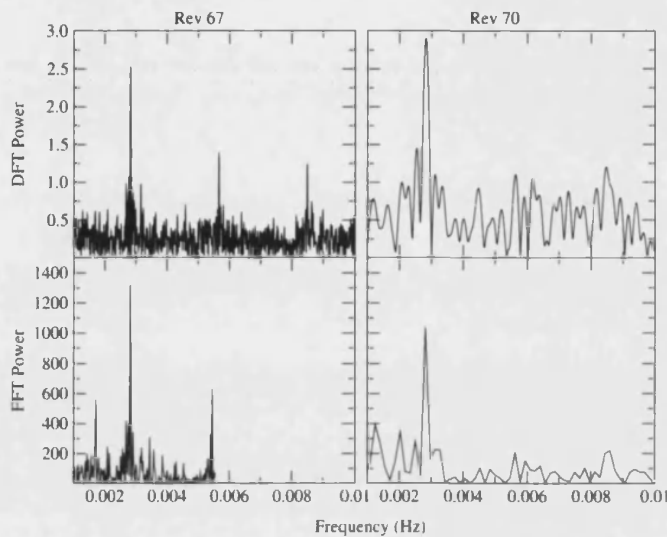


Figure 13.18: DFT and FFT for ISGRI data from revolutions 67 and 70. The peaks at the frequency which corresponds to the pulse period are clearly seen. In the revolution 67, some harmonics of the pulse period can also be seen. This is not the case of the more noisy data from revolution 70. There is a feature in the FFT of revolution 67 data at  $\sim 0.001$  Hz which is not present in the DFT.

was smaller. Fig. 13.19 shows the data sets for each revolution folded in phase with the calculated periods shown in Table 13.7.

The pulse shows a double-peak profile. No variations in the shape or amplitude of the folded light curves are seen, except in revolution 74, in which the pulse profile looks significantly different than in revolutions 67 and 70. The rise of the main peak seems to be faster than the decay in every case.

These data show evidence of a short spin down episode. Another epoch of spin down was observed by Baykal et al. (2002) during the November 1999 outburst. It is possible that the source is continuously undergoing spin up and spin down processes, the lack of coverage may be biasing our measurements and only an overall spin up trend has been detected until. The possible pulse period evolution presented here would be as follows:

- At MJD 52762.53 (during revolution 67) a  $353.34 \pm 0.01$  s pulse period is found.

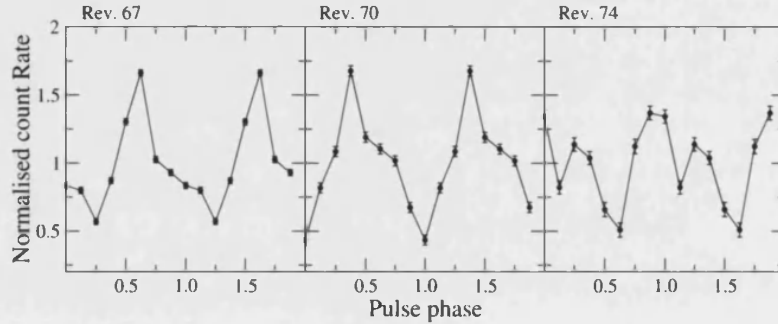


Figure 13.19: Folded light curves of the ISGRI extracted events for revolutions 67, 70, and 74. Data from each revolution was folded according to the pulse period shown in Table 13.7. All data was normalised to the average count rate in each revolution.

- The source slowed down to the  $354.6 \pm 0.5$  s pulse period at MJD 52770.56 (during revolution 70).
- The source spun up to reach the  $351.7 \pm 0.5$  s at MJD 52782.58 (revolution 74).

Within errors, these measurements are compatible with a spin down process between MJD 52762.73 (end of revolution 67) and MJD 52770.56, although this result is not conclusive. While the pulse periods obtained for revolutions 67 and 74 are in good agreement with those of Sidoli et al. (2005), the one measured for revolution 70 is different from the one they find with ISGRI data (for MJD 52770.10). However there is a good agreement between our ISGRI pulse period and their JEM-X pulse period for the same MJD. The pulse period evolution during the time span under study in this section is shown in Fig. 13.20, where data from revolution 67 has been split in 3 sets as explained below and shown in Table 13.8.

From revolution 54 only one science window was used, thus the measurement corresponding to this revolution is less reliable than the rest of revolutions. Therefore, we did not try to obtain a measurement of the pulse period from this data set.

### 13.2.6 Pulse period evolution on short time scales

We have tried to search for shorter time-scale variations in the pulse period. Because we have a good coverage along revolution 67, we divided all

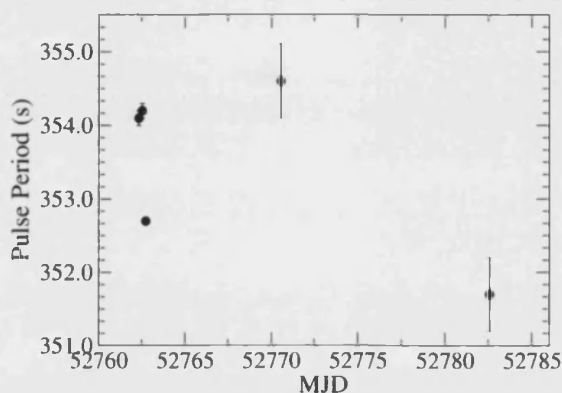


Figure 13.20: Pulse period evolution during the time span between revolutions 67 and 74 as obtained from ISGRI data. A very steep spin up followed by a strong spin down is suggested by the data. The errors shown in revolution 67 data represent the resolution of the epoch folding method used, however, they are clearly underestimated.

the data in 3 sets composed by consecutive science windows. Light curves with a time resolution of 10 s were obtained for each individual set. Table 13.8 shows the measurements of the pulse period and amplitude of the variation for each one of these sets. The average of these measurements ( $353.7 \pm 0.5$ ) is compatible with the averaged pulse period measured for the whole revolution 67 data, as shown in Table 13.7.

In revolution 67 the *INTEGRAL* instruments monitored the falling of a type-I outburst. During this decay, the neutron star spun up, although at a non-uniform rate. The folded light curves can be seen in Fig. 13.21. Each interval was folded by using the appropriate pulse period (see Table 13.8) and the MJD 52762.0 as the time reference. Note the large spin period change from MJD 52762.53 (342.2 s) to MJD 52762.73 (352.7 s). It may be difficult to believe that in a  $\sim 5$  hours interval the source increased its spin rate in 1.5 s. However we want to stress out that the average value of all three measurements of the spin period in the three intervals of revolution 67 coincides with the pulse period measured when the whole revolution 67 data set is taken into account. Moreover, this averaged value is lower (namely  $\sim 353$  s) than the pulse period measured during the first two intervals of revolution 67 (science window intervals 32–35 and 38–44). Stark et al. (2004) reported the occurrence in SAX J2103.5+4545 of two of these sudden increases of the pulse period frequency (glitches), with a

Table 13.8: Measurements of the pulse period along revolution 67 with ISGRI data. Three sets of data with consecutive science windows were used to study the pulse period changes. The errors reproduced here correspond to the resolution of the epoch folding method used, however, they are clearly underestimated.

Science windows	MJD	Exposure (ks)	Pulse Period (s)	Amplitude
32–35	52762.33	8.8	$354.1 \pm 0.1$	$\sim 1.1$
38–44	52762.53	15.4	$354.2 \pm 0.1$	$\sim 1.2$
47–50	52762.73	10.4	$352.7 \pm 0.1$	$\sim 1.2$

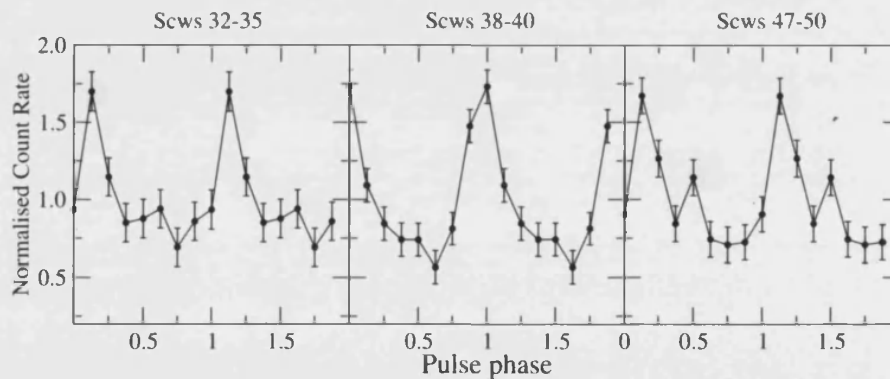


Figure 13.21: Folded light curves of ISGRI data from the three periods of revolution 67 studied independently.

fractional change of  $8 \times 10^{-5}$  and  $3 \times 10^{-4}$ , while in our case this quantity amounts to  $4 \times 10^{-3}$  (one to two orders of magnitude larger than would be expected). Another source which has shown such behaviour (sudden increase of the pulse frequency) is KS 1947+300 which showed such a pulse frequency change on time scales  $< 10$  hours (see Galloway et al., 2004).

It must be noticed that the secondary peak which was seen in Fig. 13.19 in revolution 74 also appears in the first and third panels of Fig. 13.21. The physical mechanism which produces in revolution 74 and first and third intervals of revolution 67 a secondary peak may also be the same process that produces in revolution 70 and the second interval of

revolution 67 a slow falling of the pulse peak. Something noticeable is the relative growth in intensity of the secondary peak with respect to the main peak during revolution 67. From a clearly separated small peak in the first interval of revolution 67 data we find a high secondary peak in the last interval. The ratios of secondary to main peak are 0.6, and 0.7 respectively. This observational fact may be indicating (if the main peak comes from the polar cap which is facing us, and the secondary peak comes from the opposite polar cap) that the amount of matter hiding the second polar cap is decreasing along the time span covered by revolution 67 data. In other words, this can be evidence for the evolution of the accretion disc, which may be decreasing in size.

The broad peaks seen in Fig. 13.17 (JEM-X data) and 13.19 (ISGRI data) during revolution 67 contrast with the narrower peaks shown in Fig. 13.21. The pulse period change along revolution 67 may be producing wide peaks (covering 60% of the total phase) when analyzing revolution 67 data as a whole.

### 13.2.7 Pulse period at higher energies

We have also extracted light curves with a time resolution of 10 s in the 45–60 keV energy range. In this case the periodograms obtained from the light curves were very noisy. For revolutions 67 and 70, despite the noisy periodograms, we could still find the pulse period. For revolution 74, the possible peak at the pulse period frequency was at the noise level. In Fig. 13.22 the DFT and Lomb-Scargle periodograms are shown for revolution 67 data in the 45–60 keV energy range. We see that the distributions of peaks is very similar in both diagrams. The Lomb-Scargle diagram and the search for the period corresponding to the maximum peak frequency was performed with the PERIOD package of the STARLINK set of software. We found a pulse period of  $353.6 \pm 0.7$  s, in very good agreement with the pulse period found at lower energies.

In Fig. 13.23 the DFT and  $\chi^2_{\text{RED}}$  distribution for a series of sine fits are shown for revolution 70 in the 45–60 keV energy range. The periodograms are noisier than in the case of revolution 67. We notice in the DFT that although the peak at a frequency of 0.0028712 Hz (which corresponds to the pulse period) is seen, other peaks with similar significances are also found. In particular, there is a peak at a frequency of  $\sim 0.0035$  Hz as



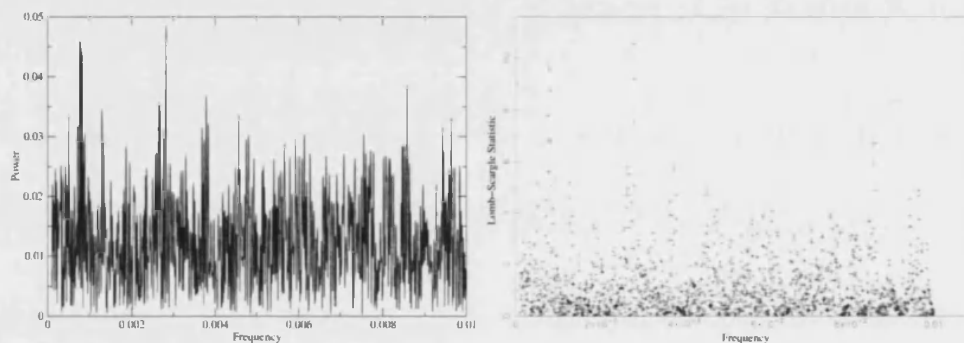


Figure 13.22: DFT (left panel) and Lomb-Scargle (right panel) periodograms for ISGRI data from revolution 67 data in the energy range 45–60 keV.

significant as the one at 0.0028712 Hz. Not all the methods to compute the periodogram could separate these two peaks. Only the calculation of the  $\chi^2$  for a set of sine fits (again with the software package PERIOD) yielded a detection of the pulse period. The right panel of 13.23 shows a minimum of the  $\chi^2_{\text{RED}}$  (best fit to the data) at a frequency of 0.0028712 Hz. The search of the most likely period resulted in the measurement of a pulse period of  $348 \pm 7$  s. Within the error, this measurement is compatible with the  $354.6 \pm 0.5$  seconds found in the 25–45 keV energy range. Using these measured pulse periods we have folded the data of both revolutions. The resulting folded light curve is shown in Fig. 13.24. We notice that the variations of intensity between the main and secondary peak are also present in this energy range. During revolution 67 we find a ratio of the secondary to the main peak of 0.6, which becomes 0.8 during revolution 70. These ratios are very similar to the ones found in the analysis of the 25–45 keV energy range light curves. Whatever the process responsible of the variation of the second peak, within the accuracy of our data, we can state that it affects the same way all energy bands within the 25–60 keV range. Above 60 keV the S/N is too low to extract meaningful counts.

In summary, we have been able to perform a detailed timing analysis on time scales comparable to the source pulse period. Within the errors, the data suggest a complex time behaviour in the 25–45 keV energy range.

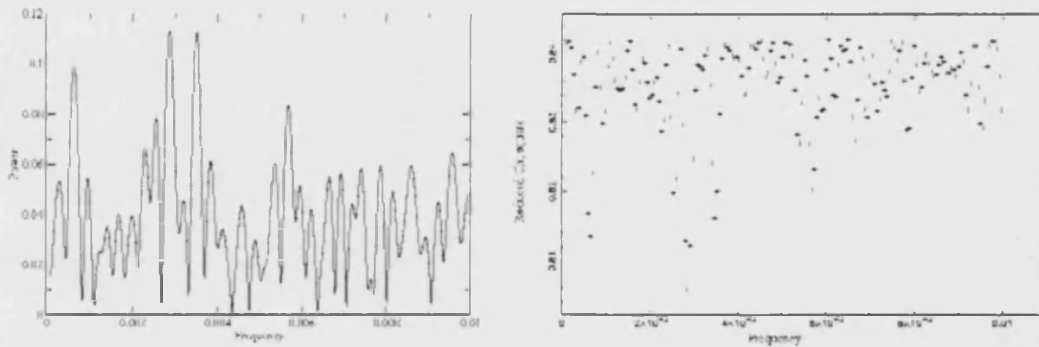


Figure 13.23: DFT periodogram (left panel) and distribution of  $\chi^2_{\text{RED}}$  for a set of sine fits to the data (right panel) for the revolution 70 data in the energy range 45–60 keV.

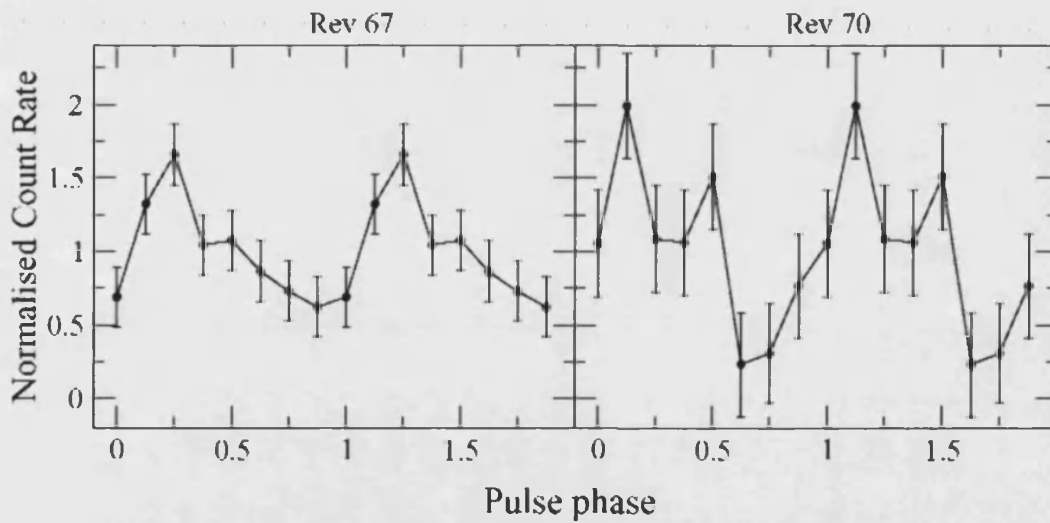


Figure 13.24: Folded light curves of ISGR1 data in the 45–60 keV energy range from revolution 67 (left panel) and revolution 70 (right panel). The folding periods used are those measured from periodograms, i.e.,  $353.6 \pm 0.7$  s for revolution 67 and  $348 \pm 7$  s for revolution 70.

Above this energy, although the results are compatible with the lower energy bands, errors are too big to confirm if the complex behaviour extends to higher energies. Spin up as well as spin down processes are suggested by our data. A secondary peak, which shows variability, is seen at all the energy ranges studied. More sophisticated timing analysis tools, such as wavelet transforms, should be used to investigate the complex timing variability of this source (both in pulse period time scales and long term time scales).

### 13.2.8 Analysis of GPS spectra

#### JEM-X spectra

Unfortunately, due to the smaller FOV of JEM-X, we only have data available for a few science windows. Available spectra, together with spectral parameters, are summarised in Table 13.9.

The quality of the spectra is not good enough to derive physical parameters from the spectral fits. For the sake of simplicity, as a first step, we fitted to the spectra a power law plus a high-energy cut-off model to check for variability. However, the large errors derived and the instability of the fits made us undertake a different approach. An average spectrum was obtained for revolution 67. This average spectrum was fitted to a power law model plus a high energy cut-off. The value of  $E_{\text{FOLD}}$  found in this average spectrum was used to freeze this parameter during the re-

Table 13.9: Spectral parameters for all the JEM-X spectra obtained with public GPS data. In all cases, the number of degrees of freedom is 147.

SCW	$\Gamma$	$E_{\text{CUT}}$ (keV)	$E_{\text{FOLD}}$ (keV)	Flux ( $\times 10^{-10}$ ) erg s $^{-1}$ cm $^{-2}$	$\chi_{\text{red}}^2$
59-29	$1.3^{+0.3}_{-1.3}$	$13^{+11}_{-13}$	$14^{+147}_{-9}$	7.6	0.9
67-39	$1.5^{+0.3}_{-0.3}$	$15^{+41}_{-15}$	$10^{+276}_{-7}$	7.0	1.2
67-40	$1.2^{+0.3}_{-1.1}$	$12^{+11}_{-12}$	$18^{+63}_{-13}$	8.8	1.0
67-41	$0.9^{+0.3}_{-2.7}$	$11^{+13}_{-11}$	$9^{+20}_{-7}$	5.9	1.0
67-42	$1.2^{+0.3}_{-1.4}$	$12^{+7}_{-12}$	$21^{+363}_{-17}$	8.1	1.0
67-43	$0.5^{+0.7}_{-1.3}$	$6^{+2}_{-6}$	$7^{+7}_{-1}$	6.7	1.1

fitting procedure in the intervals of revolution 67 considered. In this way, we restrict the analysis of variability to only two parameters: the power law photon index, and the energy cut-off. The first one will give us the information about the hardness or softness of the spectra. It has been suggested (Coburn et al., 2002) that  $E_{\text{CUT}}$  may be related to the strength of the magnetic field. The individual spectra of revolution 67 plus an averaged spectrum for this revolution are shown in Fig. 13.25. A power law with photon index  $0.6 \pm 0.4$  plus a high energy cut off at  $6_{-5}^{+2}$  keV folded at an energy of  $12_{-4}^{+8}$  keV gave a good fit, with a  $\chi_{\text{red}}^2$  of 1.1 for 154 degrees of freedom, to the average spectrum.

Table 13.10 shows the results of the new fit after freezing the value of  $E_{\text{FOLD}}$  to the one obtained with the average spectrum. Within the errors, we cannot detect spectral variability. The most discrepant spectral parameters correspond to science window 42. The spectrum from this science window yielded the most unstable fit. Although after a few iterations the fit always converged to the value shown in Table 13.10, local minima for the parameters in Table 13.10 were also found at pair values of (1.3,18) and (1.1,13), where the first member of the pair represents the power law photon index and the second the cut-off energy.

In summary, at the lower energies (4–25 keV) we cannot detect spectral variability or line emission features. The individual spectra give in general unstable fits and it seems convenient to work only with an average spectrum over the whole time span of the observations. The average spectrum of revolution 67, with a photon index of  $0.6 \pm 0.4$ , shows similar properties to those shown in the literature for similar energy ranges (see Hulleman et al., 1998; Baykal et al., 2002).

### ISGRI spectra

We can study the spectral evolution of ISGRI data on long and short time scales. By long time scales we mean the comparison of spectra from different revolutions. This will give us an idea of the spectral behaviour of the source throughout the GPS from revolution 31 up to revolution 181. For the short term, we will make use of individual spectra within the same revolution. This will give us clues about the spectral changes during an outburst (only when the source is in outburst, it can be seen in several science windows of the same revolution). This last study will complement

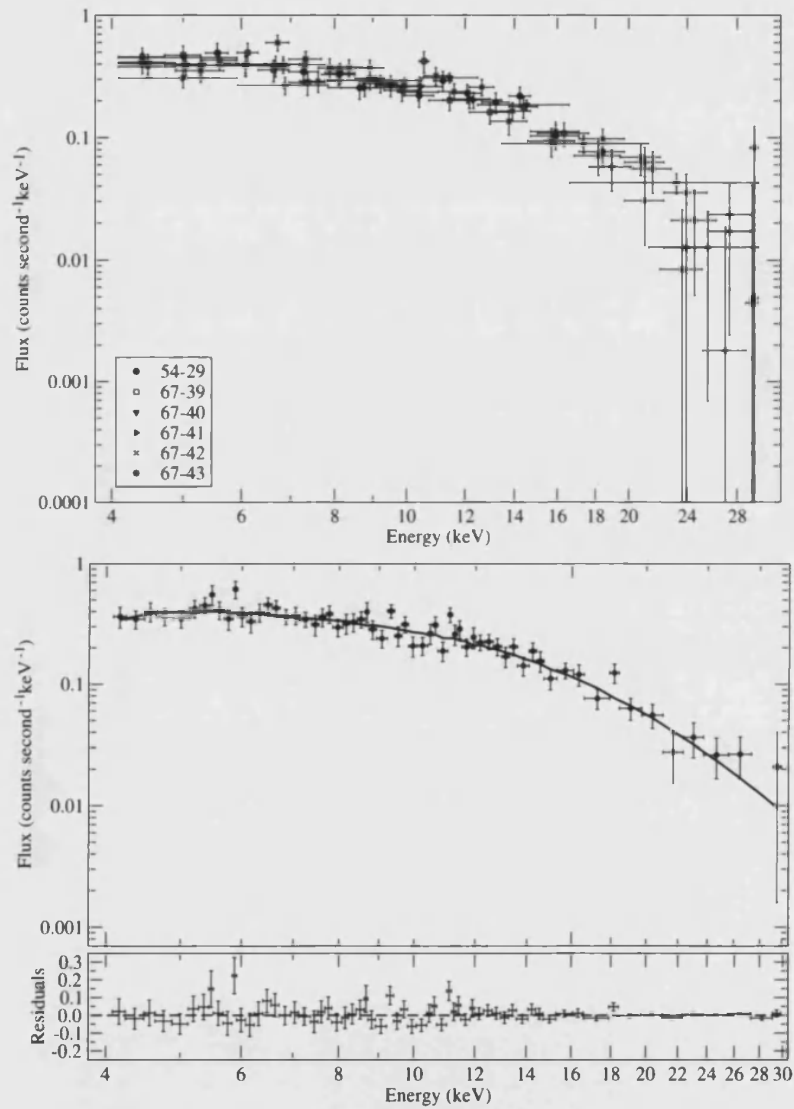


Figure 13.25: The JEM-X spectra for those science windows indicated in Table 13.9 are shown in the upper panel. Large errors prevent us from identifying spectral variability. The spectral shape remains unchanged along the time coverage of this set of data. In the lower panel, the average spectrum is shown, together with a power law model fit, together with its residuals.

Table 13.10: Results of the spectral fits to JEM-X data after freezing the  $E_{\text{FOLD}}$  parameter of the power law plus high energy cut-off model to that value derived from the averaged spectrum for revolution 67 ( $E_{\text{FOLD}}=12$  keV). The most unstable fit is that of the science window 42, where the error given (marked with an asterisk) was calculated at a 68% Confidence Level (C.L.) (while the rest represent 90% C.L.). In this science window local minima of the fit were also found for photon indexes of 1.3 and 1.1 with associated cut-off energies of 18 keV and 13 keV respectively.

ScW	$\Gamma$	$E_{\text{CUT}}$ (keV)
67-39	$1.5_{0.2}^{-0.2}$	$15_{-3}^{+36}$
67-40	$1.3_{0.2}^{-0.3}$	$15_{-0.1}^{+7.0}$
67-41	$1.0_{0.4}^{-0.6}$	$11_{-5}^{+7}$
67-42	$0.5_{0.2}^{-0.2}$	$3_{-3}^{+22*}$
67-43	$1.0_{0.4}^{-0.3}$	$7_{-2}^{+3}$

and improve the analysis of the previous sections.

Due to the uncertainties still present in the spectral extraction software, at the time of writing this thesis, we have performed our analysis using two methods, the standard OSA 4.2 software and the spectral extraction software created by A. Segreto & C. Ferrigno (SF)<sup>1</sup>. Table 13.11 shows the best fit parameters, using a power law model, to all the spectra obtained with the ISGRI instrument for all GPS detections (using public data up to revolution 181).

We plotted together the photon indexes versus the respective fluxes for both spectra extraction methods (OSA 4.2 and SF). The result can be seen in Fig. 13.26. In the case of OSA 4.2 all the photon indexes are gathered around a value of 3.0, and errors are bigger than the ones derived with SF. In the case of SF the values of the photon indexes are generally lower and with smaller error bars than in the case of OSA 4.2. Although in this latter case there seems to be some evidence for spectral variability, the error bars make the values also compatible with a constant value, namely  $\sim 2.5$ .

The fact that OSA 4.2 photon indexes are softer than those obtained with SF software can be due to one of these possibilities:

- OSA 4.2 overestimates count rates from the lower energy photons.
- OSA 4.2 underestimates, or is unable to extract the count rates from the higher energy photons.
- SF software overestimates the count rates of higher energy photons.
- SF software fails to extract count rates from the lower energy photons.

In Fig. 13.27 we show Crab spectra extracted with SF software for  $\sim 20$  ks during revolution 45,  $\sim 5$  ks during revolution 58 and  $\sim 25$  ks during revolution 102. While the spectrum from revolution 102 looks very clean, we see some spectral extraction problems in the 20–30 keV energy range for the spectra from revolutions 45 and 58. This is due to the fact that actually we have a different setup of the instrument in each revolution (this

---

<sup>1</sup><http://www.pa.iasf.cnr.it/ferrigno/INTEGRALsoftware.html>

Table 13.11: Power law fit parameters for GPS science windows with the source in the FCFOV and for which OSA 4.2 and SF software succeeded to extract a spectrum of the source. Flux is given in units of  $10^{-10}$  erg s $^{-1}$  cm $^{-2}$

ScW	OSA 4.2				SF			
	$\Gamma$	$\chi_{\text{red}}^2$	DOF	Flux	$\Gamma$	$\chi_{\text{red}}^2$	DOF	Flux
54-29	$2.8^{+0.5}_{-0.4}$	0.6	24	6.6	$2.8^{+0.4}_{-0.3}$	1.1	73	7.9
67-32	$2.7^{+0.4}_{-0.3}$	0.6	24	8.6	$2.5^{+0.2}_{-0.2}$	1.0	73	11.0
67-33	$2.9^{+0.5}_{-0.4}$	1.1	24	5.8	$2.3^{+0.3}_{-0.3}$	1.3	73	9.1
67-34	$3.3^{+0.6}_{-0.5}$	0.8	24	6.1	$2.7^{+0.4}_{-0.3}$	0.8	73	6.4
67-35	$2.7^{+0.5}_{-0.4}$	1.3	24	7.2	$2.2^{+0.3}_{-0.3}$	1.0	73	9.4
67-38	$3.1^{+0.6}_{-0.5}$	0.7	24	7.1	$2.9^{+0.5}_{-0.4}$	1.3	73	6.8
67-39	$2.8^{+0.5}_{-0.4}$	0.7	24	6.7	$2.4^{+0.3}_{-0.3}$	0.8	73	8.0
67-40	$3.2^{+0.5}_{-0.4}$	0.7	24	6.3	$2.3^{+0.2}_{-0.2}$	1.1	73	9.5
67-41	$3.3^{+0.7}_{-0.5}$	0.8	24	5.9	$3.2^{+0.6}_{-0.5}$	1.1	73	4.6
67-42	$3.6^{+0.8}_{-0.6}$	0.7	24	5.0	$2.7^{+0.4}_{-0.3}$	0.9	73	7.3
67-43	$2.7^{+0.6}_{-0.5}$	0.9	24	5.9	$2.7^{+0.4}_{-0.4}$	1.0	73	5.9
67-44	$3.1^{+0.7}_{-0.5}$	0.9	24	5.0	$2.4^{+0.3}_{-0.3}$	1.0	73	8.7
67-47	$3.0^{+0.6}_{-0.5}$	0.7	24	5.7	$2.4^{+0.3}_{-0.3}$	1.2	73	8.2
67-48	$3.0^{+0.6}_{-0.5}$	0.7	24	5.7	$2.1^{+0.3}_{-0.3}$	0.6	73	8.4
67-49	$3.2^{+0.8}_{-0.6}$	1.0	24	4.1	$2.2^{+0.4}_{-0.4}$	1.2	73	6.8
67-50	$2.8^{+0.3}_{-0.3}$	1.6	24	7.5	$2.6^{+0.2}_{-0.2}$	1.6	73	8.4
70-06	$2.9^{+0.3}_{-0.3}$	1.0	24	11.2	$2.8^{+0.2}_{-0.2}$	1.1	73	12.1
70-07	$2.9^{+0.3}_{-0.2}$	1.4	24	11.1	$2.8^{+0.2}_{-0.2}$	1.0	73	11.7
74-08	$2.9^{+0.5}_{-0.4}$	0.6	24	7.0	$2.3^{+0.3}_{-0.3}$	1.2	73	9.8
74-09	$3.0^{+0.4}_{-0.3}$	1.0	24	8.7	$2.6^{+0.2}_{-0.2}$	1.0	73	11.2



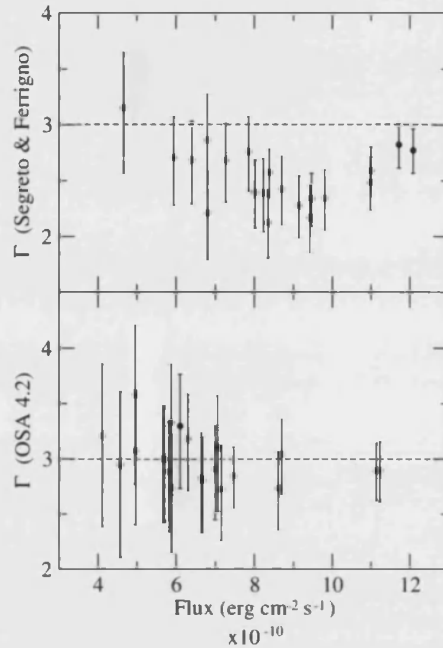


Figure 13.26: Photon indexes of a power law model fit to all SAX J2103.5+4545 ISGRI spectra for OSA 4.2 and SF software.

will be implemented in future *INTEGRAL* software releases). Ideally, a different response should be generated for each setup. The high energy part of the spectrum is more stable.

Furthermore, it is known (see subsection 3.4.2) that ISGRI spectral extraction software can be troublesome for weak off-axis sources below 25 keV. Thus, to investigate the source of the detected difference in the spectral extraction, between OSA 4.2 and SF software, in the 20–30 keV energy range, we have performed a more detailed analysis in two energy bands: 20–70 keV and 30–70 keV (excluding higher energies, because we are approaching the sensitivity limit of ISGRI and the spectral extraction can be affected by many uncertainties).

In Table 13.12 we compare the spectral parameters for the 30–70 keV and for the 20–70 keV energy ranges.

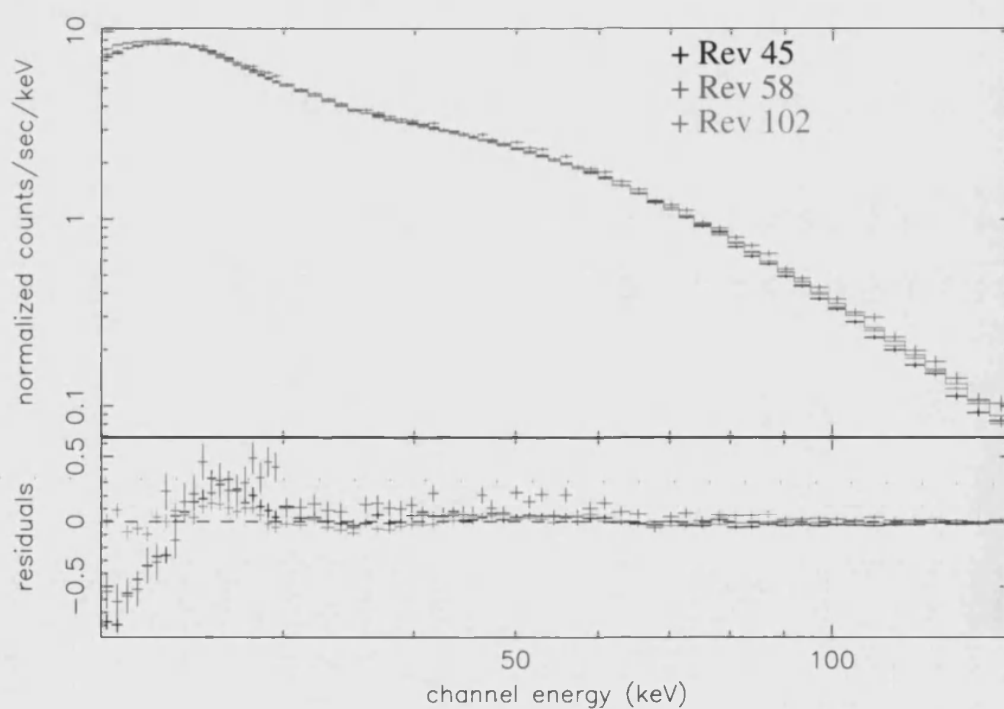


Figure 13.27: Crab spectra for revolutions 45, 58, and 102, extracted from ISGRI data with the SF method. The model used to fit the data is a power law. Residuals of the fit are plotted in the lower panel.

Table 13.12: Results of the ISGRI spectral analysis of SAX J2103.5+4545. For spectra extracted with OSA 4.2 we had 14 DOF, and for spectra extracted with SF software, 28 DOF. Those spectra producing a very unstable fit in either of the two methods (namely those of science windows 54–29, 67–38, 67–41, and 67–50) have been omitted.

SCW	30–70 keV						20–70 keV					
	$\Gamma$		$\chi_{\text{red}}^2$		Flux $\times 10^{-10}$ (erg s $^{-1}$ cm $^{-2}$ )		$\Gamma$		$\chi_{\text{red}}^2$		Flux $\times 10^{-10}$ (erg s $^{-1}$ cm $^{-2}$ )	
	O 4.2	SF	O 4.2	SF	O 4.2	SF	O 4.2	SF	O 4.2	SF	O 4.2	SF
67–32	2.6 $^{+1.7}_{-3.4}$	2.4 $^{+0.7}_{-0.6}$	0.7	1.0	4.3	5.2	2.5 $^{+0.4}_{-0.4}$	2.3 $^{+0.3}_{-0.3}$	0.6	0.8	7.0	8.3
67–33	3.6 $^{+2.6}_{-4.4}$	2.7 $^{+0.7}_{-0.7}$	0.5	1.0	3.7	4.5	2.3 $^{+0.5}_{-0.5}$	2.1 $^{+0.3}_{-0.3}$	1.3	1.0	5.5	6.6
67–34	2.8 $^{+1.8}_{-3.6}$	2.7 $^{+1.1}_{-0.8}$	0.9	0.7	3.5	3.2	2.6 $^{+0.5}_{-0.5}$	2.5 $^{+0.4}_{-0.4}$	0.9	0.7	5.8	5.2
67–35	3.7 $^{+3.1}_{-4.4}$	2.9 $^{+1.0}_{-0.9}$	2.0	1.0	3.2	3.8	2.8 $^{+0.5}_{-0.5}$	2.3 $^{+0.4}_{-0.4}$	1.8	1.0	5.5	6.0
67–39	3.6 $^{+2.4}_{-4.5}$	3.4 $^{+1.0}_{-0.9}$	0.8	0.7	3.0	3.3	2.8 $^{+0.5}_{-0.4}$	2.4 $^{+0.4}_{-0.3}$	1.1	1.0	5.5	5.7
67–40	3.2 $^{+2.2}_{-4.0}$	3.3 $^{+0.7}_{-0.6}$	0.5	1.2	3.4	4.5	2.6 $^{+0.5}_{-0.4}$	2.2 $^{+0.3}_{-0.3}$	0.6	1.2	5.7	6.8
67–42	3.3 $^{+2.1}_{-4.3}$	2.4 $^{+1.1}_{-0.8}$	1.3	1.0	2.7	3.2	3.0 $^{+0.5}_{-0.5}$	2.7 $^{+0.4}_{-0.4}$	1.1	0.8	5.0	5.5
67–43	2.9 $^{+1.7}_{-3.9}$	3.2 $^{+1.4}_{-1.0}$	1.0	0.8	2.8	2.6	2.8 $^{+0.5}_{-0.5}$	2.6 $^{+0.5}_{-0.4}$	1.0	1.0	5.0	4.7
67–44	3.1 $^{+1.8}_{-4.0}$	2.3 $^{+0.8}_{-0.7}$	1.4	1.3	2.8	3.9	2.6 $^{+0.6}_{-0.6}$	2.5 $^{+0.4}_{-0.3}$	1.4	1.1	4.5	6.2
67–47	3.2 $^{+1.7}_{-4.2}$	2.3 $^{+1.0}_{-0.9}$	0.8	1.2	2.8	3.8	2.8 $^{+0.5}_{-0.5}$	2.3 $^{+0.4}_{-0.4}$	0.9	1.1	5.3	5.9
67–48	2.4 $^{+1.4}_{-3.3}$	2.3 $^{+0.9}_{-0.7}$	0.6	0.4	3.5	3.9	2.4 $^{+0.5}_{-0.5}$	1.9 $^{+0.4}_{-0.4}$	0.4	0.6	5.6	5.7
67–49	3.6 $^{+1.9}_{-4.8}$	3.6 $^{+1.5}_{-1.2}$	1.0	1.2	2.1	2.7	2.7 $^{+0.7}_{-0.6}$	2.3 $^{+0.5}_{-0.5}$	1.2	1.5	3.7	4.5
70–06	2.7 $^{+2.1}_{-3.3}$	2.9 $^{+0.6}_{-0.5}$	1.5	1.3	5.4	5.8	2.6 $^{+0.3}_{-0.3}$	2.6 $^{+0.2}_{-0.2}$	1.1	1.2	9.3	9.9
70–07	2.8 $^{+2.2}_{-3.4}$	2.9 $^{+0.5}_{-0.5}$	0.8	0.9	5.5	5.6	2.5 $^{+0.3}_{-0.3}$	2.6 $^{+0.2}_{-0.2}$	1.3	0.7	9.1	9.7
74–08	2.5 $^{+1.5}_{-3.4}$	2.0 $^{+0.7}_{-0.7}$	0.6	1.2	3.4	4.3	2.6 $^{+0.5}_{-0.5}$	2.4 $^{+0.3}_{-0.3}$	0.7	1.2	5.8	6.8
74–09	3.3 $^{+2.5}_{-4.0}$	2.7 $^{+0.6}_{-0.6}$	0.9	1.4	4.4	5.4	2.7 $^{+0.4}_{-0.3}$	2.4 $^{+0.3}_{-0.3}$	0.9	1.1	7.6	8.8

For the 30–70 keV energy range (see left side of Table 13.12) we notice that in general the fits to the data extracted For the 30–70 keV energy range (see left side of Table 13.12) we notice that in general the fits to the data extracted with SF software give better  $\chi_{\text{red}}^2$  than those fits to the data extracted with OSA 4.2. The parameters from the fits to both sets of spectra are now more similar. When the full energy range (20–150 keV) is considered, the discrepancy in the flux derived from both sets of data is quite important. However, in the analysis of the 30–70 keV energy range the fluxes obtained from both sets of spectra are very similar.

When we repeat this analysis in the 20–70 keV energy range, despite using the 20–30 keV energy range (where we could expect some extraction problems), the same conclusions can be reached, as can be seen on the right side of Table 13.12. It seems very likely, then, that the discrepancy in the slope of the continuum and the flux is produced at the higher energy ranges (above 70 keV). Since we lack an objective reason as to which of the two methods is more accurate, we will restrict our spectral analysis (in short time scales, that is, in per science window basis) to the energy range 20–70 keV. It must be noticed, however, that SF software extracts spectra with a higher energy resolution than OSA 4.2 for the same signal to noise ratio (i.e., it allows for a finer binning). On the other hand OSA 4.2 is affected of the well known problems in the RMF. Although they are partially corrected for the Crab and strong sources there are still problems with weak and off-axis sources. with SF software give better  $\chi_{\text{red}}^2$  than those fits to the data extracted with OSA 4.2. The parameters from the fits to both sets of spectra are now more similar. When the full energy range (20–150 keV) is considered, the discrepancy in the flux derived from both sets of data is quite important. However, in the analysis of the 30–70 keV energy range the fluxes obtained from both sets of spectra are very similar.

When we repeat this analysis in the 20–70 keV energy range, despite using the 20–30 keV energy range (where we could expect some extraction problems), the same conclusions can be reached, as can be seen on the right side of Table 13.12. It seems very likely, then, that the discrepancy in the slope of the continuum and the flux is produced at the higher energy ranges (above 70 keV). Since we lack an objective reason as to which of the two methods is more accurate, we will restrict our spectral analysis

(in short time scales, that is, in per science window basis) to the energy range 20–70 keV. It must be noticed, however, that SF software extracts spectra with a higher energy resolution than OSA 4.2 for the same signal to noise ratio (i.e., it allows for a finer binning). On the other hand OSA 4.2 is affected of the well known problems in the RMF. Although they are partially corrected for the Crab and strong sources there are still problems with weak and off-axis sources.

Since we have not found strong evidence for spectral variability, we computed an average spectrum. In this way, we improve the S/N and a study of the global properties of the source can be performed.

The average spectrum is shown in Fig. 13.28. A power law model was fitted to the OSA 4.2 averaged spectrum yielding a photon index of  $2.7 \pm 0.1$  and a  $\chi^2_{\text{red}}$  of 1.6 for 17 degrees of freedom. The SF spectrum yielded a more accurate result, with a photon index of  $2.55^{+0.06}_{-0.07}$  and a  $\chi^2_{\text{red}}$  of 1.3 for 73 degrees of freedom. There seems to be a saw-like structure in the residuals of the fit in the OSA 4.2 extracted average, but it is absent in the SF spectrum. To investigate the origin of this structure we have performed a normalisation to the Crab data. Using Crab observations from revolutions 45 and 102, we have generated an average Crab spectrum. We have fit both, the SAX J2103.5+4545 spectrum and the Crab spectrum, to a power law model and then normalised each spectra by the model. Finally we have calculated the ratio of the resulting SAX J2103.5+4545 normalised spectrum to that of the Crab. The result can be seen in Fig. 13.29. Note that the saw-like residuals have disappeared. Therefore, we conclude that they were due to software extraction problems.

The ratios of the individual spectrum to the average are shown in Fig. 13.30. We can confirm through this viewgraph the absence of spectral variations in the range 20–70 keV. The source shows a very stable spectral shape (on all time scales) at the error level of *INTEGRAL* data. Thus, the use of an average spectrum over the whole GPS time span under study is justified. If the averaged spectrum is considered, a simple power law gives an acceptable fit to the data and no spectral features (emission or absorption) can be detected. The SF software has been proved to be free of spectral extraction problems, giving a better energy resolution for the same signal to noise level and allowing a more accurate determination of spectral parameters.

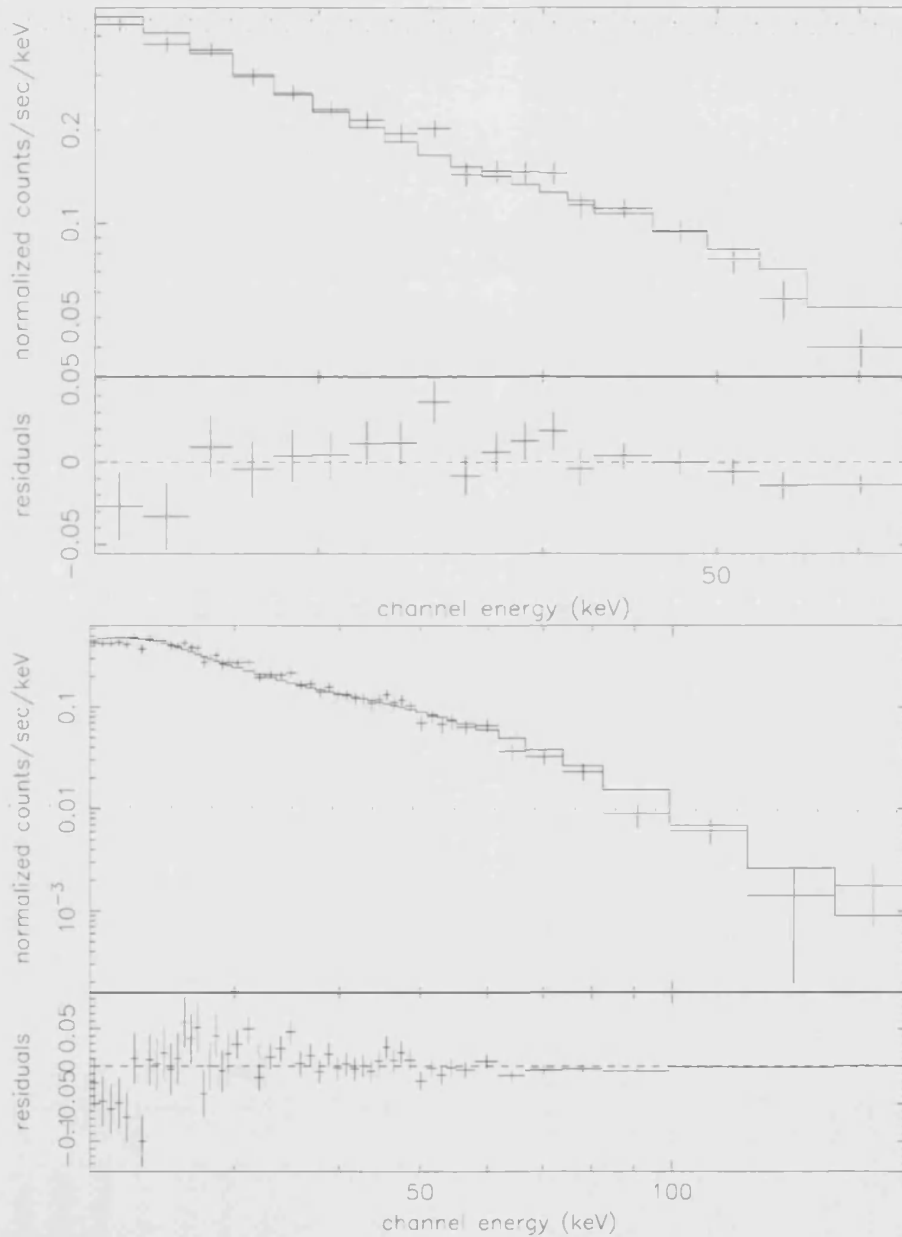


Figure 13.28: Average spectrum for all ISGRI spectra shown in Table 13.12. In the upper viewgraph the average spectrum has been obtained with the spectra extracted with OSA 4.2 software. In the lower viewgraph the average spectrum was extracted with the SF software. In both cases the fit to a power law model and its residuals are shown (see main text for more details).

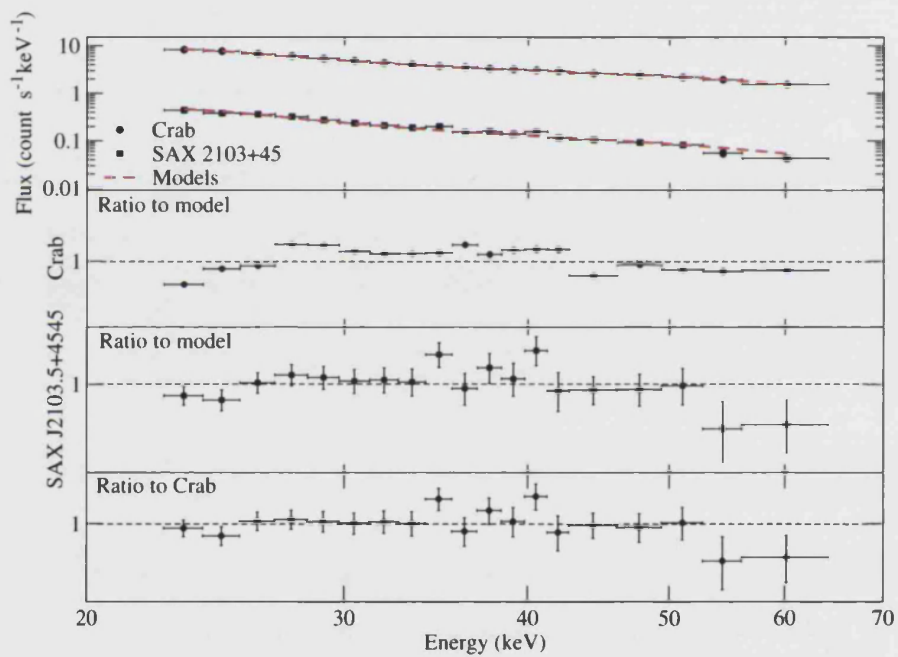


Figure 13.29: Ratio of the normalised ISGRI spectrum of SAX J2103.5+4545 to that of the Crab. The upper panels exemplify the process followed to obtain the ratio.

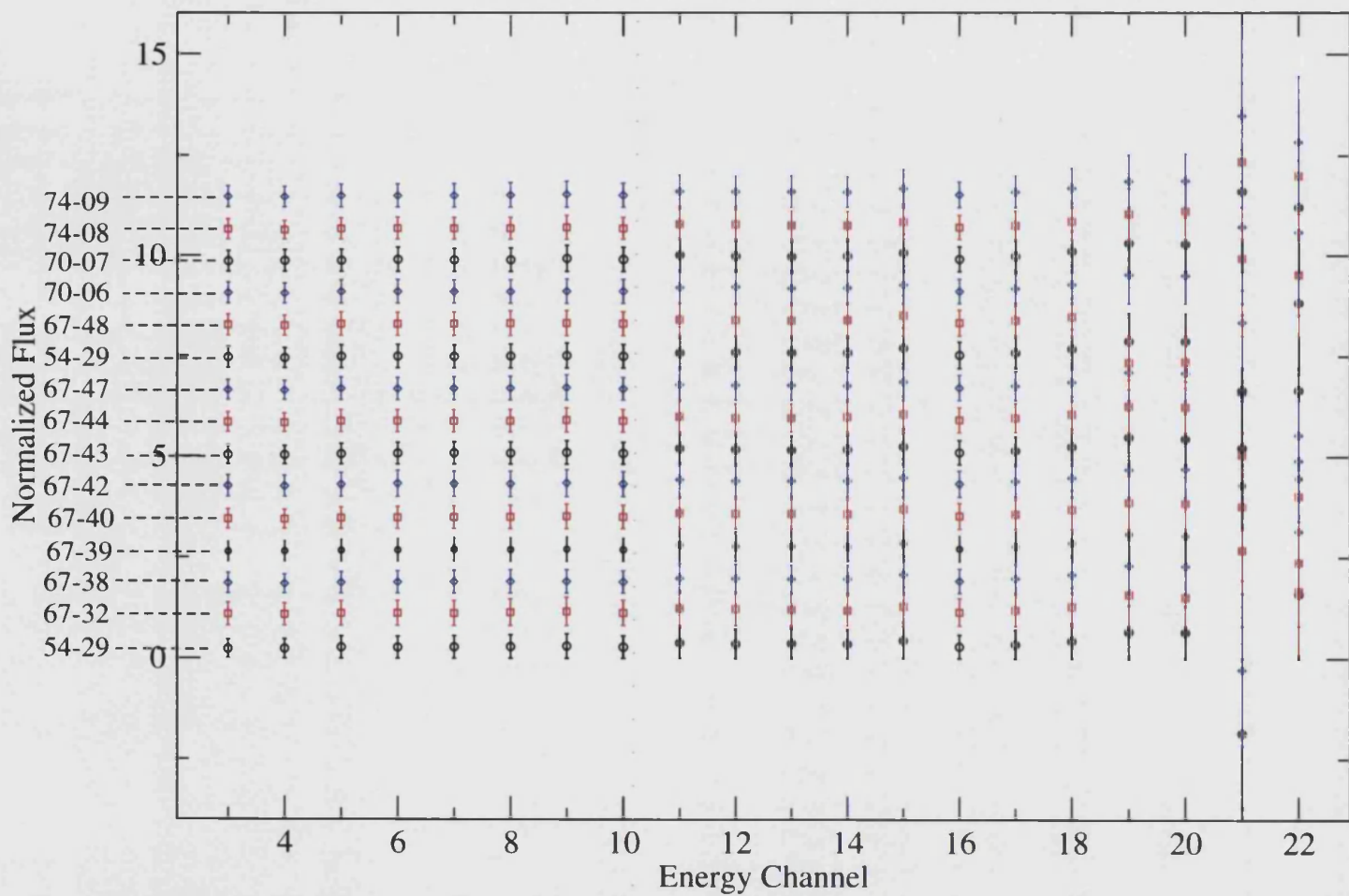


Figure 13.30: Ratio of all the ISGRI spectra shown in Table 13.12 to the average ISGRI spectrum. We notice that there is no evidence for spectral variations. The ratios have been shifted upwards for plotting purposes.



### JEM-X–ISGRI Spectra

We have obtained spectra of the source for those science windows where simultaneous JEM-X and ISGRI spectra could be obtained. This reduces to 6 the number of spectra. The science windows where simultaneity is possible are: 54-29,67-39,67-40,67-41,67-42, and 67-43 (the notation *Revolution-Science window number* was adopted). A power law plus a high energy cut off was used to fit simultaneously JEM-X and ISGRI spectra for all the individual science windows mentioned above, see Fig. 13.31. The spectral parameters are summarised in Table 13.13.

Overall, the spectral parameters derived from spectra extracted with the two methods are compatible between them. There is evidence of spectral changes in the parameters shown in Table 13.13. In particular the spectral parameters in science window 67–39 look quite different from the rest. In general, the 4–150 keV spectral photon index stays around a value of  $\sim 1.1$ , the cut-off energy takes values around  $\sim 10$  keV and the folding energy around  $\sim 20$  keV. But for the science window 67–39 all these values are clearly higher (but compatible within errors). A second extreme case can be seen in science window 67-41, where the spectral parameters follow the opposite trend and show lower values.

Table 13.14 shows the fluxes measured for all science windows in Table 13.13 in different energy ranges.

It may seem surprising to see that for science window 67–39 the flux seems to follow the average behaviour, despite the softer spectrum. On the contrary, the other extreme case of variability found, that of science window 67–41, is clearly showing a flux lower than the rest. We can conclude that some spectral variability is suggested by this set of data. As JEM-X and ISGRI spectra showed a high degree of stability in previous sections, it is difficult to assume this variability as real. It must be noticed that in all the fits, the power law index is dominated by JEM-X data, while the cut-off and the exponential folding are dominated by ISGRI data. In the case of science window 67–41, the source was close to the limit of the zero-response zone of the detector. This indicates that there may be an underestimation of the flux of the source in that particular science window, as the software fails to extract all the photons from the source when it falls inside the zero-response area of the detector. This can be the reason of the lower flux observed in this science window.

Table 13.13: Comparison of the joint JEM-X and ISGRI spectral parameters for two cases: a) ISGRI spectra extracted with standard OSA 4.2 software; b) ISGRI spectra extracted with the software developed by SF. In all cases only science windows where simultaneous JEM-X and ISGRI spectra can be obtained are used. A power law plus a high energy cut off was the model chosen to fit all the data. A constant was added to the model to allow for cross-calibration normalisation.

Software version	SCW	$\Gamma$	$E_{\text{CUT}}$ (keV)	$E_{\text{FOLD}}$ (keV)	Cross Cal. factor	$\chi^2_{\text{red}}$	DOF
OSA 4.2	54-29	$1.3^{+0.1}_{-0.8}$	$13^{+15}_{-13}$	$20^{+9}_{-5}$	$0.77 \pm 0.15$	0.9	172
SF	54-29	$1.3^{+0.2}_{-0.6}$	$13^{+9}_{-13}$	$23^{+11}_{-6}$	$0.67 \pm 0.11$	0.98	221
OSA 4.2	67-39	$1.6 \pm 0.2$	$32^{+22}_{-32}$	$20^{+18}_{-11}$	$0.99 \pm 0.14$	1.1	172
SF	67-39	$1.6 \pm 0.2$	$31^{+10}_{-31}$	$32^{+38}_{-21}$	$0.99 \pm 0.16$	1.03	221
OSA 4.2	67-40	$0.9^{+0.3}_{-0.4}$	$5^{+11}_{-5}$	$19^{+6}_{-5}$	$0.98 \pm 0.15$	0.9	172
SF	67-40	$1.4^{+0.1}_{-0.2}$	$42^{+11}_{-14}$	$18^{+24}_{-18}$	$0.79 \pm 0.14$	0.97	221
OSA 4.2	67-41	$1.1^{+0.4}_{-0.7}$	$10^{+7}_{-10}$	$18^{+8}_{-6}$	$0.69 \pm 0.16$	1.0	172
SF	67-41	$0.8^{+0.7}_{-0.9}$	$8^{+7}_{-8}$	$13^{+9}_{-5}$	$0.72 \pm 0.18$	1.03	221
OSA 4.2	67-42	$1.2^{+0.3}_{-0.8}$	$12^{+9}_{-12}$	$19^{+7}_{-4}$	$0.84 \pm 0.15$	1.0	172
SF	67-42	$1.2^{+0.3}_{-0.6}$	$12^{+10}_{-12}$	$25^{+13}_{-8}$	$0.88 \pm 0.13$	0.96	221
OSA 4.2	67-43	$1.2^{+0.3}_{-0.4}$	$7^{+4}_{-7}$	$20^{+12}_{-6}$	$0.78 \pm 0.17$	1.1	172
SF	67-43	$1.2^{+0.3}_{-0.4}$	$7^{+5}_{-7}$	$21^{+13}_{-7}$	$0.84 \pm 0.17$	1.07	221

Fig. 13.32 shows the spectral photon index and the high energy cut-off as a function of the 4–150 keV flux. The hardest and softest spectra are marked by upwards and downwards arrows on the right of the data point. We already saw in previous sections that the softening of the source with increasing of flux is very small. Once a certain flux level is reached, the *softness* of the source remains constant and becomes independent of the flux. This is confirmed by Fig. 13.32, where the only deviating points are the ones mentioned above.

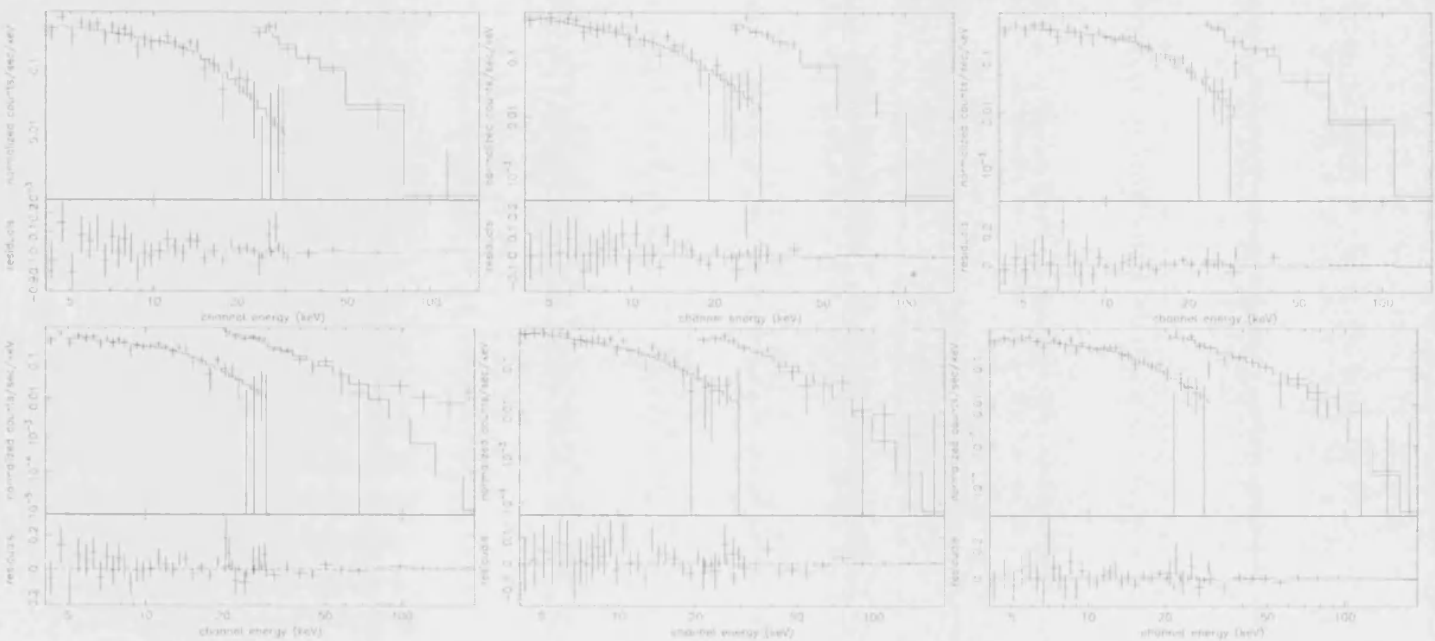


Figure 13.31: Selected joint JEM-X-*ISGRI* spectra among those whose spectral parameters are shown in Table 13.13. The first row corresponds to spectra extracted with OSA 4.2, the second row to those extracted with SF software. In all cases the fit to a power law model plus a high energy cut off, and the residuals to the fit, are plotted. **Left panels:** spectra from science window 54–29. **Middle Panels:** spectra from science window 67–39. **Right Panels:** spectra from science window 67–42.

Table 13.14: Fluxes in different energy bands measured for those science windows shown in Table 13.13. All flux measurements are given in units of  $10^{-10}$  ergs s $^{-1}$  cm $^{-2}$ . Spectra extracted with the SF software were used to derive the fluxes.

SCW	4–25 keV	20–60 keV	20–150 keV	4–150 keV
54–29	7.0	5.7	6.5	13.6
67–39	6.7	5.3	6.8	13.6
67–40	8.1	6.2	8.3	16.3
67–41	5.7	3.7	4.0	9.6
67–42	7.1	5.0	6.0	13.2
67–43	7.0	8.6	4.7	11.7

We can safely assume that the spectral properties of the average spectrum over the whole GPS time interval considered in this chapter represent quite well the spectral properties of the source during outburst. All the attempts to search for spectral variability gave negative results. The average joint JEM-X–ISGRI spectrum, in the energy range 3–200 keV (see Fig. 13.33), is well fitted by a power law plus a high energy cut-off. When we use ISGRI spectra extracted with OSA 4.2 software, the fitted photon index is  $0.9 \pm 0.1$ . The high energy cut-off derived lies at  $6 \pm 1$  keV (unlike for the rest of parameters, where the error represents the 90% Confidence Level (C.L.), in this case the error given represents a 68% C.L.), and we find a folding energy of  $17 \pm 2$  keV. The  $\chi^2_{\text{red}}$  of the fit was 1.3 for 158 degrees of freedom. When we use the ISGRI spectrum extracted with the SF software, the derived photon index is  $1.1^{+0.2}_{-0.1}$  and the cut-off and folding energies are  $7^{+5}_{-2}$  keV and  $25 \pm 2$  keV, respectively. Although in both cases the photon index (dominated by JEM-X data) and the cut-off energy are compatible within errors, the folding energy is different. We already noticed this discrepancy in the higher energy channels when comparing results from both spectral extraction methods. There is a difference in the count rate of the extracted photons above 70 keV. These spectral parameters are compatible with the ones found in the literature, demonstrating the very small spectral variability of this source while in outburst. At the

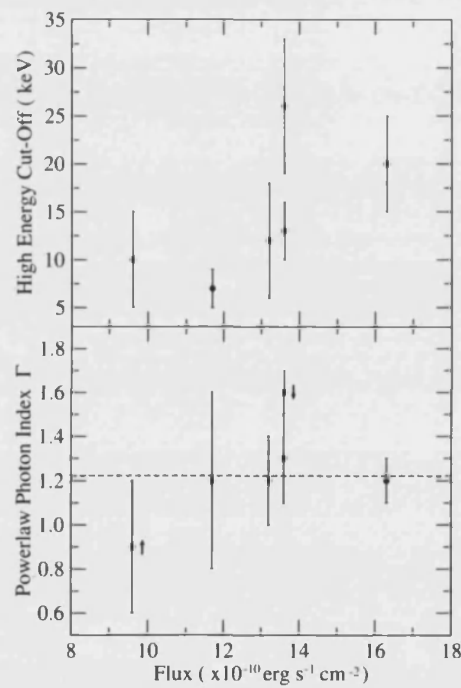


Figure 13.32: Spectral parameters (power law photon index and high energy cut off) versus the 4–150 keV flux for the joint JEM-X–ISGRI spectra shown in Table 13.13.

error level of our data we can conclude that there are no spectral features (absorptions or emissions) in the spectrum of SAX J2103.5+4545. However, Baykal et al. (2002) reported the presence of iron line at  $\sim 6.4$  keV. They may be hidden behind the large error bars of our data. We may attribute the  $\sim 6.4$  keV iron line reported by Baykal et al. (2002) to contamination from the Galactic Ridge emission. However, Baykal et al. (2002) demonstrate that the iron line detected changes its properties with the spectral state of the source, not leaving doubts about the origin of such line: the surroundings of the neutron star in SAX J203.5+4545. The fluxes measured from *INTEGRAL* GPS data are  $12.6 \times 10^{-10}$  erg cm $^{-2}$  s $^{-1}$  and  $13.7 \times 10^{-10}$  erg cm $^{-2}$  s $^{-1}$  with OSA 4.2 and SF extracted spectra respectively, in the 4–150 keV energy range. Considering a distance to the source of 6.5 kpc, this values correspond to luminosities of  $6.5 \times 10^{36}$  erg s $^{-1}$  and  $6.0 \times 10^{36}$  erg s $^{-1}$ .

### SPI Spectra

SPI has a very different way of working than JEM-X and ISGRI. As mentioned in subsection 13.1.4, for a source like SAX J2103.5+4545, to achieve a signal to noise ratio of  $\sim 10$  we need around  $\sim 550$  ks of exposure. Therefore, we have been able to extract only one spectrum for the whole bright phase (from MJD  $\sim 52600$  up to MJD  $\sim 52900$ ), in the 20–100 keV energy range. However, and for the first time, we have been able to extract a spectrum during the source's faint state with SPI data, in the 20–100 keV energy range. The faint state spectra was obtained joining observations from revolutions 153, 154, 159, and 169, in the interval MJD  $\sim 53020.0$ –MJD  $\sim 53040.0$ , with a total exposure time close to  $\sim 600$  ks (290 science windows). Both spectra (for the bright state and for the faint state) are shown in Fig. 13.34.

A single power law was used to fit the spectra shown in Fig. 13.34. The fit parameters of the bright state (BS) and faint state (FS) are shown in Table 13.15. The difference in the photon index ( $\Gamma$ ) and in the 20–100 keV flux are significant.

This is the first time that the spectral change between bright and faint states is reported for energies above 20 keV. Previously, only once this spectral change has been reported using *RXTE* data (Baykal et al., 2000).

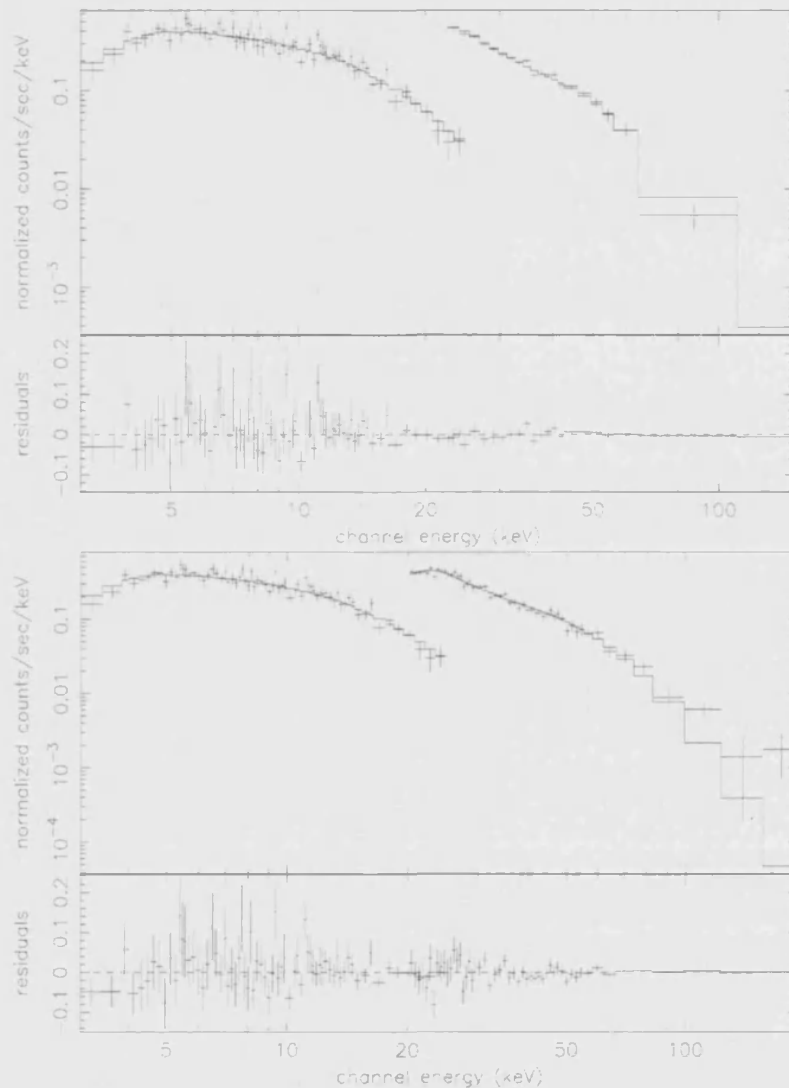


Figure 13.33: **Upper panel:** Average joint JEM-X-*ISGRI* spectrum for the GPS between revolutions 31 and 181 when OSA 4.2 is used. The spectrum is well fit by a power law with photon index  $0.9 \pm 0.1$  modified with a high energy cut-off at  $6 \pm 1$  keV with a folding energy of  $17 \pm 2$  keV. The  $\chi^2_{\text{red}}$  of the fit was 1.3 for 158 degrees of freedom. Systematic errors of 2% were introduced in both sets of data. **Lower panel:** Average joint JEM-X-*ISGRI* spectrum for the GPS time span between revolutions 31 and 181. OSA 4.2 software was used to extract JEM-X spectra but SF software was used to extract *ISGRI* data. The best fit to the 3.0–200.0 keV spectrum was a power law with a photon index of  $1.1^{+0.2}_{-0.1}$  modified by a cut off at  $7^{+5}_{-2}$  keV with a folding energy of  $25 \pm 2$  keV.

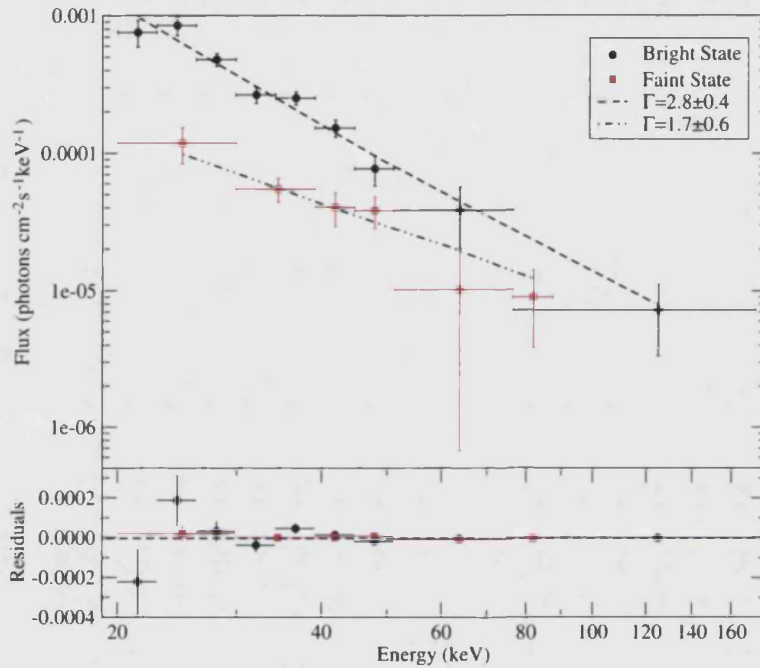


Figure 13.34: Comparison of the SPI spectra of SAX J2103.5+4545 during bright and faint states in the 20–100 keV energy range. A simple power law model was fitted to the data. A change of spectral state is evident.

Table 13.15: Parameters of the power law fit to the SAX J2103.5+4545 spectrum during the bright state (BS) and to the one during the faint state (FS). The spectra cover the 20–100 keV energy range.

	$\Gamma$	$\chi_{\text{red}}^2$	Flux $\times 10^{-10}$ erg s $^{-1}$ cm $^{-2}$
BS	$2.8 \pm 0.3$	1.1	6.6
FS	$1.7^{+0.7}_{-0.5}$	1.0	1.3





## Chapter 14

# Discussion

We have carried out a timing and spectral analysis of the two outbursts undergone by the Be/X-ray binary SAX J2103.5+4545 during the *INTEGRAL* Performance and Verification phase in December 2002. The excellent imaging capabilities of *INTEGRAL* allowed us to reduce the uncertainty in the position of the source by a factor of  $\sim 3$ . The *INTEGRAL* location of the X/ $\gamma$ -ray source agree with the position of the recently proposed optical counterpart (Reig et al. 2004).

No spectral variability on time scales of hours/days has been observed in the *INTEGRAL* data for SAX J2103.5+4545. In contrast, the source is quite rich in temporal variability. In the short term ( $\sim$ seconds), X-ray pulsations with a pulse period of 350.0 s are clearly detected (MJD  $\sim$ 52630). This value of the pulse period contrasts with that measured by Baykal et al. (2000) of 358 s (MJD  $\sim$ 51520) and indicates a long term spin-up of the neutron star. In this respect, it is illustrative to compare our results with the quasi simultaneous RXTE and XMM observations (and contemporaneous to the *INTEGRAL* observations) of İnam et al. (2004). They found a pulse period of 354.8 s (MJD  $\sim$ 52640), in excellent agreement with the one we obtained. Although a short spin-down phase was found by Baykal et al. (2002), it seems that the source has suffered a global spin up due to the accretion of matter. The change in pulse period would be compatible with a continuous spin-up of  $\frac{d\nu}{dt} = 2.5 \times 10^{-13} \text{ Hz s}^{-1}$  since 1999. Nevertheless, the spin-up is known to be linked to the accretion process, and hence, it is discontinuous and depends on the dynamics of

the system, including both the neutron star orbit and the Be star dense envelope. Unlike most BeX systems (Corbet 1986), SAX J2103.5+4545 does not rotate at the equilibrium period (Reig et al. 2004).

In the medium term ( $\sim$ days), the X-ray behaviour of the BeX system SAX J2103.5+4545 is characterised by regular increases of the X-ray flux modulated with the orbital period (type I outbursts). The *INTEGRAL* observations coincided with two of these outbursts. Assuming a distance to the source of  $6.5 \pm 0.9$  kpc, (Reig et al. 2004) the X-ray luminosity in the 4–150 keV energy range, amounts to  $\sim 6.0 \times 10^{36}$  erg s $^{-1}$ , which is typical of type I outbursts in BeX systems. The quoted error in the distance introduces a 30% of relative error in the luminosity determination.

SAX J2103.5+4545 also displays longer-term X-ray variability (of the order of months), consisting of low and high-activity X-ray states. Type I outbursts are only seen during bright states (Fig. 11.1, see also Baykal et al. 2002). We have analysed the last bright state of the source with *INTEGRAL* data. Unfortunately, during the faint state, *INTEGRAL* data is not good enough to provide spectra and fine time resolution light curves. In the majority of cases only upper limits of the fluxes can be derived. However, during the bright state we have been able to add more evidence to the spectral shape constancy of the source above a certain flux level. Both hardness ratios in all energy bands and spectral parameters fitted to data are consistent with no spectral changes. In fact, the only spectral change reported in the literature was the difference between faint and bright state (see Baykal et al. 2000). In this work, and for the first time in energy ranges above 20 keV, we report a spectral change between the bright and faint states.

Alternate spin up and spin down periods within the last bright phase also gives some hints about the possible complex timing behaviour of the source. Although a global spin up process is detected, it is possible that actually the source is suffering short spin down episodes. These episodes will coincide with moments in which the accretion onto the neutron star pole caps is not very intense. Baykal et al. (2002) already reported a spin down episode during the November 1999 bright state. The behaviour of SAX J2103.5+4545 may be similar to that of the BeX system 4U 0115+63. Spin-up episodes during type-I outbursts followed by spin down epochs between outbursts are known to happen in 4U 0115+63 (see Ricketts et al.

1981). The compact companion to 4U 0115+63 is a pulsating neutron star with a 3.6 s pulse period. The orbital period of 4U 0115+63 is 24 days and the eccentricity, namely 0.34, is very similar to that of SAX J2103.5+4545. Another source for which spin up and spin down episodes have been reported is A0535+26 (Li et al. 1979), a  $\sim 103.84$  s pulsating neutron star in a BeX system. In all these sources the spin up is detected during outburst, but the spin period is kept almost constant in the long term. This is compatible with a spin-down episode in the epochs between outbursts. This spin down can take place when the amount of matter available for accretion is very low and hence the Alfvén radius becomes larger than the co-rotation radius of the neutron star. The neutron star enters then the *fast rotator phase* and will follow the natural tendency of losing angular momentum.

Given the short orbital period (compared to BeX systems) observed in SAX J2103.5+4545 (12.7 days), the neutron star must exert substantial influence on the evolution of the circumstellar disk. In the optical band, this influence translates into a highly variable H $\alpha$  line, exhibiting V/R asymmetry and reversing from emission into absorption on time scales of a few days (Reig et al. 2004). In the X-ray band, the influence of the neutron star on the Be star envelope might be at the origin of the lack of giant (type II) outbursts and the long-term activity. In the framework of the viscous accretion model (Okazaki & Negueruela 2001), the scenario would then be as follows. The tidal interaction of the neutron star produces the truncation of the Be star envelope. The truncation radius in SAX J2103.5+4545 would be similar in size to the critical lobe radius at periastron. When the density and/or size of the Be star envelope are large enough, matter fills the critical lobe and is accreted onto the neutron star. The system is in the bright state. One periastron passage is not enough to exhaust the fuel from the disk. However, after several orbits the Be star's disk weakens, the amount of matter available for accretion decreases and the system enters a faint state. Once the disk recovers the initial conditions, the cycle starts again. During the bright state there is a first epoch of increasing size of the disk (when each successive type-I outburst becomes brighter) and a second epoch when the available matter for accretion is pulled by the neutron star little by little until the disk is disrupted or becomes too small to let accretion take place in such an

efficient way as during the bright phase. Although this scenario seems to describe properly the observed properties of SAX J2103.5+4545 in all the energy ranges studied, we must keep in mind that global changes in the flux of matter from the donor down to the neutron star can also produce a similar behaviour.

Although the number of optical observations of SAX J2103.5+4545 is scarce, the information available indicates a correlation between the long-term optical and X/ $\gamma$ -ray variability. The optical observations (August and September 2003) reported by Reig et al. (2004) coincided with the transition to an X-ray faint state (see Fig. 14.1). The H $\alpha$  emission was low (equivalent width of  $\sim -1.5$ ), and later the H $\alpha$  line appeared in absorption and the optical magnitudes were consistent with little circumstellar reddening. In contrast, the photon spectral index and the X-ray flux obtained from the spectral analysis of the *INTEGRAL* observations indicate that SAX J2103.5+4545 was in the bright state. Unfortunately, the Optical Monitoring Camera on board *INTEGRAL* suffers of source confusion with the optical counterpart to SAX J2103.5+4545 and two nearby stars, thus no data from the OMC can be used to analyse the optical properties of this source.

Fig. 14.2 shows the comparison of the high energy light curve at two energy bands (2–12 keV with *RXTE*/ASM data and 25–40 keV with IS-GRI data) with the infrared colours ( $H - K$ ) and ( $J - H$ ), the infrared magnitude  $J$  and the equivalent width of the H $\alpha$  line. The infrared magnitudes are taken from Reig et al. (2004). Optical and infrared data was retrieved right during the transition from bright state to faint state of SAX J2103.5+4545. It is noticeable that, while the high energy flux decreases, the equivalent width of the H $\alpha$  line increases, indicating that the emission is disappearing, leaving an absorption profile. The infrared magnitude  $J$  shows an unexpected behaviour: it increases in brightness while the Be disk is disappearing (weaker emission in the H $\alpha$  line profile). We would expect a fainter  $J$  magnitude. However the ( $J - H$ ) colour, although the errors are big and care must be taken when interpreting these results, seems to become smaller, that is, the colour excess becomes also smaller, as expected. ( $H - K$ ) colour shows big errors and seems to be quite constant.

We expect the enhancement of emission in the H $\alpha$  line as well as larger

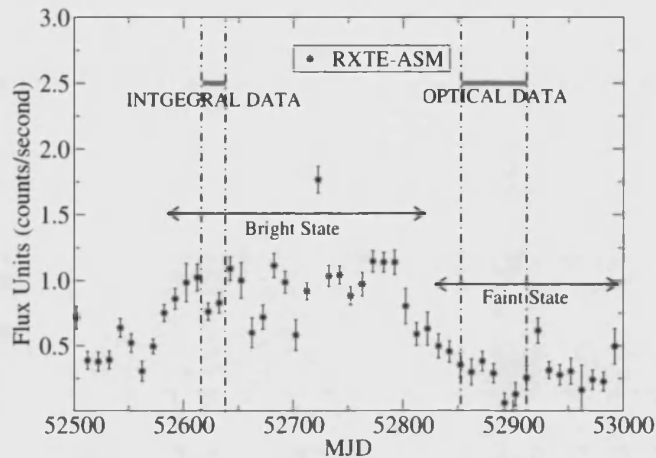


Figure 14.1: 10 day averaged RXTE-ASM light curve showing the transition from bright state (end of 2002 and first half of 2003) into faint state (second half of 2003). The epochs of *INTEGRAL* and optical observations are indicated by horizontal lines.

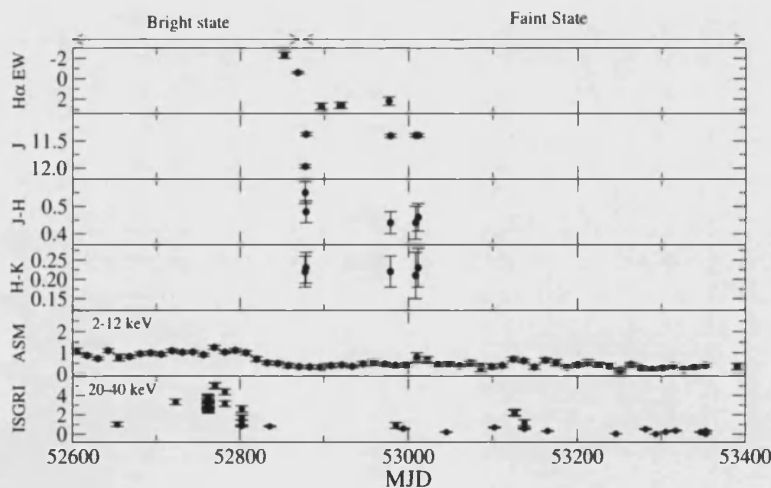


Figure 14.2: comparison of the high energy light curves with the variations in the IR J magnitude and (H-J) and (J-K) colours, and the EW of the H $\alpha$  line of SAX J2103.5+4545.

infrared excesses when the next bright state starts. The occurrence of the next bright state is unpredictable. Previous faint states had durations varying between 30 and 300 days.

## 14.1 Conclusion and Future Work

The BeX-ray binary SAX J2103.5+4545 has been observed with *INTEGRAL*. Our main results are: *i*) we have reduced to about 30 arc seconds the uncertainty in the position of the system. This has allowed to find a new optical counterpart; *ii*) we have obtained the first broadband spectrum (4-150 keV) of SAX J2103.5+4545. Above 150 keV the flux is comparable to the sensitivity limits of the instruments. Further improvements in the software and/or in the response matrices, or longer exposure times, may allow to reach higher energies; *iii*) the value of the pulse period indicates a long-term spin-up trend; *iv*) the high-energy emission correlates with the optical activity state of the system; and *v*) we have characterised the faint and bright spectral states for the first time above 20 keV.

Simultaneous observations in the optical/IR and X/ $\gamma$ -ray bands are needed to understand the connection between the changes in the Be star envelope and the behaviour in the high-energy bands. In particular, simultaneous optical/X-ray observations of SAX J2103.5+4545 during the bright state would be very clarifying. This system, with the shortest orbital period known for an accretion-powered BeX binary, represents an excellent laboratory to test current models for BeX systems.





## Bibliography

- Baykal, A., Stark, M. J., and Swank, J.: 2000, *ApJL* **544**, L129
- Baykal, A., Stark, M. J., and Swank, J. H.: 2002, *ApJ* **569**, 903
- Coburn, W., Heindl, W. A., Rothschild, R. E., Gruber, D. E., Kreykenbohm, I., Wilms, J., Kretschmar, P., and Staubert, R.: 2002, *ApJ* **580**, 394
- Corbet, R. H. D.: 1986, *MNRAS* **220**, 1047
- Del Santo, M., Rodriguez, J., Ubertini, P., Bazzano, A., Bird, A. J., Capitanio, F., Foschini, L., Goldwurm, A., Lebrun, F., Paizis, A., and Segreto, A.: 2003, *A&A* **411**, L369
- Falanga, M., di Salvo, T., Burderi, L., Bonnet-Bidaud, J. M., Goldoni, P., Goldwurm, A., Lavagetto, G., Iaria, R., and Robba, N. R.: 2005, *A&Ap* **436**, 313
- Galloway, D. K., Morgan, E. H., and Levine, A. M.: 2004, *ApJ* **613**, 1164
- Ghosh, P. and Lamb, F. K.: 1979, *ApJ* **234**, 296
- Hulleman, F., in 't Zand, J. J. M., and Heise, J.: 1998, *A&A* **337**, L25
- İnam, S. Ç., Baykal, A., Swank, J., and Stark, M. J.: 2004, *ApJ* **616**, 463
- Li, F., Clark, G. W., Jernigan, J. G., and Rappaport, S.: 1979, *ApJ* **228**, 893
- Lutovinov, A. A., Molkov, S. V., and Revnivtsev, M. G.: 2003, *Astronomy Letters* **29**, 713
- Okazaki, A. T. and Negueruela, I.: 2001, *A&A* **377**, 161
- Reig, P., Negueruela, I., Fabregat, J., Chato, R., Blay, P., and Mavromatakis, F.: 2004, *A&A* **421**, 673
- Ricketts, M. J., Hall, R., Page, C. G., and Pounds, K. A.: 1981, *Space Science Reviews* **30**, 399

Sidoli, L., Mereghetti, S., Larsson, S., Chernyakova, M., Kreykenbohm, I., Kretschmar, P., Paizis, A., Santangelo, A., Ferrigno, C., and Falanga, M.: 2005, *A&A* **440**, 1033

Stark, M. J., Heffner, C. M., Baykal, A., and Swank, J. H.: 2004, *American Astronomical Society Meeting Abstracts* 205

Walborn, N. R. and Fitzpatrick, E. L.: 1990, *PASP* **102**, 379



## Apèndix A

# Resum del treball de tesi

Encara que la novetat principal d'aquest treball de tesi és l'anàlisi de dades d'*INTEGRAL* (INTERnational Gamma-Ray LAboratory) amb les eines informàtiques associades (programari oficial distribuït per l'ISDC –Integral Science Data Center–), una bona part de les conclusions més importants no es podrien assolir sense el recolzament d'observacions amb altres instruments i/o telescopis terrestres. Volem així emfatitzar la importància dels estudis multi-freqüència en el cas de sistemes complexos com els que presentem en aquest treball de tesi. Aquests són els Sistemes Binaris de Raigs-X d'Alta Massa (SBRXAM). En concret ens centrarem en 4U 2206+54 i SAX J2103.5+4545.

Primer de tot farem una xicoteta introducció dels conceptes més rellevants tractats al llarg de tot el treball. Passarem, després, a descriure les motivacions que ens han dut a escollir aquests dos sistemes com a objectiu científic i en què es basa, precisament, la seua relevància científica. Seguidament presentarem de forma individual els resultats de cadascú dels dos sistemes. Acabarem amb conclusions generals sobre aquests tipus d'estudis.

## 1. Astrofísica d'altres energies

### 1.1. L'observació de l'univers

El fet de viure en grans ciutats té algunes conseqüències no desitjables. Una d'elles és l'allunyament de la nostra experiència quotidiana de les meravelles que ens mostra l'univers, degut a l'excesiva il·luminació en les ciutats, ja que aquesta amaga el cel nocturn de les nostres mirades. Malgrat tot, l'espai està de moda (amb la posada en òrbita de l'estació espacial internacional, els primers vols de turistes a l'espai que apareixen continuament en televisió, etc.), i és conegut per tots que fora de la terra hi ha moltíssimes més coses de les que podem imaginar. No totes aquestes coses són visibles als nostres ulls, moltes van romandre invisibles fins que la tecnologia ha desenvolupat detectors (per casualitat o per interès científic) capaços de veure per nosaltres què està esdevenint en racons llunyans de la nostra galàxia i de l'univers.

A la Terra no arriba només llum (radiació electromagnètica) des de tots els racons de l'univers, també ens arriben partícules accelerades a grans velocitats. De vegades aquestes partícules no interaccionen amb l'atmosfera terrestre, ni tan sols amb la matèria més densa de la Terra (com ara els neutrins). Altres vegades aquestes partícules són aturades en les capes altes de l'atmosfera (com és el cas de partícules massives). En aquesta anàlisi ens interessarem només en l'estudi de la radiació electromagnètica, ara bé, intentarem analitzar el rang d'energies més ample possible per tal de tenir una visió el més completa possible dels escenaris astrofísics en les quals s'està produint aquesta radiació. Igual que les partícules, la radiació electromagnètica també sofrirà una absorció selectiva en l'atmosfera abans d'arribar fins a nosaltres, aquesta absorció dependrà de la manera d'interaccionar de la radiació amb les partícules presents en l'atmosfera.

La radiació electromagnètica en el rang d'energies que anomenem *visible*, serà dispersada fins arribar a la superfície terrestre. Així, els telescopis terrestres han estat les ferramentes clàssiques que han desvelat els secrets de l'univers *visible* fins a límits difícils de creure, amb la precisió i la qualitat de les imatges assolides amb les últimes tecnologies. Igual que passa amb el rang *visible*, l'atmosfera és transparent també a les ones de ràdio i l'infraroig pròxim. Per tal d'obtenir informació de fenòmens que produeixen emissió de radiació electromagnètica en el rang UV o en

altes energies (raigs-x i raigs- $\gamma$ ), necessitarem l'ajuda de naus espacials (satèl·lits amb aparells de mesura i els seus sistemes òptics associats) ja que l'atmosfera absorbirà aquests rangs energètics (per altra banda aquest fet ha afavorit l'aparició de la vida en la Terra, protegida d'aquestes radiacions que poden ser perjudicials per als éssers vius).

Així, l'astrofísica d'altres energies no va nèixer fins que es donaren els primers passos en l'exploració de l'espai exterior.

## 1.2. INTEGRAL

*INTEGRAL* és un satèl·lit europeu (amb col·laboracions de Rússia i Estats Units) dedicat a l'observació de l'univers en altes energies. A bord d'*INTEGRAL* tenim els dos instruments principals, SPI (SPectrometer in INTEGRAL) i IBIS (Imager on Board INTEGRAL Spacecraft), junt a dos monitors, JEM-X (Joint European Monitor-X) i l'OMC (Optical Monitoring Camera) que complementen les observacions en raigs-x i en la banda òptica V, respectivament. Anem a descriure un poquet més amb detall els instruments a bord d'*INTEGRAL*:

- **SPI.** Es tracta d'un telescopi basat en tecnologia de màscares codificades. El pla detector d'SPI està format per 19 detectors de Ge, amb una àrea sensible total de  $\sim 500 \text{ cm}^2$ , el qual treballa en el rang 18 keV–8 MeV. La resolució espectral és molt alta (2.2 keV FWHM a 1.33 MeV) i permet realitzar estudis de precisió de línies d'altres energies.
- **IBIS.** Està optimitzat per aconseguir una bona resolució espacial i poder aportar imatges d'alta resolució (amb 12 arcmin FWHM de resolució angular). Una màscara codificada actua com a sistema òptic. IBIS conté dos detectors:
  1. ISGRI (INTEGRAL Spacecraft Gamma-Ray Imager), amb una matriu de  $128 \times 128$  detectors de CdTe que ofereixen una gran àrea col·lectora ( $\sim 2600 \text{ cm}^2$ ). Funciona en el rang 15–1000 keV.
  2. PICsIT (PIXellated Caesium Iodide Telescope), amb un pla detector de  $64 \times 64$  píxels que resulten en una àrea col·lectora de  $\sim 2890 \text{ cm}^2$ . Està optimitzat per al rang 0.175–10.0 MeV.

Els dos instruments que formen IBIS es complementen en energies i, conjuntament, poden treballar en mode Compton, ja que es troben disposats en capes paral·leles (ISGRI en la capa superior i PICsIT en la capa inferior).

- **JEM-x.** Aquest és el monitor en el rang x (3 – 35 keV) que complementa les mesures dels instruments més energètics. Està format per detectors bessons de cambra de gas, amb una composició del 90% en xenó i el 10% en metà, a una pressió de 1.5 bar. Els dos detectors prenen imatges convolucionades per màscares codificades també bessones.
- **OMC.** És un telescopi òptic que treballa en la banda V ( 5500 Å). Proporciona un seguiment en l'òptic de totes les fonts d'altres energies observades per *INTEGRAL*.

### 1.3. Mètodes d'anàlisi

El consorci d'*INTEGRAL* ha disposat l'ISDC, encarregat d'arxivar les dades i preprocessar-les (passar-les del format descarregat del satèl·lit al format estàndard –FITS, o Flexible Image Transport System–). A més a més, l'ISDC ha de distribuir les dades entre els equips que formen part d'*INTEGRAL*, ha de facilitar l'adquisició d'aquestes per part d'astrònoms convidats, i ha de proporcionar les ferramentes necessàries per a la seua anàlisi. El programari oficial d'anàlisi d'*INTEGRAL* s'anomena OSA (Offline Scientific Analysis). OSA es divideix en una sèrie d'executables que són cridats per *scripts*, de manera que l'usuari no interacciona directament amb l'executable, més be, li passa els paràmetres adequats a l'*script* i aquest ja s'encarrega de cridar els executables en l'ordre adient. Totes les tasques necessàries per tal d'obtenir resultats científics a partir de les imatges obteses pels instruments d'*INTEGRAL* estan presents a OSA (des de les correccions instrumentals fins a l'extracció de successos per tal de construir espectres o corbes de llum).

Les ferramentes per a treballar amb les dades científiques (els resultats que ens dona l'OSA) les proporciona el HEASARC (High Energy Astrophysics Science Archive Research Center) de la NASA, i són anomenades FTOOLS. Inclouen paquets per a l'anàlisi espectral, per a l'anàlisi temporal (variacions en el temps) i per a modificar els espectres i/o corbes

de llum, així com per a operar entre ells (calcular mitjanes, ratios, etc.). També ens ofereixen ferramentes per tal de treballar amb les matrius de calibració dels instruments (per exemple, per tal d'obtenir espectres amb una resolució energètica diferent de la recomenada pels equips instrumentals, que serà la que trobem implementada en OSA).

## 2. Sistemes binaris de raigs-x

Els sistemes binaris en els quals, per algun tipus d'interacció entre els dos components del sistema, es produeix emissió en altes energies (raigs-x) són anomenats Sistemes Binari de raigs-x (SBRX). Encara que sistemes binaris formats per dos estels massius, amb vents estel·lars forts, poden emetre raigs-x en la zona de col·lisió dels vents, aquests sistemes no seran considerats SBRXs. Mes bé, classificarem com a SBRX aquells sistemes binaris formats per un objecte compacte (estel de neutrons, forat negre o nan blanc) i un estel normal (entenem com a normal que continua produïnt reaccions termonuclears al seu nucli amb suficient intensitat com per a romandre com un sistema auto-suspès, és a dir, on l'energia emesa per les reaccions termonuclears aturen la contracció induïda per l'atracció gravitatòria de, i sobre, tota la massa de l'estel). L'estel normal també és conegut com a company òptic, degut a que normalment és aquest component del sistema el que detectem quan el *mirem* amb telescopis que treballen en les bandes del *visible*. En tots aquests sistemes l'emissió en raigs-x es produeix quan massa de l'estel normal viatja fins el company compacte i interacciona amb la seua superfície, amb el seu camp magnètic, amb el seu camp gravitatori o amb tots tres. Per al cas d'estels de neutrons, l'emissió serà detectada en forma de pulsacions, degut al moviment de rotació de l'estel compacte i a que la massa accretant serà conduïda als pols magnètics d'aquest per acció del camp magnètic intens, típic en els estels de neutrons. Per al cas de forats negres, no hi trobarem pulsacions, més be emissió tèrmica des del disc d'accreció. Segons siga, principalment, la component normal del sistema, els SBRX es classifiquen en:

- **SBRXBM** (Sistemes Binari de Raigs-X de Baixa Massa): En aquests sistemes el company normal és un estel tardívol, amb una massa de l'ordre de la massa del Sol.



- **SBRXAM** (Sistemes Binariis de Raigs-X d'Alta Massa): En aquests sistemes el company òptic és un estel primerenc, amb massa superior a les 10 masses solars. Clàssicament, aquests sistemes es divideixen en dos subgrups:
  1. Sistemes amb companys massius supergegants. En aquests sistemes el company òptic és un estel de tipus OB molt evolucionat. L'emissió en raigs-x pot ser produïda quan massa perduda pel company òptic (per vent estel·lar o per desbordament del lòbul de Roche) acreta cap a l'objecte compacte i interacciona amb aquest. En cas de pèrdua de massa per vent estel·lar, les lluminositats assolides seran més baixes i els períodes de pulsació de l'objecte compacte seran llargs (la massa perduda per vent estel·lar anirà carregada amb molt poquet moment angular i produirà una alteració mínima en l'objecte compacte). En canvi, quan la pèrdua de massa es produeix per desbordament del lòbul de Roche, la massa que deixa l'estel donant durà una quantitat important de moment angular, llavors podrà influir considerablement sobre l'estel compacte i aquests tindran períodes de pulsació més curts. Tanmateix, en aquests últims sistemes, les lluminositats assolides seran prou altes. Aquest últim punt s'explica amb la formació del disc d'acreció. Com que la massa acretant conté una quantitat gran de moment angular, pot formar un disc d'acreció al voltant de l'objecte compacte. D'aquesta manera tota la matèria disponible serà aprofitada en la generació de pulsos de raigs-x. Per contra, en els sistemes amb pèrdua per vent, l'efectivitat de l'acreció és molt més xicoteta, és per això que les lluminositats seran més baixes.
  2. Sistemes amb companys massius Be. En aquests sistemes el company òptic és un estel Be. Aquests són estels B (o estels O tardívols) que desenvolupen en algun moment (o de forma intermitent) una envoltura circumestel·lar amb densitat significativament més alta en el pla equatorial de l'estel (normalment es considera que aquesta envoltura té la forma d'un disc equatorial). Aquesta envoltura produirà emissió en una o més de les línies de Balmer i un excés en l'emissió infraroja si es compara

amb estels del mateix tipus espectral, però sense envoltura. En aquest cas la matèria disponible per a l'acreció procedirà de l'envoltura, generalment per desbordament del lòbul de Roche. Aquests sistemes són especialment interessants per les interaccions que s'estableixen entre l'envoltura, o disc, circumestel·lar de l'estel Be i l'objecte compacte. Per una banda, la proximitat de l'objecte compacte influirà decissivament en les propietats del disc. Els discs dels estels Be en sistemes BeX seran molt més compactes i densos que els corresponents en estels Be aïllats. Les torsions que actuen sobre el disc circumestel·lar es poden separar en dos termes: a) la suma de totes les torsions internes (que resulten en un transport net de moment angular cap a l'exterior, és a dir, en una decreció de matèria); i b) la torsió deguda a l'atracció exercida per l'objecte compacte, en translació al voltant de l'estel Be. La intensitat relativa d'aquestes dues torsions determinarà la grandària i la densitat del disc. El punt des de l'estel Be on la torsió deguda a l'objecte compacte es fa més gran que les torsions internes s'anomena radi de truncament. Quan la matèria del disc en decreció arribe a aquest punt perdrà moment angular i caurà de nou cap a l'estel Be, re-alimentant així, el disc. En els sistemes BeX es dona una correlació directa entre el període orbital del sistema i el període de pulsació de l'estel de neutrons. Els sistemes BeX poden presentar emissió permanent o de natura transitòria. En els sistemes d'emissió permanent la lluminositat és baixa. Aquesta emissió permanent pot ser interrompuda per èpoques d'emissió amb lluminositats molt altes i que no mostren cap tipus de variació amb el període orbital (els anomenats *outbursts* de tipus II). En els sistemes d'emissió transitòria, trobem modulacions orbitals de l'emissió amb pics de lluminositat alts (*outbursts* de tipus I) o ocurrencies esporàdiques d'*outbursts* de tipus II.

### 3. Perquè 4U 2206+54 i SAX J2103.5+4545?

- **4U 2206+54:** Aquest sistema presenta una variabilitat en X típica dels sistemes on la matèria acretant procedeix del vent estel·lar. En

aquest tipus de sistemes, el company òptic és un estel supergegant. El company òptic de 4U 2206+54 (anomenat BD+53°2790), però, mostra un espectre més característic d'un estel en seqüència principal. BD+53°2790 presenta una envoltura circumestel·lar amb propietats semblants a la de les Be. Així doncs, podem pensar que es tracta d'un sistema BeX. En aquests el company compacte és un estel de neutrons. En 4U 2206+54, en un principi, la presència d'un estel de neutrons no està confirmada, i la possibilitat de què l'objecte compacte del sistema siga un forat negre no es pot descartar (en aquest treball presentarem evidències que assenyalen l'estel de neutrons com el company compacte més probable). El fet que el sistema no presente pulsacions fa difícil la interpretació de l'objecte compacte com un estel de neutrons. Tot açò fa que tampoc poguem classificar 4U 2206+54 com un sistema BeX. Ens enfrontem amb un sistema que no encaixa en cap dels grups en què es subdivideixen clàssicament els SBRXAMs.

- **SAX J2103.5+4545:** En aquest cas la classificació dins el grup de les BeX està ben establerta. Encara així, aquest sistema presenta una sèrie de peculiaritats que el diferencien de la resta de BeX. No segueix la correlació existent entre el període de pulsació de l'objecte compacte i el període orbital del sistema. Es tractaria d'un dels sistemes BeX amb període orbital més curt conegut. La proximitat de l'estel de neutrons, i la seua interacció amb el disc circumestel·lar de l'estel Be semblen ser les causes del seu comportament tan especial. El sistema presenta períodes d'emissió de lluminositat baixa, sense modulació orbital, alternats amb períodes de lluminositat alta amb modulació orbital. Aquest comportament sembla ser una combinació de tots els tipus d'emissió observats en els sistemes BeX.

Veiem, doncs, que els dos sistemes presenten característiques que, o bé fan molt complicada la seua classificació, o bé s'allunyen de les propietats generals dels estels del seu grup.

Ens plantegem, aleshores, analitzar en detall, i en el rang energètic més ample possible, aquests dos sistemes, per poder caracteritzar-los observacionalment de la forma més completa possible. Volem arribar, així, a un coneixement més profund dels fenòmens físics responsables, per una

banda, de la creació d'unes pautes singulars que permeten la classificació de la gran majoria de SBRXAMs en grups i subgrups, i, d'altra banda, l'aparició de sistemes que presenten certes peculiaritats.

#### 4. El sistema 4U 2206+54

En la secció anterior ha quedat palés el fet que aquest sistema, en principi, no sembla encaixar en cap dels grups en què clàssicament es classifiquen els SBRXAM. Passarem, doncs, a fer un repàs de les propietats observacionals d'aquest sistema en un rang d'energies molt ample, des del ràdio fins als raigs- $\gamma$ .

En altes energies, aquesta font és persistent, però variable. En escales temporals curtes, presenta una variabilitat estocàstica, en canvi, en escales temporals grans, domina la modulació orbital ( $\sim 9.6$  dies). En escales curtes s'han mesurat variacions en un factor 3, mentre que a escales llargues s'han trobat variacions fins a un factor 10. A més a més, es desconeix (però no es descarta) la presència de pulsacions en el sistema.

En l'òptic, el sistema mostra un company massiu (BD+53°2790) amb una classificació espectral de O9.5V, encara que amb certes ambigüitats; com ara, l'espectre en l'infraroig proper, que és més semblant al dels estels supergegants. Presenta evidències de posseir una envoltura circumestel·lar, però amb diferències respecte a les dels estels Be, com pot ser, per exemple, la asimetria entre els pics V i R de la línia H $\alpha$ , que és variable i cíclica en aquests últims però que presenta una asimetria permanent amb V>R en BD+53°2790.

##### 4.1.-Ràdio

Al llarg de maig del 2003, dos conjunts d'observacions de 4U 2206+54 es van dur a terme des del VLA (Very Large Array). Els dies julians modificats mitjans d'ambdós observacions són 52771.4 i 52779.7, que corresponen al 12 i al 20 de maig respectivament. En la primera observació no es va detectar emissió en radi amb un límit superior de 0.042 mJy a un nivell de  $3\sigma$ . En la darrera observació la detecció també va ser negativa, amb un límit superior de 0.066 mJy a un nivell de  $3\sigma$ . Concatenant les dues observacions confirmem la no detecció amb un límit superior de

0.039 mJy a un nivell de  $3\sigma$ . Empíricament, s'ha demostrat que, si hi hagués un forat negre present en el sistema, caldria esperar certa emissió en el rang de les ones de ràdio. Hem trobat, aleshores, la primera indicació de que la contrapartida compacta d'aquest sistema no és un forat negre.

## 4.2.-IR

13 anys de seguiment de BD+53°2790 en les bandes  $J$ ,  $H$  i  $K$  de l'infraroig, mostren que la font és variable (amb una amplitud màxima de 0.2 magnituds) però sense cap modulació evident. En canvi els colors ( $J - H$ ) i ( $H - K$ ) sí mostren certa modulació a llarg termini (més forta en ( $J - H$ )). Aquesta modulació correspondrà escales temporals de l'ordre de  $\sim 5$  anys, però no tenim prou cobertura temporal com per a confirmar l'existència d'aquesta.

## 4.3.-Òptic

### 4.3.1. Fotometria

El conjunt de dades fotomètriques de que dispoem no és molt ample, però indiquen la presència de certa variabilitat en la banda V a voltant d'un valor de  $\sim 9.8$  magnituds.

### 4.3.2. Espectroscopia

La font ha estat contínuament observada, tant en la zona blava com en la zona roja de l'espectre, al llarg dels últims 15 anys.

En la zona blava (3000–5000 Å), l'espectre ens mostra les línies pròpies d'un estel entre O9 i O9.5 i en seqüència principal. Amb les línies d'Heli podem estimar la velocitat de rotació de l'estel. Trobem que aquesta ha de ser  $315 \pm 70$  km s<sup>-1</sup>. Comparant l'espectre de BD+53°2790 amb el d'un estel estàndard, 10 Lac, de tipus espectral O9V, es comprova que les línies d'Heli presents en BD+53°2790 són més intenses que les corresponents al seu tipus espectral. Aquest fet ens està donant pistes sobre la possible relació d'aquest estel amb els anomenats *He-strong*.

En la zona roja (5500–7500 Å), es pot estudiar amb detall la variabilitat en la línia H $\alpha$ . En molts casos també és possible estudiar la línia propera d'HeI  $\lambda 6678$  Å. La línia H $\alpha$  presenta sempre una estructura de doble pic.

Malgrat ser molt variable, sempre mostra el pic V (en la part blava de la línia) més baix que el pic R (en la part roja). Aquesta asimètria sobreviu als canvis estructurals més dràstics de la línia, com la pèrdua quasi total de l'emissió en Maig de 1982. Quan restringim l'anàlisi a un conjunt coherent de dades (aquelles que provenen d'un mateix instrument), els diferents paràmetres de la línia  $H\alpha$  mostren correlacions entre ells, com correspon al cas de línies d'emissió formades en envoltures dominades per rotació. En canvi, aquests paràmetres no mostren cap correlació amb les magnituds infraroges, fet diferencial respecte dels estels Be.

Una sèrie de campanyes intensives en Juliol de 2000, Juliol de 2002, Juliol de 2003 i Agost-Octubre de 2004 mostren variabilitat freqüent de la línia  $H\alpha$  d'una nit a l'altra, i, de vegades, variabilitat en escales temporals d'unes poques hores. Malgrat tots els intents, no hem pogut trobar modulacions periòdiques dels paràmetres de la línia  $H\alpha$  (o de  $HeI$   $\lambda 6678$  Å).

En tots els casos s'observa cert grau de correlació entre els paràmetres de la línia  $H\alpha$  i els de la de l' $HeI$   $\lambda 6678$  Å. Aquest fet ens està indicant que una part de l'emissió en ambdues línies té un origen comú.

#### 4.3.3. Velocitats radials i paràmetres orbitals

Un dels resultats més interessants de les campanyes intensives és l'anàlisi de velocitats radials dut a terme. En les campanyes intensives de Juliol de 2002, Juliol de 2003 i Agost-Setembre de 2004, es prengueren suficient nombre d'espectres en la zona blava com per a poder realitzar un estudi preliminar del moviment orbital del sistema.

En tots els casos, les operacions següents varen ser aplicades a les dades per tal de poder obtenir una mesura de la velocitat radial del sistema per nit d'observació:

1. Es va computar una mitjana per nit per als casos on tinguem més d'un espectre en la mateixa nit.
2. Tots els espectres així preparats, van ser transformats a una escala en longituds d'ona uniforme (amb la mateixa resolució) en el rang 4050–4750 Å.
3. Una línia d'absorció interestel·lar va ser utilitzada per tal d'aliniar

tots els espectres i corregir així errors en l'ajust de l'escala de longituds d'ona.

4. Totes les longituds d'ona van ser corregides a un sistema de velocitats heliocèntriques.
5. Un espectre mitjà va ser utilitzat com a plantilla per tal de fer correlació creuada amb tots els espectres observats i obtenir així una mesura del desplaçament en velocitats respecte de la mitjana.

El nostre conjunt de dades conté certes pautes en la forma d'observar (referides a la distribució temporal de les mesures) que compliquen l'anàlisi. A més a més, alguns dels espectres son molt sorollosos i donen lloc a mesures amb errors molt grans que influiran negativament en la cerca de períodes. La nostra anàlisi temporal de la corba de velocitats radials dóna lloc a la trobada d'una periodicitat de 14.89 dies. Es comprova que aquesta periodicitat no és real, sinò més bé un artefacte del procés matemàtic degut a la influència d'uns quants punts que introdueixen molt de soroll. Tanmateix, si utilitzem el període trobat amb dades d'altres energies (9.5591 dies) tots els punts de velocitat radial encaixen bé, i ben distribuïts, en la corba de velocitats radials re-escalada a la fase orbital.

Així doncs, confirmem amb dades òptiques el període trobat en altes energies. Amb la corba de velocitats radials en fase orbital, podem intentar ajustar models que ens permetran restringir els paràmetres orbitals. Podem arribar a la restricció de l'excèntricitat de l'òrbita entre els valors 0.2–0.4, amb una semiamplitud d'uns  $\sim 18 \text{ km s}^{-1}$  i una anomalia del periastre entre les fases 0.1 i 0.2. Aquest resultat coincideix amb les conclusions derivades d'una anàlisi exhaustiva de dades d'altres energies de *RXTE/ASM* i que, mentre escric aquestes línies, s'ha enviat a publicar.

#### 4.4.-UV

Disposem d'un espectre al rang UV (1200–1900 Å) procedent de l'IUE (Internacional Ultra-violet Explorer). Ens hem plantejat fer una anàlisi de quins son els paràmetres del vent estel·lar present en el company òptic de 4U 2206+54. L'espectre és sorollos, llavors, només ens permetrà fer una estimació dels paràmetres.

Amb dues metodologies independents, la comparació, per una banda, de l'espectre observat amb els espectres generats artificialment amb un codi SEI (Sobolev with Exaxt Integration), i l'ajust, per una altra banda, de l'espectre observat a models mitjançant un codi genètic que incorpora diferents aproximacions al problema del vent estel·lar, hem arribat a la conclusió que BD+53°2790 presenta un vent amb una velocitat terminal inferior a  $500 \text{ km s}^{-1}$ , i amb un ritme de pèrdua de massa de l'ordre de  $10^{-8}$  masses solars per any. Aquests paràmetres contrasten amb els típics per a estels d'aquest tipus espectral. Mentre que el que calia esperar era un vent ràpid i poc dens, el que hem trobat és un vent lent i molt dens. Cal esmentar que aquest resultat està d'acord amb el tipus de vent esperat per a poder explicar les variacions orbitals en altes energies (és a dir, produeixen un ritme d'acreció de matèria adequat per tal d'explicar les variacions observades en el flux de raigs-x).

Cal tenir present, però, que la nostra mesura fa referència només a les propietats del vent en un moment determinat. El vent, en canvi, pot ser molt variable. Tanmateix, la normalització al continu en aquesta regió de l'espectre és molt complicada, i pot afectar l'estimació de l'alçada dels perfils P-Cygni. Les velocitats trobades poden deixar un remanent del pic P-Cygni en excés d'emissió, aquest fet podria ser degut a la presència d'una segona component del vent més ràpida i dona més evidències a favor de la classificació de BD+53°2790 com un estel *He-strong*.

#### 4.5.-Altes energies

En aquest rang de l'espectre electromagnètic hem utilitzat dades dels satèl·lits *INTEGRAL* i *RXTE* per a l'anàlisi temporal i dades d'*INTEGRAL* per a l'anàlisi espectral.

##### 4.5.1. Anàlisi temporal

L'única periodicitat present en les nostres dades és aquella deguda al període orbital, ben conegut. Açò és cert només per a les dades de *RXTE*, les dades d'*INTEGRAL* no ens deixen detectar la modulació orbital per la cobertura parcial del sistema, deguda a l'estratègia d'observació del satèl·lit. Podem destacar la gran variabilitat de la font a totes les escales temporals. En temps curts (de l'ordre d'una hora), es produeixen varia-



cions en un factor 3. A més a més, l'aspecte dels periodogrames també es variable en diferents èpoques d'observació. Per exemple, un possible QPO (Quasi Periodic Oscillation) present en la revolució 87, no és detectat en la resta de revolucions analitzades.

Malgrat tots els esforços, no hem pogut detectar cap periodicitat que pogués ser associada amb el període de pulsació de l'objecte compacte.

#### 4.5.2. Anàlisi espectral

De l'anàlisi espectral podem destacar dues coes:

- Hem pogut observar 4U 2206+54 en els estats més brillants observats fins ara, amb unes lluminositats de  $1.1 \times 10^{36} \text{ erg s}^{-1}$  i  $0.6 \times 10^{36} \text{ erg s}^{-1}$  per a les revolucions 67 i 87 respectivament (i per a la distància trobada de 2.6 kpc).
- Trobem una possible línia ciclotró en absorció per a una energia de  $31.5 \pm 0.5 \text{ keV}$  i amb un nivell de confiança de  $2\sigma$ .

La presència de la línia ciclotró ha estat corroborada per la divisió de l'espectre per aquell del Crab (per tal de contrarestar els possibles efectes instrumentals) i per la utilització d'extracció espectral mitjançant mètodes alternatius, com ara el paquet de generació de mosaics d'ISGRI.

El fet que l'espectre de 4U 2206+54 presente una línia ciclotró aporta evidència a la classificació de l'objecte compacte com un estel de neutrons. Aquesta evidència es suma a la ja esmentada per la no detecció d'emissió en ràdio.

### 4.6.- Discussió i conclusions

#### 4.6.1. Company òptic (BD+53°2790)

Hem fet un repàs de totes les peculiaritats observacionals de BD+53°2790. Podem destacar:

- La presència d'una envoltura dominada rotacionalment és evident. Aquesta, però, malgrat presentar semblances, no és com la que es pot trobar als estels Be. Entre les evidències observacionals que apunten cap aquest fet podem destacar: l'asimetria permanent, amb

$V < R$ , en els pics de la línia  $H\alpha$ , que contrasta amb les variacions cíclics presents en els estels Be; les variacions en escales temporals d'hores de l'estructura de la línia  $H\alpha$ , que contrasta amb les variacions típiques en aquesta línia en les Be, les quals esdevenen en escales temporals relatives als temps de reacció del disc, és a dir, de l'ordre d'unes setmanes; la falta de correlació entre els paràmetres de la línia  $H\alpha$  i les magnituds i colors en l'infraroig, aquest fet es característic dels estels Be, ja que ambdós fenòmens (emissió en  $H\alpha$  i excés en l'infraroig) es produeixen en el mateix escenari, el disc circumestel·lar.

- La grandària de les línies d'Heli, la presència de l'envoltura i la peculiaritat de l'espectre en la zona blava, indiquen la possible connexió de BD+53°2790 amb el grup d'estels conegut com *He-strong*. Llavors, ens trobaríem amb el segon candidat primerenc (de tipus O) en pertànyer a aquest grup (llevat de  $\theta^1$ Ori C, de tipus espectral O6 V, tots els estels *He-strong* són de tipus espectral B i en seqüència principal).

#### 4.6.2. Company compacte

En aquest cas, juntant les evidències provinents de la no detecció en ràdio en el sistema i de la presència de la línia ciclotró en l'espectre de 4U 2206+54, podem concloure que el més probable és que l'objecte compacte present en el sistema siga un estel de neutrons. Amb dades de *RXTE* i *BeppoSAX* també s'han trobat evidències de la presència de la línia ciclotró. Cal destacar, llavors, que *INTEGRAL* és la tercera missió en informar sobre la presència d'aquesta. Així doncs, l'existència d'aquest tret espectral és molt probable i es descarta que es tracte de cap efecte instrumental.

La posició de la línia ciclotró a  $\sim 32$  keV, implica l'existència d'un camp magnètic amb una intensitat de l'ordre de  $3.6 \times 10^{12}$  G, valor que entra dins el rang típic d'intensitats del camp magnètic per als estels de neutrons.

L'únic punt que queda, aleshores, per acceptar la presència d'un estel de neutrons, és l'absència de pulsacions. La no detecció d'aquestes pot ser degut a un efecte geomètric o, també, a que aquestes es produeixen en escales temporals d'unes poques hores, rang temporal encara no ex-

plorat en aquest sistema. Un altre sistema amb període de pulsació llarg és 2S 0115+64, amb 2.8 hores. Amb *INTEGRAL* han sigut trobades, tanmateix, fonts amb períodes de pulsació tan llargs.

## 5. El sistema SAX J2103.5+4545

SAX J2103.5+4545 ha estat classificat recentment com a un sistema BeX, després del descobriment del company òptic en l'any 2003. Com hem vist a la introducció, a pesar d'estar confirmada aquesta classificació, SAX J2103.5+4545 presenta certes propietats que el fan especial dins del seu grup. La seua eccentricitat moderada i el curt període orbital, fan que siga un laboratori perfecte per a investigar la física associada a la interacció entre l'estel de neutrons i el disc circumestel·lar del company òptic. SAXJ2103.5+454 ens permetrà, així, testejar els models presents que expliquen l'evolució del disc i el comportament de l'estel de neutrons (que sofrirà acceleracions i deceleracions, depenent de la quantitat de matèria acretant) en aquest tipus d'escenari.

### 5.1.- Rang Òptic

Com a conseqüència del relativament recent descobriment del company òptic del sistema, no disposem de moltes dades òptiques. Tenim en total un conjunt de 22 nits d'observació repartides al llarg dels anys 2003 i 2004. Encara que és un conjunt restringit de dades i l'estadística associada serà molt pobre, aquests espectres ens donaran pistes interessants sobre la dinàmica del disc circumestel·lar.

Hem pogut confirmar la classificació espectral de B0V. Tanmateix hem mesurat la velocitat de rotació de l'estel, trobant  $230 \pm 20 \text{ km s}^{-1}$ . Aquest valor es troba dins dels valors esperats per a un estel Be, que giren amb velocitats de rotació properes a la velocitat de trencament (quan l'acceleració deguda al moviment de rotació iguala a l'acceleració gravitatòria).

El company òptic de SAX J2103.5+4545 presenta una línia  $H\alpha$  molt variable. Aquesta línia passa de mostrar un perfil de doble pic, propi dels estels Be, a presentar un perfil en absorció (però amb un cert plenament per emissió en el centre) el qual, a més a més, és variable. El pas de doble pic en emissió a un perfil en absorció es produeix amb coincidència del

pas del sistema de l'estat brillant a l'estat feble. Aquest fet és molt significatiu, ja que podria ser indicatiu de la relació directa entre la presència (o grandària) del disc amb els estats presentats pel sistema (presència de disc –o disc gran– implicarà tenir el sistema en un estat brillant, mentre que absència de disc –o disc xicotet– implicarà trobar el sistema en un estat feble).

## 5.2.- Altes energies

En aquest rang d'energies hem pogut realitzar una sèrie de troballes interessants:

1. **Dades D'*INTEGRAL*.** Presentem la primera anàlisi completa que es va realitzar del sistema amb dades d'*INTEGRAL*, incloent la mesura del període de pulsació, la caracterització espectral i la confirmació de la modulació orbital amb un període de  $\sim 12.68$  dies.
2. **Modulació orbital.** Mostrem l'anàlisi global de l'últim estat brillant pel que ha passat la font junt a part de l'estat feble en què es troba la font a partir del dia julià 2452900.5. D'aquesta manera trobem que, durant l'estat brillant, hi existeix una modulació en la brillantor total de cada *outburst* de tipus I, augmentant fins assolir un màxim per a després disminuir gradualment fins que el següent estat feble comença. Aquesta modulació es veu tant en les dades d'*INTEGRAL* com en les de *RXTE/ASM*. Observem, tanmateix, la presència sistemàtica d'augment de l'emissió prop de l'apastre.
3. **Comportament a llarg termini, estats brillant i feble.** Confirmem el fet que la font presenta dos estats espectrals, un estat brillant corresponent a un espectre en altes energies més *soft* (on predomina la part més tova de l'espectre) i un estat feble corresponent a un espectre més *hard* (on l'emissió corresponent a les bandes energètiques més altes es veu augmentada en relació a les bandes més baixes). Durant l'estat brillant, encara que trobem evidències de variabilitat espectral esporàdica, el pendent de l'espectre sembla ser prou constant. Cal destacar que és la primera vegada que es pot caracteritzar espectralment l'estat feble amb dades d'*INTEGRAL*

(en concret amb SPI) i la segona vegada que es fa des del descobriment de la font.

4. **Període de pulsació.** Fins ara només una tendència general de augment de la velocitat de rotació (disminució del període de pulsació) de l'estel de neutrons havia estat detectada. Per primera vegada, presentem evidències dels canvis complexos que es produeixen en el període de pulsació de SAX J2103.5+4545, donant suport a la idea de la complexitat en la interacció de l'estel de neutrons i el disc de l'estel Be (que influirà en la quantitat de matèria disponible per a formar un disc d'acreció al voltant de l'estel de neutrons). A més de variabilitat en diferents escales temporals (tant del període de pulsació com del perfil del pols), també trobem variacions del perfil de pulsació (però no del període) amb l'energia. Aquest fet indica la presència d'interaccions depenents de l'energia dels fotons que són lliurats a la superfície de l'estel de neutrons amb la columna d'acreció. Per últim, a través de l'evolució d'un pic secundari en el perfil de pulsació, proposem l'existència de canvis en la grandària i/o estructura del disc d'acreció.
5. **Anàlisi espectral.** Hem caracteritzat espectralment els dos estats del sistema, brillant i feble. A més a més, s'ha fet un estudi comparatiu de l'aplicació de diferents mètodes d'extracció d'espectres, posant en evidència les limitacions del software estàndard (OSA, versió 4.2).

### 5.3.- Discussió i conclusions

Hem trobat indicacions de la correlació existent entre l'emissió als diferents rangs de l'espectre electromagnètic. L'espectre en l'òptic ens indica si tenim o no presència de disc circumestel·lar en l'estel Be (o de la grandària d'aquest). Aquesta presència, o grandària, determinarà en quin estat trobarem la font, brillant o feble, ja que la matèria al disc serà la que potencialment podrà acretar cap a l'estel de neutrons. Al mateix temps, el company compacte pot influir en l'estructura del disc, degut a la seua proximitat, produint canvis, alhora, en el propi ritme d'acreció. El ritme d'acreció, finalment, produirà canvis en la velocitat de rotació de l'estel de neutrons. Quan tenim una quantitat gran de massa acretant, aquesta

transferirà moment angular a l'estel de neutrons i el període de pulsació es veurà reduït. D'una altra banda, quan disminueix la quantitat de matèria acretant, aquesta transferència de moment angular s'aturarà i l'estel de neutrons entrarà en un procés de pèrdua de moment angular i augment del període de pulsació. Veiem, aleshores, com s'inter-relacionen tots els elements del sistema, donant lloc a una fenomenologia molt interessant.

## 6. Conclusions generals

En aquest treball de tesi hem pogut aportar dades per tal de resoldre alguns dels enigmes observacionals referents a dos sistemes particulars, 4U 2206+54 i SAX J2103.5+4545. En ambdós casos hem pogut donar una classificació final o trobar una explicació per a la peculiaritat del sistema. Encara queda molt de treball per fer als dos casos.

Al cas de 4U 2206+54 falta investigar la presència d'un període de pulsació de l'ordre d'unes poques hores. Tanmateix, queda per confirmar definitivament la presència de la línia ciclotró amb un nivell de detecció per damunt dels  $3\sigma$ , i estudiar la dependència d'aquesta línia amb la intensitat de l'emissió en raigs-x/ $\gamma$ . Pel que fa al company òptic, una anàlisi detallada de la variabilitat fotomètrica ajudarà a confirmar si pertany al grup dels estels *He-strong*. També fa falta completar l'anàlisi en velocitats radials per tal de trobar una solució orbital completa només amb dades òptiques. La solució orbital combinada, òptic-altes energies, ens permetrà caracteritzar completament el sistema, restringint l'inclinació del pla orbital i donant valors acurats de la massa dels dos companys, òptic i compacte.

Per al sistema SAXJ2103.54+4545, un seguiment més complet en l'òptic ens permetrà caracteritzar les variacions en el perfil de la línia  $H\alpha$ , especialment els canvis en funció de la fase orbital. Així, podrem deduir com es comporta el disc circumestel·lar. Un conjunt més ample de dades ens permetrà, igualment, l'anàlisi de la velocitat radial del sistema i la determinació dels paràmetres orbitals amb dades òptiques. Pel que fa a les altes energies, és necessari acumular més observacions per tal de realitzar una anàlisi més detallada de l'estat feble del sistema, si aquest presenta variabilitat espectral i com es comporta el període de pulsació amb absència de disc circumestel·lar i, probablement, de disc d'acreció. Cal investigar

en més detall les variacions del període de pulsació i del perfil del pols. Aquestes últimes ens donaràn informació de com és i com es forma el disc d'acreció, i permetrà la comparació amb les teories actuals que expliquen la formació i estructura dels discos d'acreció. Per últim, cal ficar més esforços en realitzar observacions simultànies en el major conjunt de rangs possible de l'espectre electromagnètic, per tal de caracteritzar el procés de formació, pèrdua i reformació del disc, i el procés de transferència de matèria cap a l'estel de neutrons de la forma més completa possible. El començament del pròxim estat brillant del sistema ens donarà una oportunitat única per a realitzar aquest tipus d'anàlisi.

Hem vist, tot al llarg de la tesi, les possibilitats que ens ofereixen missions com *INTEGRAL* per a l'estudi d'aquest tipus de fonts astrofísiques. Al mateix temps volem resaltar la importància dels estudis multi-freqüència, ja que només aquests permeten una caracterització completa del sistema objecte d'estudi.

# List of Figures

1.1	Electromagnetic spectrum. The common names used to make reference to the different energy ranges are shown. Only visible light, a bit of infrared, and radio wavelengths reach us from outside the atmosphere. For each range, the detection system commonly used is also shown. . . . .	5
1.2	<b>Left panel:</b> Interaction of microwaves with matter. Its size and energy induces rotation and torsions in molecules. <b>Right panel:</b> X-ray interactions with the electrons in the atoms. . . . .	6
1.3	Radiation of the Sun as a function of the energy. Some other radiation curves corresponding to black bodies at different temperatures are also shown for comparison. . . . .	6
2.1	Schematic representation of the effects of the angle of view to the observer on the observed profile of the $H\alpha$ line in a Be star. When viewed pole-on the emission from the disk is superimposed over the photospheric absorption. However, when viewed more equator-on the effect of self absorption in the disk results in the characteristic shell profile, with blue ( $V$ ) and red ( $R$ ) peaks. . . . .	21



- 2.2 Schematic representation of the effects of a one armed oscillation in a Be star disk on the observed H $\alpha$  profile. When the oscillation brings a higher density of matter to the part of the disk approaching the observer (due to the rotational movement) the blue peak (V) becomes higher. If the oscillation, instead, brings matter to the side of the disk which is moving away from the observer, then the red peak (R) is enhanced. . . . . 23
- 2.3 Schematic representation of the accretion by stellar wind onto a neutron star. Only matter subtending a solid angle of  $d\frac{\pi r^2}{a^2}$  from the OB star center towards the neutron star is accreted. . . . . 27
- 2.4 Schematic representation of the three different accretion processes reviewed in this introduction. . . . . 32
- 2.5 In an eccentric binary system composed by a Be star and a neutron star (NS), mass transfer can happen by stellar wind but also by Roche lobe overflow under some circumstances. (A) When the NS is at apastron, the only way matter can be transferred into its potential well is through stellar wind or some mass ejection mechanism. (B) Before the NS approaches the periastron, some disk matter can already be transferred through Roche lobe overflow (at the first lagrangian point L). The orbital phase of Roche lobe overflow onset depends on the eccentricity of the orbit and the size of the disk. (C) At periastron the NS can be immersed in the Be disk. The size of the disk and the mass transfer mechanism depend on the particular orbital parameters and/or disk dynamics of the system. . . . . 34
- 3.1 Comparison of the creation of an image in our detector plane by placing a pin hole camera as *imaging* system and by placing a coded mask system. . . . . 37

3.2	Mask patterns of the high energy instruments aboard <i>INTEGRAL</i> as used by the instruments software. Black zones denote those places with a zero value (i.e., transparent elements) while white zones correspond to elements with a value of 1 (opaque elements). . . . .	40
3.3	Hexagonal and $5 \times 5$ dithering patterns used by <i>INTEGRAL</i> in open time observations. Hexagonal dithering is more adequate when only one source dominates in the FOV. In other cases it is more convenient to use the $5 \times 5$ , otherwise SPI software may not be able to resolve the sources properly.	41
3.4	Representation of the observing strategy followed during GPS scans. . . . .	42
3.5	IBIS instrument schematic representation and view of its detector assembly. . . . .	44
3.6	SPI instrument schematic representation and view of its detector assembly. . . . .	46
3.7	JEM-X instrument schematic representation and view of its detector assembly. . . . .	47
3.8	OMC FM before integration in the <i>INTEGRAL</i> payload. . . . .	49
3.9	FITS file with four extensions. In particular, it is the <i>ibis_vrtx_grp_0031.fits</i> file from the IBIS instrument characteristics. . . . .	50
3.10	Schematic view of the organization of <i>INTEGRAL</i> data in a working directory. . . . .	52
5.1	Images of the NRAO/VLA facilities. . . . .	78
5.2	Image around 4U 2206+54, marked with a cross, obtained with the VLA at 8.4 GHz after concatenating data from 2003 May 12 and 20. The image size is $4' \times 4'$ . Contours are $-3, 3, \text{ and } 5$ times the rms noise level of $0.013 \text{ mJy beam}^{-1}$ . The ellipse in the bottom left corner represents the Full Width Half Maximum of the synthesised beam obtained of $10.6'' \times 9.4''$ in $\text{PA} = -83.4^\circ$ . . . . .	79
6.1	<i>K</i> -band spectra of BD +53°2790. . . . .	82
6.2	Infrared lightcurves of BD +53°2790, 1987–1999. . . . .	85

- 6.3 Colour-magnitude plots showing the evolution of the infrared magnitudes. The strong correlation seen in the  $K/(H-K)$  plane is not a simple reflection of the fact that a fainter  $K$  means a smaller  $(H-K)$ , as the correlation between  $H$  and  $K$  is also strong. In the first case the correlation coefficient is  $r_{(H-K),K}=-0.46$  and the correlation is significant in a 98% confidence level. In the latter case the correlation coefficient is  $r_{H,K}=0.80$  and the correlation is also significant at a 98% confidence level. . . . . 86
- 6.4 Evolution of the infrared colours in BD +53°2790 during 1987–1999 compared to that of the EW of  $H\alpha$ . Since simultaneous measurements are rare, we cannot properly search for correlations. The lack of any obvious correlated trends could be caused by the lack of long-term trends. . . . . 87
- 7.1 Images of some of the telescopes where data of BD +53°2790 was retrieved for our analysis. . . . . 91
- 7.2 Blue/green spectrum of BD +53°2790, taken on July 21, 2000 with the 1.3-m telescope at Skinakas. Only the strongest features have been indicated. For a more complete list of photospheric features visible in the spectrum, see Negueruela and Reig (2001). The spectrum has been normalised by dividing the continuum with a spline fit. A normalised spectrum of 10 Lac (09V), shifted down for plotting purposes, is also shown for comparison. . . . . 96
- 7.3 Normalised profiles of selected He I lines (namely, He I  $\lambda 4026$ ,  $\lambda 4144$ ,  $\lambda 4388$ , and  $\lambda 4471$  Å) from BD +53°2790 together with those of the same lines from 10 Lac but rotationally broadened to 200 km s<sup>-1</sup> and to those rotational velocities yielding upper and lower envelopes to the width of the BD +53°2790 lines. In all cases rotational velocities above 200 km s<sup>-1</sup> are needed to reproduce the line widths. . . . . 98
- 7.4 Evolution of the  $H\alpha$  line profile of BD +53°2790 during 1986–2000. All spectra have had the continuum level normalised and are offset vertically to allow direct comparison. 102
- 7.5 Parameters of the  $H\alpha$  emission line for all spectra taken from INT in the long-term, 1986–1999, monitoring campaign. 104

- 7.6 The spectrum of BD +53°2790 in the yellow/red/near-IR. Echelle spectrum taken on 17th August 1999 using the 1.52-m G. D. Cassini Telescope equipped with BFOSC and grisms #9 (echelle) and #13 (cross-disperser). All the orders have been flattened by division into a spline fit to the continuum. . . . . 105
- 7.7 EW of the He I  $\lambda 6678\text{\AA}$  line versus that of the H $\alpha$  line. There seems to be some degree of correlation between both quantities. Only data from INT spectra where both lines were visible are shown. A linear regression fit to the data is shown as a dashed line. The correlation coefficient of the regression is  $r=0.62$  and the correlation is significant at a 98% confidence level. . . . . 106
- 7.8 Comparison of the near IR spectrum of BD +53°2790 (lower panel) with the supergiant (upper left panel) and main sequence (upper right panel) stars shown in Caron et al. (2003). The upper panel figures were extracted from the given reference. . . . . 107
- 7.9 H $\alpha$  parameters – EW (in  $\text{\AA}$ ), FWHM (in  $\text{\AA}$ ), peak separation (in  $\text{km s}^{-1}$ ) and V/R ratio– for the monitoring campaign in July 2000. There seems to be a high degree of correlation in the evolution of EW, FWHM and peak separation, which is not shared by the V/R ratio. . . . . 108
- 7.10 Evolution of H $\alpha$  line in BD +53°2790 during the monitoring campaign in July 2000. Note the moderate night-to-night changes of the line profile and the important difference between the spectra from the first and second week. . . . . 109
- 7.11 Blue spectra averaged in a per night basis of the INT July 2002 campaign. All the lines look quite stable over the whole observing period. . . . . 110
- 7.12 Measurements of the EW for He II, He I lines and H $\gamma$  during the night of July 30, 2002. Their values remain constant and compatible within errors with those given in Table 7.2 for the long-term monitoring. Dashed lines represent the mean values for each case. . . . . 112

- 7.13 EW of He II  $\lambda 4200 \text{ \AA}$ , H $\gamma$  and He I  $\lambda 4471 \text{ \AA}$  and  $\lambda 4541 \text{ \AA}$  lines along the INT July 2002 campaign. Values are compatible with no variability (within errors) and with those in Table 7.2 for the long-term monitoring. The spread is due to the uncertainties in the determination of the continuum. . . . . 112
- 7.14 H $\alpha$  and He I  $\lambda 6678 \text{ \AA}$  line profiles along the July 2003 campaign. . . . . 114
- 7.15 Summary of the H $\alpha$  line measurements for the July 2003 campaign. In the left panel the variations of the parameters with time are shown. In the right panel the FWHM,  $\Delta V$  and V/R ratio are plotted vs. the EW. H $\alpha$  parameters follow the expected tendency, with EW, FWHM and  $\Delta V$  correlated but all of them uncorrelated with the V/R ratio. Regression analysis tendencies are shown in the FWHM vs. EW and  $\Delta V$  vs. EW plots as dashed lines. In the former case the correlation coefficient is  $r=0.75$  and in the latter case  $r=0.54$ . . . . . 115
- 7.16 Summary of the He I  $\lambda 6678 \text{ \AA}$  line measurements for the July 2003 campaign. In the left panel we see the evolution of the parameters measured. In the right panel the correlation plots among the  $\Delta V$  and V/R ratio vs the EW of the line are shown. The parameters behave as those from the H $\alpha$  line. A Regression line fit is shown in the  $\Delta V$  vs. EW plot as a dashed line. The correlation coefficient of the fit is  $r=0.51$ . . . . . 116
- 7.17 EW of the He I  $\lambda 6678 \text{ \AA}$  line as a function of the EW of the H $\alpha$  line. We can find traces of a possible correlation between the two datasets (the correlation coefficient is  $r=0.50$ ). 116
- 7.18 Blue spectra of BD+53 $^{\circ}$ 2790 during the monitoring campaign of August-October 2004 from Skinakas Observatory, Crete, Greece. . . . . 120
- 7.19 Evolution of the H $\alpha$  and He I  $\lambda 6678 \text{ \AA}$  line profiles during the period May-October 2004, as observed from Skinakas Observatory. . . . . 121

LIST OF FIGURES

LIST OF FIGURES

7.20 In the left panel we the evolution of H $\alpha$  parameters during August–October 2004 is shown. In the right panel FWHM,  $\Delta V$ , and V/R ratio versus EW of the H $\alpha$  line during August–October 2004 are plotted. . . . . 121

7.21 EW of the He I  $\lambda 6678 \text{ \AA}$  line vs. that of the H $\alpha$  line for the August–October 2004 spectra. The correlation coefficient of the linear regression shown as a dashed line is  $r=0.54$ . . . . 122

7.22 EW of the He I  $\lambda 6678 \text{ \AA}$  line vs. that of the H $\alpha$  line for the 2003 and 2004 monitoring campaigns. . . . . 122

7.23 Radial velocity measurements for the INT campaign during July 2002, July 2003 and the period August–October 2004. 123

7.24 Periodogram computed from all the radial velocity measurements of BD+53 $^\circ$  2790. . . . . 124

7.25 Radial velocity measurements folded with the 14.89 d period derived from FT techniques, and the 9.5591 d period found by Ribó et al. (2005). In both cases  $t_0$ =MJD 51856.6. 124

7.26 Radial velocity measurements folded with the 9.5591 d period. Different eccentricities have been used to compute radial velocity curves which are compared to the measurements. Eccentricities above (i.e. 0.5) and below (i.e. 0.1) deviated significantly from the observed radial velocity curve. 125

8.1 **Left:** Artist Impression of the *IUE* satellite orbiting the Earth. **Right:** Image of the solar panel of the satellite during testing. . . . . 133

8.2 UV spectra of BD +53 $^\circ$ 2790 from 1200 up to 1900  $\text{\AA}$ . The wind resonance lines used in the analysis are marked with arrows. . . . . 134

- 8.3 **Left panels:** Examples of fits of our models for terminal wind velocities of  $300$  and  $350 \text{ km s}^{-1}$ , for the two resonance doublets  $\text{C IV } \lambda\lambda 1548.19 \text{ } 1550.76 \text{ \AA}$  and  $\text{N V } \lambda\lambda 1238.80 \text{ } 1242.78 \text{ \AA}$  **Right panels:** Fit to the same two doublets by using the genetic algorithm of Georgiev and Hernández (2005). A different normalisation has been used for  $\text{C IV}$  in both cases to stress its influence on the result, it is one of the main sources of uncertainty. In the case of the genetic algorithm, the resolution of the spectrum was degraded in order to ease and speed up the convergence of the fit. . . . 137
- 9.1 ISGRI lightcurves of  $4\text{U } 2206+54$  in the energy range  $20\text{--}40 \text{ keV}$  binned to  $50 \text{ s}$  (left) and associated power spectra (right) for a time span equivalent to  $3 \text{ INTEGRAL}$  science windows (around  $6950 \text{ s}$ ) during revolutions  $67$  (top panels) and  $87$  (bottom panels). . . . . 143
- 9.2 **Left:** Power spectrum of the  $\text{RXTE}/\text{ASM}$  lightcurve, binned to  $25 \text{ ks}$  intervals. Note the feature detected at a frequency of  $\simeq 1.2 \times 10^{-6} \text{ Hz}$ , which corresponds to the orbital period (see Corbet & Peele 2001). No other period is found at the limit of the lightcurve resolution. **Right:** Power spectrum of the  $100 \text{ ks } \text{RXTE}/\text{PCA}$  lightcurve, binned to  $96 \text{ s}$  intervals. No significant period is detected in the interval  $[0.95\text{--}5.5] \times 10^{-4} \text{ Hz}$ , which corresponds approximately to the interval from  $3 \text{ hours}$  to  $30 \text{ minutes}$ . The slope of the power spectrum is  $\sim \nu^{-0.8}$ , where  $\nu$  is the frequency. . . 144
- 9.3 Lightcurves of  $4\text{U } 2206+54$  in different energy bands (quoted inside the different panels). The top panel is for the  $3\text{-day}$  average of the  $\text{RXTE}/\text{ASM}$  data, where the arrows indicate the epochs of the radio observations. The three bottom panels are for the  $\text{INTEGRAL}/\text{ISGRI}$  data in intervals of  $\sim 2 \text{ ks}$ . Error bars represent the mean of the  $1\text{-day}$  average data errors for  $\text{RXTE}/\text{ASM}$  data and the formal errors for  $\text{INTEGRAL}/\text{ISGRI}$  data. The two triangles in the  $20\text{--}40 \text{ keV}$  lightcurve indicate  $3\sigma$  upper limits. . . . . 145

- 9.4 Spectra of 4U 2206+54 from JEM-X and ISGRI detectors. **Top:** The spectrum shown is for 2.2 ks of exposure time during revolution 67 (MJD 52761.36). **Bottom:** The spectrum shown is for 6.6 ks of exposure time during revolution 87 (MJD 52821.17). In both cases the spectral model shown in Table 9.2 (i.e. a powerlaw modified by a cutoff, with photo-absorption and the `cyclabs` component) is represented by the solid line, and the residuals to the model are displayed in the lower panels. The presence of an absorption feature around 32 keV, indicated by arrows, is suggested by the two datasets. . . . . 150
- 9.5 Observed ISGRI spectra of the Crab and 4U 2206+54 (top panel), their ratio to the powerlaw model (middle panel), and the ratio of 4U 2206+54 to that of the Crab for the former ratios. The variations above 40 keV are not smooth, but random, and show large errors, indicating that they reflect most likely extraction problems due to the fact that we are approaching the sensitivity limit of ISGRI (around  $\sim 0.04 \text{ count s}^{-1} \text{ keV}^{-1}$  for 2 ks exposures and  $3\sigma$  level detection at 45 keV). . . . . 152
- 9.6 Spectrum of 4U 2206+54 extracted from the mosaicking of all images with positive detections from ISGRI. **Top:** The solid line represents the `bmc` model (in XSPEC notation) fitted to the data. An absorption feature around 32 keV is seen in the residuals. **Bottom:** The solid line represents the `bmc` model plus a Lorentzian feature in absorption, yielding a line position of  $31.5 \pm 0.5 \text{ keV}$ . . . . . 154
- 11.1 Power spectrum of *RXTE*/ASM SAX J2103.5+4545 data separated in two sets, one corresponding to the epochs of bright state of the system, and one where only faint state data is included. The frequency peak corresponding to the orbital period is detected only in the bright state data. . . . 177
- 12.1 Spectrum of the standard B0V star *v Ori* together with the two blue spectra available of SAX J2103.5+4545. . . . . 181



LIST OF FIGURES

LIST OF FIGURES

12.2 He I profiles of SAX J2103.4+4545 from the September 14, 2003, spectrum. . . . . 183

12.3 He I  $\lambda 4386 \text{ \AA}$  and He I  $\lambda 4471 \text{ \AA}$  profiles of SAX J2103.4+4545 together with the same lines rotationally broadened line profiles of  $\nu$  Ori. . . . . 184

12.4 Evolution of the H $\alpha$  and He I  $\lambda 6678 \text{ \AA}$  line profiles. . . . . 185

12.5 Evolution of the EW and the FWHM of the H $\alpha$  line and the EW of the He I  $\lambda 6678 \text{ \AA}$  line. . . . . 186

12.6 FWHM of the H $\alpha$  line and EW of the He I  $\lambda 6678 \text{ \AA}$  line versus the EW of the H $\alpha$  line. The average value of the H $\alpha$  EW is shown with a vertical dashed line. . . . . 186

12.7 EW and FWHM of the H $\alpha$  line and EW of the He I  $\lambda 6678$  folded at the orbital phase of SAX J2103.5+4545. The average value of each parameter is shown by a dashed horizontal line. . . . . 187

13.1 Evolution of the detections of SAX J2103.5+4545 with SPI during PV phase, averaged over a revolution. The location of SAX J2103.5+4545 is shown with two orthogonal lines at the top-left corner. The time elapsed between peaks coincides with the orbital period of the system. The source at the right bottom corner is Cyg X-3. A spurious source appears in the revolution 21 image (south-west from the indicated position of SAX J2103.5+4545), being very likely an artifact of the image reconstruction process. . . . . 191

13.2 ISGRI, SPI and *RXTE*/ASM light curve during December 2002. Each data point represents an averaged one day flux for all the instruments. Units are normalised to the peak value. . . . . 192

13.3 Power-spectrum for positive detections of SAX J2103.5+4545 inside the FCFOV of ISGRI during revolution number 23. The maximum power is achieved at  $\sim 0.00281678 \text{ Hz}$ . . . . . 194

13.4 ISGRI SAX J2103.5+4545 spectra in revolutions 19 (stars), 23 (circles) and 25 (squares). Apart from a difference in flux no spectral variability is apparent. Downwards arrows denote upper limits. . . . . 196

## LIST OF FIGURES

## LIST OF FIGURES

- 13.5 Fit to joint JEM-X, ISGRI and SPI spectra. JEM-X and ISGRI spectra are mean spectra for revolution 23. For SPI a mean spectrum for December 2002 is used. . . . . 198
- 13.6 Representation of all the pointings in which the source (in the middle of the plot) lies within the field of view of the ISGRI instrument. The inner circle encloses those pointing in which the source lies within the FCFOV of the ISGRI instrument. . . . . 199
- 13.7 20–44 keV SPI light curve of SAX J2103.5+4545 from GPS pointings, from revolution 31 up to revolution 162. Downwards triangles indicate upper-limits. . . . . 206
- 13.8 Long term light curves of JEM-X and ISGRI instruments, together with *RXTE*/ASM count rate for all the GPS scans from revolution 31 up to revolution 181. Upper limits are plotted (downwards triangles) when the detection was not significant enough to be considered reliable. For ISGRI data, FCFOV observations are differentiated from PCFOV observations. . . . . 207
- 13.9 *RXTE*/ASM long-term light curve rebinned to 12.68 days (the orbital period of the system). We notice the modulation of the maximum flux achieved during each type-I outburst. The horizontal dashed line indicates the average flux while in the faint state. . . . . 208
- 13.10 Detailed view of the bright state seen by ISGRI. *RXTE*/ASM data is also shown, with an horizontal dashed line indicating the top of orbital outburst at maximum emission, for the sake of clarity. The modulation of the maximum flux of type-I outbursts is clearly seen in both ISGRI and *RXTE*/ASM data. . . . . 209
- 13.11 Light curve of *RXTE*/ASM data in dwell by dwell binning together with JEM-X and ISGRI data in the energy intervals indicated at the top left corner of each panel. A modulation of the order of  $\sim 5$  hours seems to be present in ISGRI data and supported by JEM-X and *RXTE*/ASM data. 211

- 13.12 **Upper Panel:** Folded light curve of ISGRI data (25–40 keV) and *RXTE*/ASM data (2–12 keV). The orbital epoch was taken from 2004 but the orbital period is that of Sidoli et al. (2005). **Lower Panel:** Folded light curve of SPI data (20–44 keV) (with the same orbital period and epoch as in the upper panel). . . . . 212
- 13.13 Folded light curve of ISGRI data in all energy ranges used in the analysis of this chapter. The ephemeris used are the same as in Fig. 13.12. Periastron passage, according to the estimate of Baykal et al. (2000) is indicated by a vertical dashed line. . . . . 213
- 13.14 History of hardness ratios along *INTEGRAL* GPS scans observations from revolution 31 up to revolution 181. . . . . 215
- 13.15 ISGRI hardness ratios along *INTEGRAL* GPS scans observations from revolution 31 up to revolution 181 versus ISGRI count rate in the 25–40 keV energy range. . . . . 216
- 13.16 Power spectrum of the 11.5 ks long light curve obtained after joining JEM-X events extracted from 5 consecutive science windows during revolution 67 in the 5–25 keV energy range. . . . . 217
- 13.17 Folded light curve of JEM-X events list using the  $353.0 \pm 0.1$  s pulse period. . . . . 218
- 13.18 DFT and FFT for ISGRI data from revolutions 67 and 70. The peaks at the frequency which corresponds to the pulse period are clearly seen. In the revolution 67, some harmonics of the pulse period can also be seen. This is not the case of the more noisy data from revolution 70. There is a feature in the FFT of revolution 67 data at  $\sim 0.001$  Hz which is not present in the DFT. . . . . 219
- 13.19 Folded light curves of the ISGRI extracted events for revolutions 67, 70, and 74. Data from each revolution was folded according to the pulse period shown in Table 13.7. All data was normalised to the average count rate in each revolution. . . . . 220

- 13.20 Pulse period evolution during the time span between revolutions 67 and 74 as obtained from ISGRI data. A very steep spin up followed by a strong spin down is suggested by the data. The errors shown in revolution 67 data represent the resolution of the epoch folding method used, however, they are clearly underestimated. . . . . 221
- 13.21 Folded light curves of ISGRI data from the three periods of revolution 67 studied independently. . . . . 222
- 13.22 DFT (left panel) and Lomb-Scargle (right panel) periodograms for ISGRI data from revolution 67 data in the energy range 45–60 keV. . . . . 224
- 13.23 DFT periodogram (left panel) and distribution of  $\chi^2_{\text{RED}}$  for a set of sine fits to the data (right panel) for the revolution 70 data in the energy range 45–60 keV. . . . . 225
- 13.24 Folded light curves of ISGRI data in the 45–60 keV energy range from revolution 67 (left panel) and revolution 70 (right panel). The folding periods used are those measured from periodograms, i.e.,  $353.6 \pm 0.7$  s for revolution 67 and  $348 \pm 7$  s for revolution 70. . . . . 225
- 13.25 The JEM-X spectra for those science windows indicated in Table 13.9 are shown in the upper panel. Large errors prevent us from identifying spectral variability. The spectral shape remains unchanged along the time coverage of this set of data. In the lower panel, the average spectrum is shown, together with a power law model fit, together with its residuals. . . . . 228
- 13.26 Photon indexes of a power law model fit to all SAX J2103.5+4545 ISGRI spectra for OSA 4.2 and SF software. . . . . 232
- 13.27 Crab spectra for revolutions 45, 58, and 102, extracted from ISGRI data with the SF method. The model used to fit the data is a power law. Residuals of the fit are plotted in the lower panel. . . . . 233

13.28 Average spectrum for all ISGRI spectra shown in Table 13.12. In the upper viewgraph the average spectrum has been obtained with the spectra extracted with OSA 4.2 software. In the lower viewgraph the average spectrum was extracted with the SF software. In both cases the fit to a power law model and its residuals are shown (see main text for more details). . . . . 237

13.29 Ratio of the normalised ISGRI spectrum of SAX J2103.5+4545 to that of the Crab. The upper panels exemplify the process followed to obtain the ratio. . . . . 238

13.30 Ratio of all the ISGRI spectra shown in Table 13.12 to the average ISGRI spectrum. We notice that there is no evidence for spectral variations. The ratios have been shifted upwards for plotting purposes. . . . . 239

13.31 Selected joint JEM-X-*ISGRI* spectra among those whose spectral parameters are shown in Table 13.13. The first row corresponds to spectra extracted with OSA 4.2, the second row to those extracted with SF software. In all cases the fit to a power law model plus a high energy cut off, and the residuals to the fit, are plotted. **Left panels:** spectra from science window 54–29. **Middle Panels:** spectra from science window 67–39. **Right Panels:** spectra from science window 67–42. . . . . 242

13.32 Spectral parameters (power law photon index and high energy cut off) versus the 4–150 keV flux for the joint JEM-X-*ISGRI* spectra shown in Table 13.13. . . . . 244

- 13.33 **Upper panel:** Average joint JEM-X–ISGRI spectrum for the GPS between revolutions 31 and 181 when OSA 4.2 is used. The spectrum is well fit by a power law with photon index  $0.9 \pm 0.1$  modified with a high energy cut-off at  $6 \pm 1$  keV with a folding energy of  $17 \pm 2$  keV. The  $\chi^2_{\text{red}}$  of the fit was 1.3 for 158 degrees of freedom. Systematic errors of 2% were introduced in both sets of data. **Lower panel:** Average joint JEM-X–ISGRI spectrum for the GPS time span between revolutions 31 and 181. OSA 4.2 software was used to extract JEM-X spectra but SF software was used to extract ISGRI data. The best fit to the 3.0–200.0 keV spectrum was a power law with a photon index of  $1.1^{+0.2}_{-0.1}$  modified by a cut off at  $7^{+5}_{-2}$  keV with a folding energy of  $25 \pm 2$  keV. . . . . 246
- 13.34 Comparison of the SPI spectra of SAX J2103.5+4545 during bright and faint states in the 20–100 keV energy range. A simple power law model was fitted to the data. A change of spectral state is evident. . . . . 247
- 14.1 10 day averaged RXTE-ASM light curve showing the transition from bright state (end of 2002 and first half of 2003) into faint state (second half of 2003). The epochs of *INTEGRAL* and optical observations are indicated by horizontal lines. . . . . 253
- 14.2 comparison of the high energy light curves with the variations in the IR J magnitude and (H-J) and (J-K) colours, and the EW of the H $\alpha$  line of SAX J2103.5+4545. . . . . 253

LIST OF FIGURES

LIST OF FIGURES

---

# List of Tables

1.1	High Energy missions from late 1960s which have already finished operations. Data taken from NASA's HEASARC pages ( <a href="http://heasarc.gsfc.nasa.gov">http://heasarc.gsfc.nasa.gov</a> ). . . . .	8
1.2	High energy missions presently in flight. Data taken from NASA's HEASARC pages ( <a href="http://heasarc.gsfc.nasa.gov">http://heasarc.gsfc.nasa.gov</a> ). . . . .	9
2.1	Ions which participate in the radiatively driven winds models. Typical abundances are given in units of $\times 10^{-4}$ and relative to hydrogen. Values extracted from Lamers & Cassinelli (1999). . . . .	19
2.2	Typical wind parameters for main sequence O stars. Taken from Prinja and Howarth (1986). . . . .	20
3.1	IBIS performance parameters. . . . .	43
3.2	SPI performance parameters. . . . .	45
3.3	JEM-X performance parameters. . . . .	47
3.4	OMC performance parameters. . . . .	48
4.1	. . . . .	71
6.1	Observational details, IR photometry. . . . .	82
7.1	Log of spectroscopic observations during the long monitoring campaign (1986–1999). . . . .	93
7.2	Measurement of the equivalent width of strong absorption lines (without obvious variability and presumably of photospheric origin) in the spectrum of BD +53°2790. . . . .	97



7.3	Summary of the measured rotational velocities for the selected Helium lines shown in Fig. 7.3. . . . .	99
7.4	Details of the red spectroscopy monitoring for the period 1986–1999. Some representative spectra are displayed in Fig. 7.4 (marked with ‘*’) . . . . .	99
7.5	Summary of spectroscopic observations during the period May–October 2004 from Skinakas Observatory. . . . .	114
7.6	Summary of He I $\lambda 6678$ Å line EW measurements during the May–October 2004 monitoring campaign. . . . .	117
7.7	Lowest values of the computed $\chi_{\text{RED}}^2$ by comparing the observed values of the radial velocity with the calculated theoretical profiles for a wide range of orbital parameters. . . .	120
7.8	Computed values of $\chi_{\text{red}}^2$ for the models used in the visual fitting shown in Fig. 7.26. . . . .	123
7.9	Strömgren photometry of the optical counterpart to 4U 2206+54. The last column indicates the telescope used. a stands for the 1.5-m Spanish telescope at Calar Alto. b represents the 1.23-m German telescope. c is the Skinakas 1.3-m telescope.	127
7.10	$V$ magnitude measurements from the OMC on board <i>INTEGRAL</i> . . . . .	128
8.1	Comparison of the best fit parameters obtained by all the methods used to analyse the UV lines. $v_{\infty}$ and $v_{\text{turb}}$ are both given in units of $\text{km s}^{-1}$ . For the case of doublets the opacity given is that of the red component. . . . .	138
9.1	Summary of ISGRI observations of the field around 4U 2206+54 during the <i>INTEGRAL</i> GPS. We list the revolution number, the intervals of time when the source was in the FOV of ISGRI during these revolutions in Modified Julian Days, the total on-source time within these intervals, the amount of time in which the source was detected, the mean count rate and its formal error obtained in the 20–40 keV energy range and the detection level value given by the software package. For revolutions 70, 74, 145 and 189 (with significances between $1\sigma$ and $3\sigma$ ), we give $3\sigma$ upper limits. The † symbol indicates JEM-X detections. . . . .	148

9.2	Comparison of published powerlaw+high-energy cutoff parameters, adding photon absorption at lower energies, for 4U 2206+54. We remit the reader also to tables 2, 3, and 4 of Saraswat & Apparao (1992) for earlier <i>EXOSAT</i> data. All fluxes shown are unabsorbed in the quoted energy ranges. The errors are at 68% confidence level for the entry of Negueruela & Reig (2001) and at 90% confidence level for the rest of the data except for the entry of Corbet & Peele (2001), where significance levels were not reported. Flux is given in units of $\times 10^{-10}$ erg s $^{-1}$ cm $^{-2}$ . . . . .	149
11.1	Summary of orbital parameter determinations for the BeX system SAX J2103.5+4545. . . . .	176
12.1	Spectroscopic observations of SAX J2103.5+4545 during 2003 and 2004. . . . .	180
12.2	Equivalent width measurements of selected lines for spectral and luminosity classification purposes, as outlined in the main text. . . . .	182
12.3	Equivalent width ratios of selected lines from Table 12.2 for spectral and luminosity classification purposes, as outlined in the main text. . . . .	182
13.1	Most significant SAX J2103.5+4545 detections. . . . .	190
13.2	Spectral extraction summary. Values for a power-law fitting for all 3 instruments, JEM-X, ISGRI and SPI. $\chi_{\text{red}}^2$ for a bremsstrahlung fit are also shown for comparison. . . . .	195
13.3	Time evolution of the spectral parameters (for a power-law fit) of SAX J2103.5+4545 using ISGRI data from revolution 23. . . . .	197
13.4	Summary of ISGRI and JEM-X detections during GPS scans from revolution 31 up to revolution 181 (publicly available data). Bold face numbers indicate $3\sigma$ upper limits of the count rate for those science windows where the detection level is very low or there are doubts about the detection of the source. . . . .	200

- 13.5 Summary of SPI detections from GPS core program observations between revolution 31 and revolution 181. The flux is given in mCrabs for the 20–44 keV energy range. Fluxes in bold-face indicate upper limits. . . . . 206
- 13.6 Comparison of the MJD of the maximum flux of the type-I outbursts detected by ISGRI to the MJD of the predicted occurrence of the outbursts' maxima, according to the refined orbital period of Sidoli et al. (2005) and the epoch of the maximum detected by ISGRI during PV phase (MJD 52618.73, during revolution 23). . . . . 210
- 13.7 Measurements of the pulse period with ISGRI data for all the GPS revolutions, from 31 up to 181, for which there was timing data available. . . . . 218
- 13.8 Measurements of the pulse period along revolution 67 with ISGRI data. Three sets of data with consecutive science windows were used to study the pulse period changes. The errors reproduced here correspond to the resolution of the epoch folding method used, however, they are clearly underestimated. . . . . 222
- 13.9 Spectral parameters for all the JEM-X spectra obtained with public GPS data. In all cases, the number of degrees of freedom is 147. . . . . 226
- 13.10 Results of the spectral fits to JEM-X data after freezing the  $E_{\text{FOLD}}$  parameter of the power law plus high energy cut-off model to that value derived from the averaged spectrum for revolution 67 ( $E_{\text{FOLD}}=12$  keV). The most unstable fit is that of the science window 42, where the error given (marked with an asterisk) was calculated at a 68% Confidence Level (C.L.) (while the rest represent 90% C.L.). In this science window local minima of the fit were also found for photon indexes of 1.3 and 1.1 with associated cut-off energies of 18 keV and 13 keV respectively. . . . . 229
- 13.11 Power law fit parameters for GPS science windows with the source in the FCFOV and for which OSA 4.2 and SF software succeeded to extract a spectrum of the source. Flux is given in units of  $10^{-10}$  erg s $^{-1}$  cm $^{-2}$  . . . . . 231

13.12 Results of the ISGRI spectral analysis of SAX J2103.5+4545. For spectra extracted with OSA 4.2 we had 14 DOF, and for spectra extracted with SF software, 28 DOF. Those spectra producing a very unstable fit in either of the two methods (namely those of science windows 54-29, 67-38, 67-41, and 67-50) have been omitted. . . . . 234

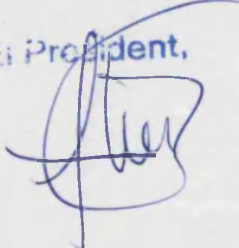
13.13 Comparison of the joint JEM-X and ISGRI spectral parameters for two cases: a) ISGRI spectra extracted with standard OSA 4.2 software; b) ISGRI spectra extracted with the software developed by SF. In all cases only science windows where simultaneous JEM-X and ISGRI spectra can be obtained are used. A power law plus a high energy cut off was the model chosen to fit all the data. A constant was added to the model to allow for cross-calibration normalisation. . . 241

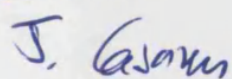
13.14 Fluxes in different energy bands measured for those science windows shown in Table 13.13. All flux measurements are given in units of  $10^{-10}$  ergs  $s^{-1}$   $cm^{-2}$ . Spectra extracted with the SF software were used to derive the fluxes. . . . 243

13.15 Parameters of the power law fit to the SAX J2103.5+4545 spectrum during the bright state (BS) and to the one during the faint state (FS). The spectra cover the 20-100 keV energy range. . . . . 247

**UNIVERSITAT DE VALÈNCIA**      **FACULTAT DE FÍSICA**

mit el Tribunal que susbscriu, en el dia de  
 data, acordà d'atorgar, aquesta Tesi Doctoral  
 a/Nº/Nº' ... Pere Blay Serrano .....  
 qualificació de ..Excel·lent cum Laude.....  
 data a ...20... de ...Maig..... de 2006...

El President,  


El Secretari,  


## Chapter 11

# Introduction

SAX J2103.5+4545 was discovered with *BeppoSAX* in 1997, when the source underwent a bright state (Hulleman et al. 1998). The source reached a maximum flux of 20 mCrab and was found to be an X-ray pulsar with a 358.61 s pulse period. An absorbed power-law of index 1.27 gave the best fit to the spectrum. The modulated nature of the high energy emission plus the spectral shape of the source pointed to an accreting compact object in a binary system as the most likely nature of the source. The presence of pulsations indicated that probably the compact object was a neutron star or a white dwarf. However, the white dwarf model was discarded because of the behaviour of the pulsation fraction, which tends to increase at lower energies in white dwarfs but showed the opposite behaviour in SAX J2103.5+4545. The orbital modulation of the outbursts suggested that the system would likely be a BeX system. A close-by B8 star, HD 200709, was proposed as candidate to optical counterpart to the system, but with some doubts because the star was never reported to have shown emission and the spectral type fell outside the O9-B2 range (typical of BeX counterparts).

Two more X-ray active phases are reported in the literature, in October 1999 and March 2001 (Baykal et al. 2000, 2002). Pulse arrival time analysis allowed the determination of the orbital parameters of the system. The orbital period was calculated to be  $12.68 \pm 0.25$  days and the eccentricity  $0.4 \pm 0.2$  (Baykal et al. 2000). A summary of the orbital parameters of the source is shown in Table 11.1.